Dynamical Studies of the Jovian Ionosphere

A thesis by

Thomas S. Stallard

submitted to the
UNIVERSITY OF LONDON
For the degree of
DOCTOR OF PHILOSOPHY

University College London April 24, 2001

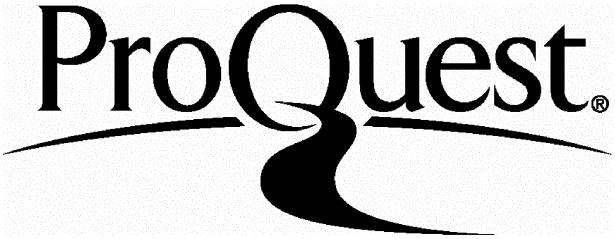

Abstract

This thesis uses H_3^+ spectroscopic observations of the Jovian ionosphere to characterise the physical conditions and dynamical processes within the aurorae. Five nights of observations were made using the CSHELL spectrometer on the NASA Infrared Telescope Facility, Mauna Kea, Hawaii. The spectrometer was set to a wavelength of 3.953 microns, sensitive to the H_3^+ molecular ion, a key component of the Jovian ionosphere. This provided an unprecedented level of detail on the processes within the Jovian H_3^+ aurora.

The first astronomical detection of the H_3^+ ($2\nu_2(0) \rightarrow \nu_2$) R(3,4$^+$) hotband allowed the detailed calculation of the variations in vibrational temperatures across the auroral region, and from this the further calculation of column density and total emission. The data was obtained under conditions where the Jovian ionosphere was hotter than previously reported, by about 100°K to 200°K. The correspondence between emission intensity and column density proves that H_3^+ intensity is a strong indicator of the location of energy deposition. The further correspondence between total emission and H_3^+ intensity shows that H_3^+ is a stabilising agent within the Jovian aurorae. Thus, energy deposition is balanced by H_3^+ cooling, which explains the lack of correlation observed between temperature and H_3^+ emission.

The CSHELL spectrometer produced spectra sensitive to Doppler shifts of as little as 300 m/s. A new observational technique was derived using a combination of spectroscopy and imaging, to take account of instrumental effects caused by spatial variations in the H_3^+ emission. Thus, a method of obtaining ion wind speeds from the Doppler shifting of H_3^+ emission lines is produced. It shows the existence of a regular electrojet around the main auroral oval, with speeds in the line-of-sight of around a few hundred m/s to 1 km/s, as well as a complex pattern of winds within the polar cap region.

Table of Contents

List of Figures

Chapter 1 : Introduction

Chapter 2 : Observations, Reduction and Data Analysis

Chapter 3 : Temperature, H_3^+ Column Density and Energy Balance in the Jovian Auroral Region

Chapter 4 : Dynamics of the Jovian Auroral Region

Chapter 5 : Summary, Discussion and Conclusions

List of Tables

Acknowledgements

Traditional acknowledgement pages are written in a very generic manner, and having at last completed the final draft of this thesis, I now, staring at a blank page, understand why.

As much as I wanted to individualise this page, as my colleges before me, I must firstly thank my supervisor. Dr. Steve Miller really *does* deserve the greatest of thanks, since he has provided me with incredible support, encouragement and guidance in both the writing of this thesis and the work which preceded it.

From the very moment I officially started this thesis, with the friends I made in a week at Liverpool, throughout the time I have spent in the Physics department at UCL, as well as a month in Honolulu, my spirits have been continually raised by the ubiquitous "too many people to mention". However, special thanks go to Andy Lim, whose love of coffee led to many an afternoon of peaceful reflection.

This thesis was enriched significantly through helpful discussions with my co-workers Daniel Rego, Nick Achilleos and George Millward, and was in part extended beyond the scope of the ionosphere through an important conversation with Renée Prangé. The time spent talking with people working at the IRTF, on both the Big Island and Oahu, was essential to the difficult calibration of the data set, and I am immensely grateful to Bill Vacca for always answering my e-mail queries, no matter how mundane.

Away from work, special thanks go to my best friends Tricia Gilbert and Ewan Willis, for both of whom friendship goes as far as editing. They should also be thanked for sexy eyes and silly trousers respectively.

The entertainment provided by the people of Bman's Pub is gratefully acknowledged, though the time spent talking to them, rather than working, should perhaps be hastily glossed over.

Finally, thanks must go to my family. My parents for love and inspiration throughout my life, my elder brother for the excellent example he sets (as well as having shown me the importance of getting a good PhD supervisor), and my younger brother for daring to follow his dreams.

This thesis is dedicated to the iife's work of Norville Rogers

Chapter 1 : Introduction

1.1 Jupiter

Jupiter is the fifth planet from the Sun, orbiting at 778,330,000 km (5.20 AU). With a mass of 1.90×10^{27} kilograms, it is by far the largest, more than twice as massive as all the other planets combined. Jupiter also rotates every 9hr 55min, faster than any other planet. It has a composition close to that of the primordial Solar Nebular, about 90% hydrogen and 10% helium (75/25% by mass), with only traces of methane, water and ammonia. The pressure in its centre is so great that, above a rock core, solid hydrogen exists, capable of producing a self-sustaining dynamo as in the Earth's iron core, and the combination of the huge mass and fast rotation produces a huge magnetic moment.

The magnetic field of Jupiter has a dipolar strength 10,000 times as strong as the Earth's. This deflects the solar wind around the planet, forming a huge cavity, a magnetosphere, in the wind. Within the magnetosphere, Io throws out huge amounts of material that becomes quickly ionised, forming an equatorial sheet of plasma away from the planet. It is effects from the interaction between this plasmasheet and the upper atmosphere of Jupiter that are to be studied in this thesis.

The precipitation of electrons and ions from the plasmasheet are responsible for the formation of highly energetic aurora in the Jovian ionosphere. Amongst other things, this energy produces the ion H_3^+, which can be observed in the infrared, and used as an indicator of temperature, heat loss and dynamics. This thesis is a detailed study of the variation in these parameters across the auroral region, studying with unprecedented detail the effects of the magnetosphere-ionosphere interaction, as well as the effects on the coincident neutral atmosphere.

1.1.1 Jovian interior

Our knowledge of the interior of Jupiter is highly indirect and likely to remain so for some time. Jupiter probably has a core of rocky material amounting to something like 10-15M_E.

Above the core lies the main bulk of the planet in the form of liquid metallic hydrogen, only possible at pressures exceeding 4 million bars, and consisting of ionised protons and electrons. This is electrically conducting and acts as a thermal convection-driven dynamo, the source of Jupiter's magnetic field (Acuña *et al.*, 1983). This layer probably also contains some helium and traces of various "ices".

The outermost layer is composed primarily of molecular hydrogen and helium, with trace amounts of water, carbon dioxide, methane and other simple molecules. Three distinct layers of clouds are believed to exist, consisting of ammonia ice, ammonium hydrosulfide and a mixture of ice and water.

1.1.2 Jovian atmosphere

Jupiter has no surface, since it is entirely gaseous, so the 1 bar level is taken as a "reference point" referred to as the Jovian "surface".

The atmosphere extends above the 1 bar "surface", in regions classified with the same names as the Earth, which are determined by the temperature profile. From the 170°K surface, the troposphere sees a drop in temperature until the 110°K tropopause at 0.1 bar. The temperature then increases throughout the stratosphere, levelling out to ~170°K at the 1 mbar stratopause. The temperature remains constant in the mesosphere up to the 1μbar mesopause, which is conventionally defined as the base of the thermosphere (Hunten, 1976).

The homosphere is a distinct region of the atmosphere, coincident with those regions described above where complete vertical mixing yields a near-homogeneous composition. The homopause, at 1-2μbar marks the ceiling of the homosphere, and above this level vertical mixing does not occur. This results in the an upper atmosphere that consists

solely of H and He, as the trace elements found lower in the atmosphere have settled out (Festou *et al.*, 1981).

The ionosphere is the region of the upper atmosphere, coincident mostly with the thermosphere, which contains a significant proportion of ions and free electrons. This, as the name implies, extends across the entire Jovian globe, but densities of charged particles vary considerably within this region. Below the ionosphere, the ionisation rate is lower than the ion-electron collision rate, keeping the charged particle population to a minimum.

The ionosphere is linked to the surrounding space along magnetic field lines. This means that the location of a field line on the "surface", as it passes through the ionosphere, can be matched with the location of that same field line as it crosses the equatorial plane in the magnetosphere. Features in the ionosphere are thus "mapped" to a distance beyond the planet, measured in Jovian radii.

If the Jovian magnetic field were perfectly dipolar, with the magnetic field and rotational axes coinciding, footprints of equipotential field lines would trace a circle of constant latitude. But the offset of Jupiter's dipolar field, and the need for higher order terms, means that an "oval" is effectively the location of an equipotential magnetic field line plotted at all longitudes on the planet; "footprint" is the location of a field line at specific point.

1.1.3 Jovian magnetosphere

Solar wind

The huge variation in pressure between the outer layers of the Sun and the surrounding interstellar space creates a pressure difference so great that it causes a flow of solar plasma to stream away from the Sun in all directions. This stream of protons and electrons travels with an average velocity of ~400 km/s, and carries with it a remnant of the solar magnetic field that dominates interplanetary space. The polarity of this field "switches" every few hours, and large systematic variations in the solar wind speed also

occur, often close to the regions of polarity change, resulting in velocities of up to 700 km/s.

When the solar wind encounters a planetary magnetic field like that of Jupiter, it is deflected at the sub-solar point where the opposing magnetic field pressure and solar wind dynamic pressure are balanced. A standing magnetosonic shock wave, known as the bow shock, is formed. This slows the solar wind, heating and deflecting it around the planet, creating a magnetospheric cavity. The planetary magnetic field is distorted by the flow of the solar wind, and is swept downstream, forming the magnetotail of the "teardrop" shaped magnetosphere.

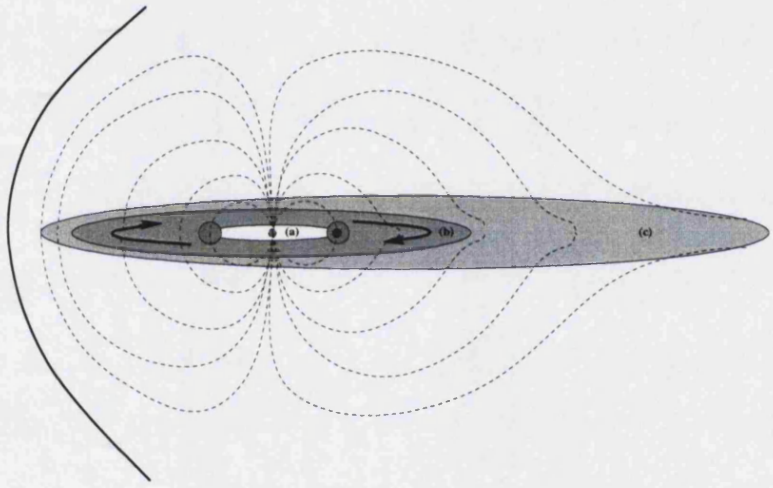

Figure 1-1: Sketch of the Jovian magnetosphere

For Jupiter, the magnetosphere can be divided into three basic regions, determined mostly by what controls its shape and physical conditions. The inner magnetosphere (a) is dominated by the planetary magnetic field, the middle magnetosphere (b) by a corotating disc of plasma originating from Io, and the outer magnetosphere (c) by the solar wind.

The inner magnetosphere

This region of the magnetosphere lies close to the planet, extending out from the planet's surface as far as Jupiter's moon Io, at $5.9R_J$. The magnetic field close to the planet is totally dominated by the field created by currents in the planetary interior. Further out it contains a torus of cold plasma beginning at $5.3R_J$, continuing until the boundary with a

warm Io torus at 5.6R_J. The warm torus surrounds the orbit of Io, extending beyond the inner magnetosphere out to 7.5 R_J.

These tori are created by the volcanic moon Io. The highly volcanic nature of the moon, powered by tidal interaction with Jupiter, means its atmosphere is continually resupplied with gases. These are quickly ionised and injected into the inner magnetosphere at a rate estimated to be at least 10^3 kg/s (Pilcher and Morgan, 1985), compared to the mass-loading rate of ~0.2 kg/s that the Earth receives from the solar wind and its own ionosphere.

The Io plasma torus feeds a "plasmasheet" in the middle magnetosphere, producing an outward flow of current from Io. A flow in the form of a "plasma ribbon" extends inward from Io, and is associated with field-aligned currents ("Ribbon currents") that connect latitudes below the main aurora in the Jovian ionosphere with the cold plasma torus in the magnetosphere (Morgan *et al.*, 1994; Rego *et al.*, 1999; and see Figure 1-2).

The middle magnetosphere

The magnetic field in this region is dominated by currents (ring current; current sheet) carried in the corotating plasmasheet (plasmadisc; magnetodisc) extending out from Io. It begins at the orbit of Io (5.9R_J) and extends out to the region where the corotation of the plasmasheet breaks down completely, between 50-60R_J. The general dipolar form of the magnetic field is maintained in this region, except close to the equatorial plane, where the radial components of the ring current stretch the field lines outwards.

The current sheet is tilted with respect to the rotational equator, resulting in a 10-hour periodic "rocking" of the sheet.

Currents flowing outwards through the sheet are part of a circuit that maintains the corotation of the plasmasheet with the magnetic field. The system described in this thesis, an extension of the Hill current system (Hill, 1979) is shown in Figure 1-2. The currents that flow through the plasmasheet flow along field aligned (Birkeland) currents, and close within the largely meridional Pedersen currents in the ionosphere. The region of corotation, starting at the orbit of Io and ending as corotation begins to break down,

marks where the field-aligned currents close on the ionosphere. The three systems shown in the figure are an extrapolation from the Hill model, showing the Ribbon current sheet described above and two regions that have been arbitrarily named within this thesis: the Inner Hill current system is associated with the maintenance of corotation in the plasmasheet and the Outer Hill current system which is associated with the production of aurora.

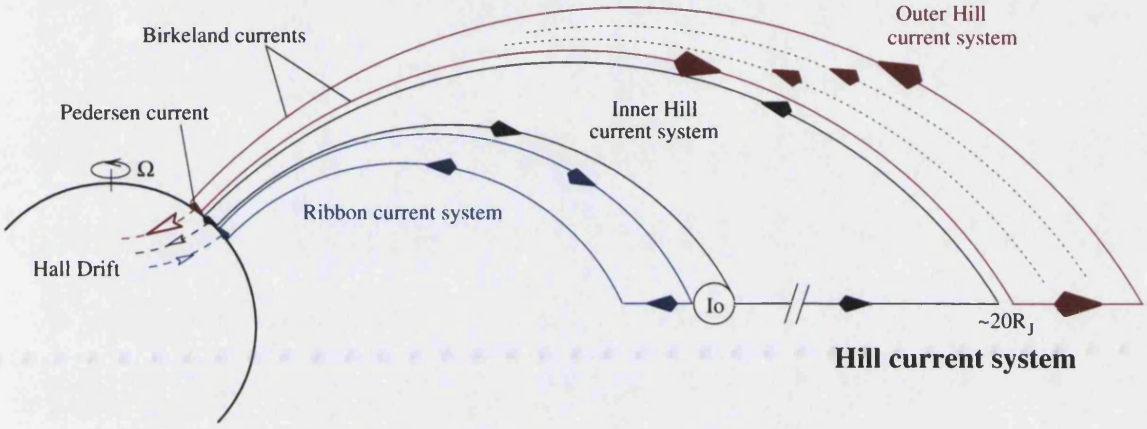

Figure 1-2: The magnetosphere-ionosphere interconnection along magnetic field lines

Newly created ions in the warm plasma torus orbit with Io, and have to be accelerated to rotate with the magnetosphere. It is the rotation of Jupiter that provides the energy for this acceleration. Friction between ions and neutrals in the ionosphere accelerate the ions into corotation with the underlying atmosphere, producing a Pedersen current via the $\mathbf{J} \times \mathbf{B}$ force induced as the ions move through the magnetic field. This torque is transferred to the magnetosphere by the Birkeland currents, which balances the inertial drag of the plasmasheet and accelerates it up to corotation, in the region described in this thesis as the Inner Hill current system.

The breakdown of corotation begins at a distance from the planet where the increasing inertia of plasma drifting outwards can no longer be balanced by the decreasing magnetic field strength. The breakdown appears to be staggered in a series of steps, and each of these have associated current produced within them, caused by the $\mathbf{J} \times \mathbf{B}$ force created by the now non-corotating plasma's motion within the corotating magnetic field, in the region described here as the Outer Hill current system. The location and magnitude of this breakdown is still a contentious issue, but it appears to begin between 12-20R_J (Hill,

1979), with the most substantial field-aligned currents occurring between 20-30R_J (Dougherty *et al.*, 1993).

The outer magnetosphere

Beyond the corotating plasmasheet, the magnetosphere becomes highly distorted due to the solar wind. The general form of the magnetosphere is a teardrop that extends 100R_J upstream (the "sunwards side"), 200R_J transverse to the solar wind, and as far as Saturn's orbit downstream (the "magnetotail"), but it shows large spatial and temporal variation as a direct response to changing wind pressure.

The magnetic field of the outer magnetosphere is, in the equatorial region, predominately in the dipolar direction, but the overriding characteristic of the field is its disturbed nature, most likely as the result of the dynamic behaviour of the plasma contained within it.

On the sunward side of the magnetosphere, the magnetopause boundary layer is located at the bow shock, separating the internal field from the magnetic field carried with the charged particles in the solar wind. Within the Earth's magnetosphere, this region is marked by viscous interaction with the solar wind, where "open" magnetic field lines link the solar wind directly to the Earth's polar caps, though no field-aligned currents have been detected over the Jovian poles (Dougherty *et al.*, 1993).

The Jovian magnetotail extends far into interplanetary space, out as far as the orbit of Saturn, some 4.3AU, so that the solar wind takes over 200 minutes to pass around the magnetosphere. The reconnection of magnetic field lines previously open to the solar wind allows material to escape from the closed magnetospheric system, and flow down the magnetotail and into the solar wind. This provides a loss process for material originally injected into the magnetosphere at Io.

Modelling the Jovian magnetosphere

Jupiter's magnetosphere can be represented, to a first order, by an offset tilted dipole model; but this is inaccurate, as the contributions from higher order magnetic multipoles are non-negligible. In order to properly model the magnetic field, it is necessary to incorporate higher order components, which in previous models, such as O_4 and O_6

(Acuña and Ness, 1976; Connerney, 1992), were produced from spacecraft measurements. However, tying these measurements to the surface has proved difficult, as they are confined to the spacecraft flyby trajectory, are generally obtained at considerable distance from the planet, and span a small range of planetocentric latitudes and longitudes. As a result, the models obtained are non-unique and incomplete.

The discovery of a distinct emission feature at the foot of the Io flux tube (Connerney *et al.*, 1993) provided a means to resolve some of these uncertainties. The feature traces a path around each magnetic pole, providing an unambiguous reference on Jupiter's surface through which magnetic field lines with an equatorial crossing distance of $5.9R_J$ must pass, providing a one-to-one mapping between the ionosphere and magnetosphere.

Using the footprint of the Io flux tube (IFT) as a constraint to the magnetic field model provides a "ground truth" to the spacecraft measurements. The VIP4 model (Connerney *et al.*, 1998) combines Voyager 1 and Pioneer 11 magnetometer observations with the IFT footprint imaging to produce a dual model consisting of a fourth order internal planetary magnetic field with an explicit model of the plasmasheet. It can be used to represent the magnetic field from the surface throughout the inner magnetosphere, and out to $\sim 30R_J$, and is especially effective in the polar regions, in which the aurorae lie.

1.1.4 Jovian aurorae

The aurorae on Jupiter consist of emission from a broad span of spectral lines and bands covering a wide range of wavelengths. These emissions are primarily due to a two-step process in which energetic particles (ions and electrons) precipitate into the upper atmosphere, colliding with neutral atoms and molecules, and in part converting their kinetic energy into energy stored in the chemically excited states of the particles. These chemically excited states then relax, and thus emit at a wavelength determined by the energy transitions in the relaxation process. The aurorae are thus a direct indicator of the effects of energetic particle precipitation from the magnetosphere into the atmosphere.

Preciptiation through field-aligned currents

The plasmasheet that extends out from Io corotates with the planetary magnetic field out as far as ~20R_J. Beyond this, the inertia of the plasma is too great for that corotation to be maintained, and the sheet lags behind the magnetic field. This produces the "Outer Hill current system" associated with the corotation breakdown in the plasmasheet, shown in Figure 1-2. This current is closed along field aligned currents and through Pedersen currents in the ionosphere, in the same way as the entire Hill current system, but the breakdown in corotation provides a far greater potential across it.

This means that the amount of charged particles carried within the circuit is far greater, and the electrons, flowing in the reverse direction to the current, flow into the ionosphere at the point where corotation breaks down, starting at 12-20R_J. This flow is the major cause of precipitating charged particles into the Jovian atmosphere, resulting in the ionisation of neutral material within the atmosphere, and ultimately the majority of the auroral emission seen in the ionosphere.

Pitch-angle scattering

Particles in the magnetosphere execute three motions directly related to the magnetic field: (1) cyclotron motion about the magnetic field line, (2) bounce motion along the field line, and (3) drift perpendicular to the magnetic field. The motion along the field line is centred around the equatorial plane, and extends as far as the combination of its kinetic energy and magnetic moment (which is conserved with the motion along the field line) are balanced against the increasing magnetic field strength as the field line nears the planet.

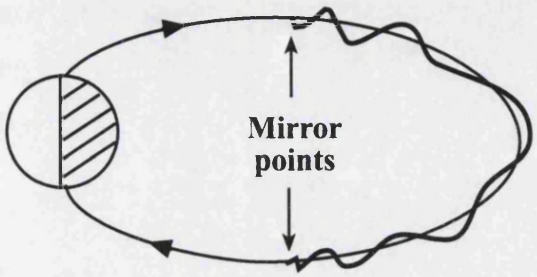

Figure 1-3: Sketch of the bounce motion of a charged particle

This results in the particle being "bounced" between two mirror points, as shown in Figure 1-3. However, when the kinetic energy of the particle is increased or the magnetic field strength decreases to a point where the mirror point enters the ionosphere, the particle can collide with the atmosphere and break this perpetual loop. This precipitation can produce visible effects on Jupiter where the mirror points lie very close to the ionosphere, so that as the particles drift around the planet (the third motion, above) into a region of lower magnetic field strength, the depth they can penetrate increases enough to extend into the atmosphere.

Auroral emission

The energy of the precipitating charged particle determines the depth to which it can penetrate into the atmosphere, and the energy it imparts determines the type of emission that ionised molecules will result in. The energy of impacting charged particles covers a wide range, and auroral emissions have now been detected from Jupiter at a full range of wavelengths, from X-rays to radio waves.

High energy X-ray emissions have been detected in the auroral region, caused by highly ionised S and O ions (Waite *et al.*, 1994). Nearly stripped of electrons while precipitating, these are either directly excited or charge exchanged into an excited state through further collisions, to emit an X-ray photon on decay back to the ground state. The precipitation occurs with energies in excess of 300 KeV nucleon^{-1} from 8-12 R_J in the magnetosphere (Cravens *et al.*, 1995), and are deposited well below the methane homopause (Horanyi *et al.*, 1988).

The molecular and atomic hydrogen in the Jovian atmosphere is collisionally excited by energetic electron impact to a greater extent than by heavy ions (Trafton *et al.*, 1998). The Jovian UV emissions result from the radiative de-excitation of this hydrogen, leading to H_2 Lyman and Werner bands, and the H Lyman α line.

The timescale between collisional excitation and radiative de-excitation is relatively small compared with other auroral processes, and thus UV emission is considered to be the indicator of the location of particle precipitation flux, produced by a "pump and dump" method. The associated temperatures of this emission are ~25000°K, so UV emission is

not representative of the thermospheric temperature. The bulk of the auroral emission is produced near the methane homopause (Harris *et al.*, 1996), though the depth of penetration depends both on initial energy and the angular distribution of incoming particles (Prangé *et al.*, 1995).

The Voyager spacecraft tentatively identified a visible wavelength aurora, but it was the Galileo satellite that first properly imaged the Jovian night-side aurora (Ingersoll *et al.*, 1998). It has an apparent width of <200 km in some cases, and was located at ~10μbar, beneath the homopause.

Infrared auroral emissions have been detected on Jupiter from a variety of molecular species. Extensive hydrocarbon emissions have been studied (Caldwell *et al.*, 1980; Caldwell *et al.*, 1983; Kim *et al.*, 1985), as well as quadropole H_2 transitions (Trafton *et al.*, 1989) and H_3^+ ro-vibrational (rotational-vibrational) transitions like those used in this thesis.

Hydrocarbon aurora provide a direct probe of the ~10μbar region, and exhibit features ("hot spots") of enhanced emission and increased temperature (Livengood *et al.*, 1993). The most notable of these is fixed at 150°-180° longitude and 60° latitude in the north. The quadropole transitions are caused by the rotational-vibrational relaxation of H_2. These have only been used marginally in Jovian auroral observations, and provides a method of deriving the auroral temperatures, albeit relatively inaccurately (Kim *et al.*, 1990).

The study of the H_3^+ aurora began with the discovery by Drossart *et al.* (1989) and Trafton *et al.* (1989), of the $2\nu_2$ overtone band at ~2μm. Further successful observations were made of the fundamental ν_2 band emission at ~4μm (Oka and Geballe, 1990; Miller *et al.*, 1990), which were used to better understand the temperature of the ionosphere. These studies showed that the H_3^+ emissions were highly variable in brightness and derived temperature.

Not long after these initial results, the first images of the H_3^+ aurora were made (Kim *et al.*, 1992; Baron *et al.*, 1991), using the 4μm emissions. Further studies concentrated on expanding the number of H_3^+ lines detected (Drossart *et al.*, 1993), locating the Io flux

tube (Connerney *et al.*, 1993), and making a comprehensive study of the H_3^+ morphology (Satoh *et al.*, 1996) and physical conditions both in the aurora and on the body of the planet (Ballester *et al.*, 1994; Lam *et al.*, 1997; Miller *et al.*, 1997a). H_3^+ emissions were also used to monitor the comet Shoemaker-Levy 9 (SL-9) collision with Jupiter, both during and after the impacts. A chronological history of the effects of the SL-9 collision is given by Miller *et al.* (1997b).

The use of H_3^+ emission has now become an established technique for probing the physical conditions of the Jovian auroral regions. With excitation temperatures equivalent to ~750°K (4μm) and ~1000°K (3μm), H_3^+ wavelengths sample the range of ionospheric/thermospheric temperatures very effectively. This thesis builds on the extensive studies previously made, improving upon spectroscopic studies of temperature and column density structure (Lam *et al.*, 1997; Miller *et al.*, 1997a), energy balance (Rego *et al.*, 2000) and dynamics of the auroral region (Rego *et al.*, 1999a), and providing comparative data for imaging studies (Satoh *et al.*, 1996; Satoh and Connerney, 1999).

Decametric radio emissions (~10m wavelength) have considerable temporal and frequency structure within them, associated with instabilities in the plasma in the inner radiation belt, and with instabilities in field-aligned currents connecting Io to the ionosphere (Zarka, 1998). The presence of the magnetosphere was first revealed through radio emission, and the study of the magnetosphere continues to use radio waves extensively.

Auroral morphology

As stated above, UV emissions are the best indicator of the location of particle precipitation into the ionosphere. In addition, recent UV observations, made with the Faint Object Camera (FOC), the Wide Field and Planetary Camera (WFPC), and most recently the Space Telescope Imaging Spectrograph (STIS) onboard the Hubble Space Telescope (HST), allow a previously unparalleled level of spatial resolution.

H_3^+ observations also provide a detailed view of the morphology of the auroral region (Satoh *et al.*, 1996), and also an extensive understanding of the physical conditions within the aurorae. The basic morphology of the H_3^+ aurora is similar to that of the UV

emission, but as the timescale from ionisation to emission is longer, H_3^+ is a less accurate probe of the location of particle precipitation. In addition, since infrared observations have to be made using ground-based telescopes, the spatial resolution of H_3^+ imaging is lower.

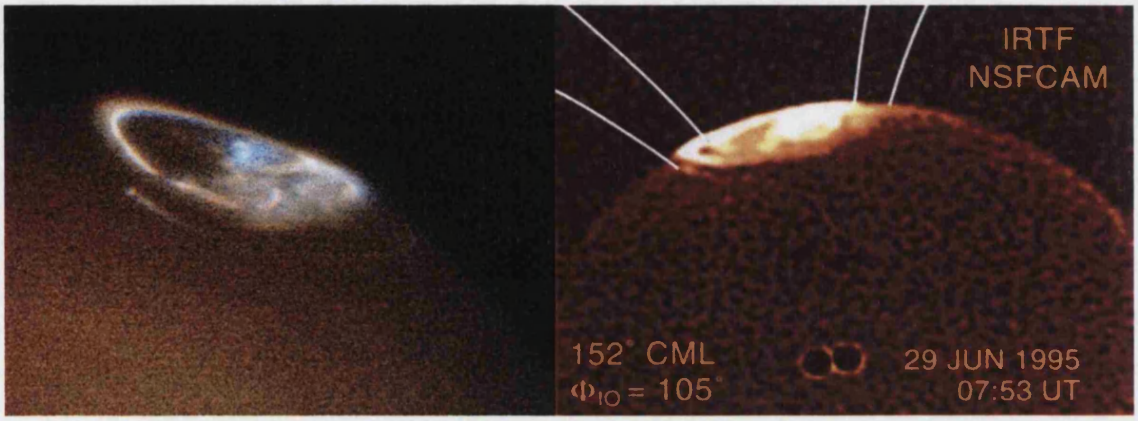

Figure 1-4: Images of the UV (by J.T. Clarke, using the HST/STIS) and IR (by J.E.P. Connerney, using the IRTF/NASCAM) Jovian northern aurora

The UV auroral region is divided into dawn and dusk sectors, across which there is significant variation in emission morphology. The emission is confined to an auroral oval consisting of an arc of variable width (Clarke *et al.*, 1996), narrow on the dawn side of the aurora, and broader on the dusk side.

On the dusk side of the aurora, there is also a region of broad and diffuse emission (Gérard *et al.*, 1994a, 1994b; and Kim *et al.*, 1995), which lies poleward of the main auroral oval. This emission constitutes a separate feature from the main oval, both in its location and because its brightness varies independently. These are similar to another feature, "dawn storms", fixed local time near the dawn terminator, rather than rotating with System III (Clarke *et al.*, 1998). These are associated with the "sub-storms" seen on Earth.

Such features may be connected with regions in the outer magnetosphere, as the auroral signature of solar wind driven convection, compared with aurorae resulting from corotation in the middle magnetosphere. Another proposed cause of these emission features is an ionospheric current system in the polar cap driven by heating in the main oval (Clarke *et al.*, 1996). Discrete emission from the foot of Io's magnetic flux tube has

been observed equatorward of the main ovals (Clarke *et al.*, 1996), as well as possible analogous footprints associated with Europa and Ganymede.

Analysis of the HST/WFPC2 images has been used to attempt to better locate the auroral main oval, which has recently been linked to a region within the magnetosphere greater than $12R_J$ (Clarke *et al.*, 1996) and between $9\text{-}15R_J$ (Grodent *et al.*, 1997). However, uncertainties with the magnetic field model used to get these values means that this value does not contradict previously used values of $30R_J$ (Gérard *et al.*, 1994a).

Ionospheric models

There have been many successful attempts to model the Jovian ionosphere and aurorae (*e.g.*, Gross and Rasool, 1964; Atreya and Donahue, 1976; Waite *et al.*, 1983; McConnell and Majeed, 1987; Kim *et al.*, 1992). These models are, however, all restricted to one (vertical) dimension, so the effects of horizontal dynamical mixing on the energy balance and chemistry of the atmosphere cannot be reproduced.

The Jovian Ionosphere Model (known as JIM; Achilleos *et al.*, 1998) is the first time-dependent, three-dimensional, fully-coupled model for the thermosphere and ionosphere of Jupiter. Initial studies using the model have shown its strong potential as a companion to observational work, providing information including wind speeds, ionisation levels, temperature and neutral composition, with future publications extending this role further (Achilleos *et al.*, submitted).

1.2 The H_3^+ Molecule

H_3^+ was first discovered in 1911, using an early form of mass spectroscopy (Thomson, 1912). The existence of the H_3^+ line was questioned, however, until a series of electronic structure calculations were made in the 1930s, which proved the stability of the now-accepted triangular structure (Hirschfelder, 1938).

By the early 1970s, H_3^+ was predicted to play a very important role in interstellar chemistry, initiating the chains of chemical reactions that produce the wide variety of species seen within the dense clouds in the interstellar medium (Herbst and Klemperer,

1973; Suzuki, 1979). Because of this, the initial celestial searches for H_3^+ were made in the interstellar medium, but such a detection eluded observers for years. The first astronomical detection of a H_3^+ spectrum was made unwittingly in an object and at a wavelength no one had thought to look in, by observations designed to detect another molecule.

In late 1987, Trafton *et al.* observed the H_2 S(1) quadropole transition in Jupiter's auroral region, using a grating spectrometer at the McDonald observatory. Along with the expected emission at 2.121μm, they also observed a strong unidentified emission feature at 2.093μm, as well as other weaker emissions. Drossart *et al.* (1989) also studied the H_2 transitions, but at higher resolution. They, too, detected unexpected strong emission lines around the H_2 line, and after a month of international discussion with *ab initio* spectrum modellers and laboratory spectroscopists, it was identified as the $2\nu_2\,(2) \rightarrow 0$ band of H_3^+. This initial detection opened up a decade of investigations using this fundamental ion as a probe of the physical and chemical conditions in the Jovian upper atmosphere.

Beyond Jupiter, H_3^+ has since been detected on both Uranus (Trafton *et al.*, 1993) and Saturn (Gaballe *et al.*, 1993), although no detection has been made for Neptune. The first detection of H_3^+ outside the solar system was made in the remnants of the supernova SN1987a in 1992 (Miller *et al.*, 1992), and it was not until 1996 that the detection of interstellar H_3^+ was finally made (Geballe and Oka, 1996).

1.2.1 The H_3^+ lifecycle

H_3^+ is formed in the Jovian atmosphere through a fast chain reaction process beginning with ionisation. H_2^+ is created within the Jovian ionosphere by two separate processes. Lower concentrations of H_2^+ are created globally by solar EUV radiation ionising molecular hydrogen:

$$H_2 + h\nu \rightarrow H_2^+ + e$$

Large amounts of H_2^+ are formed in the high latitude aurora, through the ionisation of molecular hydrogen by energetic electrons, which precipitate into the atmosphere along magnetic field lines:

$$H_2 + e^* \rightarrow H_2^+ + e + e$$

The H_2^+ ion is then rapidly converted to H_3^+ by the strongly exothermic reaction:

$$H_2^+ + H_2 \rightarrow H_3^+ + H$$

H_3^+ is, in most conditions, a highly reactive molecule, and is used in the modelling of interstellar species as a powerful protonating agent through the reaction:

$$H_3^+ + X = HX^+ + H_2$$

However, in the upper atmosphere of Jupiter, where only H and He occur above the homopause, such reactions cannot take place (since He has a lower proton affinity than H_2). As a result, the lifetime of the H_3^+ molecule is directly controlled by dissociative recombination:

$$\begin{aligned} H_3^+ + e^- &\rightarrow H_2 + H \\ &\rightarrow H + H + H \end{aligned}$$

The rate that this reaction occurs at is controlled by the electron density at the particular altitude of the Jovian atmosphere in question, and the recombination rate constant $\kappa_r(H_3^+)$:

$$\tau_r(H_3^+) = \left([e^-] \times \kappa_r(H_3^+)\right)^{-1}$$

At the 0.1μbar region of the aurora, where the H_3^+ density reaches a maximum, the electron density $[e^-]$ peaks at values of the order 10^6 cm^{-3}; the measurements of Leu *et al.* (1973) yield a recombination rate constant $\kappa_r(H_3^+) = 2.3\times10^{-7} cm^3 s^{-1}$, so the minimum molecular lifetime of H_3^+ $\tau_r(H_3^+)$ is of the order 10s (Achilleos *et al.*, 1998).

1.2.2 H_3^+ spectroscopy

H_3^+ is the simplest and most stable polyatomic molecule. In equilibrium the three protons form an equilateral triangle, though this structure is considered to be highly "floppy" (Sutcliffe and Tennyson, 1986), resulting in a highly complex spectral signature.

Observational spectroscopy relies on the coupled rotational and vibrational transitions of a molecule in the infrared: H_3^+ has no permanent dipole, thus there is no pure rotational spectrum; excited electronic states are unstable, so there is no UV/visible spectrum.

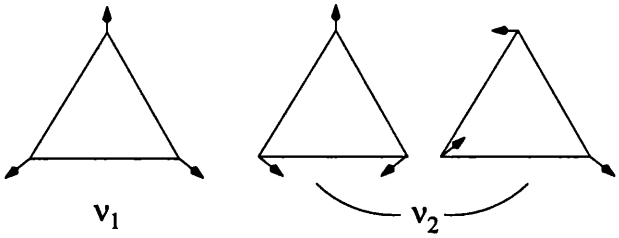

Figure 1-5: The motions involved in the H_3^+ vibrational modes, ν_1 and ν_2

H_3^+ has two vibrational modes: a symmetric "breathing" mode, ν_1, and an infrared active bending mode, ν_2 (Figure 1-5). Because its equilateral triangle shape provides no dipole, H_3^+ does not have a pure rotational spectrum, but it does have ro-vibrational (rotational-vibrational) modes caused through the dipole created with the varying position of atoms by vibration.

Figure 1-6, based on a figure in Tennyson and Miller (1994), shows the fundamental (ν_2) and overtone ($2\nu_2$) levels of the bending mode, resulting in fundamental, overtone and "hot" ($2\nu_2 \leftrightarrow \nu_2$) bands in emission. For clarity only a few rotational levels have been shown on the diagram and the splitting of the rotational levels has been neglected.

Transitions involving states with rotational angular momentum, J, up to 9 have actually been observed on Jupiter. In laboratory work, there have been over 600 spectral lines assigned from the fundamental, overtone and hot bands, and *ab initio* calculations of the predicted spectrum of H_3^+ have produced a line list that contains in excess of three million transitions (Neale *et al.*, 1996).

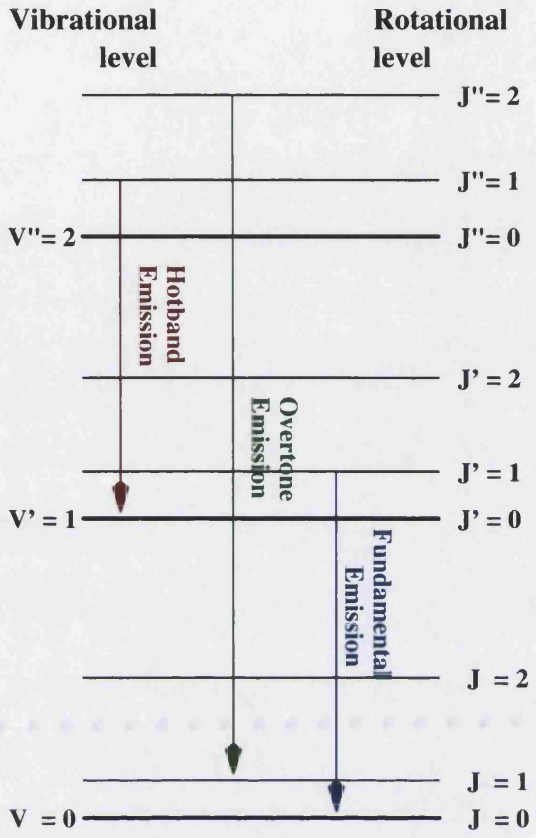

Figure 1-6: Rotational and vibrational energy levels, and the associated emission features

1.3 Physical Conditions in the Ionosphere

1.3.1 Composition of the ionosphere

Above the homopause region, the chemistry of the ionosphere is very simple, since only hydrogen and helium exist as significant species. This thesis concentrates upon the ionisation chemistry of hydrogen, and specifically the processes that lead to the creation and destruction of H_3^+.

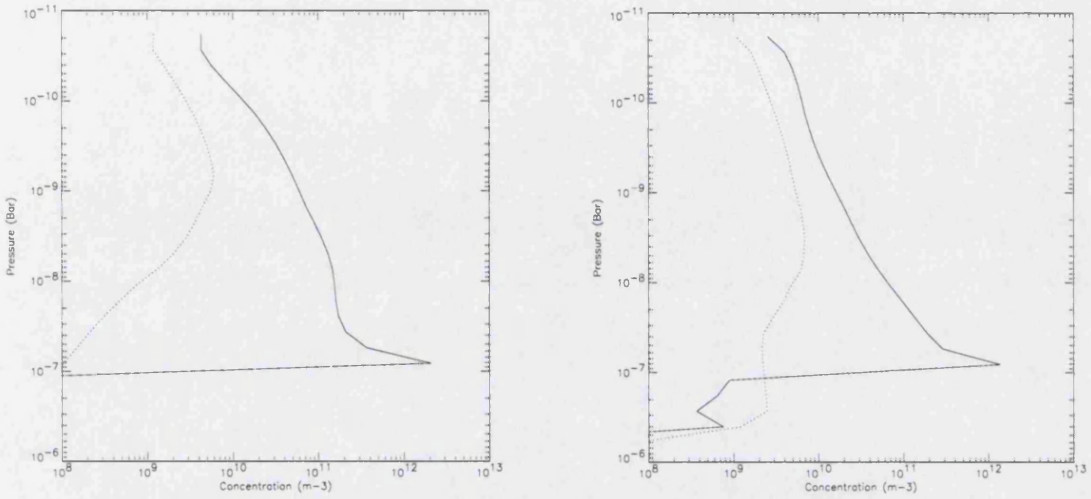

Figure 1-7: The vertical profile of H^+ (left) and H_3^+ (right) taken from JIM; the auroral profile (solid) is shown for a simulated 100 ergs cm^{-2} input, with the equatorial profile (dashed)

In Figure 1-7, the total density of both H^+ and H_3^+ are given for the auroral and equatorial regions, produced by JIM. The non-auroral component shows the concentration of both species through EUV production. The auroral component in both populations increases with decreasing pressure, as far as the 0.3μbar region. Below this pressure level lies the homopause, and with the introduction of hydrocarbon species below this point, the population of H_3^+ decays very quickly.

1.3.2 H_3^+ auroral emission

The original detection of H_3^+ was made with the overtone spectra (Drossart *et al.*, 1989), but the majority observations since then have used the fundamental spectra, in which some of the most important transitions occur between 3-4μm. This wavelength corresponds with the astronomical "L window", a region that lacks excessive absorption in the Earth's atmosphere, as well as the absorption of incoming solar radiation in the Jovian atmosphere, by the methane fundamental ν_3 band, which makes the background planetary disk very dark. Thus the 3-4μm region is very sensitive to the abundance and distribution of H_3^+ on Jupiter.

The H_3^+ infrared emission, because of the indirect creation process, may or may not occur in proximity with the UV molecular hydrogen emissions. In appearance at least, the two

seem morphologically analogous, and a direct correlation is generally assumed (Satoh *et al.*, 1996). Using an emission source model, Satoh and Connerney (1999) have delineated the regions of H_3^+ emission from 3.43μm images taken using with a 0.148 arcsec per pixel resolution.

They divide the Jovian upper latitudinal region into five major zones, based on the equipotential magnetic field strength footprints taken from the VIP4 model, and a separate emission spot from the footprint of Io (Connerney *et al.*, 1998):

1. The Io footprint, a distinct emission feature at the foot of the Io Flux Tube, located where the magnetic field lines thread the satellite, at an orbital distance of $5.9R_J$, intersect with the Jovian ionosphere.

2. A region between the $6R_J$ and $8R_J$ ovals, representing emissions originating near or just beyond Io's orbit. This region contains only weak emission (~10% of the total auroral emission) except for that directly associated with the Io flux tube.

3. A region between $8R_J$ and $12R_J$, potentially including Europa emission sources, containing a significant amount of emission. The peak emission in this region occurs at λ_{III}~215° in the north, and is explained as resulting from relatively slow pitch angle scattering of drifting electrons, which impact with the ionosphere when the path of their drift traverses the location where the magnetic field weakens significantly, the "windscreen wiper" effect. This zone accounts for ~20% of the total auroral emission.

4. A region between $12R_J$ and $30R_J$, which contains the main auroral emission, assumed to be coincident with the main UV auroral oval. The peak emission occurs at λ_{III}~260° in the north, corresponding to the minimum surface field magnitude in the VIP4 model. This zone accounts for ~25% of the total auroral emission.

5. A region poleward of the $30R_J$ oval, known as the polar cap. This region is filled with weak emission and contains significant levels of local-time enhancements to the emission levels. This enhancement is modelled with a "Yin-and-Yang" shape, with the polar cap split into two regions of equal area:

a. Local-time enhancement in the dusk-side cap; this feature has a terrestrial analogue attributed to the enhanced Joule heating of the Earth's ionosphere (Rees and Fuller-Rowell, 1991);

b. Background polar-cap emission in the dawn-side cap.

These regions appear to be analogous with the bright and dark polar regions seen within the UV observations.

At latitudes below this complex auroral emission region, mid-to-low latitude H_3^+ emission also exists (Miller *et al.*, 1997a). It is likely that this is caused by particle precipitation from regions of space inside the orbit of Io, extending down to the planet, and not H_3^+ transport away from the poles, which has been ruled out by modelling (Achilleos *et al.*, submitted).

Daily variations in the overall H_3^+ auroral brightness may correlate with variations in the solar wind ram pressure (Baron *et al.*, 1996). This correlation is caused by the increased magnetic field strength within the magnetosphere caused by the compression by increased ram pressure, allowing an increase in pitch angle scattering. This is the currently the only, albeit indirect, linking of the Jovian auroral processes with the solar wind.

1.3.3 Ionospheric temperature

The temperature of H_3^+ can be calculated by ratioing the emission intensities from two or more separate excitation levels. Rotational temperatures are calculated using spectra of different rotational energies from the same vibrational manifold, and vibrational temperatures using spectra that originate from or between separate vibrational manifolds.

This measured temperature is specific to H_3^+, unless H_3^+ can be shown to be thermalised with the surrounding neutral atmosphere, in which case the measured temperature is comparable to the kinetic temperature. The assumption of thermalisation is made regularly in the literature, as it is necessary to produce calculations of column density and total emission, but Kim *et al.* (1992) questioned this basic assumption.

Local thermal equilibrium

In the model of Kim *et al.* (1992), high Einstein coefficients associated with (Δv_2) transitions of H_3^+ are shown to result in the radiative depopulation of vibrationally excited ($v_2 > 0$) levels being comparable with timescales for collisional population from the ground or (v_1, $v_2 = 0$) state.

This comparison is defined clearly in Rego *et al.* (2000). The rate of emission is given by the Einstein coefficient, A_{if}, which for the fundamental H_3^+ (v_2=1) Q(1,0$^-$) line is 129s^{-1}, so the average radiation lifetime is ~7.8x10^{-3}s, compared with the value of $\tau_r(H_3^+)$ of ~10s already noted.

However, the key consideration beyond this is that collisions capable of exciting a H_3^+ molecule from its ground state to the emitting (v_2=1) level occur at a reasonable rate compared with the radiation lifetime.

We assume the mechanism for efficient H_3^+ collisional excitation ("proton hopping") as:

$$H_3^+ + H_2^* \rightarrow H_2 + H_3^{+*}$$

where the fraction of H_2 molecules with enough energy to cause this excitation is given by:

$$\exp\left(\frac{-E^*}{kT}\right)$$

From this, the average collisional excitation rate at the altitude of highest H_3^+ density can be calculated by factoring the "proton hopping" rate (10^{-9}cm^{3}s^{-1}), the fraction of collisions that produce an excitation into the (v_2=1) level (0.05), and the molecular density of H_2 (2.4×10^{13}cm^{-3}). This results in a collision rate of ~1.2×10^{3}s^{-1}, which provides an average collisional excitation time of 8.3x10^{-4}s. This is only a factor of 10 shorter than the radiation lifetime and results in a radiative depopulation, predicted by Kim *et al.* to result in an overpopulation of the ground state by a factor of ~10. There is, however, almost full thermalisation within rotational levels of any individual vibrational manifold, because

the lack of a permanent dipole makes radiative transitions involving only a changed rotational state very slow (~10^4s), leaving time for collisional thermalisation.

The relative overpopulation of energy states also occurs to some extent at higher vibrational manifolds, so that the same factor that leads to the depopulation of (v_2 = 1,2,3 etc.) with respect to the ground state would also lead to a depopulation of H_3^+ (v_2 = 2,3,4 etc.) with respect to (v_2 = 1). However, Kim *et al.* emphasise that the fractional populations of (v_2 = 1) and (v_2 = 2) are only slightly smaller than those of a Boltzmann distribution.

In a direct attempt to address this issue, Miller *et al.* (1990) observed ($v_2 \rightarrow 0$) and ($2v_2(l=2) \rightarrow 0$) spectra of the Jovian northern aurora in quick succession. They came to the conclusion that ro-vibrational temperatures derived from within individual vibrational manifolds and vibrational temperatures derived by ratioing between two separate levels could not be distinguished beyond the threshold of observational noise. They proposed that H_3^+ was at least in "quasi-thermal equilibrium", so that even though the ground-state might be overpopulated, the vibrationally excited levels can be considered to be populated as might be expected from a Boltzmann distribution at the given rotational (and thus kinetic) temperature.

This assumption of quasi-thermal equilibrium means that H_3^+ is thermalised with the predominantly H_2 neutral atmosphere, making it possible to use effective vibrational temperatures to calculate both kinetic temperatures and the total column densities from observations.

However, the assumption made should be considered in the context of its potential relation to true local thermal equilibrium. If radiative depopulation leads to a significant non-Boltzmann fractional population of (v_2 = 1) and (v_2 = 2), then the (v_2 = 1) level will be appreciably overpopulated, just as the ground state is. This will lead to a calculated effective vibrational temperature that under-estimates the kinetic temperature of the atmosphere.

1.3.4 Column density

Given the assumption of quasi-thermal equilibrium discussed above, the calculated temperature can be used to produce a value for the column density, the density within a column of material down through the atmosphere along the line-of-sight. This is calculated by using the temperature to determine the emission from a single molecule of H_3^+, and using this with the intensity of the spectrum to calculate the line-of-sight density.

1.3.5 Total emission

Lam *et al.* (1997) found that temperature and column density were 99% anticorrelated for any given observed spectrum, giving a range of uncertainty taken as a pair that exceed that attributable to the individual parameters. By assuming local thermal equilibrium, they were able to combine the two parameters into one, the total emission of H_3^+ - $E(H_3^+)$.

Total emission of H_3^+ is defined as the emission from all the possible transitions of H_3^+, calculated by finding the total emission per molecule for the given temperature (using a previously calculated function from the literature), assuming local thermal equilibrium (LTE), and multiplying it by the corresponding column density. The total emission is a useful parameter in its own right, providing the total power output attributable to H_3^+, showing regions of cooling clearly and thus giving insights into the energy balance in the Jovian ionosphere and thermosphere.

1.3.6 Previous measurements of the physical conditions

Previously observed measurements of the different H_3^+ parameters discussed above are shown in Table 1-1. The temperature of the H_3^+ auroral emission has been recorded in observations ever since the first detection of the ion by Drossart *et al.* (1989). The temperatures appear to vary considerably across all those recorded, ranging between 600-1100°K in the aurora regions. The column density appears to vary between $1\text{-}10\times10^{16}$ m^{-2}, though the variation does not appear to be controlled greatly by the corresponding temperatures. The total emission is a relatively new parameter to be measured, but the recordings so far made suggests it varies between $1\text{-}4\times10^{-3}Wm^{-2}$.

Table 1-1: Previous measurements of H_3^+ parameters, shown where applicable for the northern aurora only

Publication	Temperature (°K)	Column Density ($\times 10^{16} m^{-2}$)	Total Emission (Wm^{-2})
Drossart *et al.* (1989)	1099 (±100)	6-10*	---
Oka and Geballe (1990)	670 (±100)	1.1-11[†]	---
Miller *et al.* (1990)	1100 (±100)	---	---
Maillard *et al.* (1990)	830(±50); 850(±110)	---[‡]	---
Kim *et al.* (1992)	950 (±100)	---	---
Miller *et al.* (1991)	1020; 810	Varied	---
Ballester *et al.* (1994)	680-900	11.5	---
Miller *et al.* (1995)	800-1000	~10	---
Lam *et al.* (1997)	779-909	1.21-3.96[§]	0.0013-0.0026[§]
Miller *et al.* (1997a)	822	5.42	0.0037

* Predicted column density; a value of 1.39 (±0.13)$\times 10^{13} m^{-2}$ was measured for the $2\nu_2(l=2)$ vibrational state

[†] This assumes an equivalent vibrational temperature; a value of 0.1-1.0$\times 10^{15} m^{-2}$ was measured for $\nu_2=1$ level

[‡] Measured values of 1.16-2.36(±0.14)$\times 10^{14} m^{-2}$ were made in the north for the upper state of the ν_2 band

[§] Value before line-of-sight correction

1.3.7 Energy balance in the ionosphere

The temperatures recorded in the Jovian ionosphere are far beyond the expected temperatures from solar flux energy input, which should produce a temperature no higher than 200-300°K (Atreya *et al.*, 1979). Non-auroral temperatures, which vary between 700°K and 950°K (de Bergh *et al.*, 1992; Miller *et al.*, 1997a) are several hundred degrees higher than expected from the solar influx to the ionosphere thermosphere of just 60$\mu W m^{-2}$ (Atreya, 1986). Waite *et al.* (1983) proposed that energy from the auroral regions might be transported to lower latitudes by thermospheric winds, but the energy source to power these winds is still not unambiguously identified.

Proposed sources for the missing energy source that causes this heating include energetic particle precipitation, acceleration of photoelectrons, gravity waves and large-scale energy transport (*e.g.*, Atreya *et al.*, 1979; Prangé, 1986; Hunten and Dessler, 1977; and Sommeria, 1995). Of these mechanisms, only energy transportation appears to explain the main features of the Jovian thermospheric structure in a self-consistent way (Waite *et al.*, 1983; Clarke *et al.*, 1991).

1.3.8 Dynamics of the Jovian aurorae

The "Outer Hill current system" associated with the breakdown in corotation described above (**1.1.3 The middle magnetosphere**) results in large-scale meridional Pedersen currents flowing through the auroral regions of the ionosphere, approximately coincident with Jupiter's bright auroral ovals. This meridional potential difference projected across the ionosphere interacts with the near-vertical planetary magnetic field to produce an oval aligned $\mathbf{E} \times \mathbf{B}$ Hall drift, which causes both ions and electrons to flow in an anti-corotational direction - the auroral "electrojet" (Figure 1-2).

Indirect evidence of the electrojet

Prangé *et al.* (1997) detected an asymmetry in their Lyα line profiles, with differences in intensity between blue and red peaks, which they argue may be indicative of Doppler motions of up to a few kilometres per second along the line-of-sight.

The effects of a supersonic electrojet have been modelled by Sommeria *et al.* (1995) to explain both the permanent "bulge" in Lyα emission fixed at λ_{III} ~100°, and the planetwide excess in temperature in the Jovian upper atmosphere (see above). For the collisional acceleration process to transport material and energy to the equator, the electrojet velocity is required to be ~20 km/s, considerably above the speed of sound at the 0.1μbar level, where V_{sound} ~3 km/s.

The presence of mid-to-low latitude H_3^+ emission has been suggested as evidence of such a transport of energy from the aurora to lower latitudes (Miller *et al.*, 1997a), with transport to the equator possible if H_3^+ is carried up the nanobar region, where the low electron densities produce $\tau_r(H_3^+)$ ~10^4s. (Mid-to-low latitude precipitation was also suggested as an alternative source of the H_3^+ emission, and is preferred in recent modelling (Achilleos *et al.*, submitted).)

Direct evidence of the electrojet

Rego *et al.* (1999) observed an "auroral event" using the CSHELL spectrometer on the IRFT on Mauna Kea, on August 6, 1997 (see **2.1 The CSHELL Instrument**, for details

of the spectrograph). This 20-30 minute fortuitous event resulted in the first ever measurement of Doppler-shifted H_3^+ in the Jovian ionosphere. Using the slit aligned along the rotational axis of the planet, the H_3^+ latitudinal intensity profiles showed a "double peak" structure. The outer peak was red-shifted, and the inner peak slightly blue-shifted. For the period that the two-peaked structure was present, the poleward peak was seen to be red-shifted relative to the equatorward peak by -2.5 ±0.2 km/s.

These observations were shown to be consistent with H_3^+ ions flowing in a clockwise, anti-corotational, direction along the ~30R_J auroral ovals in both hemispheres. This is consistent with an $\mathbf{E} \times \mathbf{B}$ Hall drift forcing an ion wind around the planet along equipotential magnetic field strength. This ion wind is the first direct evidence for a Jovian auroral electrojet. The term electrojet applies to electric current, so the detection of an ion wind cannot directly be equated with an electrojet. The $\mathbf{E} \times \mathbf{B}$ Hall drift that forms the electrojet causes the electrons and ions to flow in the same direction, which in theory results in zero net current.

However, the terrestrial auroral electrojet is commonly ascribed to a Hall current (Boström, 1964), with the electrons undergoing an $\mathbf{E} \times \mathbf{B}$ drift and the ions being constrained by collisions with the neutral atmosphere. JIM (Achilleos *et al.*, submitted) shows that collisions between the ions and neutral molecules in the upper atmosphere are slowing, yet not halting, the flow of the ions around the magnetic pole. The velocity difference between ions and electrons equates to an electric current, and thus an electrojet does occur; the ion drift follows the same path as this electron drift, at a slower relative velocity, allowing a H_3^+ Doppler shift to be detected with respect to the rest frame of Jupiter.

The only other evidence for H_3^+ Doppler shifting from Jupiter currently made is a tenuous detection of 2 km/s retrograde winds made on the Jupiter north and south-eastern limb (Maillard *et al.*, 1999). This was made with an estimated accuracy of 1 km/s, but the work was only presented at conference, and remains unpublished in the literature.

1.4 The Aims of this Study

The focus of this study is to investigate the role that H_3^+ plays in controlling the conditions of the Jovian atmosphere above the homopause. This involves the energy balance not only of the ionosphere, but also of the surrounding thermosphere, as well as conditions within the magnetosphere, to which the ionosphere is connected. The measurement of a variety of interconnected parameters enables us to put forward an integrated analysis, and the methods by which they are collated gives rise to an unprecedented level of detail.

The use of IR images has provided a powerful technique to investigate the morphology of the H_3^+ aurora. The greater sensitivity that spectroscopy provides can be used to extend the general forms seen in images to more accurate measurements of the different emission strengths of different regions.

Investigations into the temperature structure of H_3^+ on Jupiter have previously focused on the general variation with latitude and longitude, looking at non-auroral contributions as well as the auroral ionosphere. However, previous to this study, a detailed high spatial resolution study of the variation within the auroral region itself has not been attempted.

In addition to this, studies looking at spatial variation in temperature have used rotational temperatures, which, while providing a temperature measurement that can be clearly defined as being in LTE, and thus corresponding directly with the kinetic temperature, provide a poorer sensitivity to the measurement, compared to the effective vibrational temperature used in this study.

Improvements in temperature calculation are extended to the column density and total emission calculation. Column density will be used to test the assumption of correspondence between H_3^+ emission and H_3^+ production (which reflects energy deposition). It will also, through the higher spatial resolution, provide a more accurate determination of the true column density of narrow auroral features, which may have been smoothed out with the lower spatial resolution used in previous studies. The total emission will provide an accurate measure of the H_3^+ cooling over the auroral region.

The measurement of Doppler shifts across the auroral region provides an unprecedented direct measure of the dynamics of the ionosphere. This allows the direct dynamical link between the ionosphere and magnetosphere to be analysed for the first time. It also shows how the indirect probing of some magnetospheric regions that have undergone no previous measurements may be attempted. By comparision with modelling studies, the measurement of the dynamics of the ionosphere allows extrapolation through to the underlying thermosphere, providing essential information in the understanding of the energy balance of the upper atmosphere of Jupiter.

Since we make use of observations across a total of five nights, our data can also be presented in the context of an extended time frame. The observations provide examples of Jupiter at all rotational positions, allowing us to choose the best viewing angles as required.

Chapter 2 : Observations, Reduction and Data Analysis

The observations made for this thesis were obtained using the NASA InfraRed Telescope Facility (IRTF) on Mauna Kea, Hawaii, between the nights of 7th September and 11th September 1998. The IRTF is a 3.0-meter infrared telescope, which we used with the CSHELL spectrograph to produce a spectral data set that provides a detailed examination of the Jovian aurora across a wide range of Jovian configurations.

Using this data, it is possible to produce information about the physical conditions in the Jovian ionosphere and thermosphere, to study the role of H_3^+ in maintaining an energy balance in the upper atmosphere, and derive new insights into the dynamic interaction between the Jovian magnetosphere and ionosphere.

2.1 The CSHELL Instrument

CSHELL is a long-slit high-resolution spectrograph, using an echelle grating with narrow-band circular variable filters that isolate a single order within a spectral range of 1-5μm. It has a single 256×256 SBRC InSb charge-couple device (CCD) sensitive between 1.08-5.60μm, which results in a detector array output of 256 spectral by 160 spatial pixels. Its slit is 30" (arcsec) in length, with discrete slit widths of 0.5", 1.0", 1.5", 2.0" and 4.0", which can achieve resolving powers up to 42000, or 7 km/s. The spatial resolution allows 0.2" per pixel, equivalent to 575 km at the equator of Jupiter for the observations described here, although the area within a pixel increases dramatically towards the limbs.

CSHELL also has a direct imaging mode in which a plane mirror substitutes for the grating and provides an image of the 30" field-of-view on the infrared array, with a spatial resolution of 0.2" per square pixel. Further technical information on the design and performance of CSHELL is beyond the remit of this thesis, but can be found in the literature (Greene *et al.*, 1993; Tokunaga *et al.*, 1990; and the CSHELL user's manual).

2.1.1 Instrument design overview

Figure 2-1 and Figure 2-2 are taken from the CSHELL manual, and show the light path through the instrument. The incoming beam from the IRTF is intercepted by the input lens, forming an image of the focal plane at the slit while forming an image of the pupil at the secondary mirror of the collimator. Alignment with the optical axis of the telescope is achieved by translating and rotating the input lens and the first flat mirror together as a unit.

A dichroic mirror, a special type of interference filter, reflects the IR to the slit while permitting the visible light to be viewed with a visible CCD camera (not shown). This allows the telescope to acquire and guide by the object being viewed, with a visible light counterpart. The infrared light is then separated into the specific order required by the Circular Variable Filter wheels (a CVF is an interference filter, where the thickness of the interference layer varies along an arc); individual filters allow through only one order onto the IR array.

After the filter wheels, the beam passes through an off-axis collimator designed to produce a collimated beam, a beam of photons aligned in a single direction. A "direct imaging mirror", shown in Figure 2-2, can be inserted into the beam, sending the beam back to the collimator, to form an image of the focal plane at the IR array. The telescope focal plane can thus be viewed directly in the IR, and the slit positioned before a spectral image is taken. It is also possible to record an image of the field if desired.

The light travels through the echelle grating or, if in direct imaging mode, a second flat mirror placed in front of the grating. It is then directed via a third and fourth flat mirror

onto a spherical relay mirror, which forms the final image of the spectrum on the IR array. A pupil image is masked in front of the IR array to reject stray light.

A particular observation wavelength is selected by setting the echelle grating to a specific angle, so the filtered light produces a single wavelength range to appear on the array.

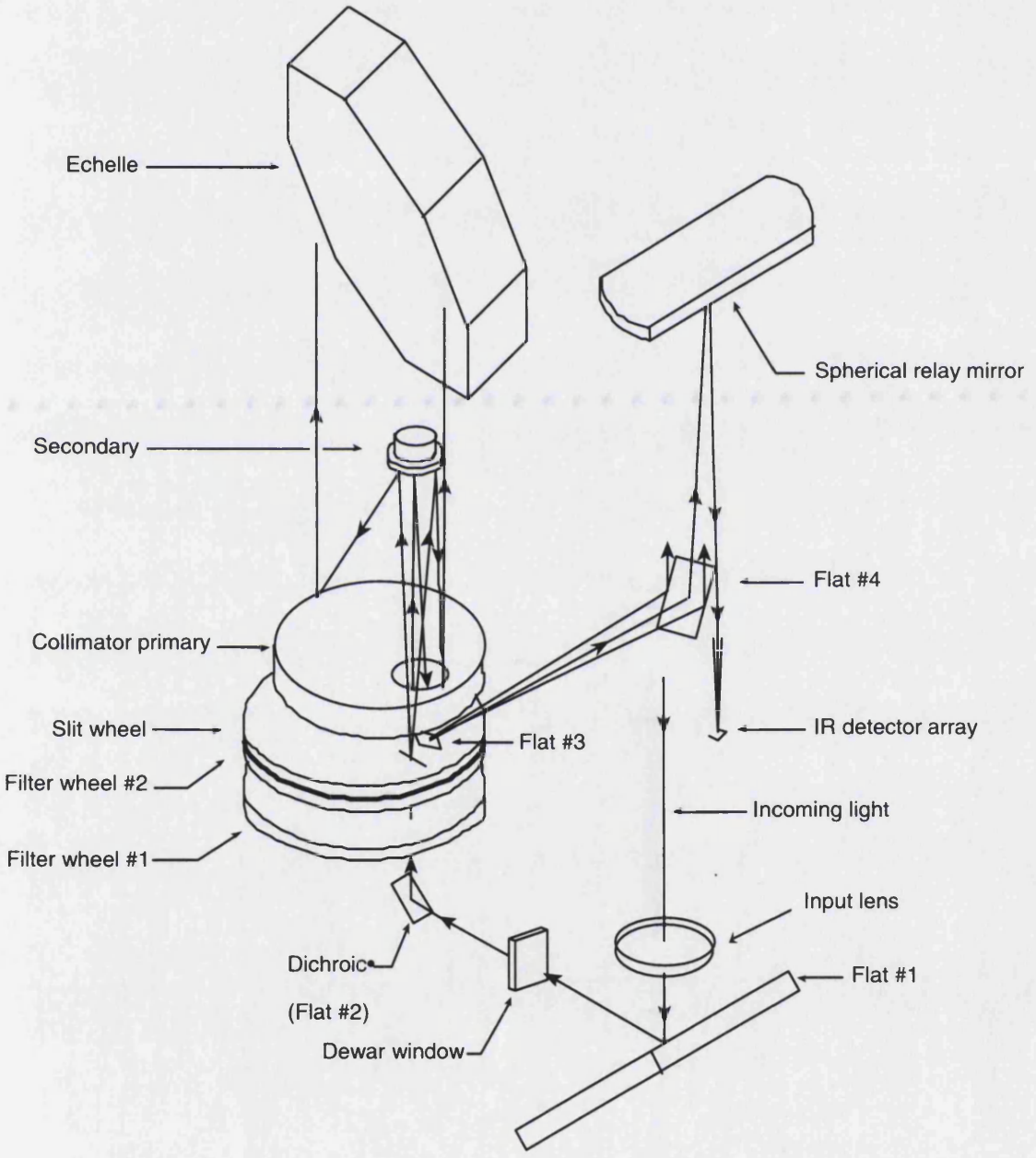

Figure 2-1: CSHELL optical layout, the CCD is mounted behind the dichroic but is not shown; taken from the CSHELL manual

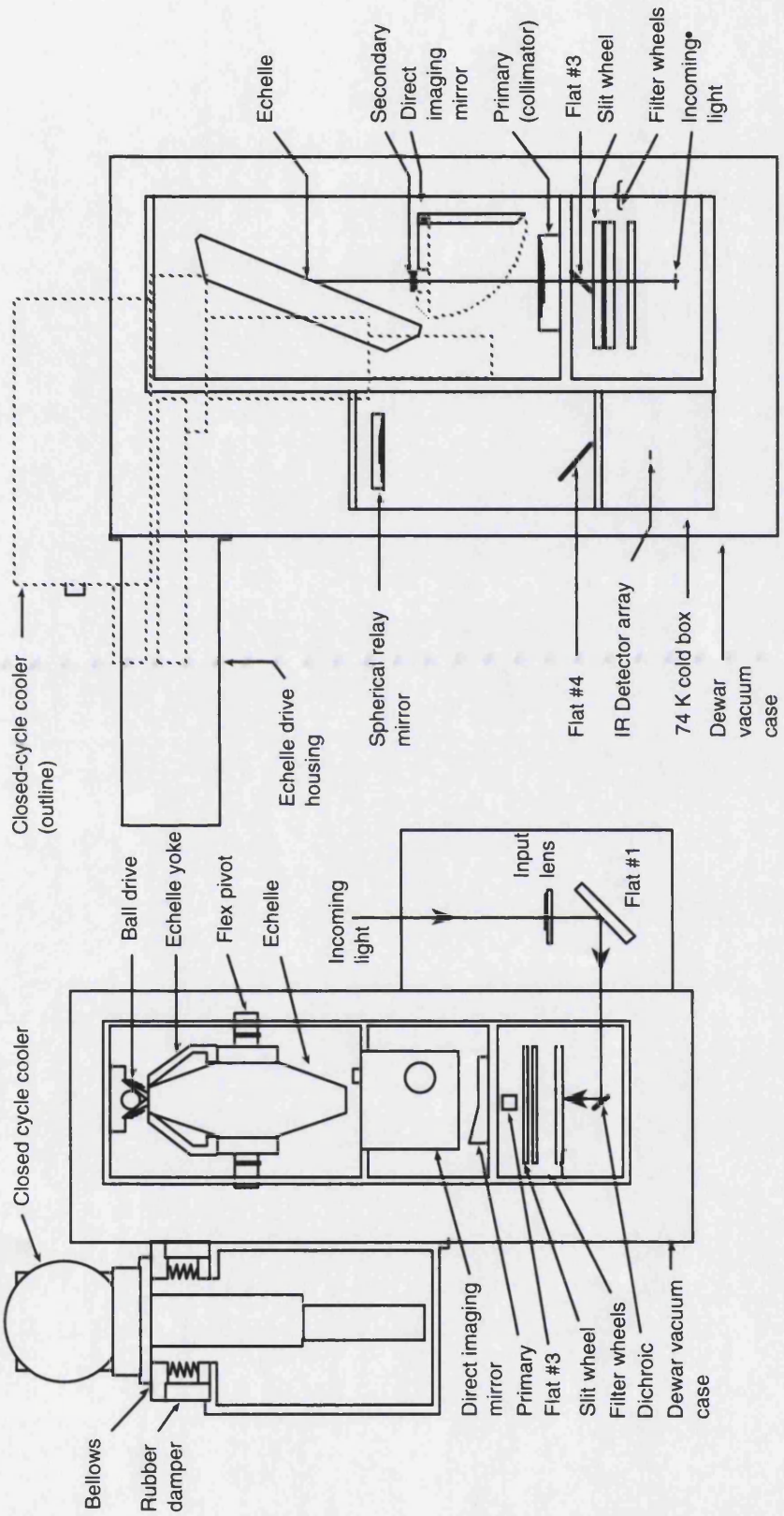

Figure 2-2: Front and side views of CSHELL; taken from the CSHELL manual

Labelling convention within this thesis

Throughout this thesis, Jupiter's reference frame is defined by the Central Meridian Longitude (CML), which is defined as the position of noon on the planet in System III (magnetic) co-ordinates.

The x and y directions referred to within this thesis are defined to correspond with the array as shown here.

For spectral images:

The wavelength variation is in the x-direction, increasing from blue to red with the value of x;

$$x_{(s)} \equiv \lambda$$

The spatial variation is in the y-direction, moving from east on the sky to west on the sky with increasing values of y;

$$y_{(s)} \equiv \textbf{Distance}\,(E - W)$$

For images:

The x-direction is aligned with the rotational axis of Jupiter, with increasing values of x corresponding to position down the planet, north to south;

$$x_{(i)} \equiv \textbf{Distance}\,(N - S)$$

The y-direction is identical to that of the spectral images, with increasing values of y moving from east to west on the sky;

$$y_{(i)} \equiv \textbf{Distance}\,(E - W)$$

2.1.2 Known instrumental limitations and faults

Effects of anisotropic light sources

While light is split into a spatial and spectral element before reaching the final output array, there are important effects that can cause a spatial effect to occur in the wavelength direction. This is important to this thesis because we are trying to measure Doppler shifts caused by Jovian winds. To find *real* wind velocities, we need to ensure spurious shifts due to spatial effects are removed. The instrument requires a finite-sized slit width; light that falls within this width is displayed on the array in the x-direction, so a 4" slit appears much broader than a 0.5" slit.

The major consequence of this occurs when the light varies across the slit width. In using the spectra, it is usual to assume an isotropic intensity of the light curve forming a Gaussian that peaks at the centre of the slit. However, when looking at a light source with complex emission morphology such as the Jovian aurora, this assumption is inadequate.

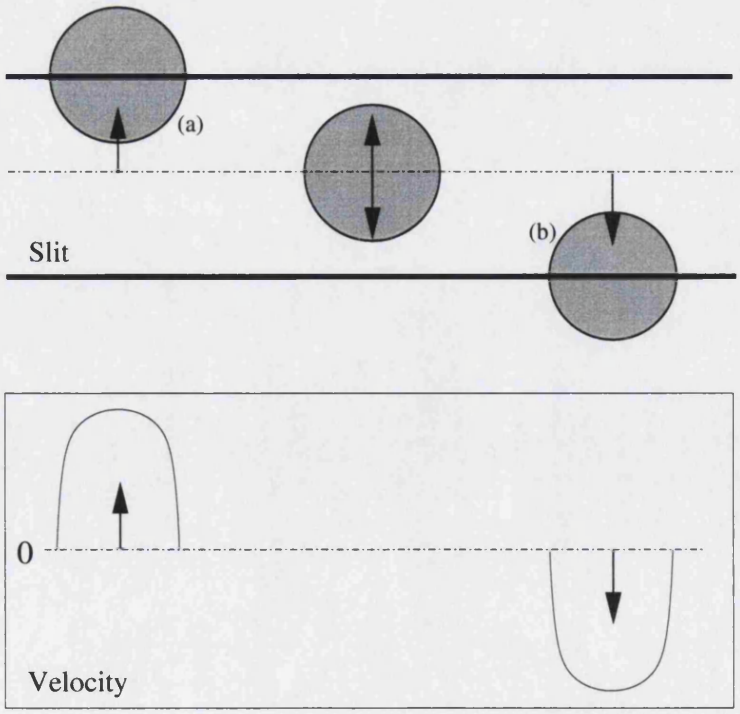

Figure 2-3: Asymmetry in light source leading to an apparent velocity shift

If a light source is anisotropic across the slit width, the apparent position of the peak intensity will be shifted from the true position. While this effect is not greatly important in most data analysis, when looking at Doppler shifts associated with the aurorae, the variations caused by the anisotropy in the slit will significantly alter the peak intensity position (Figure 2-3). This variation occurs in the very regions where true velocity variations are predicted to be strongest, across the electrojet.

True CSHELL resolution

Recent reports by the CSHELL technicians suggest that, although the stated resolving power of the instrument is 43000 with a 0.5" slit, there are indications that the maximum resolution achievable with CSHELL has degraded substantially from the nominal value. Resolutions of 20000-30000 have been estimated, which amounts to a broadening of 1-2 pixels over the expected value of 2.5 pixels. Such a decrease in resolution effectively causes a 0.5" slit to perform as it were significantly wider, between 0.7-1.0". It is not currently known what has caused this degradation of resolution.

However, the problem was first reported to the scientific community in January 2000, a year and a half after the observations discussed in this thesis were made. It is thus plausible that the problem did not exist at the time of observations and, when the resolution was tested on our data, there appeared to be no degradation in quality. The work presented here thus assumes that there is negligible effect on the resolution of our measurements because of this effect.

Positioning of the Direct Imaging Mirror

The CSHELL technicians have reported that the Direct Imaging Mirror has experienced problems with its limit switches, which control the positioning of the mirror. As a result, the mirror may not come back to exactly the same position in the beam if it is moved out, causing the slit to appear in a different column on the array each time the mirror is replaced.

The technicians recommend that observers using the smallest slit width, and those who require precise information about the location of the slit on their targets, should image the

slit with the DI Mirror in the beam before each observation. This imaging is included in each sequence of spectra (see Figure 2-6 and Figure 2-10).

2.2 Observations

CSHELL was used to collect the entire data set used in this thesis. The data was collected over a period of the five nights of 7^{th}-11^{th} September 1998. Each night of observations followed a predetermined sequence of collection, which was adapted and improved as the evenings progressed.

The H_3^+ ($\nu_2 \rightarrow 0$) Q(1,0$^-$) fundamental line located at 3.953μm or 2529.72cm^{-1} was used for the observations. This wavelength is in the L' window for terrestrial atmospheric transmission. It is one of the strongest emission lines of H_3^+ at 1000°K, and also lies within a region of methane absorption, centred on 3.43μm. Thus stratospheric Jovian methane effectively reduces the reflected solar and deeper Jovian emission to zero.

The original objective for these observations was to locate, characterise and measure the variations in Doppler shifts from the Jovian auroral region. The first detection of these shifts (Rego *et al.*, 1999) clearly originated from an "auroral event", which may have lasted only 20 minutes. The implications of this original detection for ionospheric and magnetospheric conditions were profound. Further investigations were required to produce a better understanding of the dynamics within the aurora. Our observations were made to provide a detection of these Doppler shifts under more "normal" conditions, and produce continuous observations of the dynamic effects seen over an extended period.

However, during the observations taken on the first night, it became clear that in addition to the fundamental H_3^+ line there appeared to be a secondary spectral line located at 3.949μm, which matched the 3.953μm line in spatial morphology. Further investigation discussed below showed this to be a hotband of H_3^+, which was subsequently used to provide detailed information on the temperature and column density in the Jovian auroral region.

2.2.1 Definition of the terms used in data recording

Nodding of the instrument

At the wavelengths used in this thesis, the Earth's sky emits considerably more radiation than the object of interest. In order to remove "sky emission" properly, the observations of the object (the "A" frame) require an additional frame consisting of a second exposure of the sky alone (the "B" frame). This is made with an equivalent exposure, with the telescope "nodded" by about 1' (arcmin) off the object. By setting the telescope into "*A/B* mode", a sky B frame can be taken automatically. It should be noted that this takes twice as long to observe as using the telescope in A-only mode.

Exposure styles

To produce the spectral image, CSHELL allows three variable observation parameters, and the style of exposure used is given by the code *time/coadds/cycles*. This should be read right to left to distinguish what the observation consists of.

Cycles is used in the CSHELL macros (see **Appendix C : Examples of Programming Code**) to allow repeated observations to occur consecutively. If this value is set above 1, the instrument will repeat the observation, and record the result in a separate file.

An individual observation can consist of a single or a set of coadded exposures on the object. *Coadds* are taken consecutively and added together once the observation is completed, before the file is saved. Nodding of the instrument is performed at the end of a sequence of coadds on the object.

The *exposure time* is the recording time of each part of the coadd and copies of the observation, given in seconds. Coadd and copies are often set to 1, so that time is the total time of exposure. When nodding is used, time describes the exposure time for the object and sky frames individually.

Airmass

Airmass (z) is a measure of the amount of the Earth's atmosphere through which the light from an observation passes. This assumes flat-plane atmosphere, and is defined as:

$$z = \sec(ZA)$$

Where, *ZA* is the zenith angle, the angle between the position of object in the sky, and the zenith (the point directly above the observer in the sky). Thus, the airmass varies from 1, directly above the observer, upwards; observations beyond z = 2.5 are usually of poor quality.

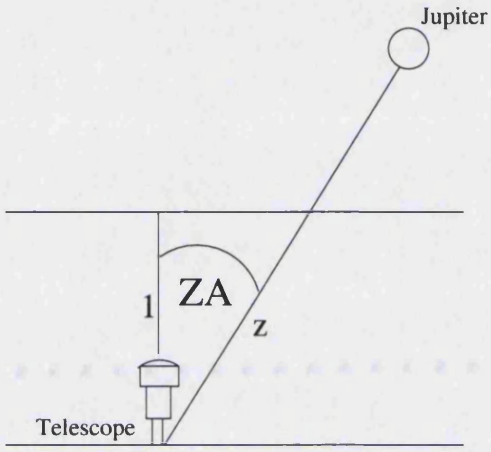

Figure 2-4: The zenith angle, used to calculate the airmass

2.2.2 Observing strategy

In order to ensure consistency between individual observations, each night the CSHELL echelle grating was set to an angle of 64.8°. This allowed the H_3^+ 3.953μm line to be observed with the Order 14 filter. The grating was then left in position for the entire night's observing. These observations consisted of three elements, which when combined ensured that the data was not only reliable and repeatable, but could be properly calibrated in later analysis. Through the application of detailed calibration, it is possible to produce the high degree of accuracy that is required to measure the variations in Doppler shift expected.

Thus, in addition to the Jovian spectra, Jovian images and extensive calibration spectra were collected. Images were taken in both the K band (1.9μm ↔ 2.5μm) and at 3.953μm to provide understanding of the general form of the aurora, and planetary position. The

final calibration combined these with arc lamp, sky line and star spectra to understand the full instrumental effects seen in collected data.

1. Early evening set-up observations

The initial step of each night's observation began before the sun had set. A sequence of arc lamp lines was collected, along with supporting darks (spectral images taken with no source and a closed shutter) to remove bad pixels and dark current.

The main use for these in the work of this thesis was to provide calibration for wavelength dispersion and non-linearity on the array. The echelle grating is fixed for the night at the optimum position to align the 3.953μm line of H_3^+ with the centre of the array. The lamp lines are observed through a higher order filter than is required by the H_3^+ lines, so their position on the array appears as a forced wavelength centred around the wavelength corresponding to the grating chosen.

Four Krypton lines were chosen for their position on the wavelength direction of the array, to allow coverage over the majority of the array. On the discovery of the hotband that will be described in **2.4 Secondary Line in the Spectra**, an additional argon line was added to provide reasonable calibration on the far left (blue) of the array. All the arc line observations were made using a 0.5" slit. The apparent wavelength position of all the lamp lines are shown in Figure 2-5.

Table 2-1: The macro for observations of the lamp lines

Arc Lamp	Exposure time (s)	Actual Wavelength	Apparent Wavelength
Krypton	40	1.5373	3.95389
	120	1.4957	3.955297
(double line)	40	1.7852	3.951964/ 3.951971
	500	1.3835	3.953331
Argon (double line)	500	1.84328	3.94783 & 3.949886/3.950019

Once the lamp line spectral images were recorded, the celestial observations could begin. All subsequent data taken was of astronomical objects and, by changing only the filter used, the echelle grating could be kept in its original position throughout the night.

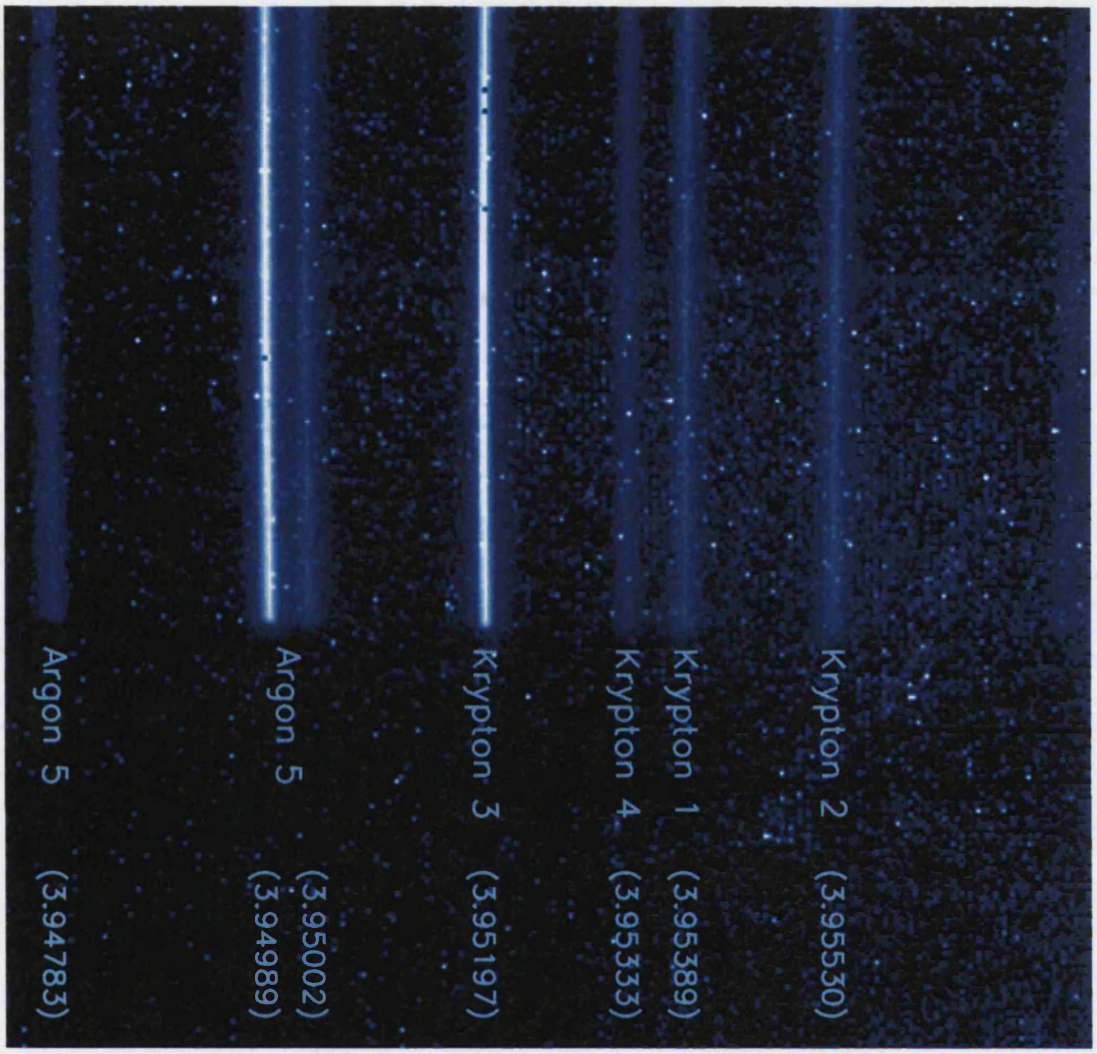

Figure 2-5: The position of the order filtered argon and krypton arc lamp lines on the array under the optimum grating setting for a centred 3.953μm line

2. Star observations

Observations were then made of the standard star BS8647, an A_0 star with an apparent visual magnitude of 6.41, chosen because of its location close to Jupiter at the time of our observations. This enabled us to match the airmass of Jupiter seen during the observations. Stellar observations were used to focus the instrument, as well as to provide flux calibration and variations in the array for a point source at 3.953μm. Three sets of observations were used: an image of the star, a spectral image taken using a 0.5" slit, and two spectral images each with a 4" slit.

Focusing was performed by taking short exposure time K-band images, each lasting a few seconds, within a macro that effectively repeated the exposure *ad infinitum.* This allowed the

instrument to be refocused by eye quickly and effectively, using the measured maximum intensity values.

The following macro was then run to produce a sequence of observations for later use in calibrations:

Table 2-2: The macro for observations of the standard star BS8647

No.	Image/Slit	Wavelength	Exposure
(i)	Image	K-band	.08/100/1
(ii)	0.5" slit	3.953	120/1/1
(iii)	4" slit	3.953	15/4/2

Examples of these observations can be seen in Figure 2-6.

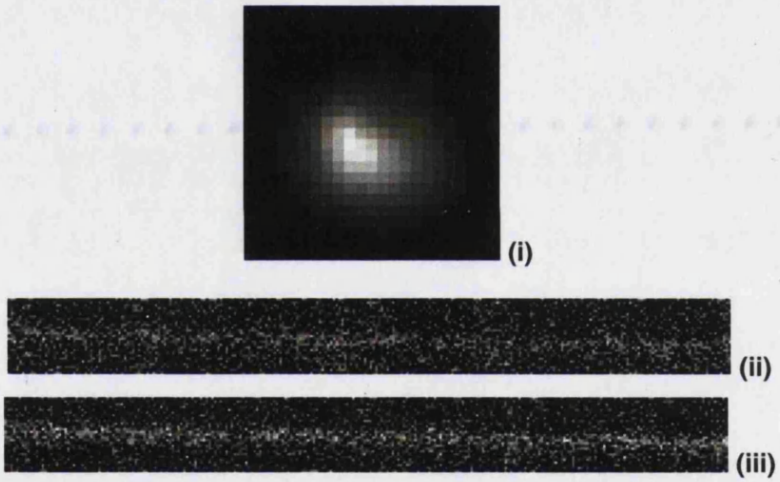

Figure 2-6: Sequence of observation for BS8647

3. Jovian observations

An individual set of Jovian observations consists of a series of different macros, which systematically locate the planet with respect to the slit, make the recorded observations, and then re-establish the position of the planet. This sequence is what will be referred to as a "set of spectra", although it includes within it images of both the planet and the slit, so as to align the telescope with Jupiter, with the instrument slit aligned parallel to the equator. The addition of a second image after the spectral images were taken was made from the fourth night onwards, to establish the exact position of the planet after the large telescope offsets required by the sequence of spectral observations, and to provide information about apparent drift of the planet within the array.

The sequence for each "set of spectra" was as follows:

a. Image slit

This is an image on the array of the slit, taken on the recommendation of the CSHELL technicians (**2.1.2 Positioning of the Direct Imaging Mirror**). It is made simply by taking an image (*i.e.*, an exposure with the grating obscured by a Direct Imaging Mirror), but with the slit in place, as shown in Figure 2-7. This allows the position of the slit to be quickly determined and then replaced with a flat mirror to allow the object to be imaged.

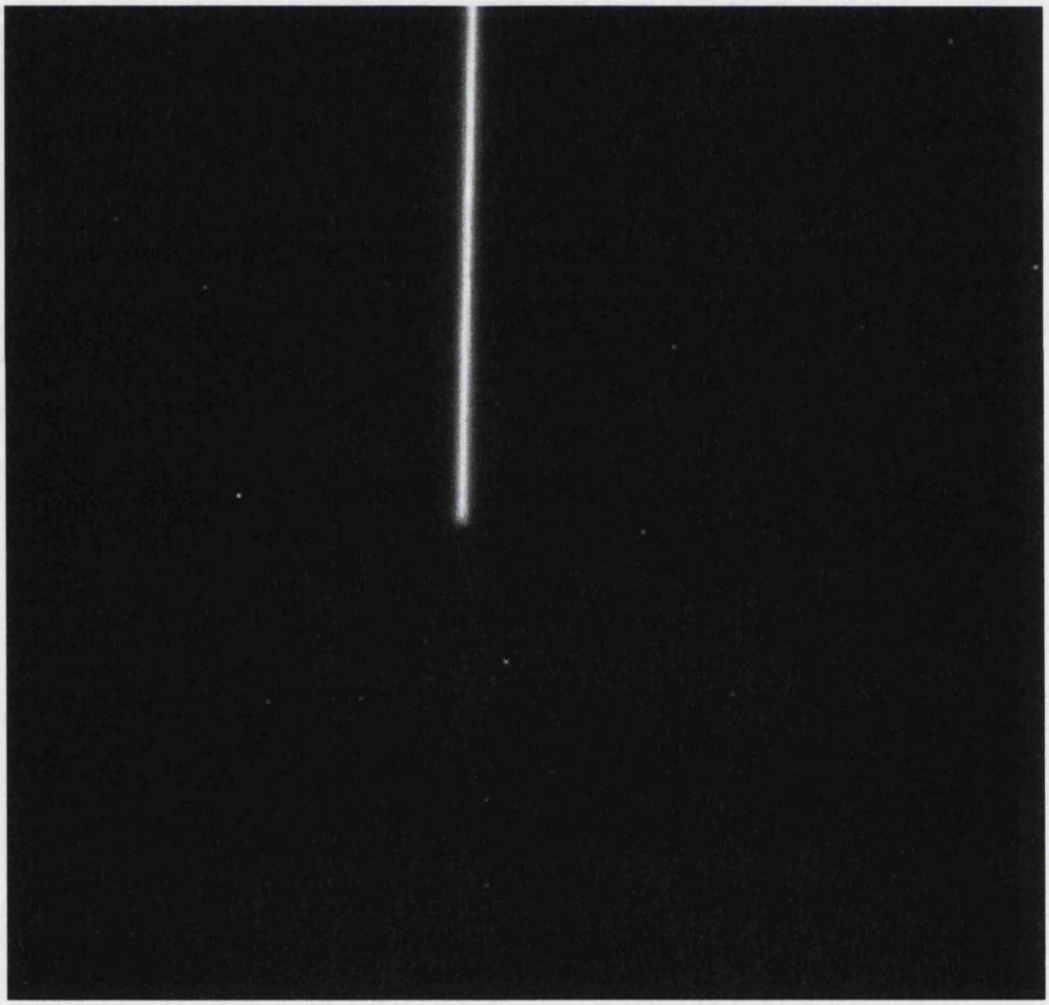

Figure 2-7: An image of the 0.5" slit, for calibration purposes

b. Image Jupiter in K-band and at 3.953μm

Two images are taken, one in the K-band and another at 3.953μm, both using only the object, without sky subtraction, for speed. The K-band image is used to find the position

of the limb of the planet in the wavelength direction, and the centre of the planet in the spatial direction. However, using the 3.953μm image to locate the aurora, it is possible to determine whether the centre of the slit is the best place to position centre of the planet, to view the aurora within all the subsequent spectral images.

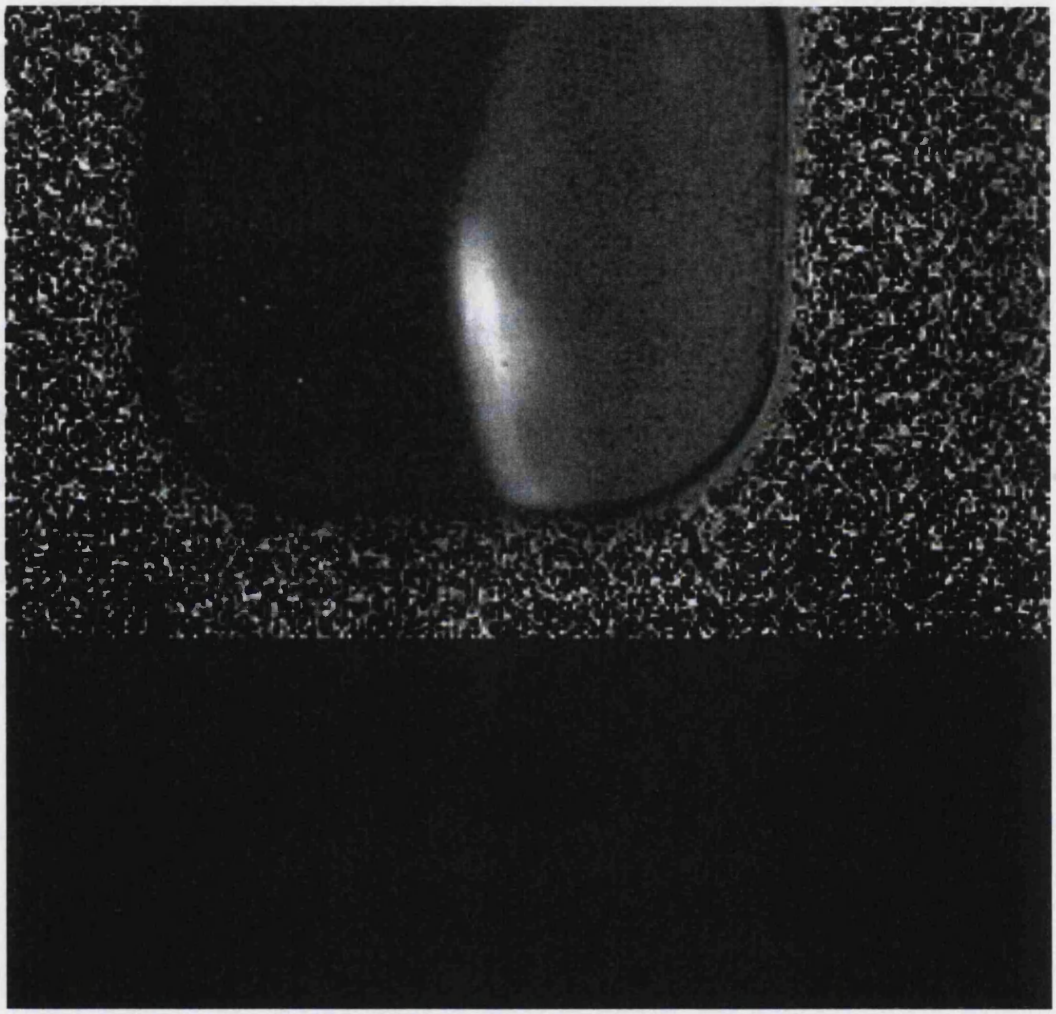

Figure 2-8: An example of a 3.953μm image in its original CSHELL output, showing a lopsided aurora before the planet has been placed off-centre to contain the aurora wholly in the output image

c. Move the telescope so the slit coincides with the planetary limb

Using the given position of the slit and the planet, corrections are directed to the telescope so the slit is positioned on the limb, and the planet is centred within the slit in the spatial direction. Although the slit is long enough to cover both planetary limbs at auroral latitudes, to record emission associated with auroral output at lower latitudes, the slit was

aligned off-centre when the aurora was seen on only one side of the planet, as was the case in Figure 2-8.

d. Re-image to check the position

Re-imaging checks that the planet is positioned where desired and, if required, step c is repeated until the planet is correctly positioned. An example of the transposed image and slit in the final position before recording is shown in Figure 2-9.

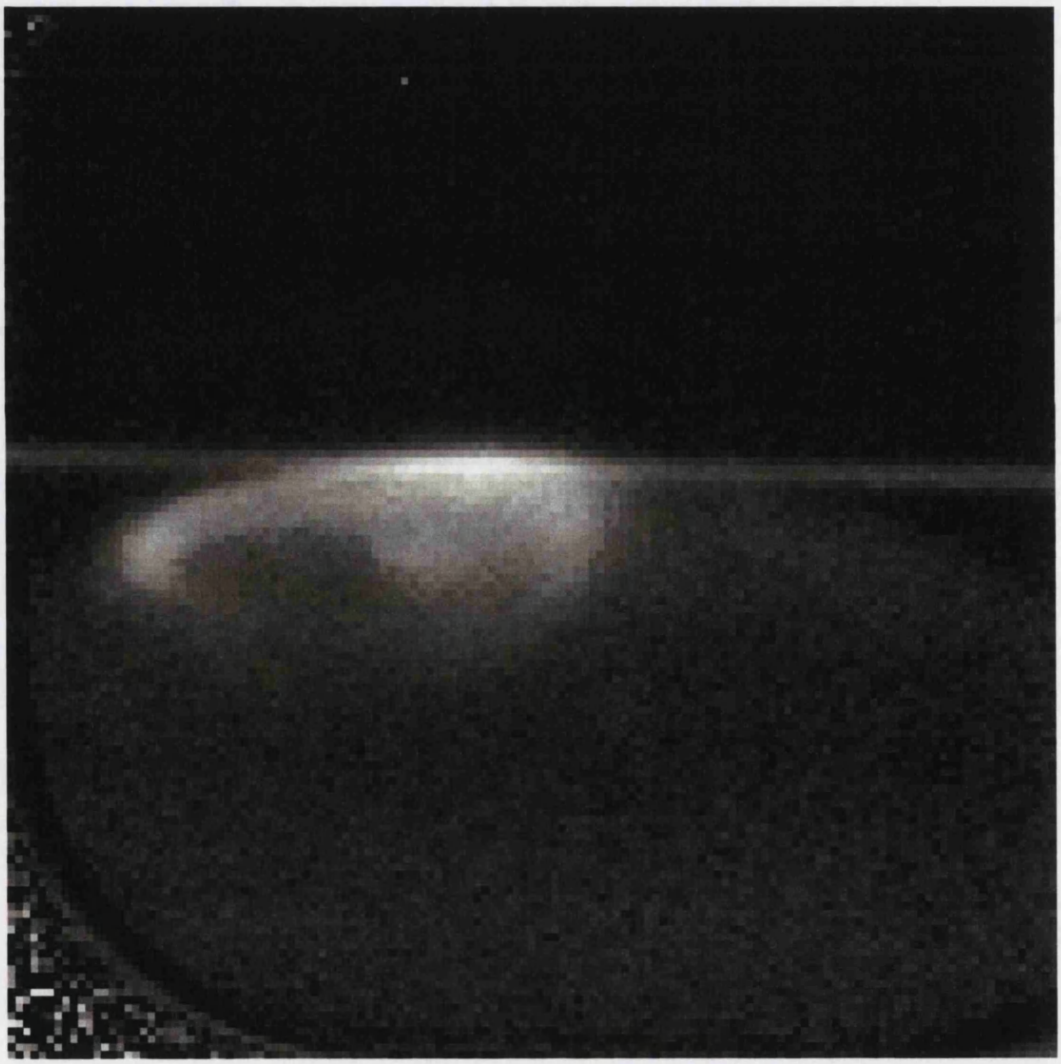

Figure 2-9: An image of the slit directly aligned with the limb of the planet

e. Run the recorded sequence

With the planet properly positioned, the telescope could then be directed to take a series of recorded exposures using a pre-written macro. This produced the following input of data for each set of spectra:

Table 2-3: The macros for observations of Jupiter

No.	Wavelength	Slit Wheel	Mode	Exposure	Night first used
(i)	K-band	Open	A/B	0.08/100/1	8th
(ii)	3.953	Open	A/B	0.08/100/1	7th
(iii)*	3.953	0.5"	A/B	50/1/1	7th
(iv)	K-band	Open	A	0.08/100/1	10th
(v)	3.953	Open	A/B	0.08/100/1	11th
(vi)	n/a	0.5"	A	0.08/100/1	10th

* Multiple spectral images were taken, each exposure lasting 50 seconds. The slit was aligned to cover the polar limb of the planet as already described, where the first spectral image was taken. The macro then moved the slit to each subsequent position and took another spectral image. Two steps of 1" were made above the planetary limb to ensure that the planet was entirely covered, and then 1" steps were made below the planetary limb until the aurora was entirely covered. A final spectral image was taken at the equator to provide a control. The full sequence is shown in Figure 2-10.

Each night of observations consisted of several sets of spectra, with the instrument being refocused on the star every 2-3 sets. This allowed as many as twelve sets of spectra to be made, covering either the northern or southern aurora.

The IRTF is provided with an on-axis guide which maintains telescope positioning on the object by fitting a Gaussian to the emission profile in both the x and y directions, and using the results of these to centre the object. However, this proved problematic because Jupiter is not a point source and the guide was having problems fitting a Gaussian to the disc, which proved to remain non-linear even when reduced in size. As a result, we had to calculate a tracking rate for the telescope and correct this through the night by providing guiding by hand. This was done by outlining the image from the on-axis guide on the monitor, and correcting its positioning using a joystick.

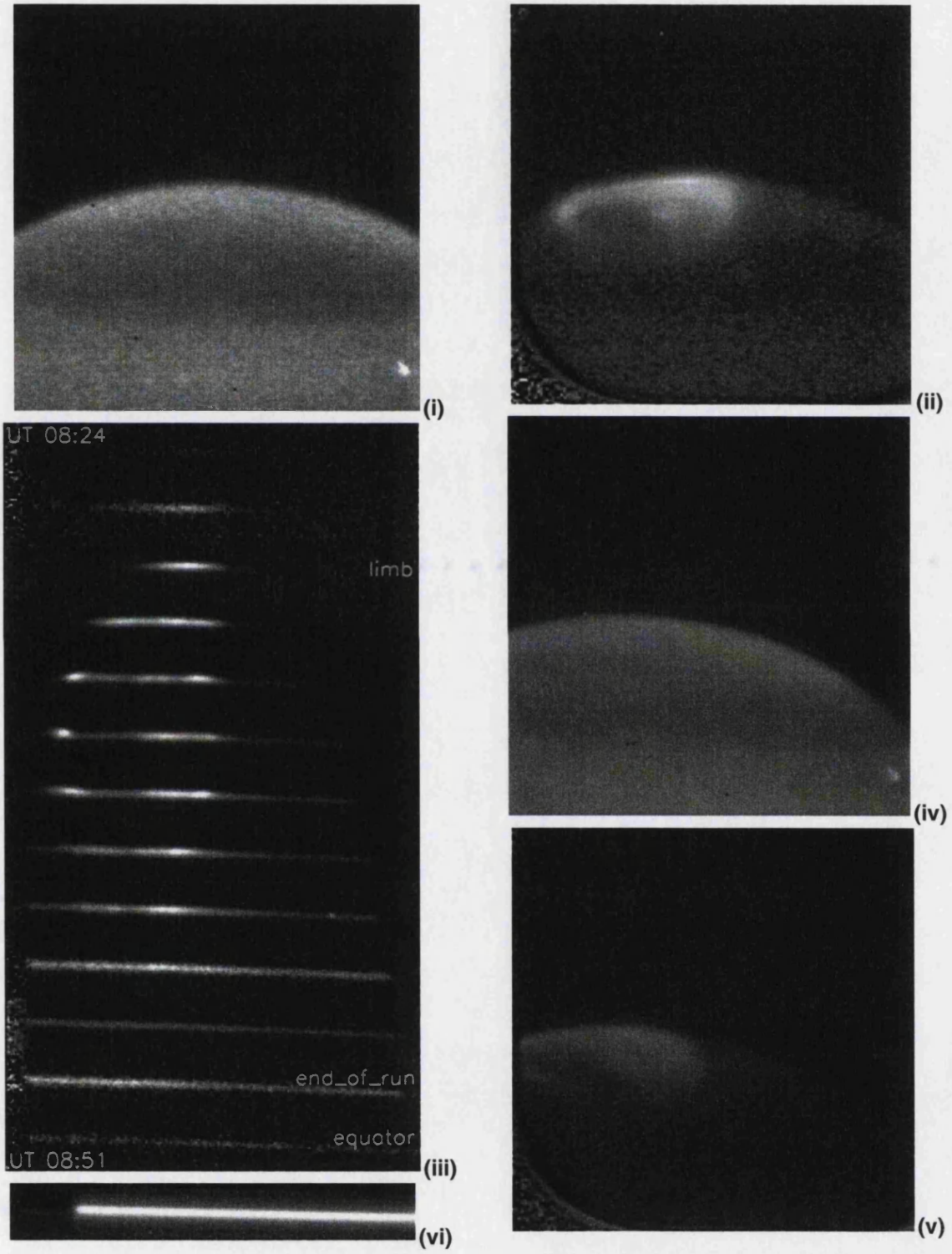

Figure 2-10: Sequence of recorded observation for Jupiter

2.3 Data Reduction

All data reduction and subsequent analysis was performed using the Interactive Data Language (IDL) produced by Research Systems Inc. IDL provides a set of intrinsic functions and procedures within the program itself, and also allows users to write their own procedures that use these, alongside the system commands, to manipulate and display data.

Data was originally stored as an "array image" in the CSHELL FITS data type, which has no distinguishing differences for either image or spectral observations, since both are simply array outputs. The array image was loaded into the IDL program using merged adaptations of Daniel Rego's BUILDATA sky removal procedure, and the READFITS procedure provided by the Institute of Astronomy, Hawaii (N.B. all Daniel Rego procedures are detailed in the IDL guide he produced for UCL, 1998).

The BUILDATA1 (**B.2.1 buildata[1-2]**) adaptation simply loads a single array image into IDL, useful for arc lamp observations and checking individual outputs. The BUILDATA2 adaptation, used for all object based observations, loads the matching object and sky images into the program as individual arrays, and subtracts the sky from the object using the following equation:

$$\frac{(o_{xy} - s_{xy})}{s_{xy} / |s|_{ave}} \times (\text{total number of pixels})$$

Where, o is the value of the pixel on the object frame and, s is the value of the pixel on the sky frame

The sky image subtraction removes sky lines and atmospheric effects from the object, and also provides flat-fielding to counter the effects of anisotropy in the performance of the detector. Multiplying by the total number of pixels results in very high values in order to maintain accuracy in processing, but is taken account of in subsequent procedures.

The result of either BUILDATA can then be processed to remove any remaining bad pixels using the REMOVEMAX procedure written by Daniel Rego, which locates pixels of extraneously high intensity and allows the user to set them to zero.

2.3.1 Gauss fitting

Once the spectral images had been reduced to the point where they were ready to be processed, the detailed information in the spectral lines was extracted using a procedure called SPECTRA (**B.3.7 spectra.pro**). (This procedure was a development of SHIFTSPEED, the procedure written by the author to calculate the velocity variations seen in Rego *et al.* (1999).)

The program fits the specific spectral line in each spatial row with a Gaussian. The data often consists of a small number of data points, so in order to produce an accurate and smooth Gaussian fit, a linear interpolation of 100 points is made between each data point. This then allows the peak intensity, peak position and the half-width of the line to be calculated for each point recorded on the planetary disc to a greater accuracy than an individual data point.

The spatial region chosen to analyse the H_3^+ line was chosen by eye, using an image of the spectral image displayed on the screen. The region selected was chosen as an estimate of where the planetary limb falls on the array, fairly easily located due to the lack of emission off the planet. With both limbs selected, an array of data covers the entire planetary disk at a particular latitude, which is fed into the procedure and processed automatically.

The procedure then processes each spatial row as an individual one-dimensional array, and accesses the IDL procedure GAUSSFIT to compute a non-linear least-squares fit with six unknown parameters, with the following function:

$$F(x) = A_0 e^{\frac{-z^2}{2}} + A_3 + A_4 x + A_5 x^2$$

$$\text{Where, } z = \frac{(x - A_1)}{A_2}$$

Here, A_0 is the height of the Gaussian, A_1 is the centre of the Gaussian, A_2 is the width of the Gaussian, A_3 is the constant term in the continuum background, A_4 is the linear term, and A_5 is the quadratic term.

Fitting accuracy

The intrinsic Gaussian fitting procedure provided by IDL does not record any measure of the accuracy of the fitted Gaussian to the original data. In order to ascertain the accuracy, a procedure called CALC_GAUSSACC (**B.4.1 calc_gaussacc.pro**) was used to transform a known Gaussian into simulated spectral data, and then to refit it to estimate the errors involved in the fitting process. The precision of the Gaussian fit varies depending upon the shape of the Gaussian it has to fit, so the fundamental and hotband data were fitted separately to fully test the accuracy, as follows:

1. The initial Gaussian, against which the fitting accuracy will be tested, was found by fitting a Gaussian to a standard spectral row of the original data. This is shown for both the fundamental and hotband spectra in Figure 2-11, Figure 2-12 and Figure 2-13.

2. Having generated an initial Gaussian, which simulates the "pure" spectral line of emission from Jupiter, it is necessary to convert this into a simulated output from the instrument, to which a Gaussian would have to be fitted. The first step in producing this simulation was to contract the expanded Gaussian back to the original source size. This resulted in a jagged "Gaussian", which correlated well with the shape of the original data from which the "pure" Gaussian was taken (Figure 2-14).

3. To this condensed Gaussian was added uniformly-random simulated noise. These noise levels were set by looking at the background noise on each spectral line, and a fixed value of ±0.015 of the peak value for the fundamental and ±0.1 of the peak value for the fundamental were used. These values provide a mid-ground between the highest and lowest signal-to-noise values actually seen.

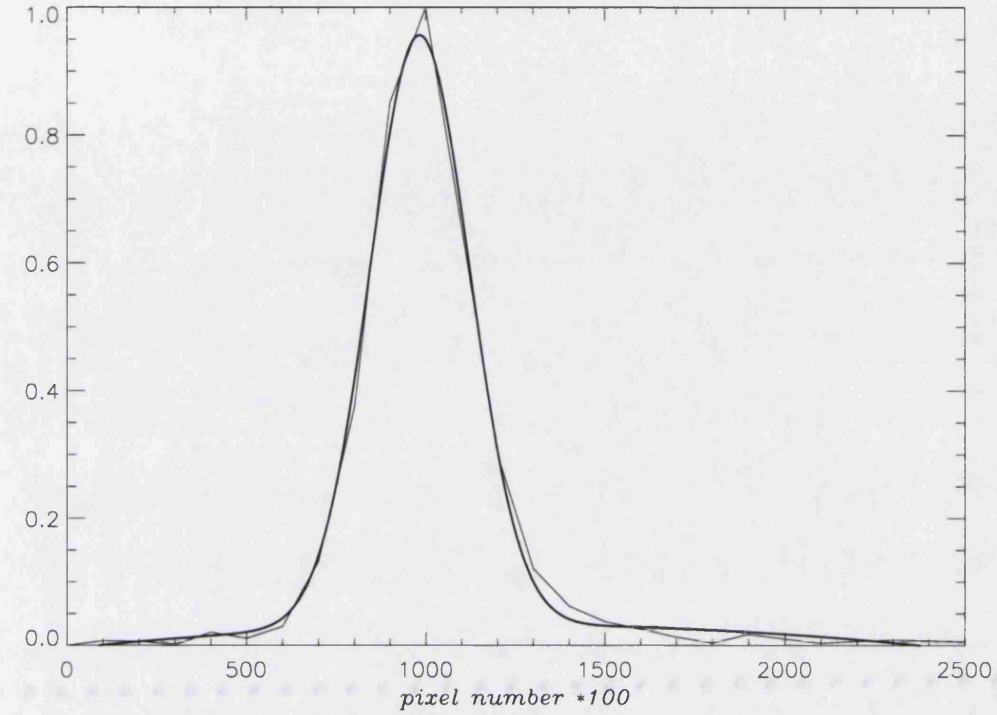

Figure 2-11: Fitting of the fundamental spectral line to produce an original test Gaussian

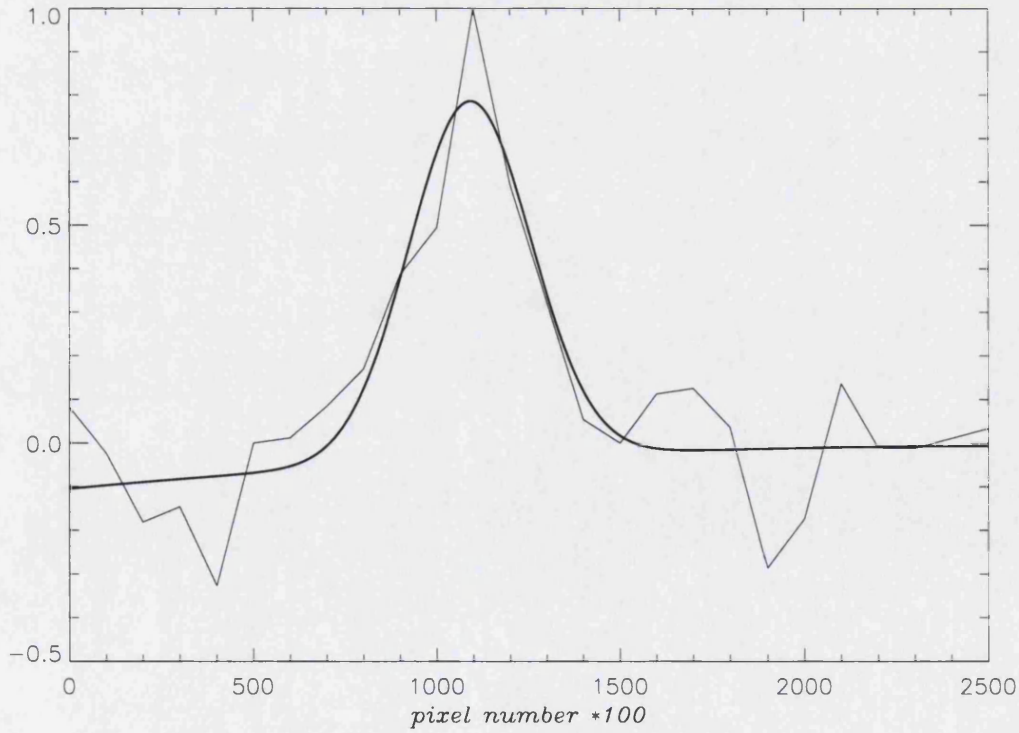

Figure 2-12: Fitting of the hotband spectral line from a single row, to produce a test Gaussian. The signal-to-noise on the spectral line is low, leading to the need to collate separate spectral lines with a running average of nine in the spatial direction (see 2.4.4 Hotband Gauss-fitting, below)

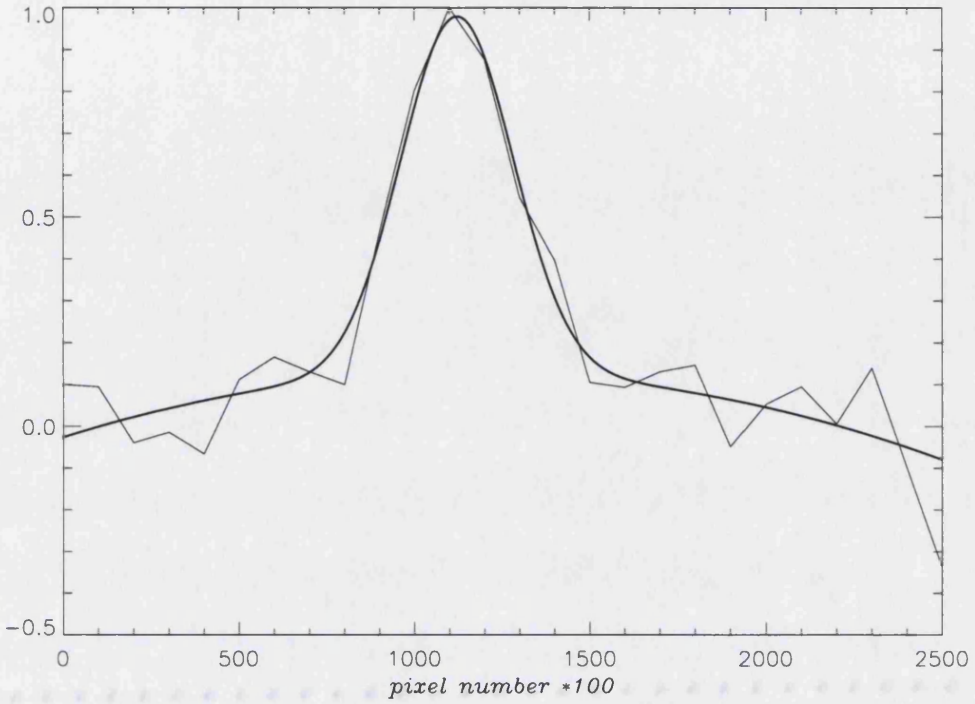

Figure 2-13: Fitting of a collated nine-pixel running average hotband spectral line to produce a test Gaussian. Collation has produced a significantly improved signal-to-noise

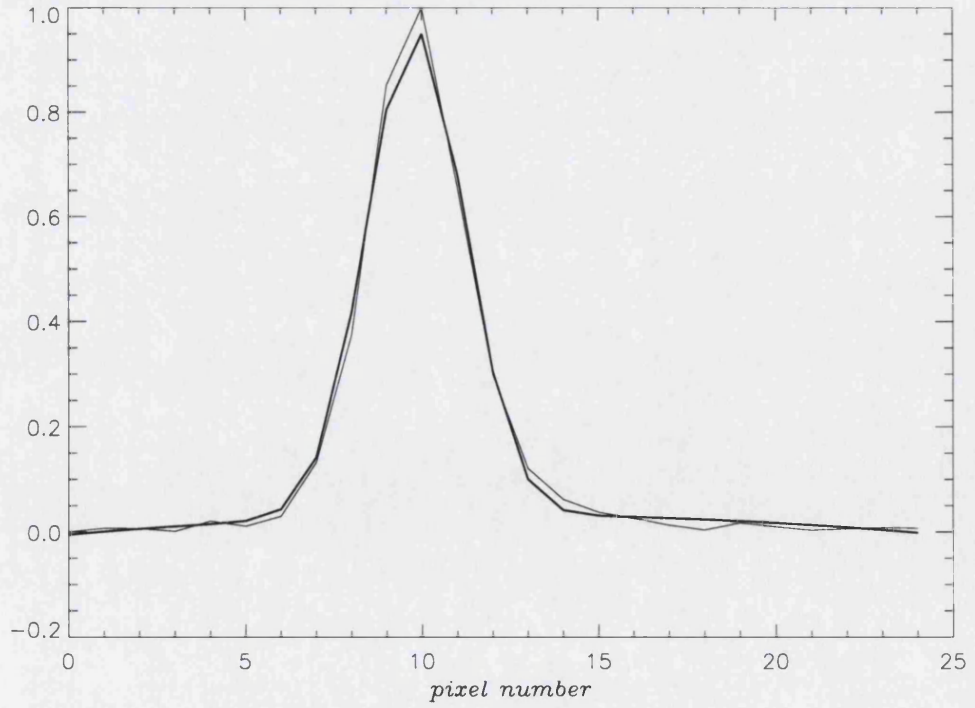

Figure 2-14: The truncated "pure" Gaussian (in bold), compared with the original data, from which the Gaussian was fitted

4. Having produced the "simulated" spectral lines, they were then fitted as if they were original data, in both the noisy and non-noisy forms, examples of which - the noisy spectral lines - are shown in Figure 2-15 and Figure 2-16. This produces a secondary Gaussian, which can be compared directly with the original (Figure 2-17 and Figure 2-18).

To ascertain an accurate average variation between the initial and secondary Gaussian and reduce the effect of random noise in the data and the specificity of using only one row, the process given above was looped 100 times for each row and covered 10 spectral rows. By averaging the absolute variation from each of these, a final value can be produced, suggesting the effective accuracy of the fitting procedure in IDL.

This accuracy test shows that the IDL Gaussian fitting finds the peak intensity to an accuracy of 4.0% and the *fundamental* peak position to better than 0.1 of the nearest pixel, approximately 0.3 km/s. This method of fitting also fits the background within the Gaussian, so the intensity of separate peaks can be compared directly from the A_0 value.

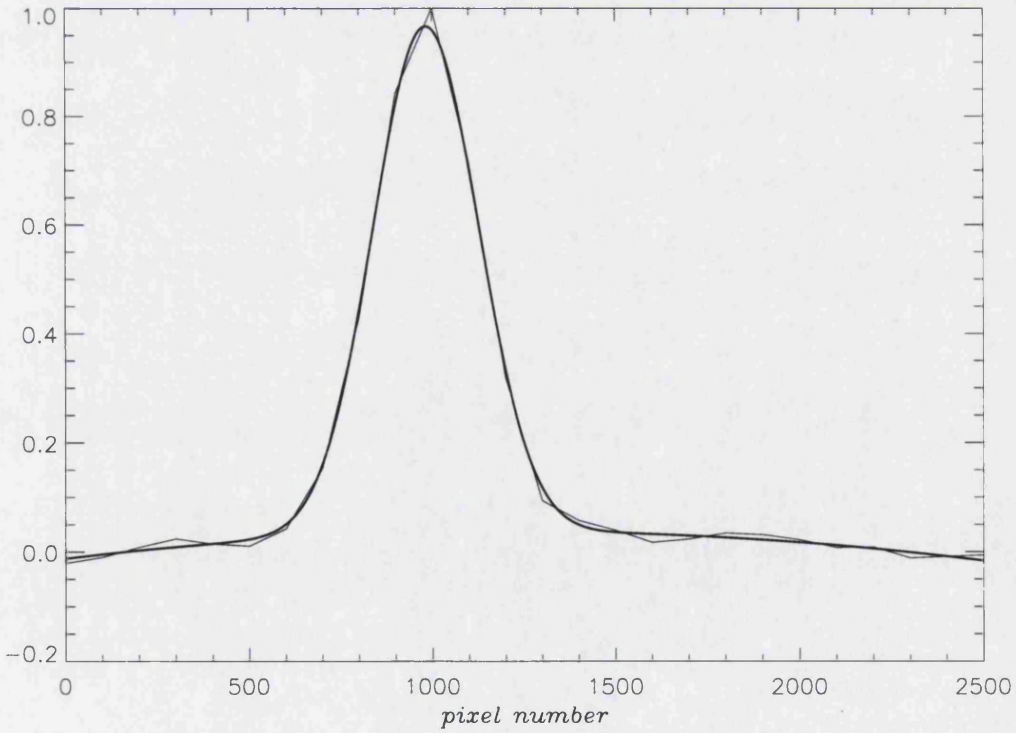

Figure 2-15: The noisy "simulated" fundamental spectral line fitted with a Gaussian

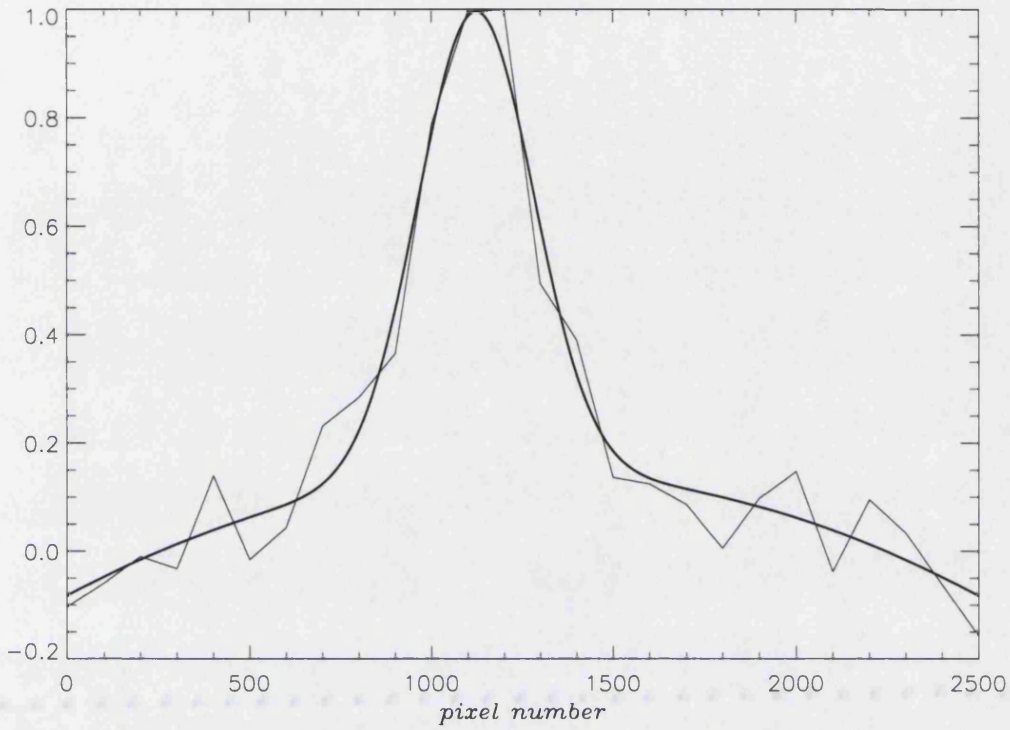

Figure 2-16: The noisy "simulated" hotband spectral line fitted with a Gaussian

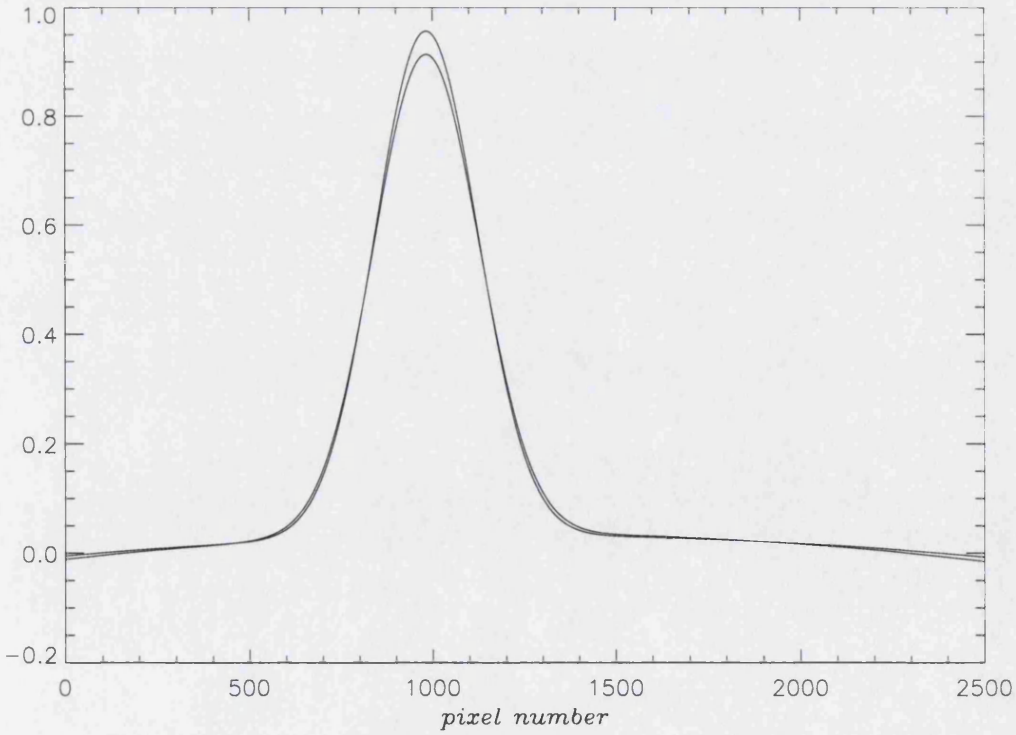

Figure 2-17: The fitted Gaussian (in bold) compared with the original "pure" fundamental spectrum

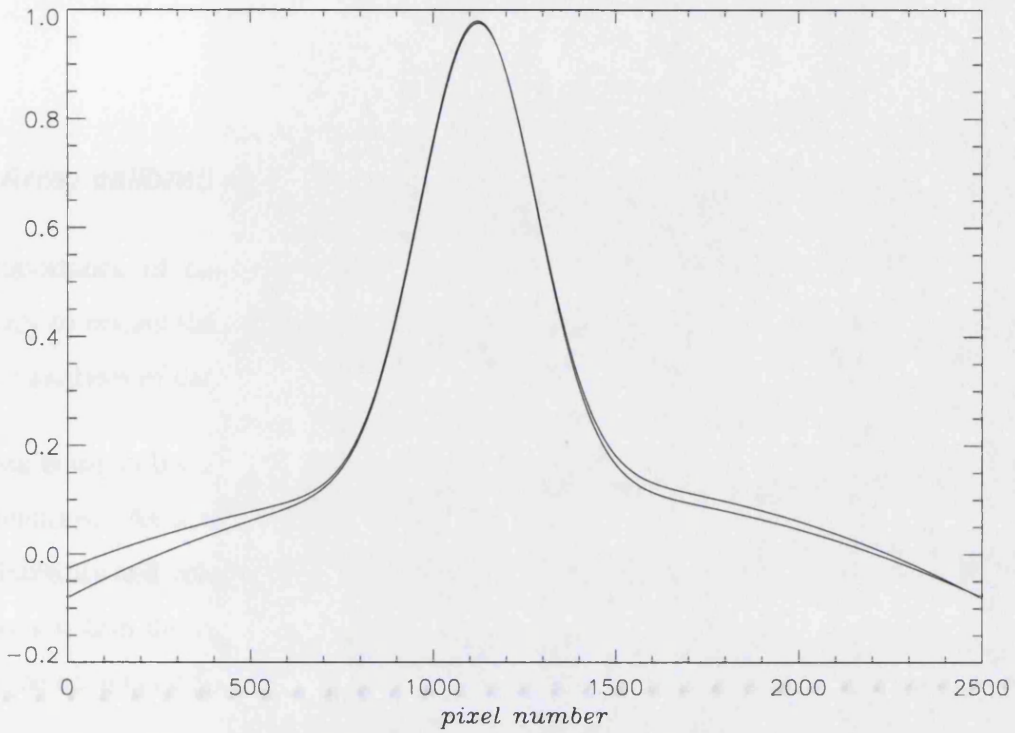

Figure 2-18: The fitted Gaussian (in bold) compared with the original "pure" hotband spectrum

2.3.2 Gaussian output

The output of SPECTRA is an array consisting of the six A values for each separate spectral position. These values are directly relative across the separate spectral rows. Only the first three values are saved unless the second three, which represent the background emission, are particularly required. The A values are all in units attributable to the instrument itself, but can easily be converted into SI values:

A_0 can be converted into Wm^{-2} by flux calibration against the standard star, to be explained later in this chapter.

A_1 is a measure of peak position in the wavelength direction, which can be ascribed a relative Doppler shift. The instrument has a resolution ($\lambda/\Delta\lambda$), capable of detecting variations of 2.89 $kms^{-1}pixel^{-1}$.

A_2 is the half-width of the Gaussian, given in pixels. In order to convert this into microns, which will be needed later, it is necessary to multiply the value by the resolution of a single pixel ($\lambda/\Delta\lambda$):

$$A_2(\mu m) = A_2(pixel) \times \left(\frac{3.953}{103750} \right)$$

2.3.3 Array calibration

The importance of calibration has already been mentioned in this chapter, but it is necessary to restate the importance of establishing accurate calibration before continuing with the analysis of data.

The data being collected is of a high accuracy, but was taken at the limits of CSHELL's specifications. As a result, although the quality of the observations is good enough to allow intensity and velocity variations to be measured, such measurements are effected by variations within the instrument, the Earth's atmosphere and the source - Jupiter. These need to be accounted for, if the final data is to be used with confidence.

To counter the effects of non-Jovian deviations, a proper understanding of how the light is distorted by the atmosphere and the instrument is needed.

The use of a sky frame removes atmospheric emission lines, and provides flat-fielding. Using the calibration data taken, it is possible to measure both the variation in wavelength across the spatial direction for an individual emission source (arc lamp spectra) and the variation in spatial position with wavelength for a point source (star spectra). Analysing the results of these calibrations suggests that the CSHELL instrument varies in both these ways.

Arc lamp calibration

The CSHELL arc lamps provide an even illumination across the entire slit, and can be made to register at different wavelengths without moving the echelle grating, by altering the filter to allow different orders of light onto the array. This allows the lamp lines produced to be used to show variations in the intensity, dispersion in wavelength and non-linearity at each measured wavelength along the entire slit.

What this effectively means is that deviations from a perfectly straight and equally bright spectra can be seen, as an effective measure of the way a spectral image taken in

observation will vary in measurement from the "true" spectra emitted from Jupiter. Since none of the lamp lines recorded lie directly at the position of either the fundamental or hotband spectra, the effective variations are found by measuring variations on the lamp lines and interpolating between these positions.

By using the SPECTRA procedure on the arc lamp data, it is thus possible to find the variations seen across the entire array.

1. Intensity

   The intensity profile of the lamps shows significant variation across the array. Modelling this variation is potentially inaccurate, although variations are always significantly less than the total intensity of the spectra. The best method of countering the effects of intensity variations is with the flat-fielding method used when removing the sky image from the object image (**2.3 Data Reduction**). This removes the variations in intensity caused by inaccuracies on the array.

2. Wavelength calibration

   The extent of calibration required for calculating the wavelength dispersion is limited. The only requisite for an accurate wavelength positioning is the identification of the hotband spectral line seen on some of the spectral images (see **2.4 Secondary Line in the Spectra** and especially Figure 2-30). Beyond this general identification, and the highly accurate measure of the non-linearity of any particular line explained below, the dispersion across the array did not require accurate calibration.

3. Non-linearity

   The non-linearity, the variation in the spectral line position with spatial position on the array for a given wavelength, has an important effect on the calculation of relative peak position across the planetary surface. The non-linearity varies depending on the specific wavelength in question, although this variation does appear to change gradually across the whole array, rather than with sudden variations.

   The region where the non-linearity is important for this thesis lies in a very close region of a few pixels around the fundamental spectra. This removes the need to model the variation across the whole array, and we can concentrate upon the two closest arc lamp lines.

The 3.953μm line is positioned such that it is located particularly close to the 1.3835μm Krypton line, which has an effective wavelength of 3.953331μm, shown fitted in Figure 2-19. While the non-linearity on the fundamental line will vary from that shown on this line, it will be very similar in comparison with other arc lines (for the full calculation see **2.8.2 Array adjustment (□Vd(y))** on page 113).

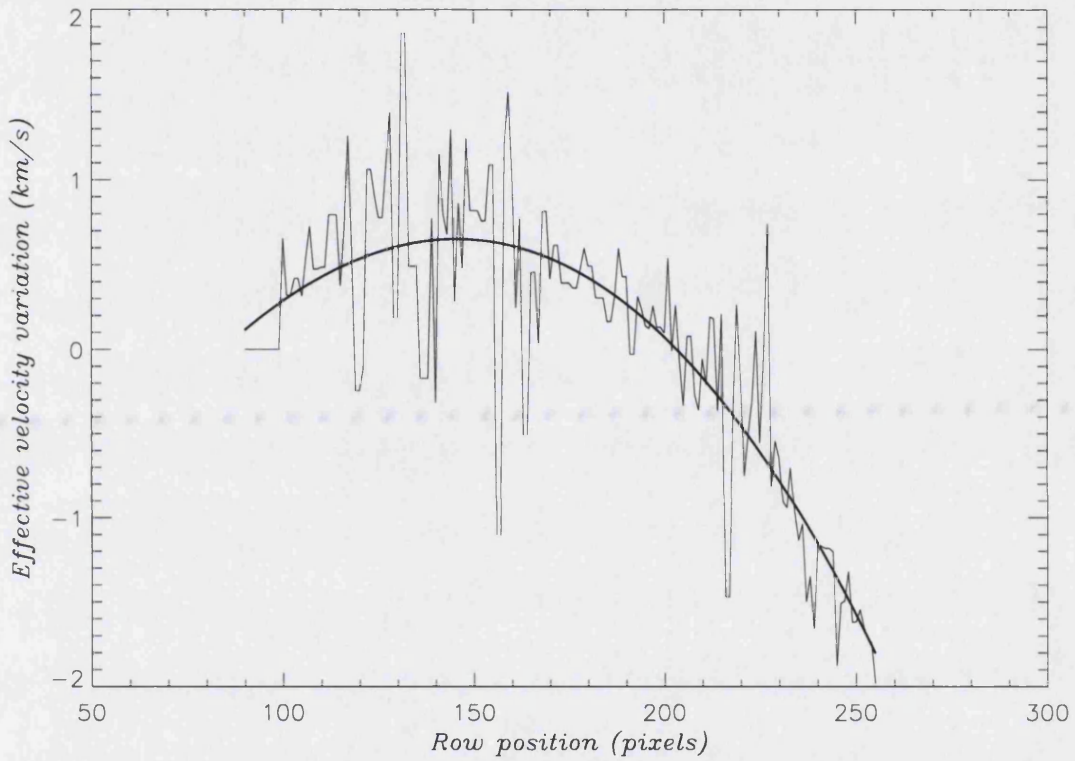

Figure 2-19: The non-linearity of the 1.3835μm Krypton line, positioned closest on the array to the 3.953μm line, which has been fitted with a curve to remove the noise from the correction it represents

Star slope calibration

The star spectra provide a point source in the spatial direction, with emission at all wavelengths. This allows a measurement of variations in the position of a particular point on the slit with different wavelengths, and provides a method to flux calibrate the instrument at intervals through the night.

Measuring the star spectra reveals a linear variation in a point source, with a slope of about 4 spatial-pixels across the entire 256 wavelength-pixel array. For a visual guide to this slope, see Figure 2-20.

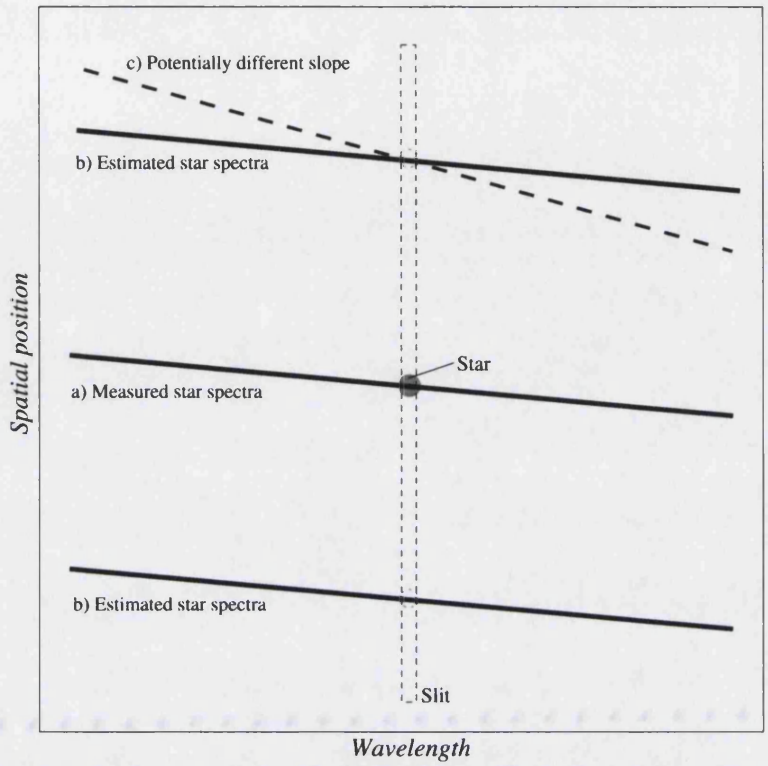

Figure 2-20: The slope in star spectra is represented here. The stellar observed for this thesis were positioned in the centre of the array (a), and were measured with a consistent slope in the x-direction throughout the observations. Given a different spatial y-position in the slit, this slope could theoretically vary in gradient (c), but evidence suggests it remains the same across the entire slit (b).

Unfortunately the star spectra were all made in the same position on the slit. By comparing the peak positions of the fundamental and hotband intensities, however, it is possible to show that there does not appear to be a variation of the slope with the position on the array.

Further to this, communications with support scientists working on CSHELL (Bill Vacca, private communication), suggest that the slope we have measured is consistent with that normally seen, and that variations in the slope across the slit have not been reported by other users. In addition, previous star spectra made at different slit positions show a consistent slope across the array. From this we conclude that no significant variation exists.

The effective variation seen across the few pixels in which a single spectrum lies is not enough to produce a measurable effect. However, the wavelength difference between the fundamental and hotband results in a shift in the spatial direction of 1.9 pixels between

the two. This misalignment needs to be corrected when calculating the hotband temperatures, so the two intensities match in spatial position.

2.3.4 Flux calibration

Flux calibration for all the Jovian spectra can be provided by comparison with the stellar spectra, allowing the intensity of the Jovian emission to be given in Wm^{-2}. This is done using the following equation:

$$\text{Flux}\{I_J(3.953\mu m)\} = \frac{I_J(3.953\mu m)}{I_*(3.953\mu m)}$$

The flux factor I_* is calculated entirely within the FLUXCALIBRATION procedure (**B.4.2 fluxcalibration.pro**), and represents a divisional factor that calibrates the Jovian intensities to Wm^{-2}. This is performed for each stellar spectrum with a 4" slit, a width that allows all the light to enter the instrument regardless of light dispersion from the instrument or the atmosphere.

To find I_*, it is necessary to find the total output of the star at 3.953μm. This was done by taking an area of the array twenty wavelength (x-direction) rows wide and forty spatial (y-direction) rows deep, centred on the stellar spectra at 3.953μm. This was added in the wavelength direction to improve the signal-to-noise ratio of the spectra, producing a light curve across the slit, an example of which is shown in Figure 2-21.

This curve was then fitted with a Gaussian as in the SPECTRA procedure:

$$F(x) = A_0 e^{\frac{-z^2}{2}} + A_3 + A_4 x + A_5 x^2$$

$$\text{Where, } z = \frac{(x - A_1)}{A_2}$$

which produces an accurate curve without the noise. By removing the background ($A_3+A_4x+A_5x^2$) from this, it produces a light curve that consists of only the light from the

star. Each element in this array is then added together to provide the total flux in hits per pixel for the star.

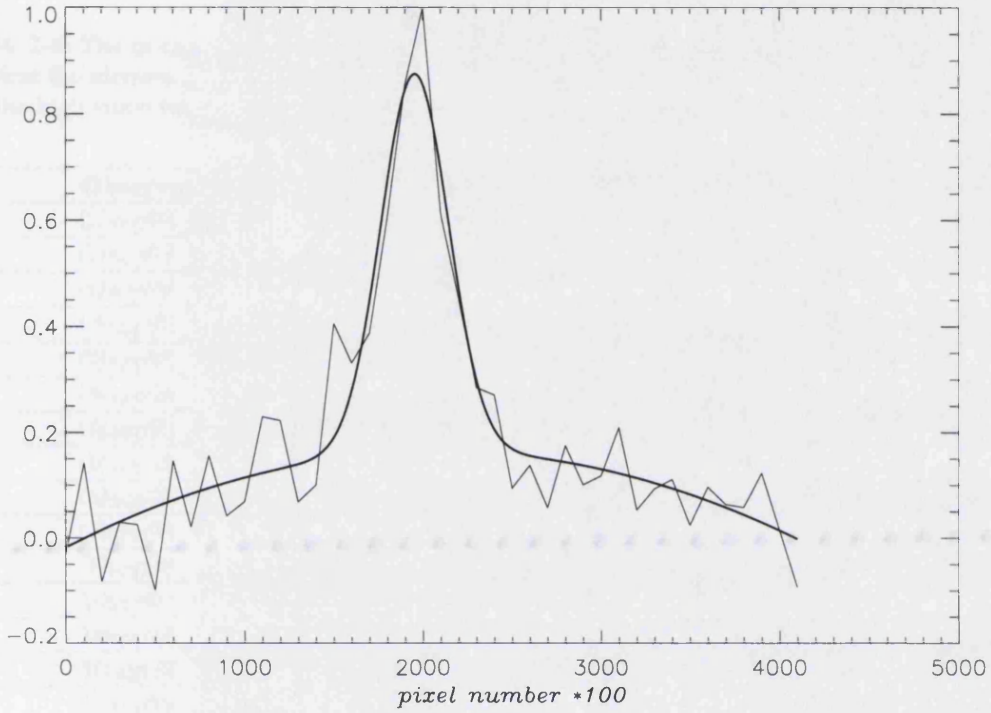

Figure 2-21: The stellar light curve in a y-direction, from a 4" slit collated over 20 wavelength pixels, fitted with a Gaussian

Our standard star, BS8647, has an actual output of $1.19\text{x}10^{-13}\text{Wm}^{-2}\mu\text{m}^{-1}$ at 3.953μm, which allows the calibrational factor I_* to be calculated:

$$I_*(3.953\mu m) = \frac{\text{Calculated Flux}}{1.19\text{x}10^{-13}}$$

Interpolating between separate flux factors within a specific day proved difficult. Variations in the flux factor originate from atmospheric effects, as well as the specific airmass (z) at the time of observation. However, there appears to be no systematic airmass dependency in the variations (Table 2-4). The flux factor varies by, in the worst case, over 300% between spectral images taken only minutes apart, although this may be due to a slight telescope misalignment.

Since the variations cannot be correlated with z, the daily average flux factor is used in order to produce as accurate a value of calibration as possible (Table 2-5). Since the

maximum variation across a single night is generally about 20%, with the one exception noted, (compared with the maximum variation across all five nights of 78%), this is a reasonable way to determine variations in flux factor.

Table 2-4: The intensity of the stellar spectra used to calibrate the intensity of the Jovian spectra, against the airmass at the time of the observation, with which there appears to be no correlation. Note the high value for intensity, resulting from the flat-fielding method of sky removal (see 2.3 Data Reduction, above)

Observation	Intensity (hits * no. of pixels)	Airmass (z)
07sep98_017	3.42078e+07	1.779
07sep98_052	3.02771e+07	1.121
07sep98_104	2.20175e+07	1.319
08sep98_016	3.20909e+07	2.488
08sep98_081	2.55993e+07	1.304
08sep98_116	2.86398e+07	1.160
08sep98_183	2.43447e+07	1.140
08sep98_337	2.95609e+07	2.286
09sep98_010	8.14975e+06	1.280
09sep98_016	2.98056e+07	1.233
09sep98_125	1.93088e+07	1.149
10sep98_011	2.23536e+07	2.151
10sep98_149	2.87262e+07	1.125
10sep98_276	3.07830e+07	1.365
11sep98_012	2.78967e+07	2.931
11sep98_108	1.98045e+07	1.365

Table 2-5: The averaged flux factor used to calibrate the Jovian fundamental emission for each night

Date	Average flux factor I_* (1×10^{20})
7th Sept, '98	2.42
8th Sept, '98	2.36
9th Sept, '98	1.60
10th Sept, '98	2.29
11th Sept, '98	1.34

2.3.5 Bounce feature on images

Upon reducing the data, it became apparent that some of the images taken of the aurorae showed a "doubling" feature in the x-direction that could only be explained by an episodic instrumental effect. This effect occurs on most of the 10^{th} and early 11^{th} 3.953μm images, with images from other times showing little, if any, such effects.

Figure 2-22 shows a H_3^+ image taken on the 11^{th} after the episodic "doubling" effect had cleared up; this image can be considered high quality. Figure 2-23 shows an image taken

at a similar CML (~160°) on the previous night of the 10th. The doubling effect on this image is clearly evident, distorting the image such that the details within the auroral oval are blurred. The third figure (Figure 2-24) shows the first image with an affected "doubling". This image was produced by shifting the image by 5 pixels (~1 arcsec), and adding it to the original. The result is very similar to the image from the 10th, including the relative strengths of the upper and lower limbs.

The origin of this doubling is unclear. The doubling effect is notably not seen in the K-band images taken immediately before the 3.953μm images that show even the worst doubling effect (Figure 2-25). Comparing this with the K-band image from the 11th (Figure 2-26), and simulating a bounce on the 11th (Figure 2-27), leaves no doubt to the lack of a K-band bounce.

Nor can the effect be seen on the spectral data. Looking at the relative intensities of spectral line and image taken at a CML of 302°, shown in Figure 2-28, a lack of doubling can be clearly distinguished from the corresponding position on the image, which shows strong doubling across the entire western limb (Figure 2-29).

Thus this effect is caused in a short enough time period to form on the images, and yet the doubling is not seen in the bad pixels remaining at the end of processing, which can be attributed in part to cosmic rays. This indicates a mechanical fault in the instrument during the collection of data. Since the spectral images appear unaffected by this, it suggests that the fault may lie in the mirror that overlays the grating for images. CSHELL has reported problems with repositioning the Direct Imaging Mirror when it is moved (**2.1.2 Positioning of the Direct Imaging Mirror**), and the "bounce" may be attributable to the mirror not fitting in place properly and slipping slightly during each exposure, until the grating is replaced. This sudden shift from one position to another is further borne out by the lack of blurring between each of the two "doubles", particularly emphasised by the modelled doubling seen in Figure 2-24.

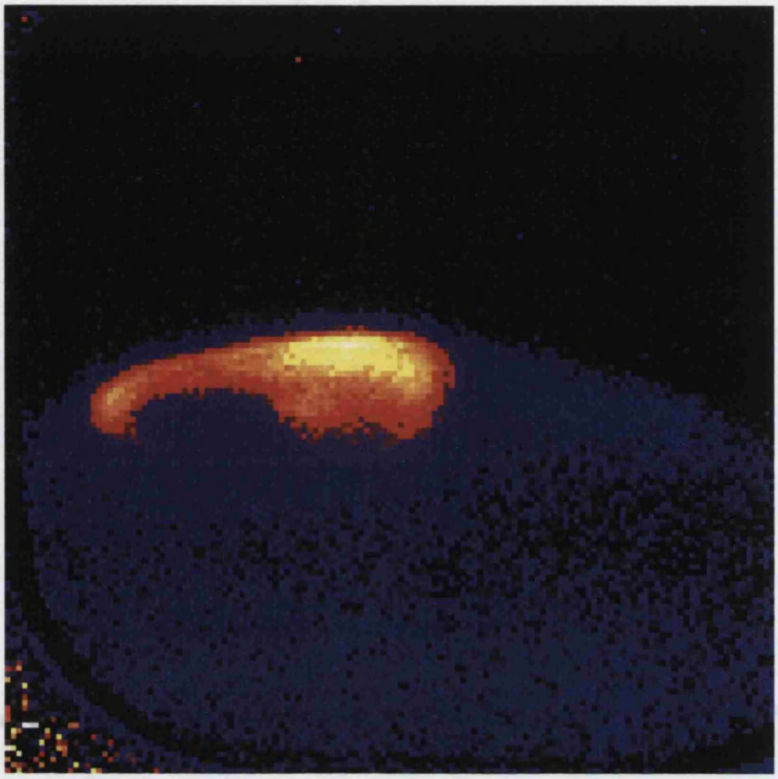

Figure 2-22: The 3.953μm image of the Jovian aurora, taken at a CML of 154° on the 11th, showing no "double-bounce" effect

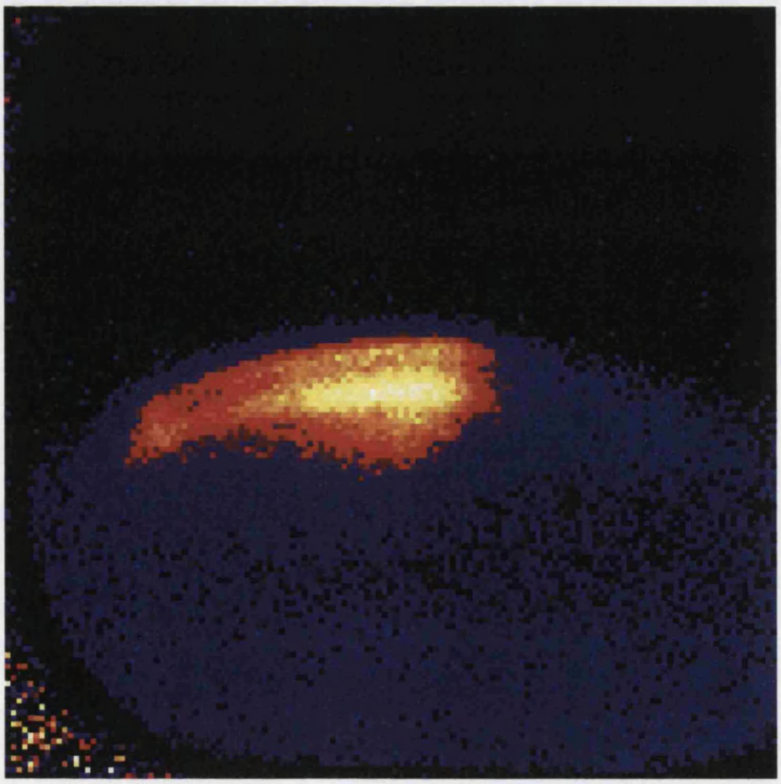

Figure 2-23: The 3.953μm image of the Jovian aurora, taken at a CML of 144° on the 10th, showing a significant "double-bounce" effect

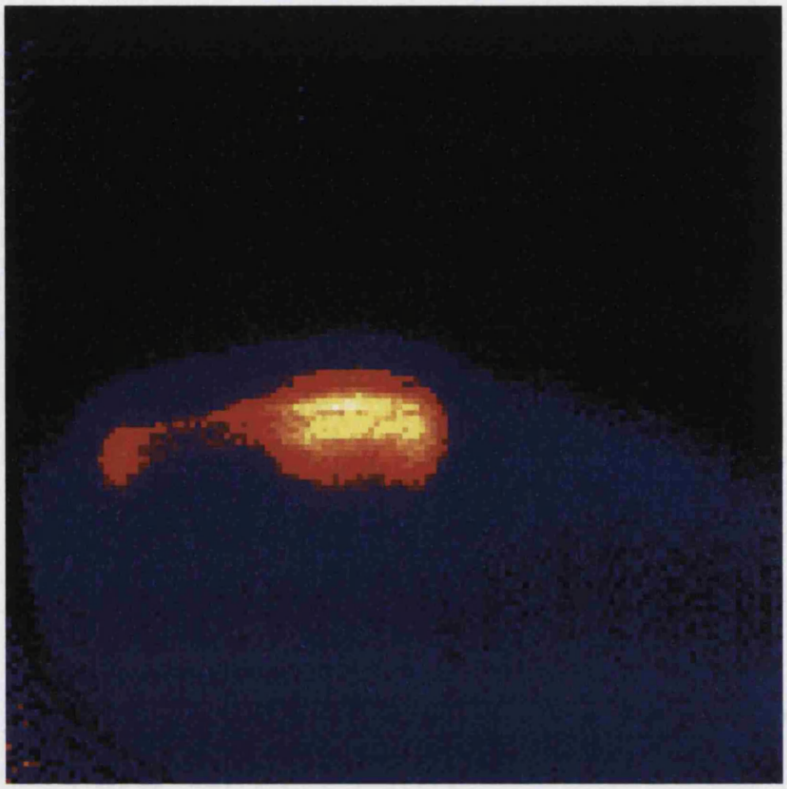

Figure 2-24: A simulated "double-bounce" effect of 5 pixels, using the 3.953μm image of the Jovian aurora, taken at a CML of 154° on the 11th

Figure 2-25: A K-band image of Jupiter, taken on the 10th, when the corresponding 3.953μm image (Figure 2-23) had a significant "double-bounce" visable

Figure 2-26: A K-band image of Jupiter, taken on the 11th, when the corresponding 3.953μm image (Figure 2-22) had no apparent "double-bounce" effect associated with it

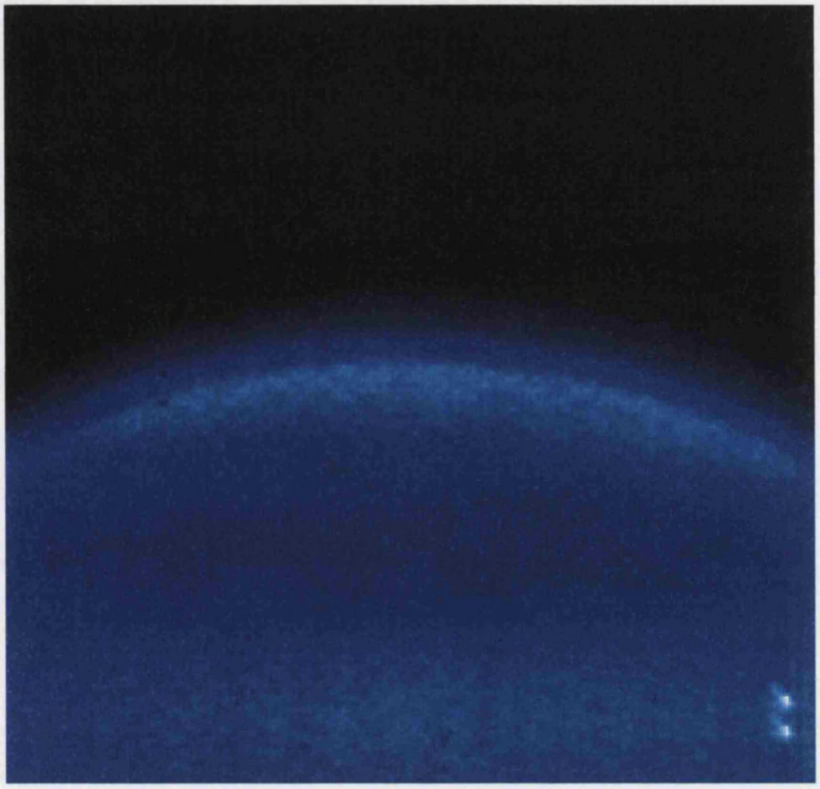

Figure 2-27: A simulated K-band image of Jupiter, showing the effects of a 5-pixel "double-bounce" effect, using an image taken on the 11th (Figure 2-26)

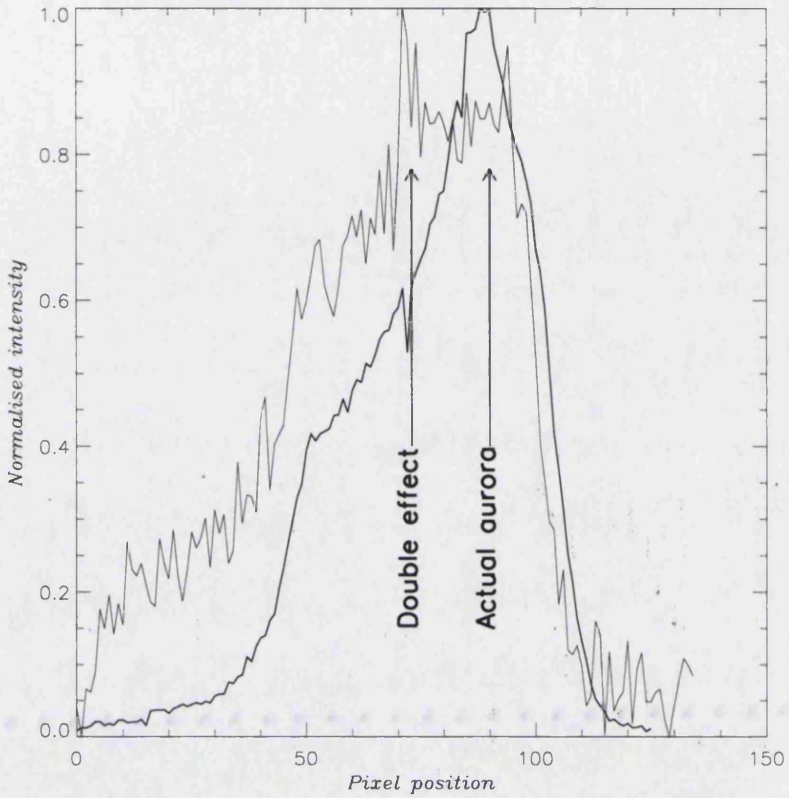

Figure 2-28: The spectral intensity profile (in bold), and the corresponding image profile for a CML of 302° on the 10th, proving the lack of the "double-bounce" effect on the 3.953μm spectra

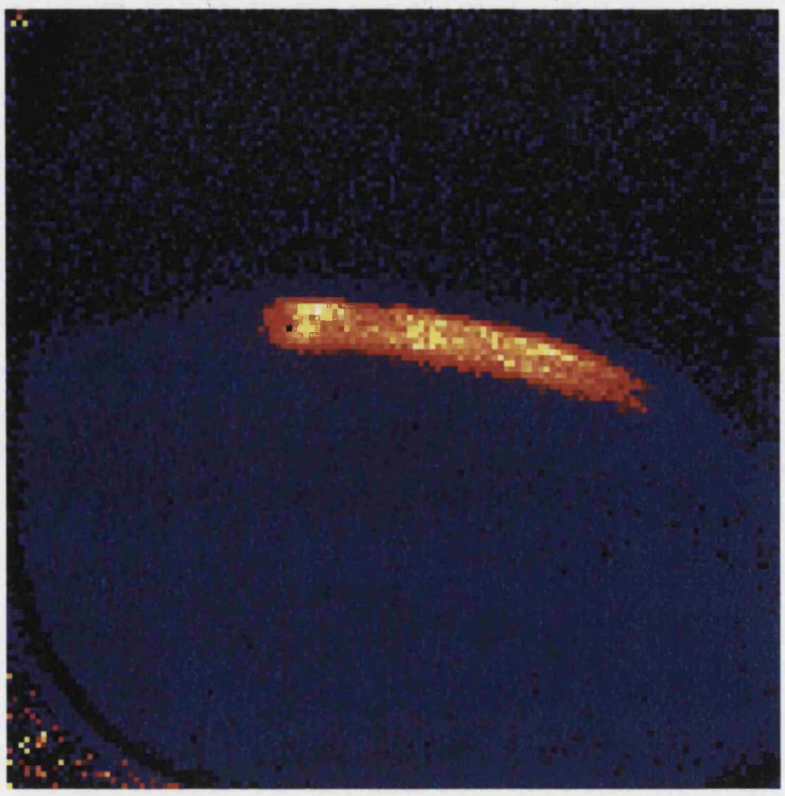

Figure 2-29: The 3.953μm image of the aurora that corresponds with Figure 2-28

2.4 Secondary Line in the Spectra

Even with only the preliminary reduction of the data made during the observations, it became clear that, as well as the fundamental signal centred on the array, an additional line fainter but clearly delineated could be seen on the far left of the array (Figure 2-30). The measurement, characterisation and subsequent implications of this line are discussed in this chapter.

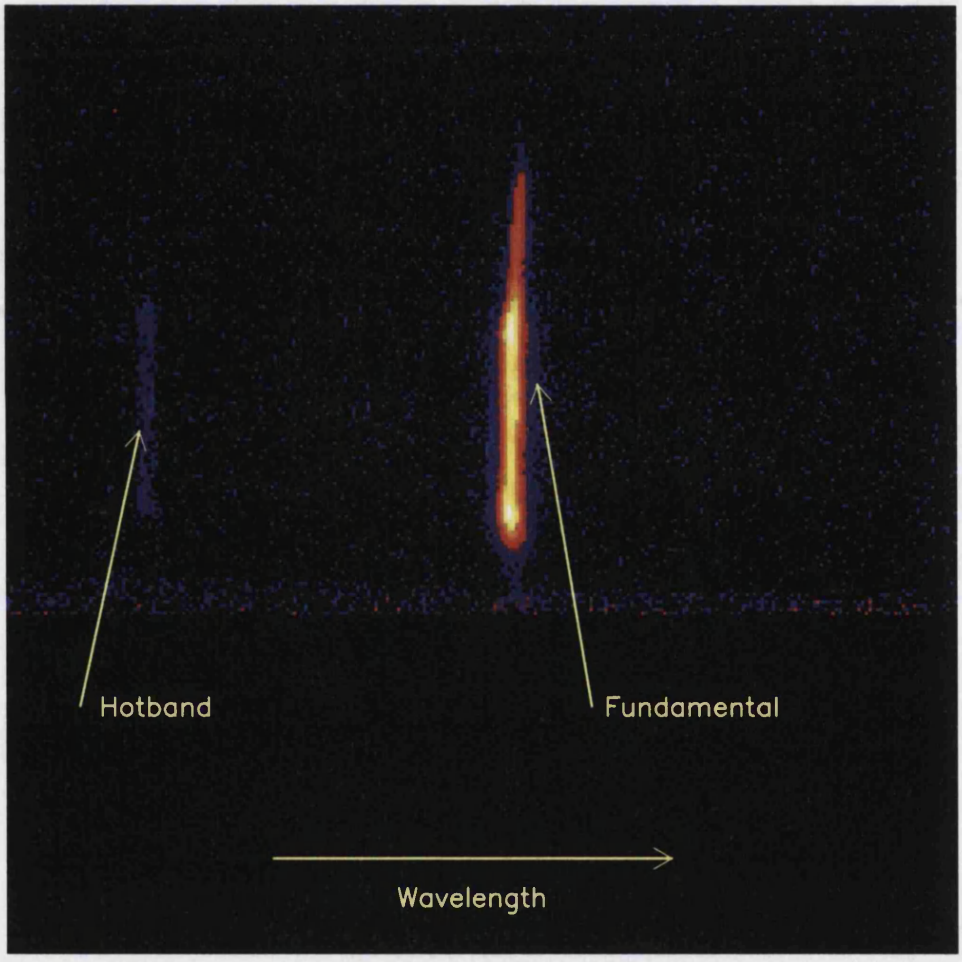

Figure 2-30: The hotband spectra shown on the spectral image taken at 159° CML on the 11th

2.4.1 Line characteristics

The secondary line appeared in all five nights of observation, as a faint signal in the far left of the spectral array. The strength of the signal largely mirrored the intensity structure seen in the fundamental line (the $Q(1,0^-)$ transition), so the secondary line is

only seen within bright auroral regions; the brighter the fundamental signal, the stronger the secondary signal is delineated.

The line is discernible in individual object ("A" frame) spectral images before sky ("B" frame) subtraction (**2.3 Data Reduction**), shown in Figure 2-31, and with the sky subtracted can be determined as having an intensity of a few percent of the fundamental line.

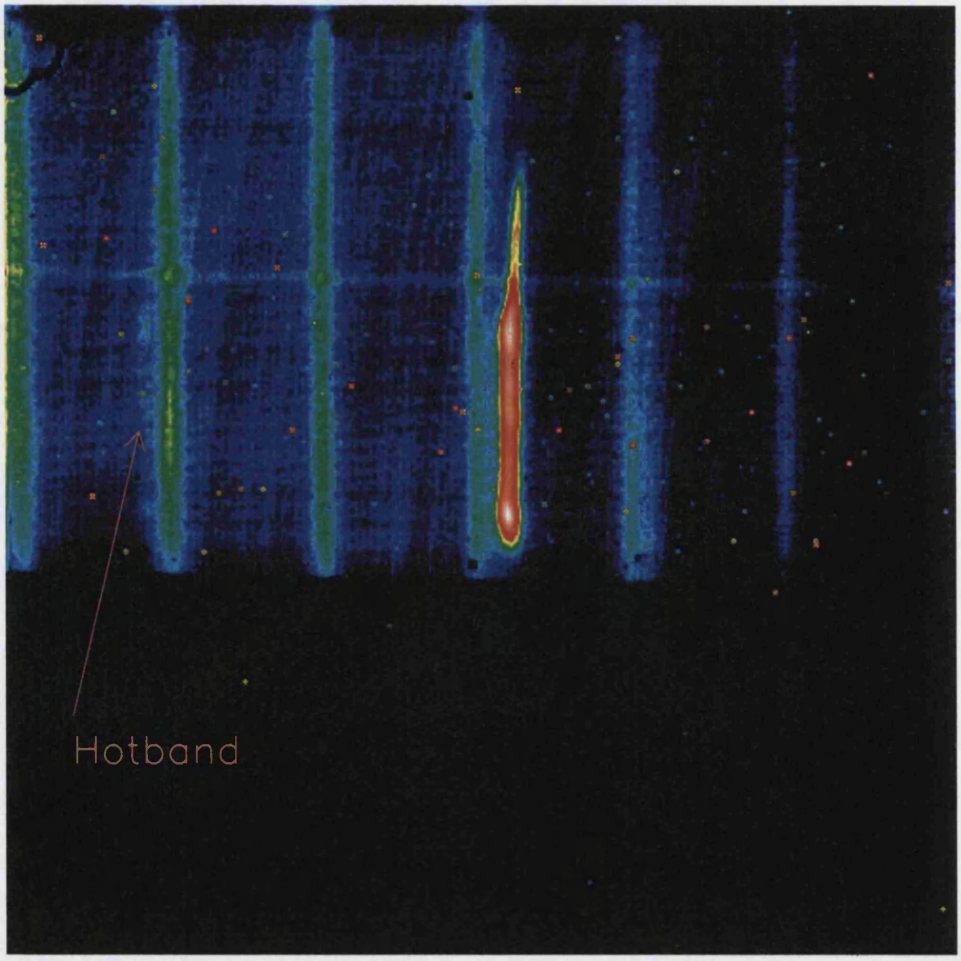

Figure 2-31: The hotband shown without sky removal, on the same spectral image as Figure 2-30

Such a secondary line has not been seen in previous data taken by the UCL group. Nor have any other researchers reported it. Data was taken on the night of 8th August 1997 using very similar instrumental conditions to those described here. The only major variation was the use of a 1" slit, which would have the effect of increasing both the Jovian emission received and the background noise within the array itself, but the conditions are so similar as to make the data very useful for direct comparison.

This data set was reanalysed for evidence of the secondary line, but even by summing the entire set, consisting of 40 spectral images amounting to a total exposure time of 2000 seconds, shown in Figure 2-32, no clear signal could be seen. There is faint emission in the wavelength region close to the secondary line observed in the 1998 data, but this is not peaked in the way the 1998 line is, and is better ascribed to incomplete sky subtraction due to the great length of total exposure. In comparison with this, the combined fundamental spectra are very strongly delineated and sharply peaked, with a signal-to-noise ratio of more than 200.

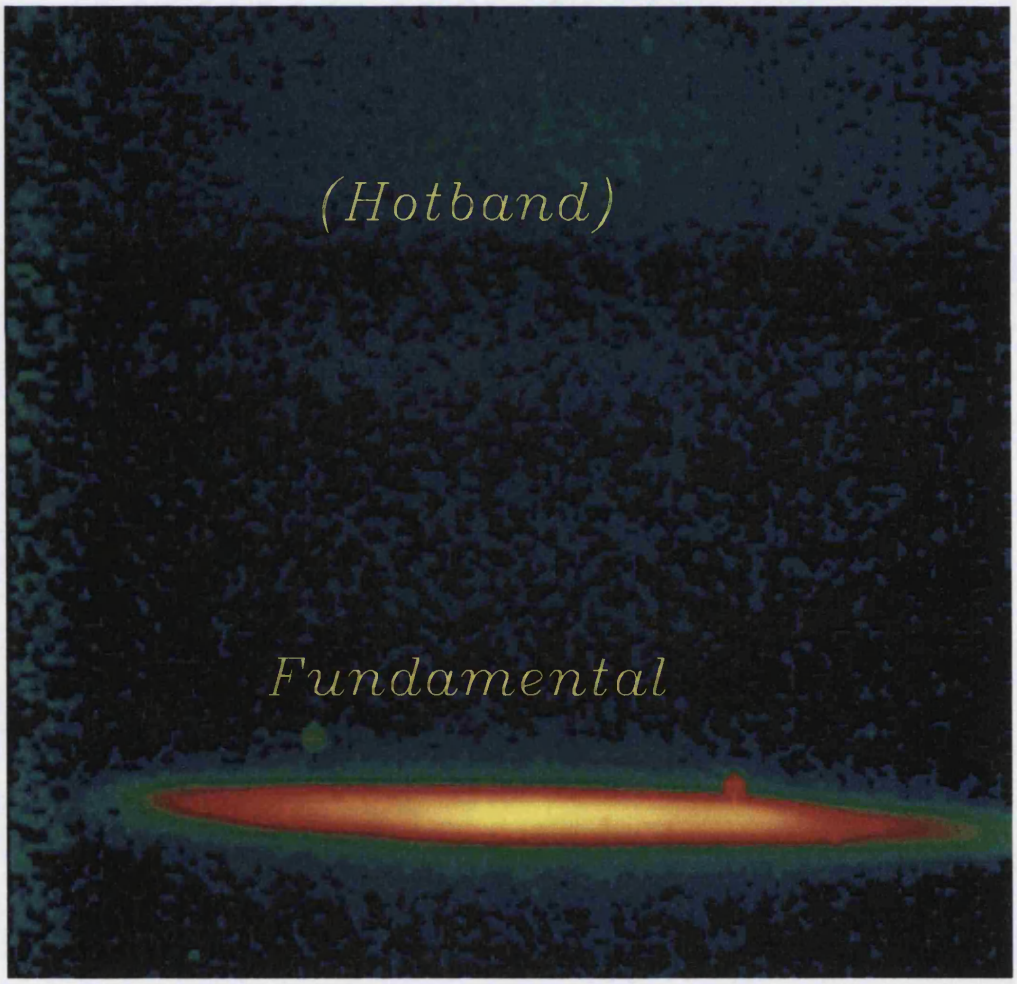

Figure 2-32: The combined 3.953μm spectral image of the entire 1997 dataset

2.4.2 Elimination of instrumental effects

Before the secondary line can be attributed to a physical spectral line, it is important to establish that the line could not have been caused by an instrumental effect.

Because of the clear spatial correspondence between the secondary line and the fundamental line, any instrumental effect would have to have been caused in the form of internal reflections of the fundamental line. However, discussion of such "ghosting" effects with the CSHELL support scientists (W. Vacca, J. Rayner, private communication) allows the instrumental origin of the line to be ruled out, by further examining the characteristics of the secondary line:

- Internal reflections in CSHELL are generally symmetric about the centre of the array. Since the fundamental line was centred on the array, any "ghosting" will have been overlain upon the original line, rather than near the edge of the array, as is the case with our data;

- The wavelength displacement between the secondary line and the fundamental line is constant throughout the nights measured, even though the exact positioning of the fundamental line varied slightly due to the slit wheel motor having some "play" in its motion. Any reflection would have varied in relative position to the fundamental line under such conditions;

- While the intensities of the two lines are generally mirrored, on closer examination there are notable differences in their exact form across the slit. Such variations are not feasibly produced by a reflection, because a "ghost" should maintain a constant relative intensity with its source;

- Such reflections would have been seen in previous observations that used the same instrumental conditions, such as those taken in 1997. This is not the case.

Since the above attributes of "ghosting" are clearly not seen within the data, the secondary line cannot have been caused repeatedly throughout the data by any known instrumental effect. This results in the conclusion that the line is of an observational origin; the lack of the line in the sky frames ("B" frame) shows this to be of a Jovian origin.

As has been discussed in the introduction (**1.3.1 Composition of the ionosphere**), the methane absorption of sunlight results in emission at this wavelength range being possible only from species of H and He. The line could be the product of "leaky methane" (Drossart *et al.*, 1989), but the general matching between the secondary and fundamental lines suggests an auroral origin, since "leaky methane" features are inversely correlated with the intensity of H_3^+ emission. Measurement of the line characteristics would allow the species to be determined.

2.4.3 Wavelength measurement

Location of the exact position of the secondary spectral line could be problematic, because of the variation in the wavelength position of the slit (**2.1.2 Positioning of the Direct Imaging Mirror**). However, since the relative position of the secondary line to the fundamental line should always remain constant, measuring the secondary line relatively removes this problem. By using the relative position of the two lines, considerations over the exact positioning of the slit over the array and the relative motions of the Earth and Jupiter are removed.

By simple adding of rows across the slit, a single spectrum can be produced, which can then be compared with the position of the lamp lines (Figure 2-33). The rotation of Jupiter results in spectral lines that are not exactly vertical on the array, causing some broadening of the peaks. Since the two lines vary by the same amount, this is not a problem.

To find the position of the secondary line, it was assumed that there was a linear variation in wavelength between the two lamp lines that enclose it. To provide a more accurate position for each line, they were all fitted with Gaussian, and the relative position of the secondary line to the two lamp lines gave a calculated wavelength position of 3.94895μm.

This measured wavelength corresponds with a wave number of 2532.319cm^{-1}. This value is within the experimental error of the laboratory-measured frequency of 2532.253cm^{-1} of the H_3^+ ($2v_2(0) \rightarrow v_2$) R(3,4$^+$) hotband transition. Since it is the only possible known emission line in this region of the spectrum, this can be regarded as an unambiguous

identification of the line. This identification is the first reported detection of a H_3^+ hotband transition.

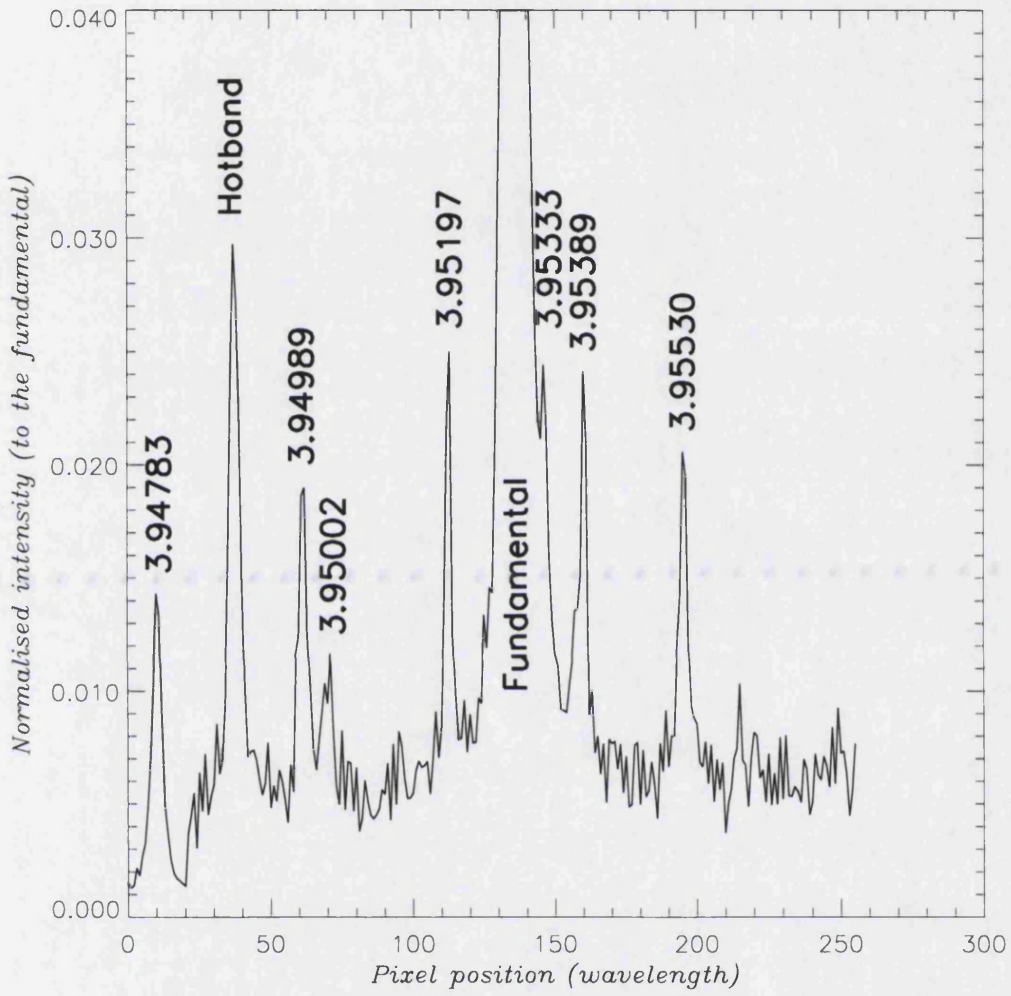

Figure 2-33: The relative position of the hotband spectral line on the array, compared to the position of the arc lamp lines and the fundamental (3.953μm) spectral line

2.4.4 Hotband Gauss-fitting

The hotband can be processed in the same manner as the fundamental. Since the signal-to-noise of the hotband is significantly lower, while the fundamental could have a direct Gaussian fitted for each row of spatial data, this is not practical for the hotband. However, the required quality is less for our purposes, since only an accurate value for the intensity is important (see **2.5.2 Temperature calculation**). The peak position of the

spectral line is not needed, as the strength of the fundamental line provides the better accuracy required for determining Doppler shifts.

To increase the signal-to-noise of the line, the SPECTRA procedure was adapted to allow each spatial position on the hotband spectral image to be combined from the four surrounding pixels on each side. This produces a "rolling average" of nine rows, effectively reducing the spatial resolution from 0.2" to 1". This results in an estimated four-fold increase in the signal-to-noise, at the cost of a loss in spatial resolution. Figure 2-12 and Figure 2-13 (on page 70) show the same spatial row with a single row of data, and with a nine-row average.

In all other respects, the modified procedure works in the same way as the original.

2.5 Effective vibrational temperatures

2.5.1 Improved temperature analysis

The discovery of the H_3^+ hotband on the spectral images introduced the possibility of calculating temperature across the auroral region to an unprecedented level of detail. In the past the only spectral observations that have reached an equivalent spatial resolution to these observations have been made by the UCL group, with the slit aligned along the rotational axis of Jupiter, with no provision for longitudinal variations. Other than this, only imaging has managed to match the spatial resolution used here, and that provides no way to calculate temperature accurately.

The pixel-to-pixel variation measured across the fundamental profiles has a spatial resolution of 0.2". While the nine-pixel rolling average reduces this spatial accuracy to ~1", this remains the highest resolution spectral observations made of the Jovian H_3^+ temperature. In addition to this, the variations across the profile can be measured closer to the fundamental resolution, as the rolling average moves in steps of 0.2".

Within this thesis, three temperatures will be discussed: the kinetic temperature is the temperature of the neutral thermosphere; the rotational temperature is the rotational

temperature obtained by measuring H_3^+ rotational sub-lines within a particular vibrational band; and the effective vibrational temperature, obtained by ratioing H_3^+ lines from different vibrational bands.

Previous studies that have examined both longitudinal and latitudinal spatial variations in the auroral temperature (Miller *et al.*, 1997a; Lam *et al.*, 1997) have only calculated the rotational temperatures within the $v_2 = 1$ (ν_2) vibrational manifold as a function of spatial position. However, by using the hotband spectral lines, this study can calculate the effective vibrational temperatures. In using spectral lines from different vibrational manifolds (**1.2.2 H3+ spectroscopy**), the separation between upper energy levels is much greater than is available in rotational temperatures, made using spectral lines from within the same vibrational manifold. Thus, measuring the effective vibrational temperature provides a greater sensitivity to kinetic temperature variations than has been possible in previous studies.

However, unlike the rotational temperature which is clearly thermalised with the surrounding neutral atmosphere, the effective vibrational temperature is assumed to relate to the local kinetic temperature through "quasi-thermal equilibrium" (QTE). This assumption states that while the vibrationally excited levels of H_3^+ can be considered to be populated as might be expected from a Boltzmann distribution at the given kinetic temperature, the ground state is overfilled. If this assumption begins to break down, then the ($v_2 = 1$) level will become overpopulated compared with the ($v_2 = 2$) level, and so effective vibrational temperatures will underestimate the kinetic temperature.

2.5.2 Temperature calculation

Assuming that H_3^+ is in an effective QTE (**1.3.3 Local thermal equilibrium** and above), it is possible to calculate the effective vibrational temperature, and thus the kinetic temperature, of H_3^+ from the relative intensities of the fundamental and hotband spectral lines.

The intensity of an emission line may be calculated from:

$$I(\omega_{if}) = \frac{g_{ns} \times (2J'+1) \times hc\omega_{if} \times A_{if} \times e^{\left(\frac{-E'}{kT}\right)}}{4\pi Q(T)}$$

Where, g_{ns} is the nuclear spin weighting of the transition;

J' is the angular momentum of the upper state;

ω_{if} is the transition frequency in wave numbers;

A_{if} is the Einstein A coefficient for spontaneous emission;

E' is the energy of the upper level;

And, Q(T) is the partition function.

This provides a direct link between an individual intensity and the temperature. By taking values of the ratio of intensities of two different spectral lines (a) and (b), this equation gives:

$$\frac{I(\omega_a)}{I(\omega_b)} = \frac{g_{ns}^{(a)} \times (2J'_a+1) \times hc\omega_a \times A_a \times e^{\left(\frac{-E'_a}{kT}\right)}}{g_{ns}^{(b)} \times (2J'_b+1) \times hc\omega_b \times A_b \times e^{\left(\frac{-E'_b}{kT}\right)}}$$

And defining γ as the pre-exponential ratio of spectroscopic constants;

$$\frac{I(\omega_a)}{I(\omega_b)} = \gamma \exp\left[\frac{(E'_b - E'_a)}{kT}\right]$$

Table 2-6: Parameters of the fundamental and hotband lines (Kao *et al.*, 1991)

	Fundamental ($\nu_2 \rightarrow 0$) Q(1,0⁻)	**Hotband ($2\nu_2(0) \rightarrow \nu_2$) R(3,4⁺)**
Upper energy level *E'*	2616.5cm^{-1}	5250.2cm^{-1}
Einstein coefficient A_{if}	129s^{-1}	66s^{-1}
Nuclear spin weighting g_{ns}	4	2
(2J'+1) [angular momentum of upper state = *J'*]	3	9
Transition frequency ω_{if}	2529.5	2532.3

The value of γ can be calculated once, using the values given in Table 2-6, leaving the intensity ratio as the only variable from which temperatures are derived:

$$T = \frac{\frac{[E'_b - E'_a]}{k}}{\left[\ln\gamma - \ln\left(\frac{I(\omega_b)}{I(\omega_a)}\right)\right]}$$

This intensity ratio is calculated from the hotband and fundamental peak intensities resultant from the SPECTRA procedure, which is used to produce a final temperature within the procedure HBTEMP (**B.3.3 hbtemp.pro**).

The procedure loads in the two intensities, and then converts the fundamental into a format that can be directly used against the hotband intensities. This conversion is required because the hotband is only detectable in regions of particularly strong fundamental intensity, and thus has a more limited spatial extent than the fundamental. The hotband was also smoothed over nine pixels in its processing, to produce a stronger signal-to-noise. The fundamental line has to be smoothed to an equal extent, to produce comparable intensity data. An example of this smoothed fundamental intensity is shown in Figure 2-34.

A secondary correction is required because of the spatial slope in the array as a function of wavelength (**2.3.3 Star slope calibration**), which produces a y-axis variation between the spectral profiles of 1.9 pixels. This effectively means that the hotband is shifted in the spatial direction by approximately 2 pixels, compared to the fundamental (Figure 2-35). Thus, when correcting for the difference in hotband and fundamental spatial extent, it is also necessary to shift the comparative position of the two slightly.

Once these corrections have been made, the effective vibrational temperature was calculated by taking the ratio of the two lines (Figure 2-36), and using this ratio in the following equation:

$$T_v(K) = \frac{3783.3}{\left[-0.2637 - \ln\left(\frac{I(3.949)}{I(3.953)}\right)\right]}$$

This is taken from the equation that gives the ratio between the two intensities, I_{HB}/I_{FUND} where:

3783.3 is the difference in the upper energy level of the two transitions expressed in Kelvin;

and, -0.2638 is the natural logarithm of γ, defined above.

This produces a profile of effective vibrational temperature across the aurora, which is also assumed to be a profile of kinetic temperature under QTE, an example of which is shown in Figure 2-37.

The hotband data, which has a low signal-to-noise in some regions and is often not visible at all, makes the calculation of temperature difficult on much of the data. However, for the strongest data sets, these intensity variations provide a detailed view of spatial variation in temperature.

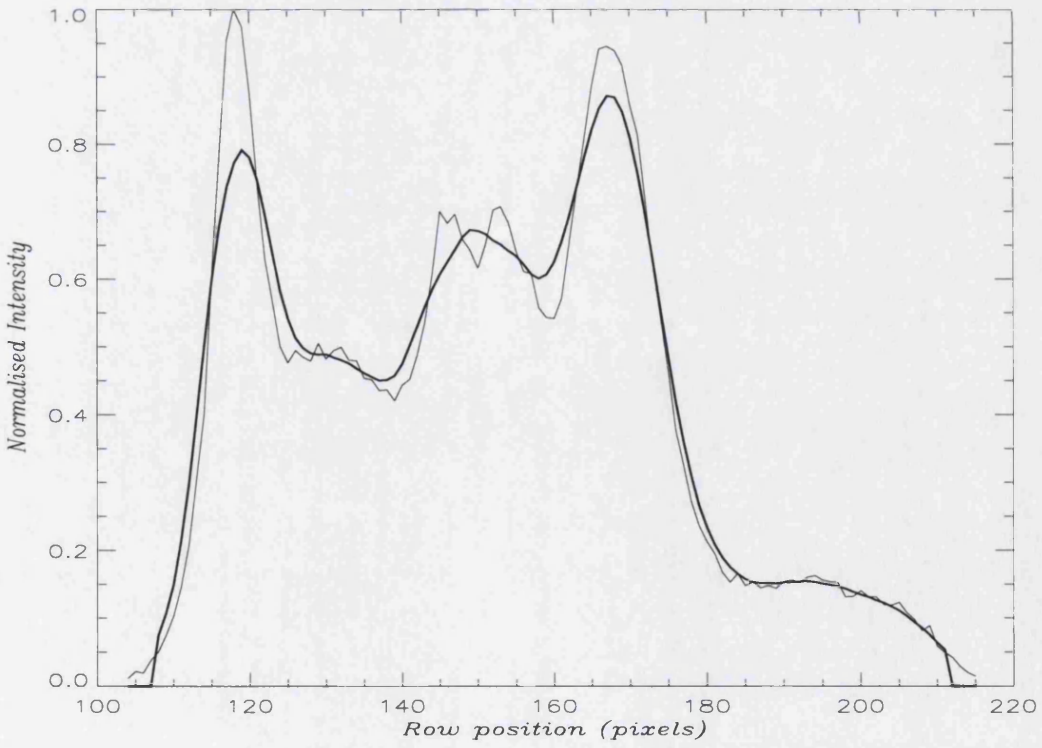

Figure 2-34: The fundamental intensity profile smoothed over nine spatial pixels (in bold), and the original intensity profile, for a CML of 159°, taken on the 11th (11sep98_166)

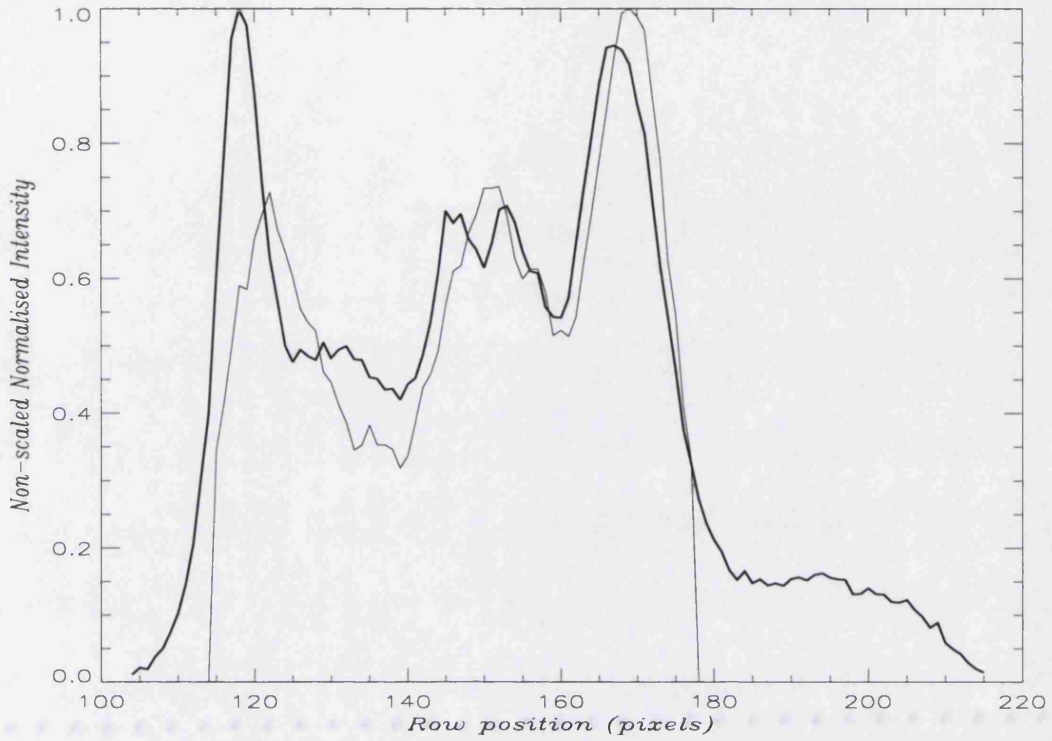

Figure 2-35: The fundamental intensity profile (in bold) and corresponding hotband intensity profile, showing the two-pixel relative shift in spatial position

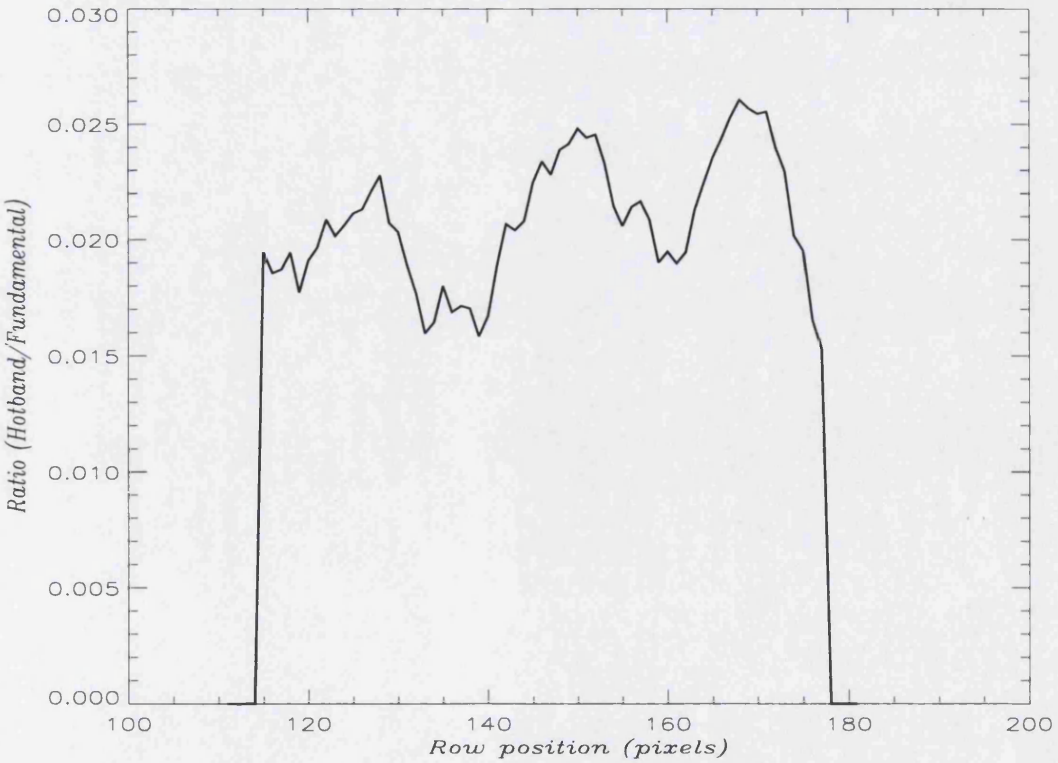

Figure 2-36: The ratio between the fundamental and hotband intensities, for 11sep98_166

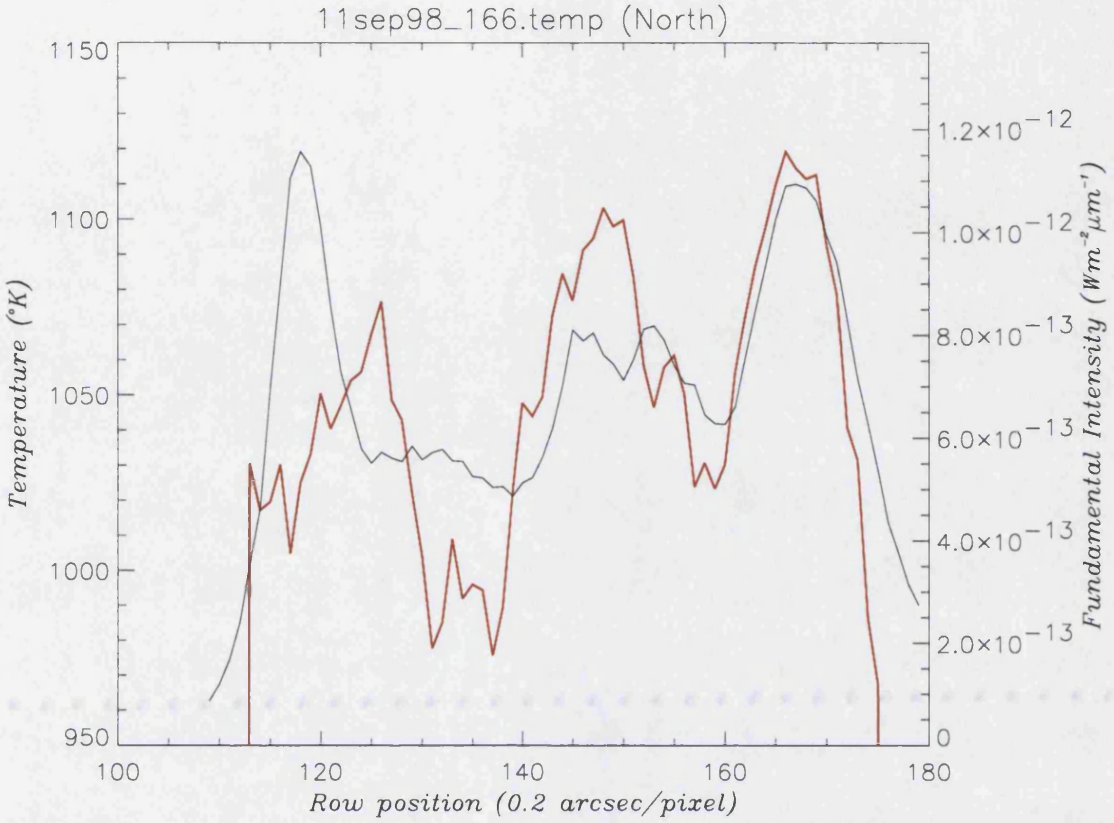

Figure 2-37: The output temperature profile (red) calculated in HBTEMP, plotted with the fundamental intensity profile, for 11sep98_166

Average spectral temperature

In an attempt to use more of the data and to find a temporal trend in the data, a secondary temperature calculation was used, within the AVTEMP procedure (**B.3.1 avtemp.pro**).

This changes the emphasis from spatial quality to getting the best possible temperature calculation for each spectral image. The procedure requires the user to click the location of the two limits of the hotband spectral profile, as in SPECTRA, and then the location of the two spectral lines.

From this it produces individual two-line spectra, by adding all the rows of each spectral image together (including the two-pixel shift between the hotband and fundamental position). This produces somewhat broad lines in each case because of the rotational slope, but since this affects both spectra equally, it should have no effect on the ratio of the two peaks.

Each of these collated lines is fitted with a Gaussian, as in SPECTRA, and the temperature is calculated as shown above. The only difference here is that the signal-to-noise is much better, at the cost of losing spatial information. Because the data is fitted with a Gaussian, a temperature can be produced with even the most weakly displayed hotband, allowing nearly the whole data set to be sampled.

2.6 Column Density

2.6.1 Significance of column density

Showing the detailed variation in column density across the auroral region is a very useful advance upon the current understanding of the distribution of H_3^+ production.

It has been widely assumed in previous literature (*e.g.*, Satoh and Connerney, 1999) that H_3^+ emission intensity is a strong indicator of the location and degree of energy deposition in the aurora. This assumption is based on the presumption that H_3^+ emission is coincident with H_3^+ production.

For the correlation between emission and energy deposition to hold, there needs to be an equal correlation between the H_3^+ column density and the H_3^+ emission. However, previous tests of this second correlation have always been made using a resolution too poor to be able to pick out details within the aurora itself, and thus successfully test the extent of correspondence between emission intensity and column density.

With this data set, it will be possible to test this assumption properly for the first time, and to show whether there is a direct correspondence between, in this case, the fundamental intensity and the calculated column density. This relies upon the assumption of quasi-thermal equilibrium (QTE) made in calculating temperature (**1.3.3 Local thermal equilibrium**), and so by not taking account of the overfilled ground state, the calculated column density underestimates the true value. If QTE begins to break down, then the effective vibrational temperature will underestimate the kinetic temperature, and so the calculated column density will overestimate the true value. These effects will be discussed in terms of the results in **3.3 H3+ Column Density and Production**.

2.6.2 Calculation of column density

The column density is calculated in the COLDEN procedure (**B.3.2 colden.pro**), using the following equation:

$$N(H_3^+) = \left(\frac{I_J}{E_{H_3^+}(\lambda, T)} \right) \times \left(\frac{4.2545 \times 10^{10}}{pixarea} \right)$$

Where, I_J is the intensity of the fundamental line in Wm^{-2};
$E_{H3+}(\lambda,T)$ is the emission from a molecule of H_3^+ in the ($v_2 \rightarrow 0$) (1,0$^-$) line, dependant upon temperature, given in $W^{-1}molecule^{-1}sr^{-1}$;
$4.2545x10^{10}$ is equal to (1 radian^2/1 arcsec^2);
And, *pixarea* is the pixel area in arcsec^2.

To produce a value of column density, a value for the intensity and a correlation between emission and temperature are thus required.

1. Emission against temperature

   By fitting values for temperature vs. molecular emission $E_{H_3^+}(\lambda, T)$, taken from Neale *et al.* (1996), with a curve of reasonable accuracy (see Figure 2-38 and Figure 2-39), it is possible to produce the following function relating the two:

$$E_{H_3^+}(T) = 2.2701x10^{-6}T^2 - 0.277204 - 0.000422385T - 9.79231x10^{-10}T^3$$

   Using this equation, it is possible to input the temperature profile of the spectral image in question, calculated in the above section, and from this directly calculate the corresponding H_3^+ emission per molecule for the Q(1,0$^-$) line (Figure 2-40). Figure 2-39 shows this can be done to within 5% accuracy for temperatures between 750°K and 1350°K.

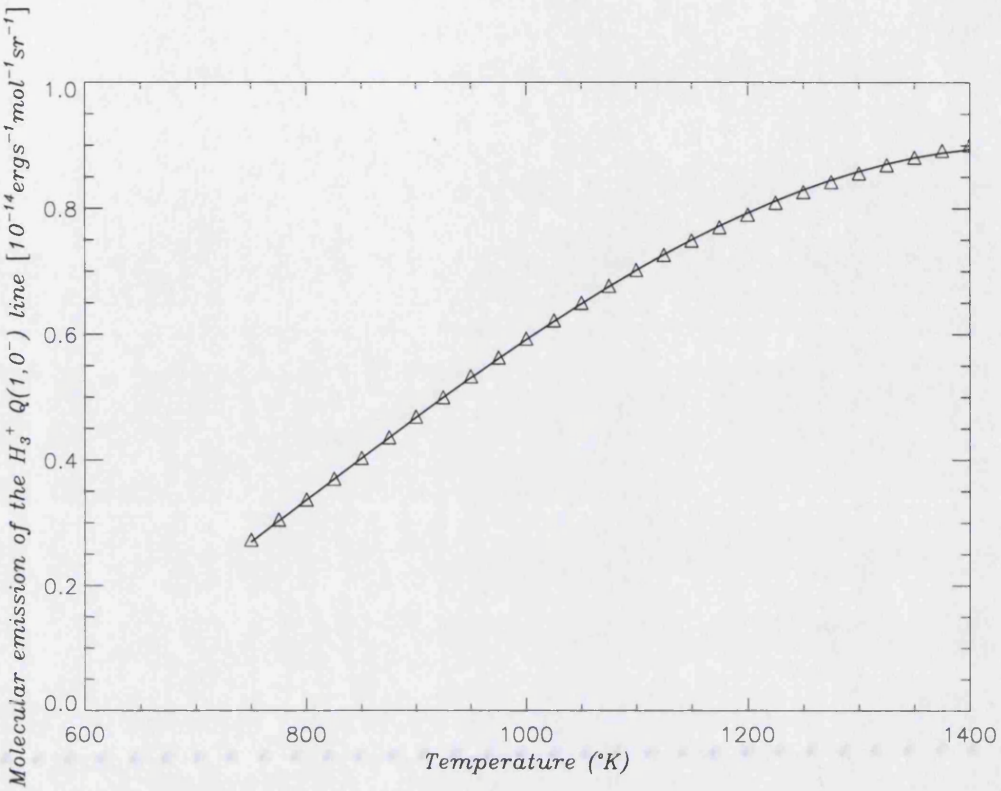

Figure 2-38: The fitted curve (in bold) and the original values (as triangles) for the change in H_3^+ fundamental emission per molecule with temperature, taken from Neale *et al.*, (1997)

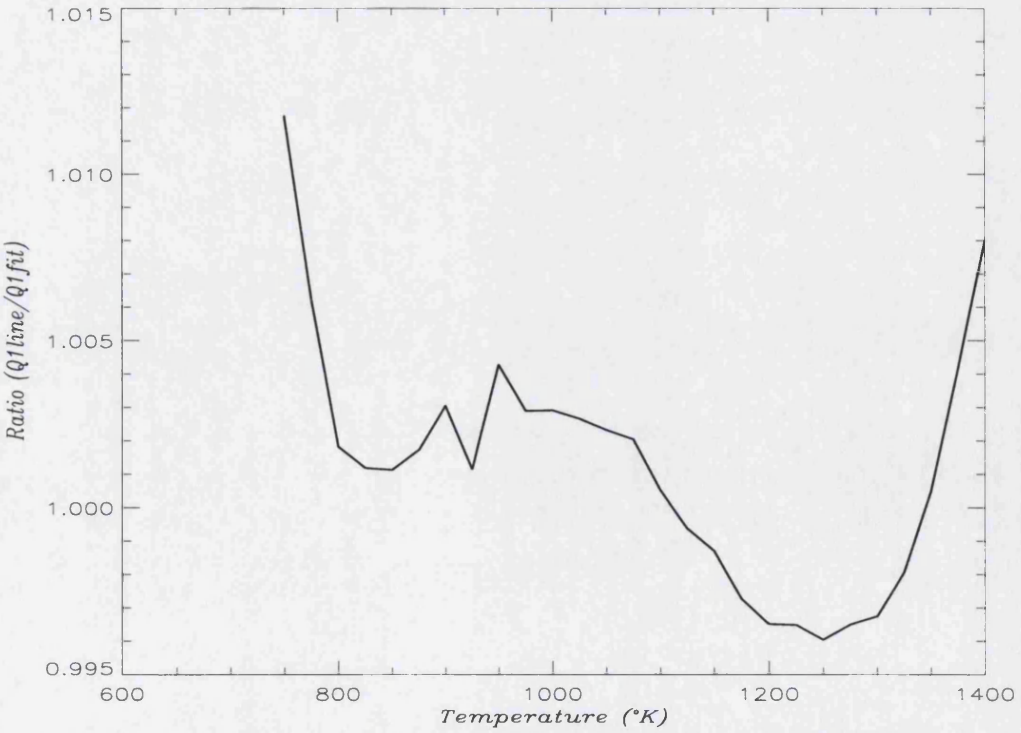

Figure 2-39: The ratio difference between the fitted curve and actual values for temperature vs. fundamental emission, shown in Figure 2-38

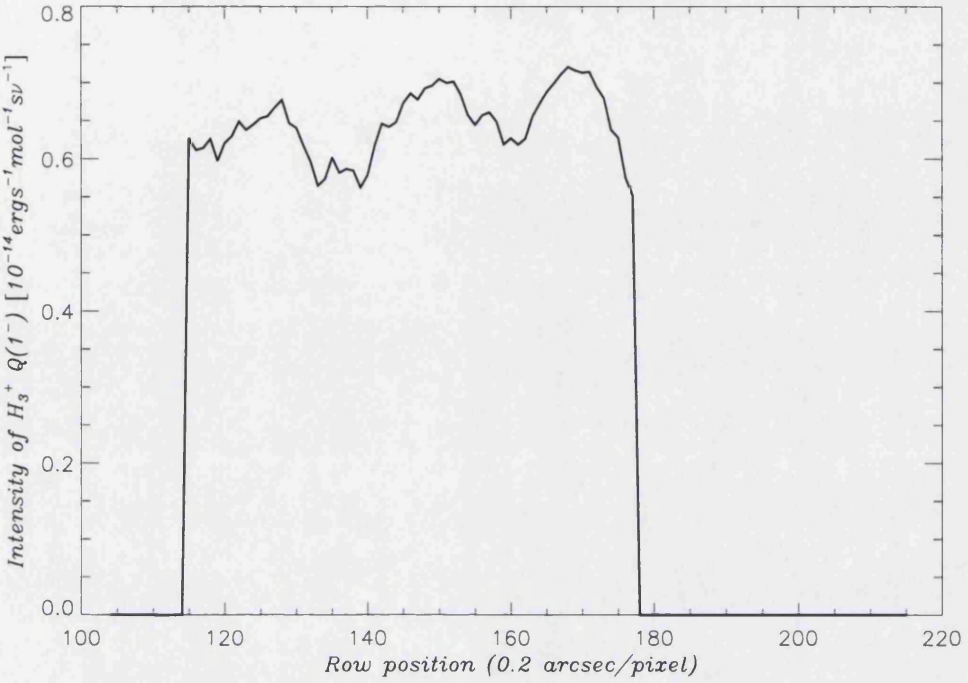

Figure 2-40: The calculated fundamental intensity profile from the temperature, for 11sep98_166

2. Intensity of Jovian emission

   The peak intensity of the emission has already been flux calibrated. However, the value required for column density calculations is the total light curve, rather than the peak figure. Therefore, before this can be used, the peak intensity has to be factored against the half-width of the Gaussian that fitted the original curve. This was recorded as A_2 and converted into microns earlier, so the final calculation is recorded as:

$$I_J(Wm^{-2}) = A_0(Wm^{-2}\mu m^{-1}) \times A_2$$

   The half-width profile also needs to be smoothed with a nine-pixel running average to make it consistent with the temperature profile (Figure 2-41).

Once these factors have been determined, it is possible to calculate the column density for each position in spatial extent on the spectral profile, an example of which is shown in Figure 2-42.

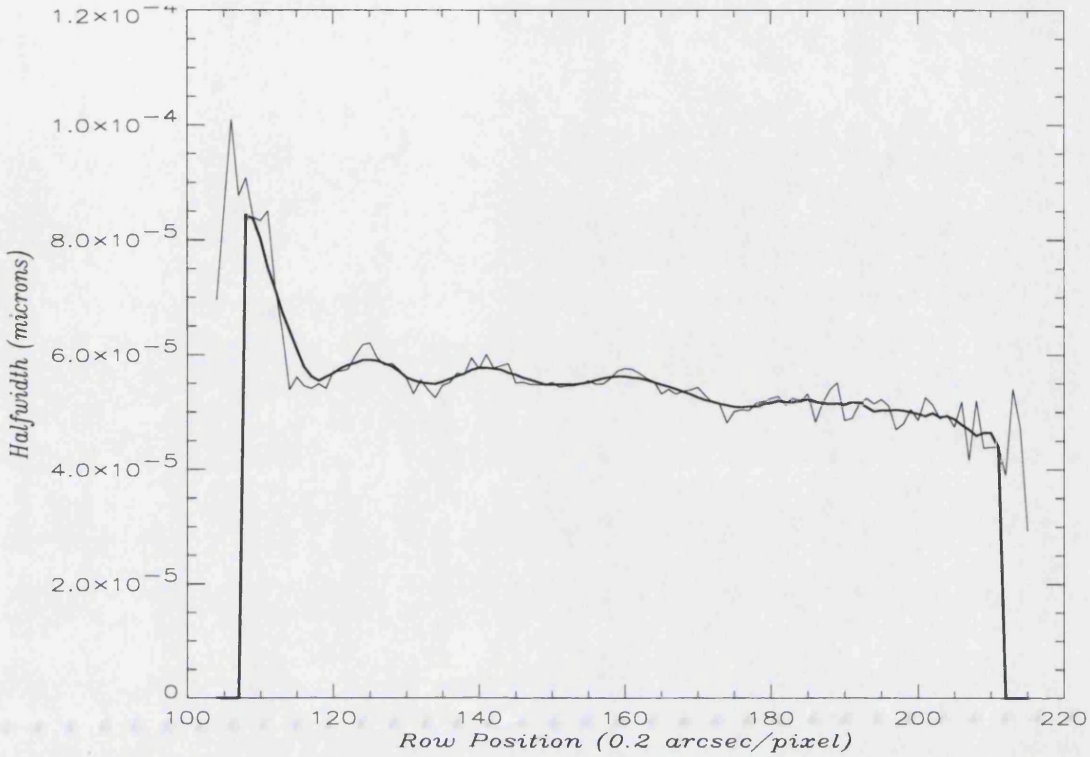

Figure 2-41: The smoothed half-width profile for 11sep98_166 (in bold), with the unsmoothed profile

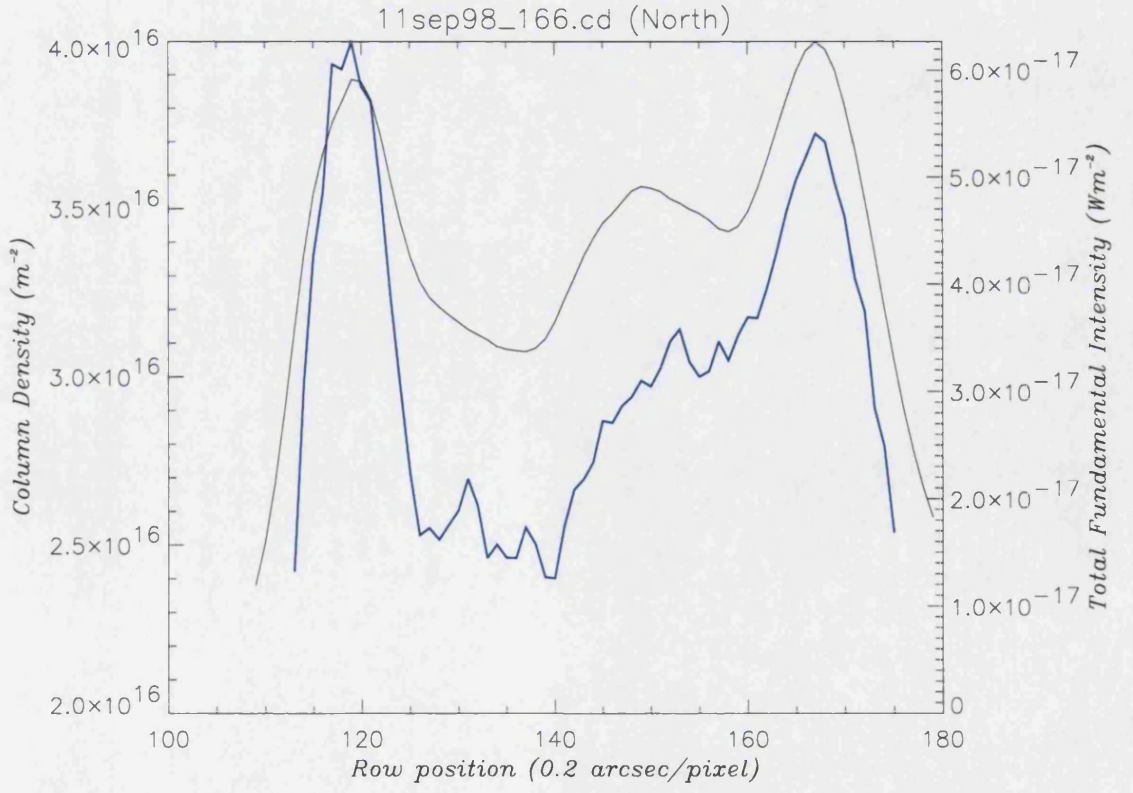

Figure 2-42: The output column density profile (blue) calculated in COLDEN, plotted with the calculated total fundamental intensity profile, for 11sep98_166

2.7 Total Emission

The total emission, $E(H_3^+)$, gives a calculated value for the emission of H_3^+ across all the possible energy transitions at a given temperature. It was historically introduced in the literature (**1.3.5 Total emission**; Lam *et al.*, 1997; Miller *et al.*, 1997a), because the poor temperature sensitivity of individual ν_2 rotational lines resulted in a strong (anti-)correlation between their fitted temperatures and column densities. $E(H_3^+)$ was used to produce useful information on the distribution of H_3^+, where there was relatively low confidence in fitting temperature and column density independently.

Our observations were made with a significantly higher sensitivity, but the parameter itself proves to be very useful in its own right. $E(H_3^+)$ effectively shows the location and amount of energy output from the auroral region, and therefore the extent of H_3^+ cooling of the atmosphere. The distribution of H_3^+ total emission can be used to show the dominant effects on heat loss, depending on the parameter's correspondence with temperature and column density.

This dependence upon both temperature and column density again relies upon the assumption of quasi-thermal equilibrium (QTE). However, since the ground state does not emit, the underestimation of column density doesn't effect the calculation of total emission. With a breakdown in QTE, the calculation of temperature produces an underestimation of kinetic temperature and an overestimation of column density, so that when these parameters are combined in the calculation of total emission they balance out, resulting in a total emission that is within ~10% of the actual value (Lam *et al.*, 1997). This can be considered reasonable despite the coverage of only the (ν_2 = 1 & 2) levels, since the proportion of emission from energy levels ($\nu_2 \leq 3$) is negligible in comparison with the errors associated with the calculation of temperature and column density.

2.7.1 Calculation of total emission

The total emission of H_3^+ across each row of a spectral profile is calculated in the TOTEM procedure (**B.3.8 totem.pro**), using pre-calculated values for total emission per molecule, with the following formula:

$$E(H_3^+) = E_{H_3^+}^{Total}(T) \times N(H_3^+) \times 2\pi$$

Where, $E_{H_3^+}^{Total}(T)$ is the total emission per molecule, at a given temperature

$N(H_3^+)$ is the column density

2π is a hemispheric emission factor to produce total emission outwards, rather than a value in Sv^{-1}

Calculating the total emission per molecule

The curve used to find the total emission per molecule for a given temperature is taken from published work (Dinelli *et al.*, 1992), and fitted with an intrinsic polynomial-fitting procedure (POLYFIT) in IDL to produce as accurate a fit to the data as possible. This curve (see Figure 2-43 and Figure 2-44) can then be used to produce values for $E_{H_3^+}^{Total}(T)$:

$$E_{H_3^+}^{Total}(T) = 2.13944\times10^{-13} - 4.36908\times10^{-16}(T) - 2.38479\times10^{-19}(T^2) + 8.55820\times10^{-22}(T^3) - 1.78320\times10^{-25}(T^4)$$

The temperature of the spectral profile can then be transformed with this equation to find the corresponding total emission per molecule for each point on the spectral profile (Figure 2-45). Once the total emission per molecule has been determined, it is possible to factor in the column density and calculate the total emission profile (Figure 2-46).

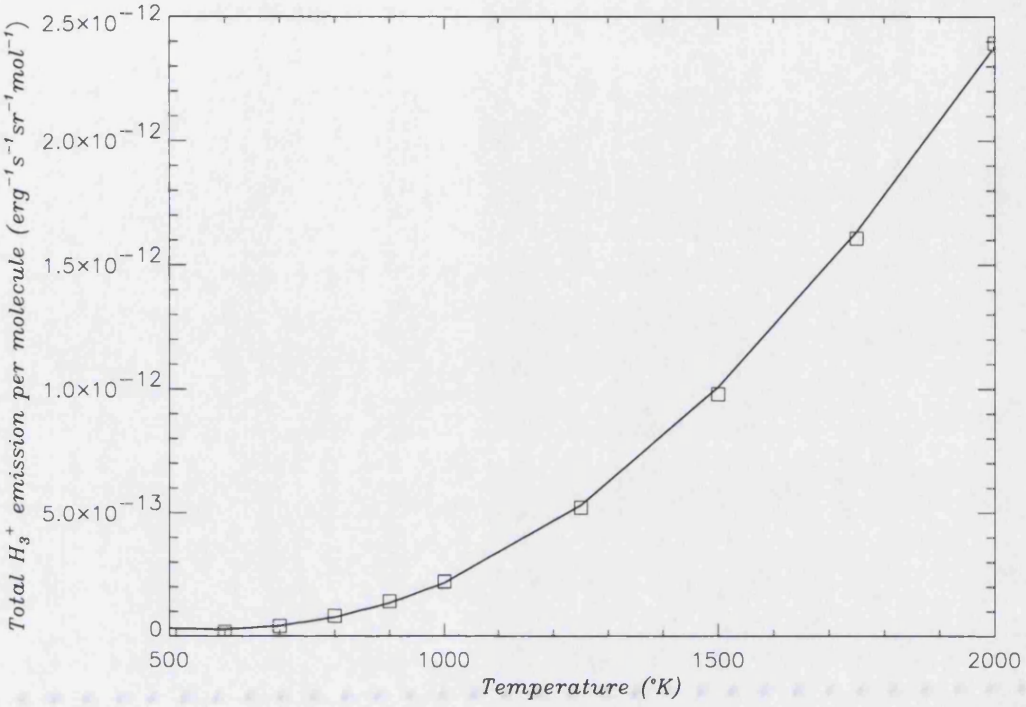

Figure 2-43: The fitted curve (in bold) and the original values for the change in the H_3^+ total emission per molecule with temperature

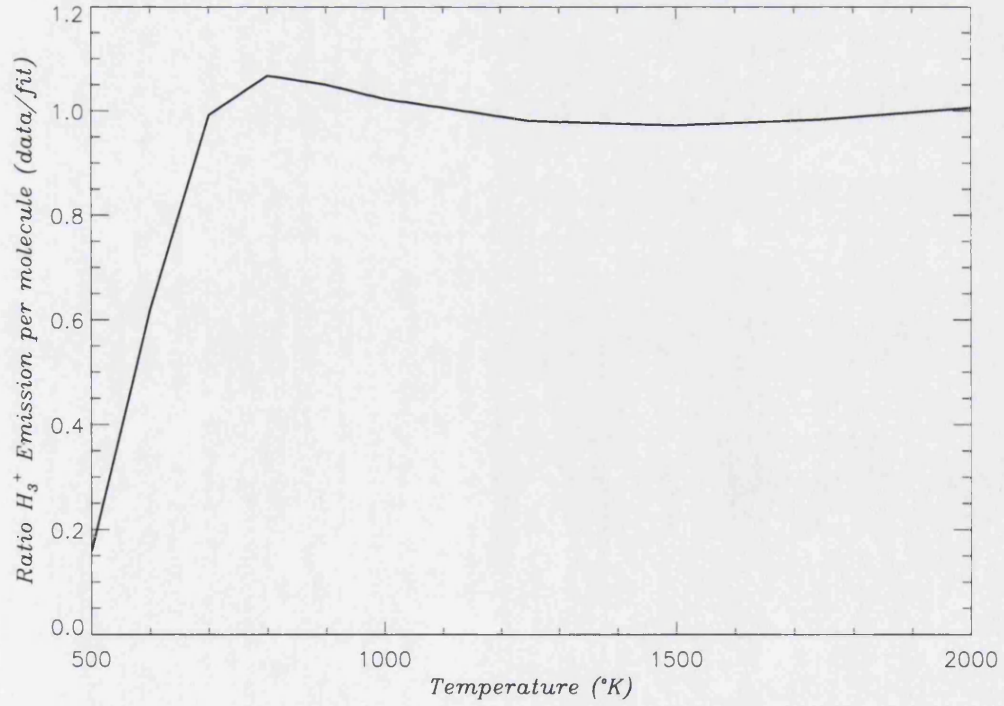

Fi **Figure 2-44: The ratio difference between the fitted curve and actual values for temperature vs. H_3^+ total emission per molecule, shown in Figure 2-43**

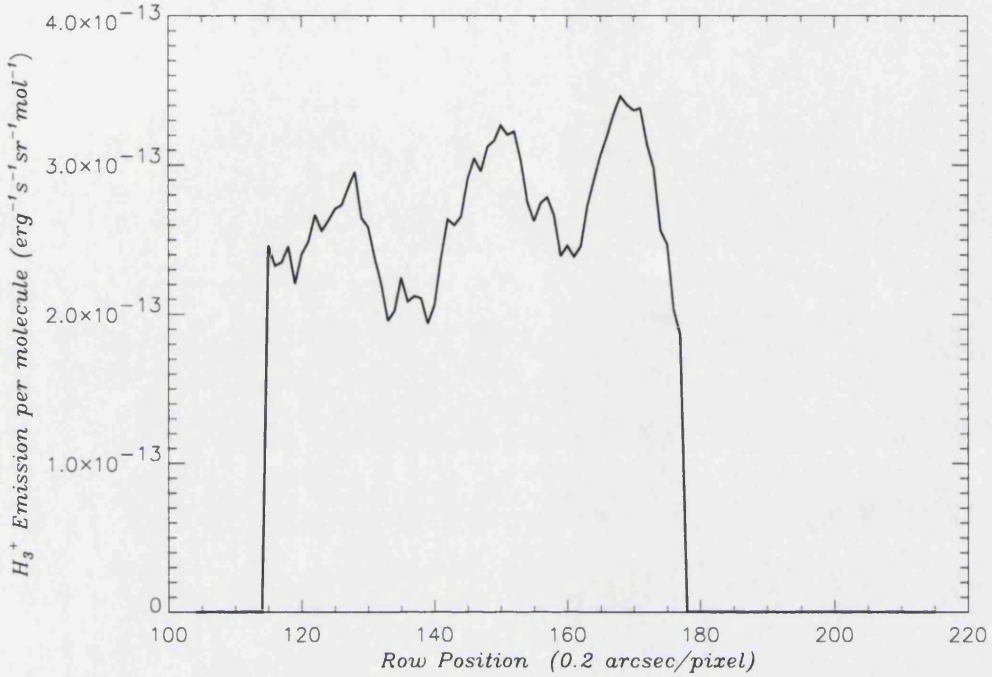

Figure 2-45: The calculated H_3^+ total emission per molecule profile from the temperature, for 11sep98_166

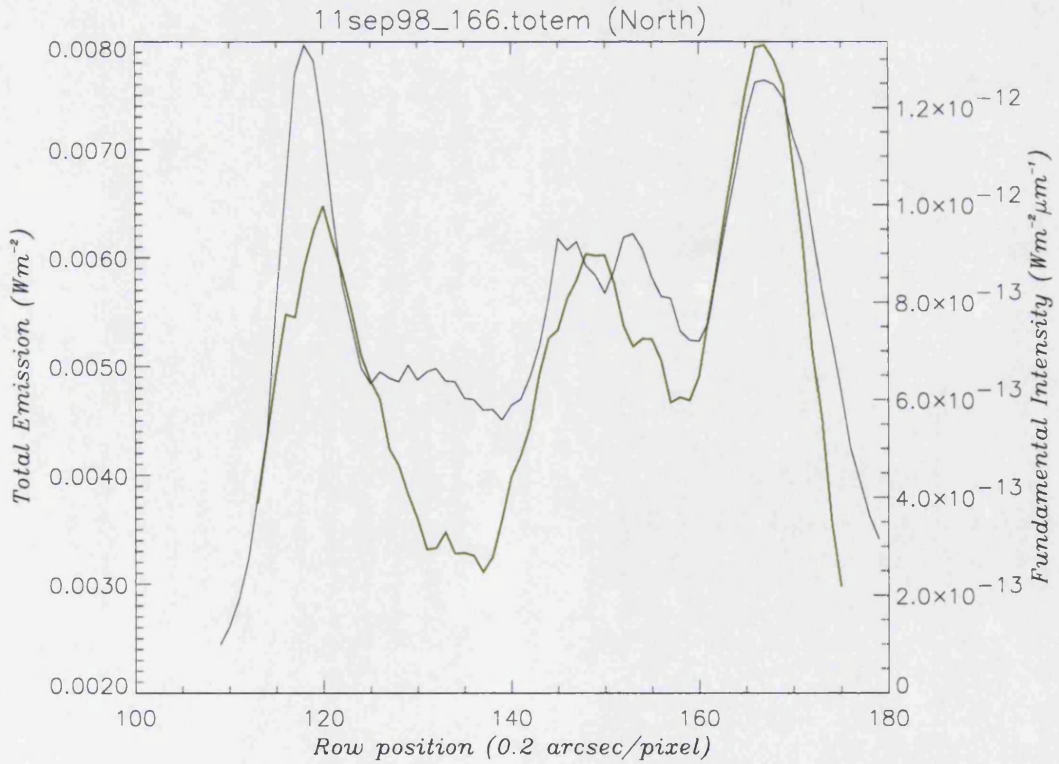

Figure 2-46: The output total H_3^+ emission profile (green) calculated in TOTEM, plotted with the fundamental intensity profile, for 11sep98_166

2.8 Line-of-sight Velocities

2.8.1 Significance of velocity measurements

A number of publications have inferred the presence of an electrojet from indirect evidence since it was first predicted (**1.3.8 Dynamics of the Jovian aurorae**). There exists only a single published direct detection of an ion jet, accepted as direct evidence of an electrojet. This originated from an "auroral event", which may have lasted only 20 minutes (the observations began in the initial stages of the event). Observations of a continuously present Jovian auroral electrojet have never been made.

Our understanding of the ionosphere-magnetosphere interaction, as well as many fundamental properties of the outer magnetosphere, could be significantly enhanced if the electrojet could be observed and analysed properly. Unlike the earlier study, such an investigation would need to detect, characterise and analyse the motions in the ionosphere across an extended period of time.

The observations taken here were made in a direct attempt to produce data that would allow such an investigation to take place. By providing extensive coverage of Jupiter across the auroral region, and over an effective period of nine Jovian rotations, the completed analysis of this data should provide a more detailed understanding of the dynamics of the Jovian ionosphere, information previously unavailable.

We have attempted to do this using our SPECTRA procedure. However, while SPECTRA outputs the effective Doppler shift in wavelength in units of kms^{-1}, this output requires significant further analysis and correction before the values correspond to actual line-of-sight ion velocities. It is the careful correction of the data that allows determination of these velocities, and further allows accurate determination of the relative velocity across the spectral profile.

This process is carefully detailed below for a single example spectral profile, that of 11sep98_166 (with a CML of 159°); the techniques discussed are shown in use across a wider range of data in **Chapter 4 : Dynamics of the Jovian Auroral Region**.

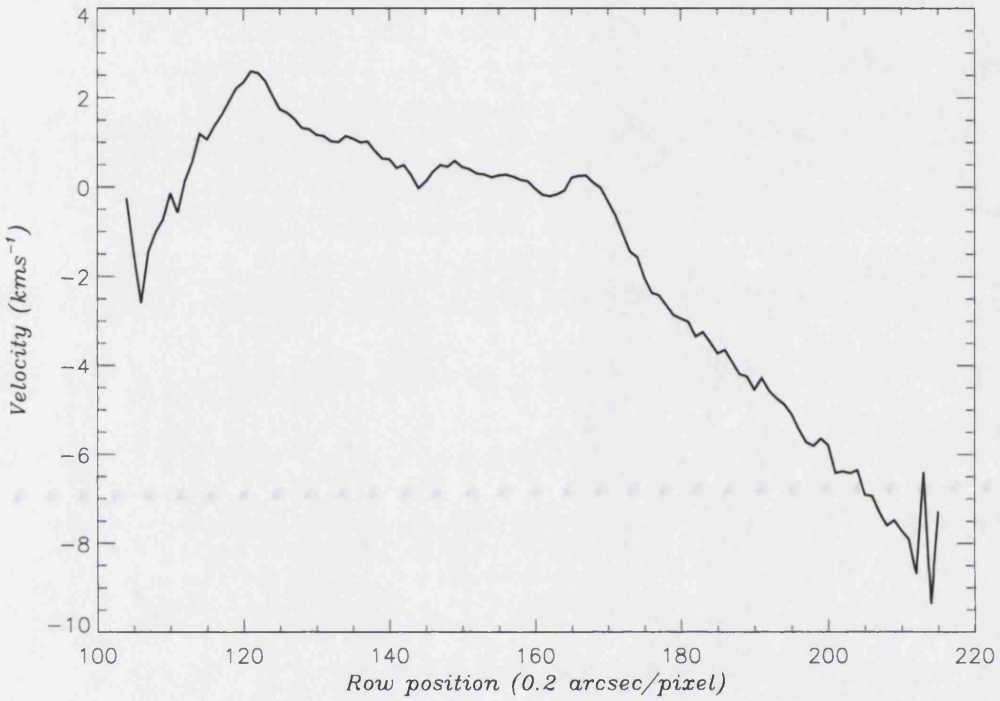

Figure 2-47: The initial velocity output from SPECTRA, as an uncalibrated line-of-sight relative velocity profile, for the spectral image 11sep98_166. At this point the velocity zero is arbitrary, but has been set to the notional λ position of the 3.953μm line

2.8.2 Velocity calibration

The initial output from the SPECTRA procedure gives the relative wavelength variation of the 3.953μm line in terms of a measured velocity ($V_m(y)$) in km/s (Figure 2-47), where y represents the spatial axis on the detector array. $V_m(y)$ can be considered to consist of the actual line-of-sight velocity structure on Jupiter caused by the Doppler shifting motion on the surface ($V_a(y)$), and the addition of a number of components which are also recorded in $V_m(y)$, and need to be corrected for. These components are the effect of Jovian rotation ($V_r(y)$), the non-linearity of the detector array ($\Delta V_d(y)$), the effect of the anisotropy of light in the slit causing a spatial shift in the line position ($\Delta V_s(y)$), and the correction to move from a relative velocity to one with an accurate zero point (V_0), in the Jovian frame of reference. This is shown clearly in the following equation:

$$V_m(y) = V_a(y) + V_r(y) + \Delta V_d(y) + \Delta V_s(y) + V_0$$

For the purposes of explanation and analysis, an additional "pre-spatial velocity" $V_{ps}(y)$ is defined, consisting of $V_m(y)$ minus the $V_r(y)$ and $\Delta V_d(y)$ corrections, but ignoring $\Delta V_s(y)$ and V_0, thus:

$$V_{ps}(y) = V_m(y) - V_r(y) - \Delta V_d(y)$$

or

$$V_{ps}(y) = V_a(y) + \Delta V_s(y) + V_0$$

The use of $V_{ps}(y)$ in analysis will be discussed in **4.1.1 Pre-spatial velocity profiles**.

1. Rotation ($V_r(y)$)

The largest effect on the velocity shift profile comes from the rotation of Jupiter, which produces the noticeable linear variation in wavelength in Jovian spectral lines (Figure 2-49), as a function of east-west position. Adjusting for $V_r(y)$ is a simple calculation, because the slit is aligned perpendicular to the rotational axis, so the effect of rotation on the line-of-sight velocity in the y-direction is the same linear function of y no matter the longitude or latitude being examined. This can be shown, with reference to Figure 2-48:

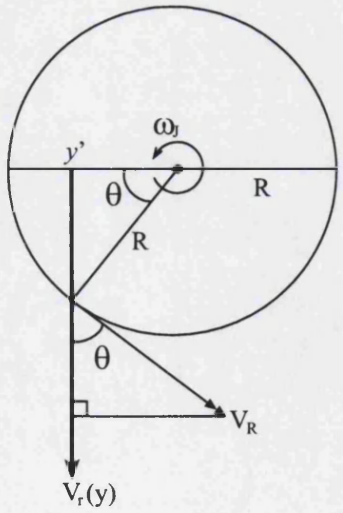

Figure 2-48: Diagram showing values involved in the calculation of $V_r(y)$

For a *fixed* value of $\omega = \omega_J$, the angular velocity of Jupiter given by $\omega_J = \frac{2\pi}{t_J}$,

Where, t_J is the rotational period of Jupiter

Then for any value of R (in arcsec) corresponding to the radius of any circle of latitude, and any θ,

$$V_R = R\omega_J$$
$$V_R(y') = V_R \cos\theta$$
$$= R\cos\theta\,\omega_J$$

Where, $y' = y - R$

But, $\cos\theta = \frac{y'}{R}$

$$\therefore V_R(y') = y'\omega_J$$

At the equator, this becomes:

$$V_R(y') = R_J\omega_J = V_R$$

And thus, for any value of y, and thus any value of θ:

$$V_R(y') = \frac{y'}{R_J} \times V_R$$

With the sidereal rotation period of the planetary interior of 9.9250 hours, this gives the limb velocity as +/- 12.572 km/s. The planetary diameter on 8th September was 49.6", so with each pixel covering 0.2", this gives a slope for $\Delta V_r(y)$ of 0.101387 $kms^{-1}pixel^{-1}$ (Figure 2-49). Once the rotation has been removed, the finer-scale details on the velocity shift profile become much clearer, as shown in (Figure 2-50).

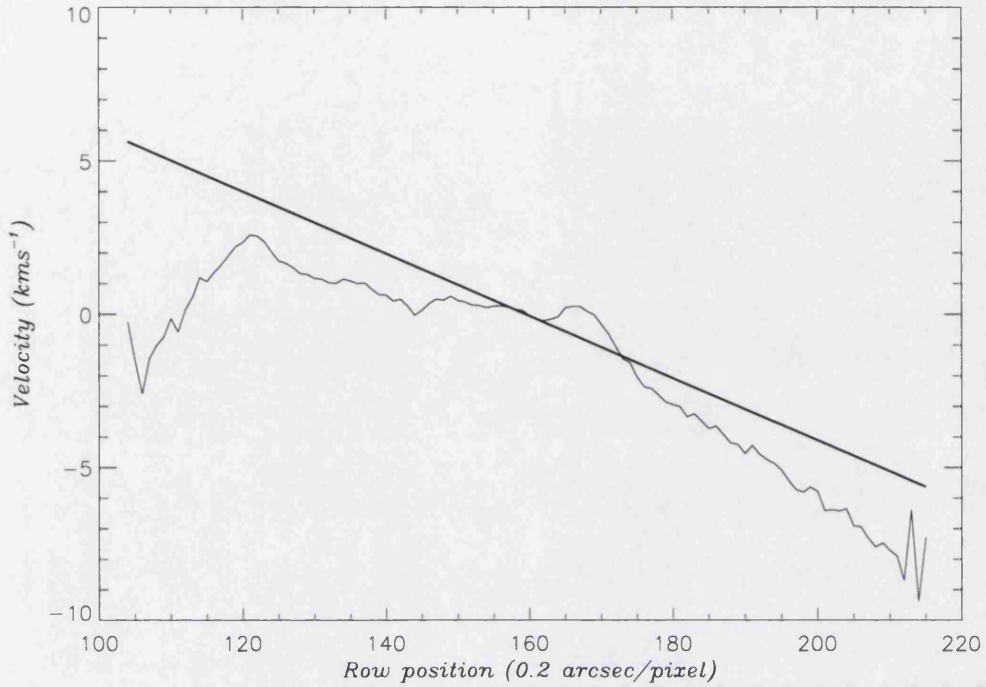

Figure 2-49: The velocity effect of the Jovian planetary rotation (in bold), plotted against the uncalibrated velocity profile

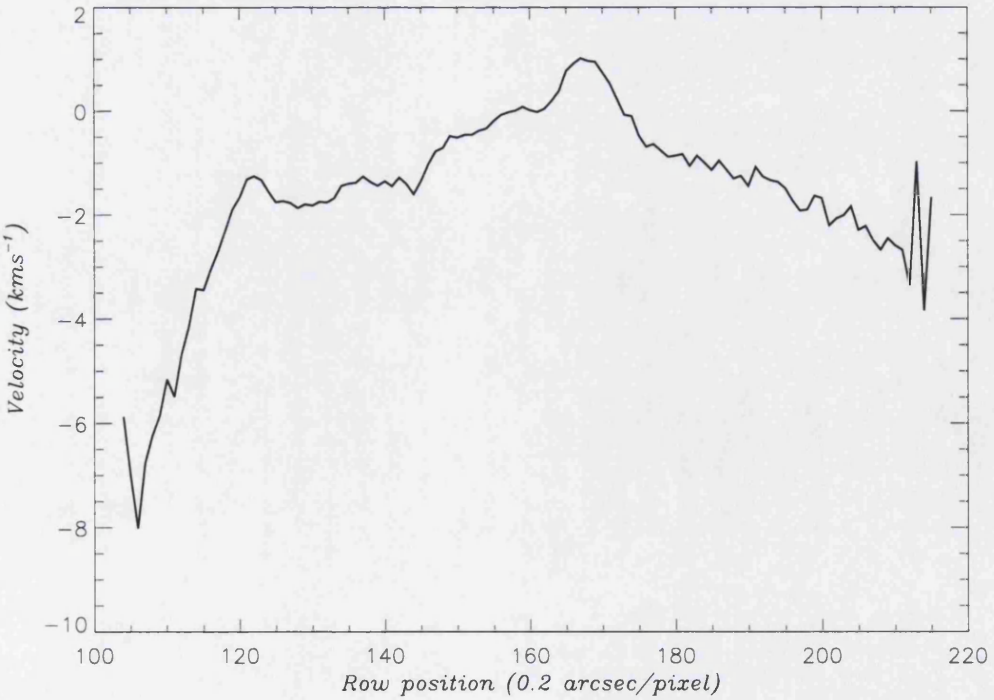

Figure 2-50: The velocity profile with the rotational velocity removed (arbitary velocity zero)

2. Array adjustment ($\Delta V_a(y)$)

As has been shown earlier (**2.3.3 Arc lamp calibration**), the optics of CSHELL produce a degree of non-linearity on the array. This error can have a significant effect of up to 1-2 km/s across the entire spatial dimension of the array, and so needs to be rectified in the velocity profile. The array adjustment is performed after $\Delta V_r(y)$ is removed, to better see the effects it produces.

The non-linearity of CSHELL's wavelength dispersion is already known for specific wavelengths on the array, corresponding to the positions of the arc lamps. However, none of these directly coincides with the position of the 3.953μm line, so these cannot be used to compensate for non-linearity directly. Instead, for each day of observations a procedure called LAMP (**B.4.3 lamp.pro**) was used to calculate $\Delta V_d(y)$ for the velocity profile at 3.953μm:

a) For each night, the two arc lamp spectral lines that are positioned closest to the 3.953μm line, the K3 double line at 3.9519μm and the K4 line at 3.9533μm, are used. However, since the lamp lines are relatively weak, with the noise about 20-40% of the signal strength, each is fitted with a curve that matches the general curve of the non-linearity in the line (see Figure 2-19 on page 76).

b) These fitted non-linearities are loaded into LAMP. The procedure then makes a linear interpolation between the relative position of the non-linearity on a spectral image, calculating the variation of non-linearity with y-pixel position. Since the location of the 3.953μm is known, LAMP outputs the non-linearity in km/s to be used with that night's velocity profiles.

$\Delta V_d(y)$ is calculated for each night separately, using the lamp line measurements taken at the start of every night (see Figure 2-51 and Figure 2-52 for the values of $\Delta V_a(y)$ across the spectral profile of the 11th). The date-specific adjustment can then be removed from the individual velocity profiles (Figure 2-53).

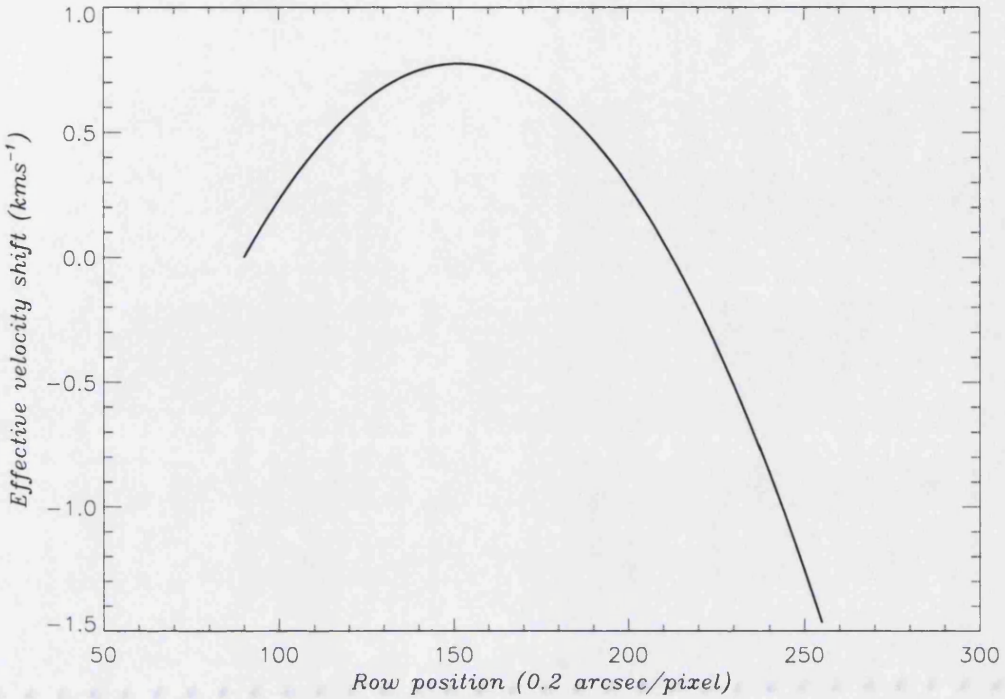

Figure 2-51: The velocity correction applied to correct for the non-linearity of the array at 3.953μm

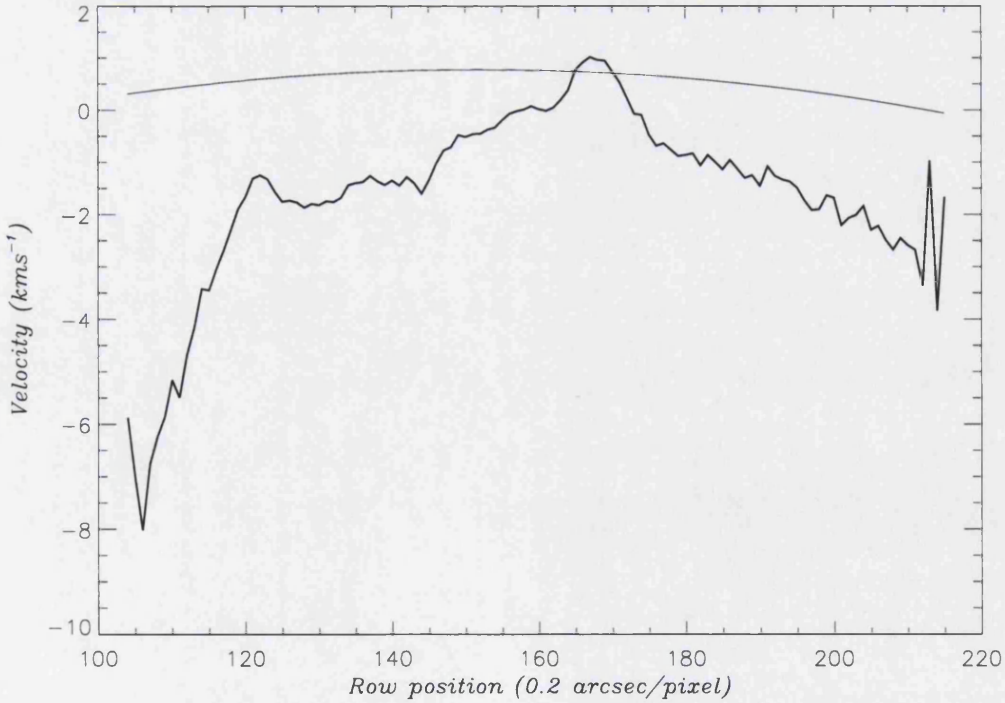

Figure 2-52: The array adjustment shown in Figure 2-51, plotted against the velocity before correction

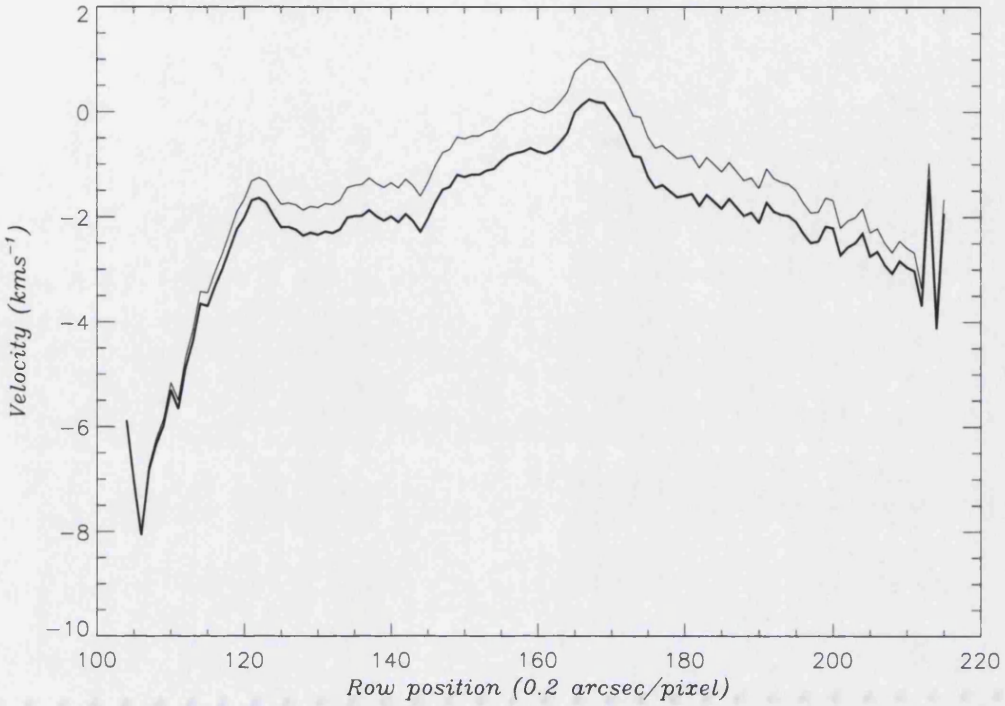

Figure 2-53: The velocity profile corrected by the array adjustment (in bold), shown with the profile before adjustment

3. Spatial correction ($\Delta V_s(y)$)

As shown earlier in this chapter (**2.1.2 Effects of anisotropic light sources**), while the array on CSHELL has separate spatial and wavelength axes, a spatial effect may affect the precise wavelength of a line as measured on the array.

This spatial effect, caused by anisotropy in the intensity across the width of the slit, can be significant in Jovian spectra. The slit's width of 0.5" covers a region on the Jovian surface of 1400 kilometres at the equator, which increases significantly towards the limbs, in which a large variation in the H_3^+ emission intensity may occur, especially in the regions of the auroral ovals, where the largest wavelength variations due to Doppler shifting by the electrojet are also predicted.

Using the 3.953μm images, the anisotropic variation in intensity ($\Delta I(x,y)$) has been defined for the purposes of this thesis as the difference between the light one spatial pixel (0.2") above and below the slit in the x-direction (*i.e.*, one pixel north and south of the slit position):

$$\Delta I(x,y) = \frac{\left(I(x+1,y) - I(x-1,y)\right)}{\left(I(x+1) + I(x-1)\right)}$$

This value then has to be converted into a relative velocity in the velocity shift profile, so that $\Delta V_s(y)$ can be removed from $V_m(y)$. In order to make this connection, within the limits of the accuracy of our data, we assume a linear relationship:

$$\Delta V_s(y) = b\Delta I(x, y)$$

Thus, in order to find the value of $\Delta V_s(y)$, it is necessary to calculate the value of both b and $\Delta I(x,y)$. The following is the entire methodology used to calculate $\Delta V_s(y)$, as used by the SPATIALCALI (**B.4.4 spatialcali.pro**) procedure:

A: To find $\Delta I(x,y)$ for a set of spectra, we use the associated 3.953μm images. (An image of the auroral region was taken at the beginning, and in some cases the end, of every spectral sequence taken. These CVF images are generally observed with 15 minutes of any particular individual spectral image, so the similarity between image and spectral intensity is fairly close.)

By taking a cut across the image in the North-South direction, it is possible to simulate the intensity of a spectral profile across the CSHELL slit. Since the image is effectively an array of these profiles at 0.2" steps continuously down the planet, it is possible to model the variations in intensity that would have been acquired within the slit.

(One problem with using the CSHELL CVF images is that the wavelength gradually varies across the array, from top to bottom relative to the planet. But this only amounts to a ~2% wavelength shift across the array; these variations are small when viewed over the width of the slit, and have been ignored.)

The measurement of $\Delta I(x,y)$ for each individual spectral profile involves the location of the profile on the planet, and the subsequent calculation of $\Delta I(x,y)$ for each pixel in the profile.

a. Location of spectral profile on the image

Before the image can be used to simulate any spatial effect, the location of the spectral profile must be matched with a position on the image, both in latitude and longitude.

i. North-South

Our IDL procedure opens a second procedure called INTMATCH (**B.3.4 intmatch.pro**), which displays the image and allows the user to move a cursor over it. In a separate window, the spectral intensity profile ($I_s(y)$) is plotted, with the intensity of the particular row over which the cursor is positioned $I(x,y)$ over-plotted on top. This effectively allows the user to move the cursor up and down the planet's surface, and compare $I_s(y)$ and $I(x,y)$ for different values of x, which on the image moves north-south on the planet, until the two match.

Matching is done by eye, which is the most effective way of matching the two intensity profiles when they often vary in form due to the longer exposure time and higher quality of the spectral intensity. Despite these difficulties, the two match up surprisingly well in most cases, often having similar peaks and troughs (Figure 2-54). In the cases where more complex intensity structure is unavailable, for example towards the poles of the planet, the width of the peak was used as an indicator of latitudinal position.

ii. East-West

When the two intensities have been matched north-south, it is also necessary to adjust the arrays so the features on the two profiles are aligned. The misalignment is caused by the limited size of the image, and requires the arrays to be shifted with respect to each other, and the ends to be trimmed off so that all that remains is the regions where the two arrays overlap (Figure 2-54).

This second adjustment is also made by eye, by modifying the relative y-direction position until the two plotted arrays coincide.

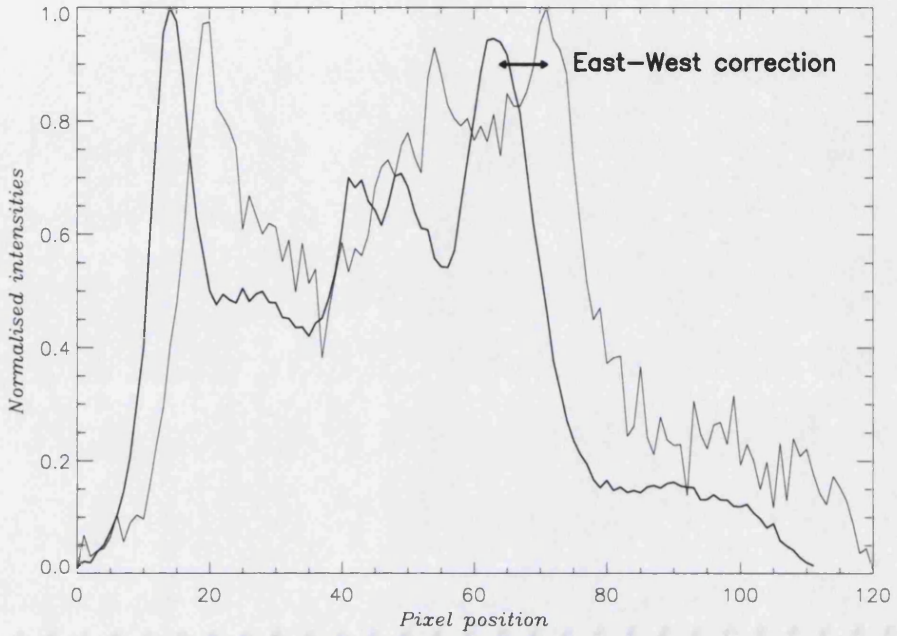

Figure 2-54: The normalised fundamental intensity profile (in bold), plotted against the intensity profile of the image at the matched spectral latitude

The procedure also allows the user to return to the N-S positioning once this has been completed, to allow both these steps to be used together iteratively to find the best match of position of the spectral profile on the planet. This can be repeated as often as required until the match between the two profiles is acceptable.

b. Derivation of spatial effect from the image

Once the position of the spectral profile on the image is known, $\Delta I(x,y)$ can be calculated by the procedure. The ratio in intensity between the rows directly above $I(x - 1,y)$ and below $I(x + 1,y)$ the measured position, separated by 0.6", can be used as an effective approximation of what light should have entered into the slit. By calculating the fractional difference between these two rows of intensity from the image, it is possible to simulate $\Delta I(x,y)$ (Figure 2-55).

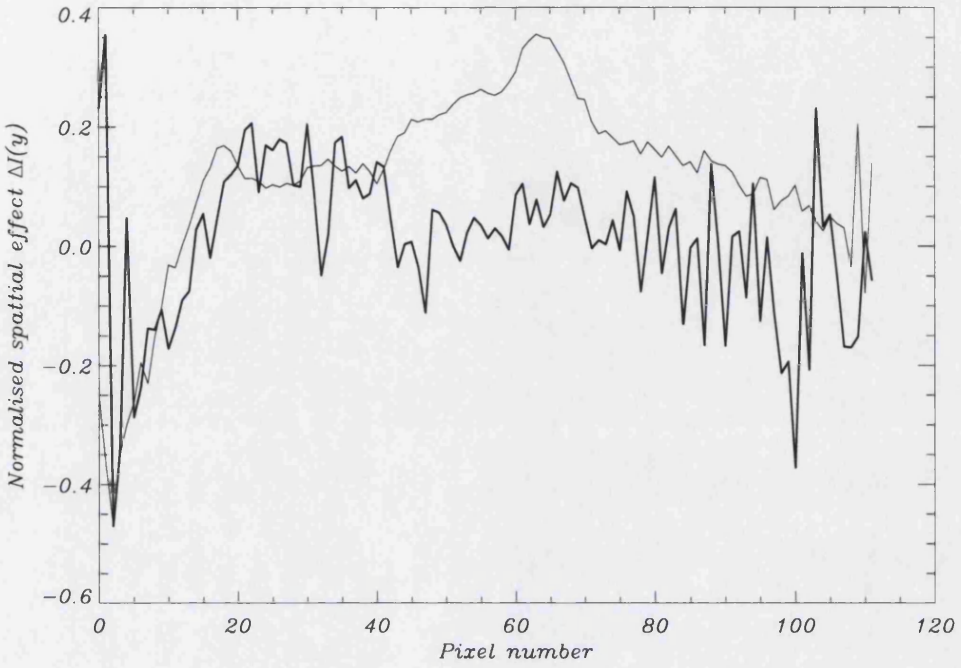

Figure 2-55: The normalised spatial effect (in bold), plotted against a normalised "pre-spatial" velocity

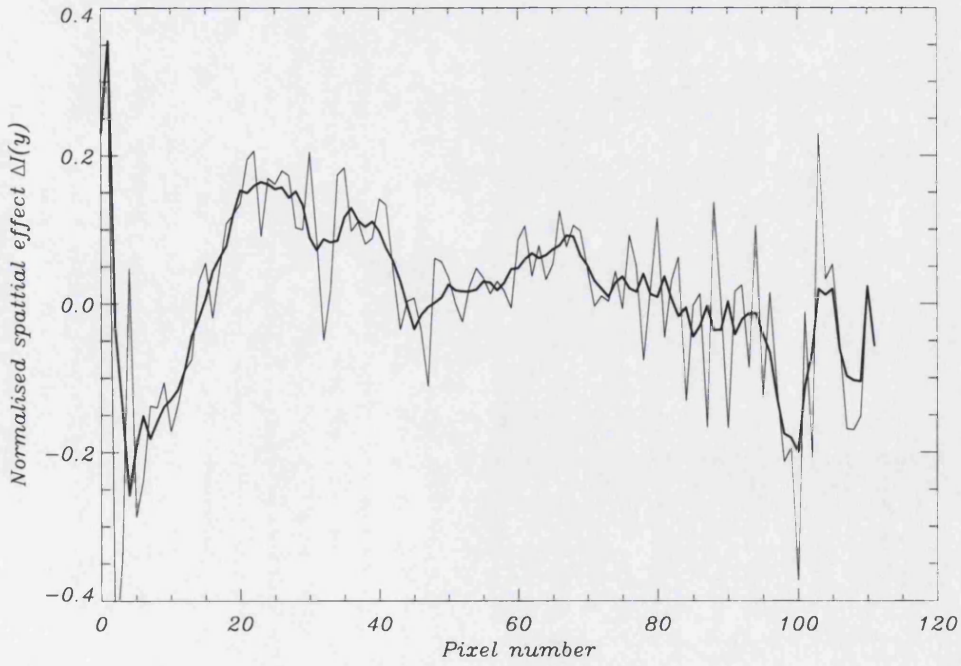

Figure 2-56: The smoothed and normalised spatial effect (in bold), plotted over the preceding unsmoothed effect

The simulated spatial effect is, however, very noisy because of the lower quality of the CVF H_3^+ images, compared to that of the spectral images. In order to produce values of $\Delta I(x,y)$ that can be used effectively for calibration purposes, the spatial effect was smoothed using a nine-pixel running average (Figure 2-56). This results in a reduction in spatial resolution, but is necessary in order to produce good estimates of the effect on the measured H_3^+ wavelength resulting from spatial effects.

B: Calculating the value of *b* is essential to the final calibration of the data, but there is no established way of finding this value. Thus, we have had to consider new ways to calculate this. We consider three possible methods:

a. Making *a priori* calculations of the light path through the CSHELL instrument. Such a calculation would require detailed optical ray tracing that in turn needs detailed plans of the instrument, which are not available to us. This method for calculating *b* is beyond the scope of this thesis.

b. Calculation of *b* through the theoretical shift caused by a delta function in the slit. The resolving power for the CSHELL 0.5" slit is given as 7.224 km/s and, even taking into account the possible reduction in resolution (**2.1.2 True CSHELL resolution**), this value will in the range of ~10 km/s.

   Assuming a delta function intensity is positioned on either side of the CSHELL slit allows the maximum resultant $\Delta V_s(y)$ to be modelled. This means that the ratio of intensity $\Delta I(x,y)$ will be ± 1. This results in a shifted intensity peak that is positioned on the edge of the slit width, and so the velocity shift produced is the resolving power of the slit itself. In the case of the 0.5" slit, this results in a velocity of 7-10 km/s, depending upon the degradation of the slit resolution (**2.1.2 True CSHELL resolution**). Since $\Delta I(x,y) = \pm 1$, the scaling factor between intensity and velocity shift is the same as the resolving power of the slit, $b = 7\text{-}10$.

c. Using an experimental method of calculating *b*, by means of variations within the data itself. This was done in three conceptual steps:

   i. Finding the best place to calculate a value for *b* in the data. This is where the variation on the profile of both $\Delta I(x,y)$ and $\Delta V_m(y)$ is sharpest within the data. The limb of the planet clearly fits this criterion, with the cut-off between the

emission on the planet and the background of sky being abrupt. The boundary is not only clear on the predicted spatial effect, but also on the velocity profile itself (pixel numbers 0-20 in Figure 2-55).

ii. Assume that $V_a(y)$ on the limb is approximately zero, so that the measured velocity is equivalent to the spatial effect:

$$V_{ps}(y) - \Delta V_s(y) = V_0$$

and the measure velocity can be directly scaled against the anisotropic intensity variation:

$$V_{ps}(y) = b\Delta I(x, y) + V_0$$

Some real velocity variations do occur on the limb, but we assume these have a minimal effect. In order to check this assumption, a secondary calibration, on the body of the planet below the auroral region, is also performed. While the H_3^+ intensity is weaker below the aurora than on the limb, the number of points covered is greater, and $\Delta V_a(y)$ can be assumed to be zero, since any winds on the body of the planet are too small to be detectable (Clarke *et al.*, 1996; Dinelli *et al.*, 1997; Achilleos *et al.*, submitted).

The value of b can now be calculated for the limb by plotting the intensity anisotropy $\Delta I(x,y)$ against the measured velocity profile $\Delta V_m(y)$, and finding the gradient of a linear fit to this plot (Figure 2-57). The variation in both $\Delta I(x,y)$ and $\Delta V_m(y)$ on the body of the planet tends to be masked by effects of noise. But, since the plots are nearly linear, a fitted line can be produced for each (Figure 2-58 and Figure 2-59). Using these fitted values, it is thus possible to produce a plot of $\Delta I(x,y)$ against $\Delta V_m(y)$ (Figure 2-60), and to check the value of b found from the limb of the planet.

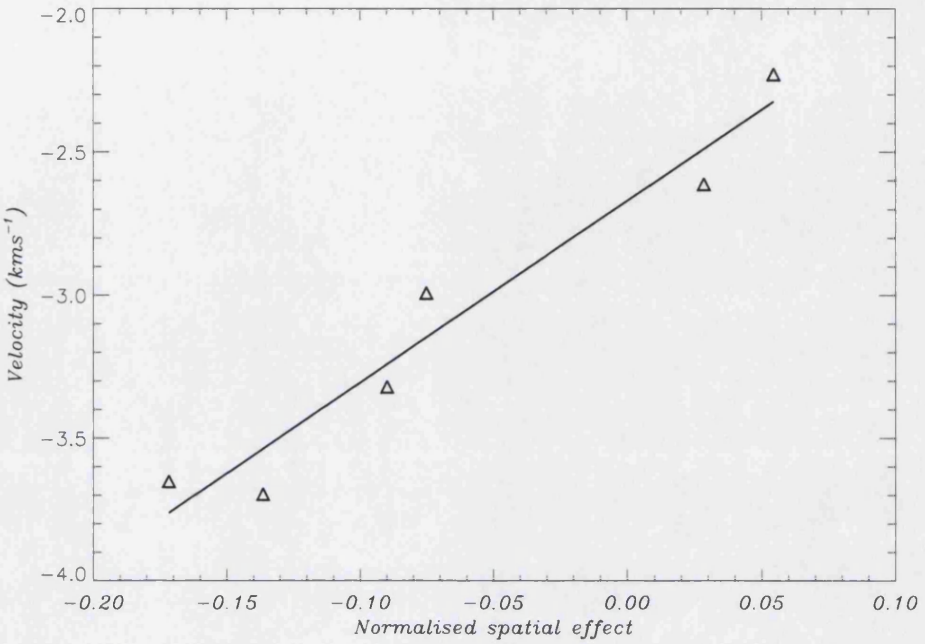

Figure 2-57: The match between the intensity anisotropy $\Delta I(x,y)$ and the measured velocity profile $\Delta V_m(y)$, on the dawn limb

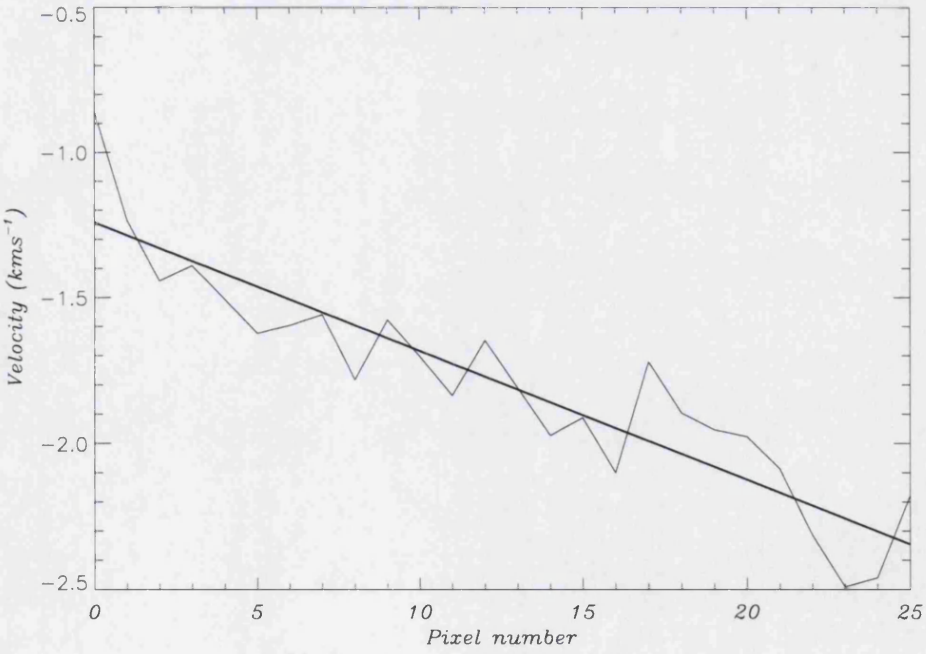

Figure 2-58: The velocity profile for the body of the planet, fitted with a linear progession (in bold) to reduce noise

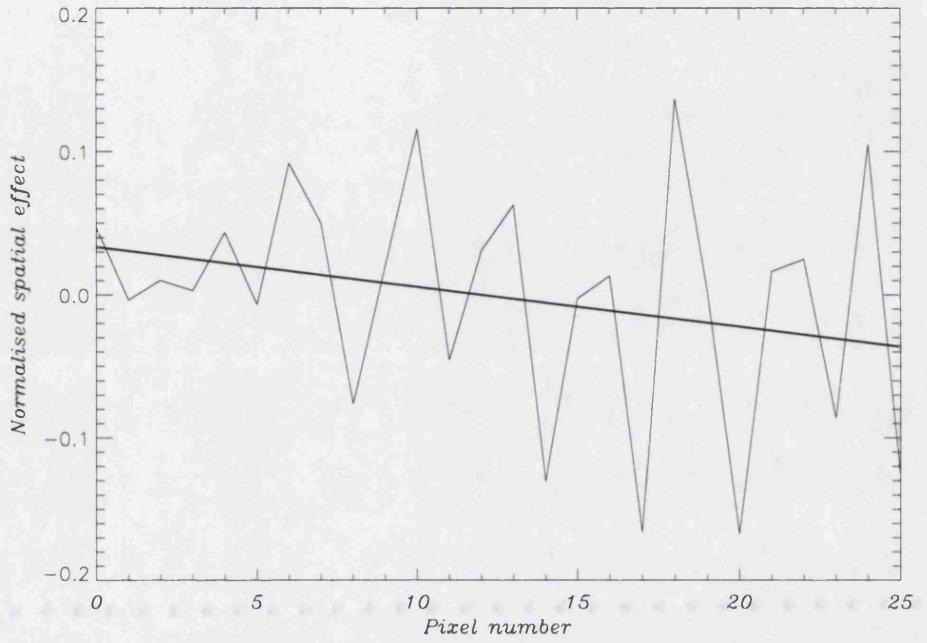

Figure 2-59: The normalised intensity anisotropy $\Delta I(x,y)$ for the body of the planet, fitted with a linear progession (in bold) to reduce noise

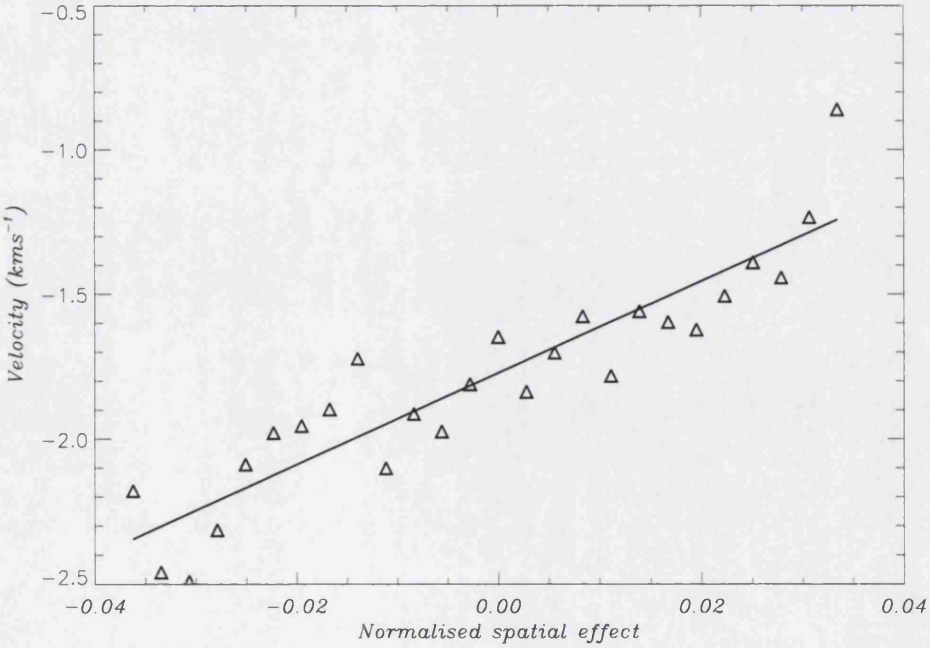

Figure 2-60: The actual intensity anisotropy $\Delta I(x,y)$ against the fitted velocity profile $\Delta V_{ps}(y)$, on the body of the planet. Plotting the two fitted values of $\Delta I(x,y)$ and $\Delta V_{ps}(y)$ results in the straight line automatically.

The results of these calculations, when repeated over several separate spectral profiles, are that the value of b lies in the range of 5-15. Thus our empirically calculated value of b agrees well with that predicted theoretically from the resolution of CSHELL.

Using this range of resultant scaling factors on the velocity data itself shows the degree of variation expected in producing a final velocity output (from Figure 2-61 to Figure 2-65). While the value of b does have an observable effect on the velocity distribution, the overall velocity profile's form remains largely unchanged: the major features associated with the auroral region vary in magnitude, but the relative positions of each feature remain the same. One feature of key concern to us here is that the velocity associated with the dawn auroral oval is consistently red-shifted compared with the dusk oval.

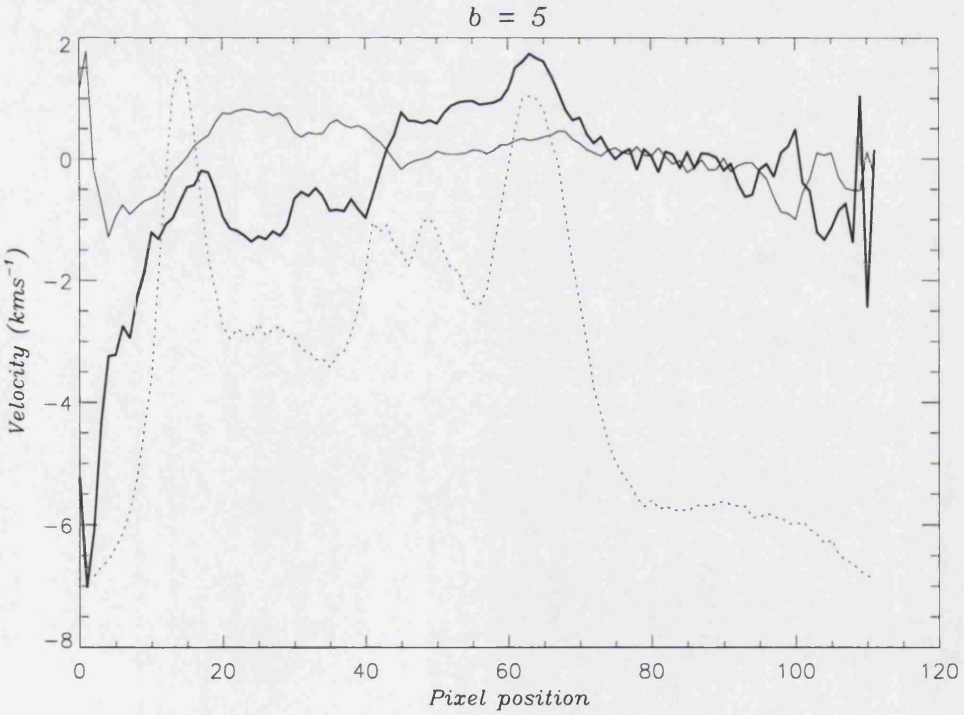

Figure 2-61: The spatial correction and resultant velocity profile (in bold) after the spatial effect is removed, using b = 5; fundamental intensity is shown for reference (dotted line)

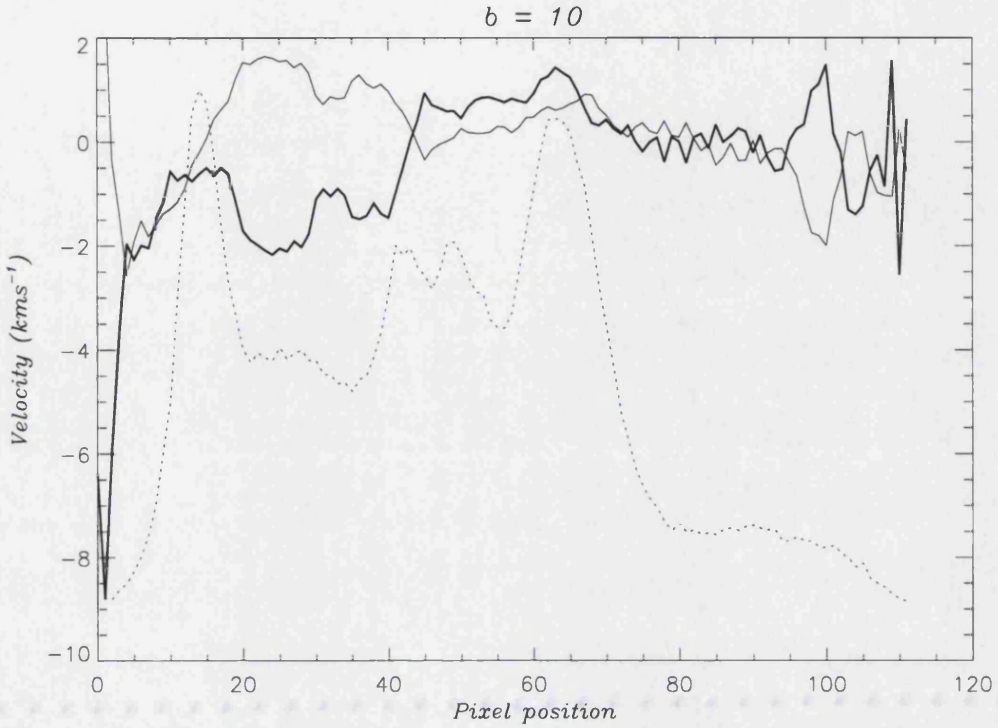

Figure 2-62: As previous figure with $b = 10$

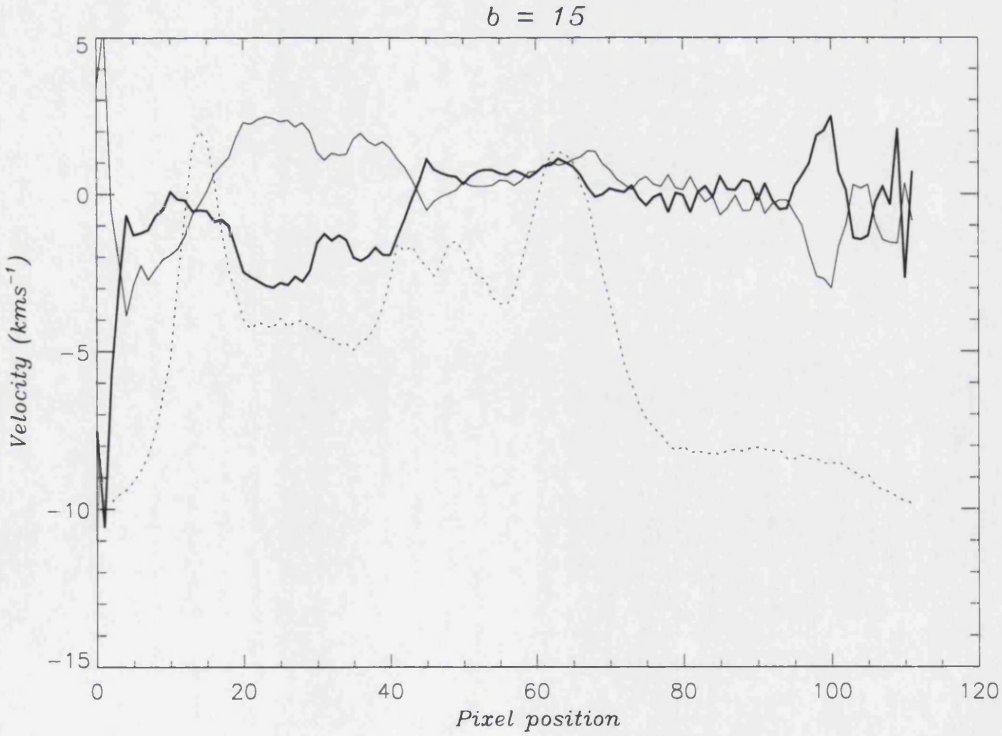

Figure 2-63: As previous figure with $b = 15$

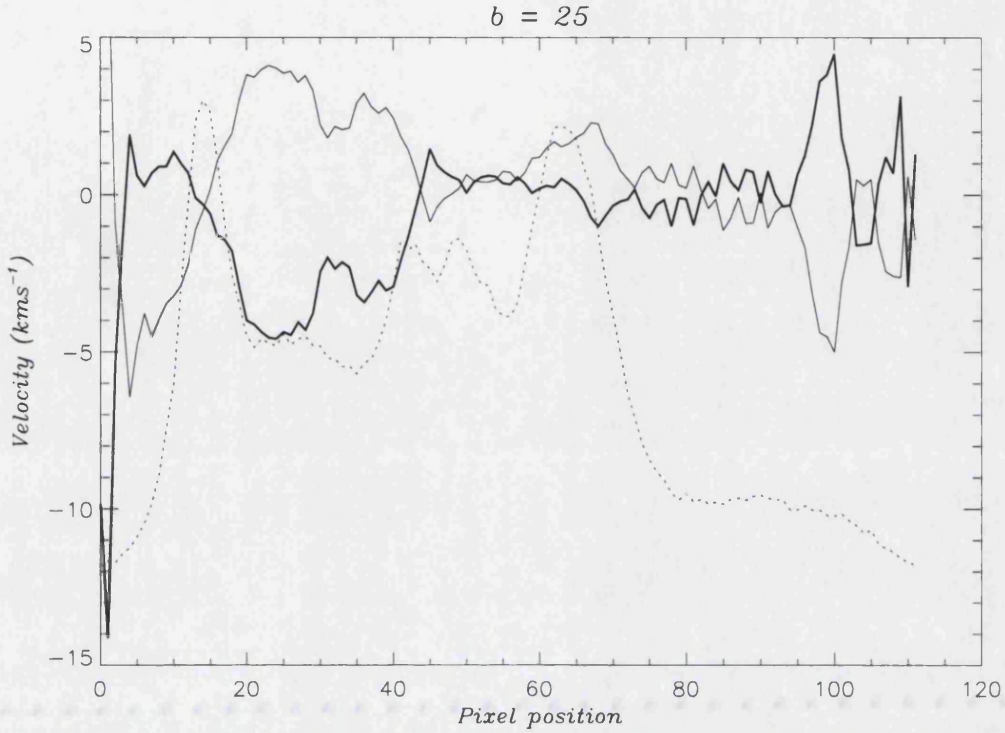

Figure 2-64: As previous figure with b = 25; despite the excessively high scaling, the red-blue/dusk-dawn relative velocity is still present

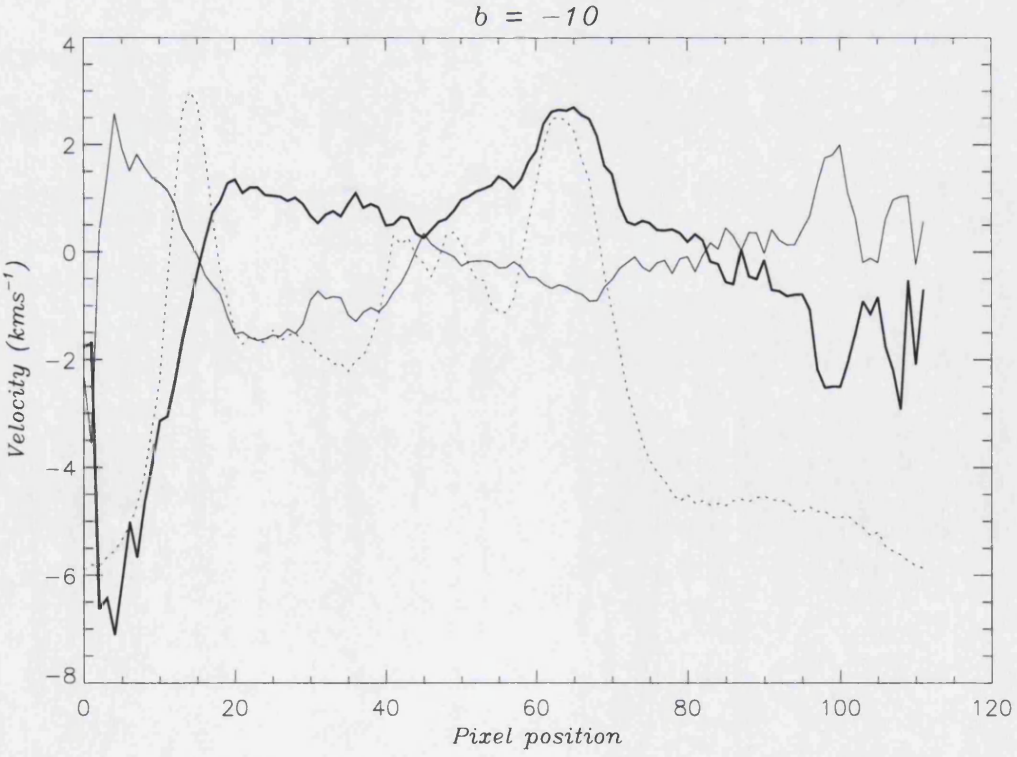

Figure 2-65: As previous figure with b = -10; reverse of the required correction for the limb and body of planet shift, but required to remove variation in relative velocity between the dawn and dusk ovals

In order to attempt to level features which match with the two peaks in intensity, a value of $b = 30$ is required. This suggests that for different values of b from the range provided, only the absolute velocity values are going to be overtly affected, with the relative velocity structure remaining comparable.

Since both the theoretical and empirical techniques produce a scaling factor that is close to 10, for the rest of this thesis, we assume that $b = 10$, so that:

$$\Delta V_s(y) = 10 \times \Delta I(x, y)$$

C: Having calculated the value of $\Delta I(x,y)$, and thus $\Delta V_s(y)$, for a particular spectral profile, it is now possible to remove the calibrated spatial effect from the velocity profile, and produce an accurate relative line-of-sight velocity profile (Figure 2-66).

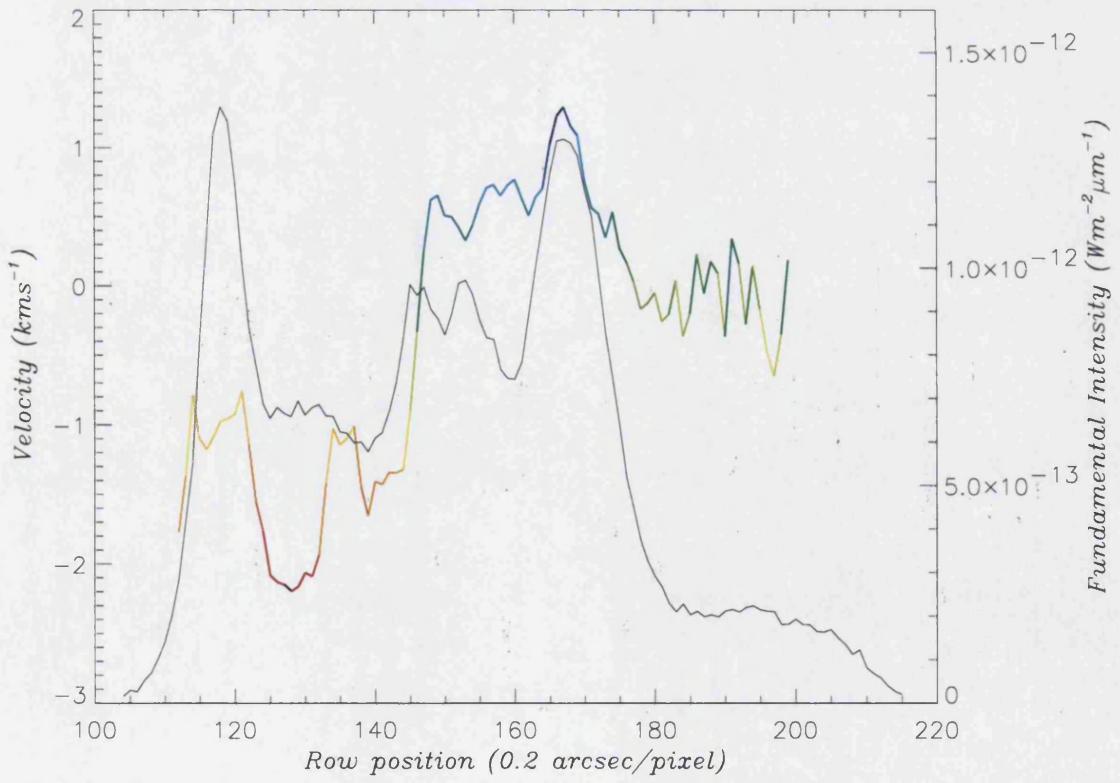

Figure 2-66: The actual velocity profile (a non-linear blue-red shift colour-scale, used for clarity) calculated in SPATIALCALI, plotted with the calculated total fundamental intensity profile, for 11sep98_166

4. Finding the zero point (V_0)

The zero point of our velocity scale may be affected by three factors:

i. Any residual error in the wavelength calibration of the CSHELL detector array;

ii. Any residual error in the laboratory measurement of the H_3^+ line;

iii. The relative motion of the telescope and Jupiter, made up of the orbital motion of Jupiter, the orbital motion of the Earth and the diurnal rotation of the Earth.

To avoid having to *calculate* absolute velocities, a known velocity zero point was needed by which to calibrate the final relative velocities. This was provided by our stated assumption, that non-auroral regions of the planet have no H_3^+ winds associated with them. H_3^+ velocities at latitudes below the auroral oval are significantly smaller ($\ll$300m/s) than the high-energy regime in the aurora, if motions are present at all. This is justified through comparison with the Jovian Ionospheric Model (JIM) (Achilleos *et al.*, submitted), as shown in Figure 2-67, as well as the observations of Clarke *et al.* (1996) and Dinelli *et al.* (1997).

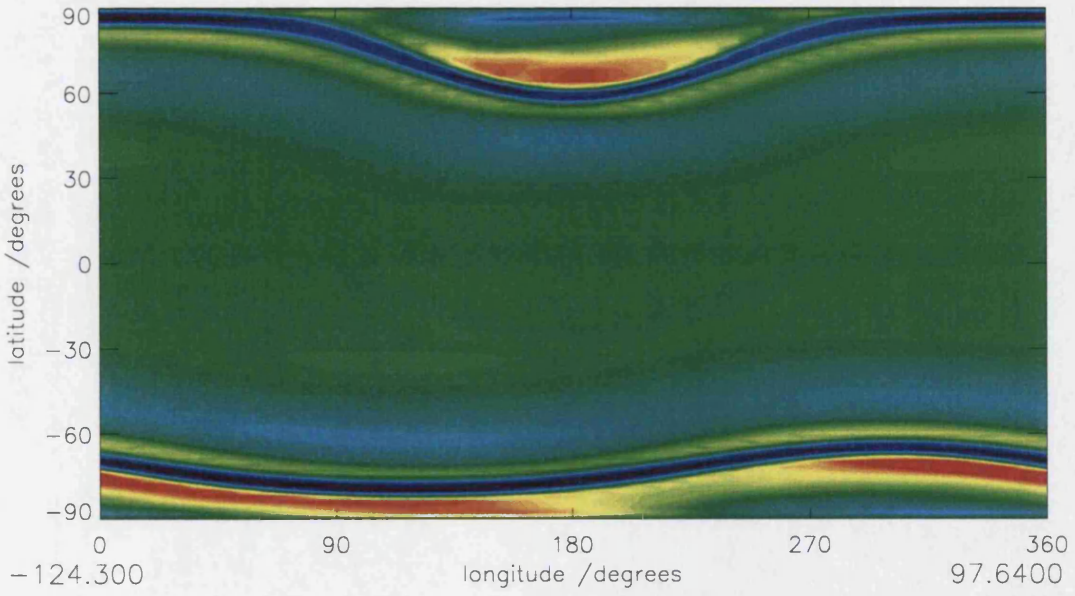

Figure 2-67: H_3^+ velocity in a corotational frame taken from JIM (Achilleos *et al.*, submitted); blue is subrotational and red superrotational, plotted on a linear scale ranging between -124.3 and 97.6 m/s. Note that below the subrotational auroral electrojet, there are only insignificant amounts of motion (equivalent to a scaled value of $\ll$300 m/s)

These theoretical and observational considerations are also supported by our own data: the body of planet velocity profile is essentially flat, also indicating essentially zero wind velocities.

Thus, by setting the velocities on the body of the planet of each spectral profile to zero, we effectively account for the relative motion between the Earth and Jupiter and any other residual wavelength inaccuracies, to produce the actual velocity profile $V_a(y)$. This correction has already been completed in Figure 2-66.

2.9 Line-of-sight Corrections

All of the calculations shown so far are made using the intensities received in the instrument. However, it is necessary to correct for the geometric thickness through which any observation has been made (see Figure 2-68 showing this geometric effect). We assume an optically thin shell of H_3^+ emitting gas (see Lam *et al.* (1997) for a justification of this assumption), uniform in both thickness and density. The line-of-sight correction has been made in two separate stages, using the LOS_LAT and LOS_LONG procedures, set-up and run together from the LOS (**B.3.6 los.pro**) procedure.

As this procedure has its own intrinsic inaccuracies, we apply it only after quantities like column density and total H_3^+ emission have been derived. (The temperature does not require this correction, because the variation in the two intensities used in its calculation is the same due to the assumptions of uniformity.)

Splitting the correction into longitudinal and latitudinal components simplifies the problem into two relatively simple calculations. For the purpose of both these calculations, Jupiter is effectively viewed at an infinite distance.

2.9.1 Calculation of longitudinal line-of-sight

Jupiter is an ellipsoid with an eccentricity of 0.9415, flattened at the poles. Since the spectrometer was aligned perpendicular to the rotational axis, in the longitudinal direction the planet is circular in shape. Figure 2-68 shows the diagram used in this explanation.

In choosing the limits of the spectral profile from the planetary limbs (see **2.3.1 Gauss fitting**), each profile covers the entire planet, so the start and end of the profile marks the two limbs of the planet, denoted in the figure as X_l and X_r. When calculating the correction for column density and total emission, each of which has a size dependent on the hotband intensity, it is thus necessary to place the values into an array that corresponds with the fundamental intensity.

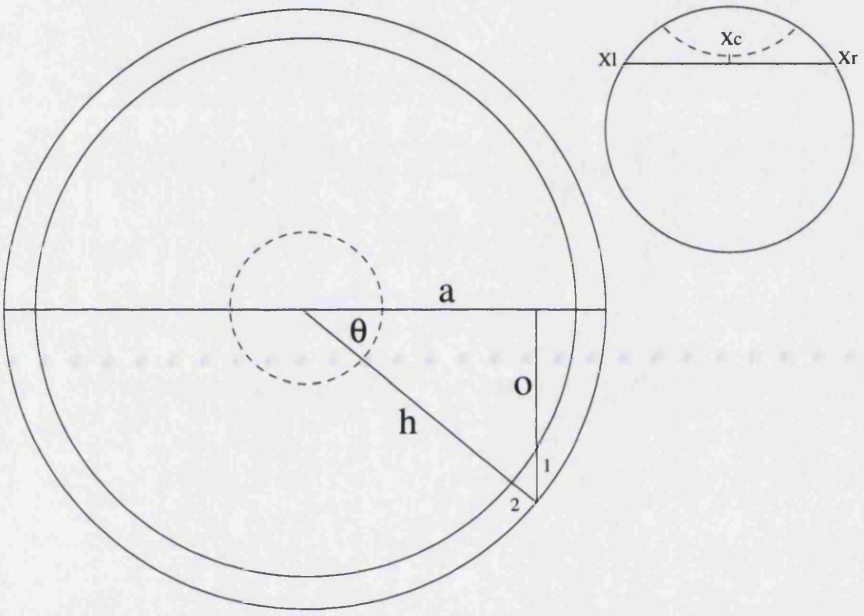

Figure 2-68: The longitudinal line-of-sight effect is effectively the ratio required for a particular value of X_P that scales (1) to become (2), the value of sin(θ). The observer looks through the planetary atmosphere as with (1), perpendicular to the rotational plane

In the diagram, the recorded path-length through the atmosphere is shown by **(1)** and the line-of-sight corrected path by **(2)**. The correction must calculate the ratio between these two points. Thus the correction required is given by:

$$I_{corr}(x) = I(x) \times \sin(\theta)$$

and with *o* (opposite) derived using Pythagorus as:

$$o = \sqrt{h^2 - a^2}$$

This produces a final correction for each position on the spectral profile of:

$$I_{corr}(x) = I(x) \times \frac{\sqrt{h^2 - a^2}}{h}$$

Where, $h = \frac{(X_r - X_l)}{2}$;

and, $a = |X_p - X_c|$.

Where, X_p is the position to be corrected;

and, X_c is the centre of the planet at the given latitude.

This correction breaks down above the limb, so to adjust for the far greater corrections seen directly above the limb when the value of $\sin(\theta) < 0.05$, it is set to zero.

2.9.2 Calculation of latitudinal line-of-sight

The latitudinal correction for line-of-sight requires an elliptical solution. Since the longitudinal correction has accounted for the horizontal component of the line-of-sight, the planet can now be represented by a flattened ellipse, the shape of which is calculated from the size of the equatorial and polar radii of Jupiter at the time of observation.

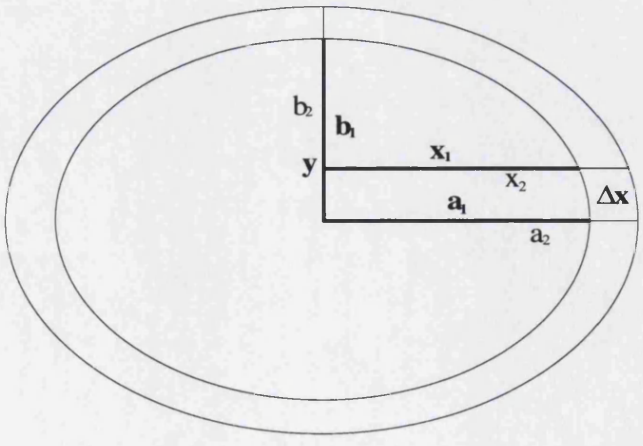

Figure 2-69: The latitudinal line-of-sight effect, calculated using two ellipses to create an isotropic shell of atmosphere. By calculating the relative values of X for the latitude required, the fraction of ΔX at the equator over ΔX at the y-position in question gives the normalised line-of-sight effect

In order to calculate the ratio between the recorded path-length and the line-of-sight, it is necessary to find the difference between the size of two similarly shaped but differently scaled ellipses at a particular position. These, with the subsequent variables used, can be seen in Figure 2-69.

The equation for any position on an eclipse is given by:

$$\left(\frac{x^2}{a^2}\right)+\left(\frac{y^2}{b^2}\right)=1$$

Thus, if we consider looking at the planet at a position of y, then it is simply a matter of calculating Δx, the difference between an inner and outer ellipse that models an elliptical shell. This can be found by rearranging the equation for an ellipse thus:

$$\Delta x=\sqrt{a_2^2\times\left(1-\left(\frac{y_2^2}{b_2^2}\right)\right)}-\sqrt{a_1^2\times\left(1-\left(\frac{y_1^2}{b_1^2}\right)\right)}$$

Where, a_1 is the equatorial radius;

a_2 is the equatorial radius with the atmosphere included ($a_1 + \Delta h$);

b_1 is the polar radius;

b_2 is the polar radius with the atmosphere included ($b_1 + \Delta h$);

y is the latitude in pixels.

Once this is calculated for y, the result can form a ratio with the value produced when viewing the equator, and this fraction (y/y_{equ}) will give the line-of-sight correction.

In order to find the position of y, it is necessary to compare the spectral intensity profile with the image, using the INTMATCH procedure described in **2.8.2 Spatial correction** (also see Figure 2-54 on page 118). This will provide a position on the planet, but it is also necessary to find the position of the limb to produce an absolute value for y.

To locate the position of the limb, an adapted version of the INTMATCH procedure was designed, called LIMB. This allows the user to move the cursor over the K-band image and determine the position of the limb by eye, in the same manner as in INTMATCH. There is some difficulty in this because the limb is not exactly defined, fading away over a

number of pixels. However, by using specific colour scale, the limb can be better determined repeatedly, although this in itself is open to inaccuracies (Figure 2-71).

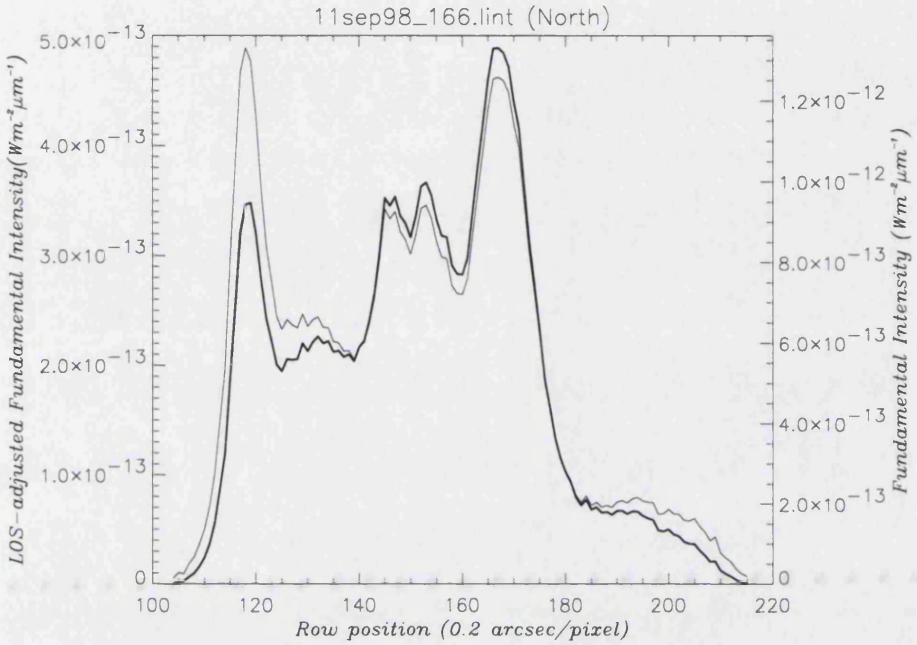

Figure 2-70: The line-of-sight intensity profile (in bold) and uncorrected intensity profile, calculated in LOS for 11sep98_166

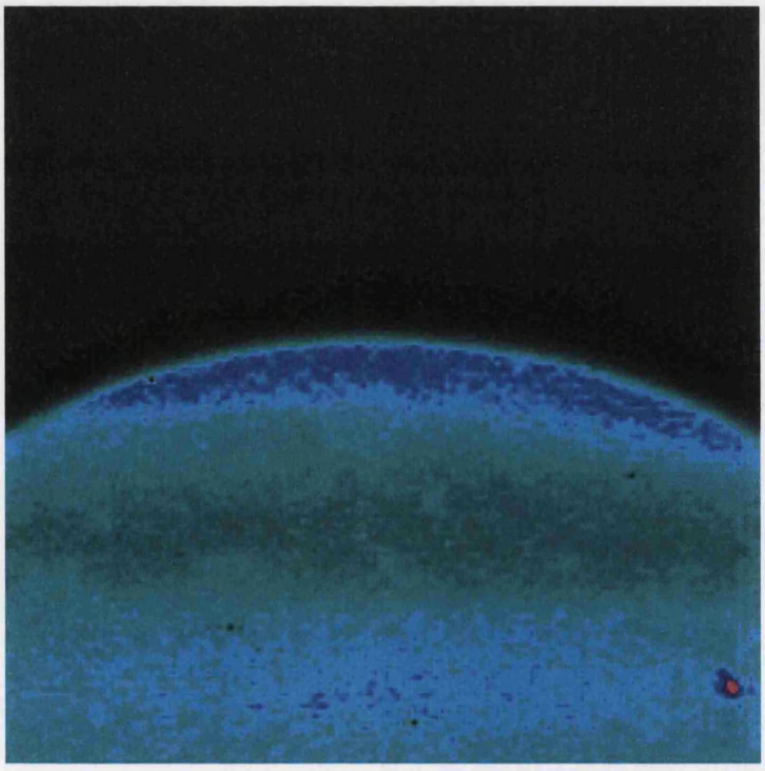

Figure 2-71: A K-band image of Jupiter, displayed using a colour scale that enhances the visibility of the limb

Because of these inaccuracies, unlike the longitudinal correction, when the region near the limb is reached outputs are not zeroed. In the latitude calculation, if the ratio falls below 0.1, it is set to equal 0.1. This allows a suitable correction for spectral profiles beyond the "limb", without nullifying the results completely.

2.10 Line-of-sight Maps

2.10.1 Implications of line-of-sight mapping

The data so far has been shown only in plot form, each showing a particular spectral profile of data. However, the data was taken specifically to cut through the aurora, allowing a better overall picture to be seen (**2.2.2 Jovian observations**). Displaying all the spectral profiles taken on a particular run is desirable, and the simplest way to show this is to produce a two-dimensional map of the sequence of data, as if it had been taken instantaneously. This is best produced by linearly interpolating between each subsequent spectral profile down the planet, filling the spaces between. To facilitate this interpolation, it is necessary to "stretch out" all the profiles so that they are the same size, allowing a simple interpolation between rows to occur.

However, in converting one-dimensional profiles into a two-dimensional map, it is necessary to accept considerable limitations. By interpolating linearly, and resizing the array to appear as a planetary shape, the spectral profiles will be correctly shown. However, the regions between these profiles have effectively been interpolated along lines of same longitude, so when phenomena in the data, such as the auroral oval, vary both longitudinally and latitudinally, the ability of the map to show these variations will be limited.

In addition, the sequence of spectra were taken over an extended period of time, usually around 15 minutes, which will result in the lower spectral images being taken at a slightly "shifted" Jovian CML. This results in some degree of spatial smearing, especially on maps created with a significant number of spectral profiles. However, this is kept to a

minimum in the interpolation of the data because adjacent profiles will always have been taken within only a couple of minutes.

2.10.2 Creation of maps

The creation of a line-of-sight map consists of a number of steps contained within the MAP procedure, and its offshoots (**B.2.4 map.pro**). These separate steps are generally subdivided into separate procedures that MAP calls as it progresses. The program must load and resize the separate arrays into a form in which they can be interpolated between; it must then locate where each spectral profile is located in respect to another, then interpolate between these profiles, and reform the resulting array back into the shape of a planetary surface.

1. Setting up the required arrays

   Arrays are set up to contain the positions of the spectral profiles on the planet, and the resized profiles ready for interpolation. The map itself cannot be set up until the number of steps between each profile is known.

2. Limb positioning

   The location of the limb is found using LIMB, described in **2.9.2 Calculation of latitudinal line-of-sight**.

3. Loop for each spectral profile

   a. Data loading and calibration

      The procedure loops through the number of profiles. In each loop, the procedure MAP_LROW loads a profile and resizes it to a predefined base size, which is the same for all of the profiles. The output of this goes into the input matrix that stores each row separately.

b. Positioning

While still within this "number of profiles" loop, the procedure calls INTMATCH (see **2.8.2 Spatial correction**) and allows the user to locate the position of that particular profile on the image. This position is recorded in the position matrix.

4. Interpolation

Having collated all the information about the separate spectral profiles, the procedure calls MAP_INTERP. This uses the positioning information to build a map of the correct size (the difference between the position of the highest and lowest spectra on the array) (Figure 2-72). Having built the unfilled map, it places all the profiles in the correct row positions, and interpolates linearly between them. This outputs an interpolated rectangle of data (Figure 2-73).

5. Resizing back to a planetary surface

The procedure MAP_CONV takes the interpolated map and runs through each row of the array, calculating the width required to match the planetary surface using the MAP_CALC procedure. This calculates the width as follows:

$$d = P_l + 2.4 - P_s$$

Where, d is the distance below the limb;

P_l is the position of the limb;

P_s is the position of the spectral profile;

and, 2.4 is added to account for the additional H_3^+ atmosphere above the limb;

$$Q = \frac{\text{acos}(|\, b\text{-}d \,|)}{\sqrt{a^2 - \left[\left\{\left(\frac{1}{e^2}\right) - 1\right\} \times (b-d)^2\right]}}$$

$$R = \sqrt{\frac{a^2}{1 + \left[\cos(Q)^2 \times \left\{\left(\frac{1}{e^2}\right) - 1\right\}\right]}}$$

$$\text{base} = \text{FIX}[(2R \times \sin(Q)) + 0.5]$$

Where, base is the width of the profile when fitted to a planetary shape (the lowest profile is used as the size determinate of the base of the final map output array);

a is the equatorial radius;

b is the polar radius;

and, *e* is the eccentricity (*b/a*).

This outputs the map as an array, which has the data, interpolated and fitted to a planetary shape, producing what appears to be an "image" of the data (Figure 2-74).

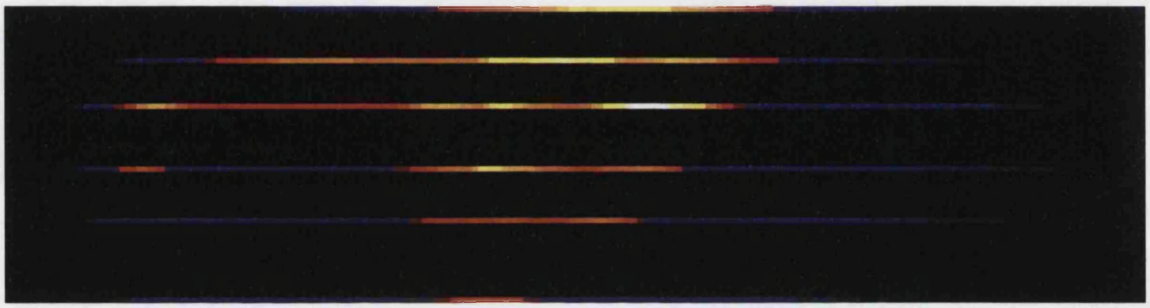

Figure 2-72: The uninterpolated map array, with the intensity profiles scaled to the same size and positioned in the correct relative latitudinal position

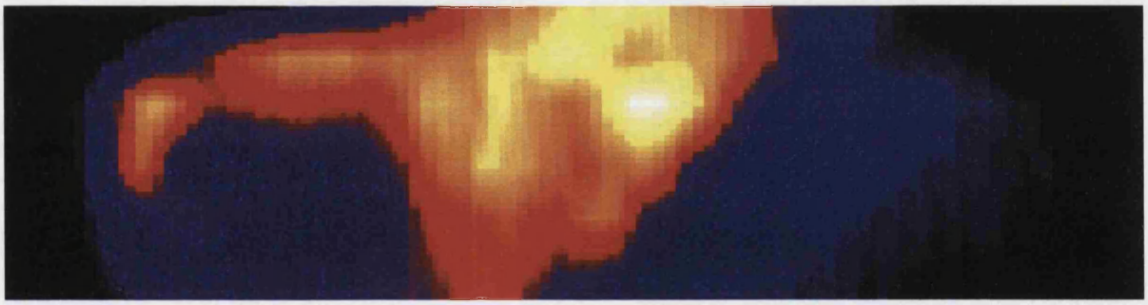

Figure 2-73: The interpolated map array

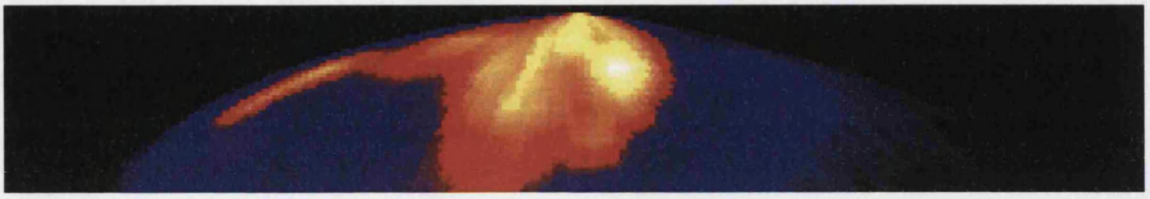

Figure 2-74: The completed map, with the limbs fitted to the calculated size required for the each specific latitude, converting the spectral profiles into a line-of-sight map

Chapter 3 : Temperature, H_3^+ Column Density and Energy Balance in the Jovian Auroral Region

Although the physical processes at work in the Jovian aurorae are understood in principle, much of the work produced to date has relied upon sensible but untested assumptions, such as the use of H_3^+ emission intensity as a direct signature of input energy. These assumptions may be reasonable, but they have not been verified because of the lack of a study using a resolution capable of determining variations in basic physical conditions inside the auroral region. This chapter will use the results of the processing described in Chapter 2 to study the Jovian aurora at the resolution, both spatially and spectrally, capable of investigating previous assumptions.

Our data enables us to look in detail at temperature, column densities and total H_3^+ emission across the entire Jovian aurora. The results discussed here cover the production and distribution of H_3^+ within the auroral region. Due to the size of the data set produced within this project, a compete analysis of all the data is not presented. Instead, we have chosen a subset which best illustrates the physical conditions prevalent in the auroral region as a whole.

The data selected shows the northern aurora fully displayed to the observer, with a Central Meridian Longitude around 160° (Figure 3-1). The southern aurora was also observed in this data set, but is displayed less clearly, because the sub-solar point is

located in the northern hemisphere. Four sets of northern spectral images, from three separate nights, the 8th, 10th and 11th, have CMLs which match reasonably well:

Table 3-1: The sets of spectra analysed for temperature, column densities and total emission

Name of sequence	CML at start of sequence	U.T. at start of sequence
8N5	150	10:46
10N5	144	12:13
10N6	164	12:48
11N4	154	08:19

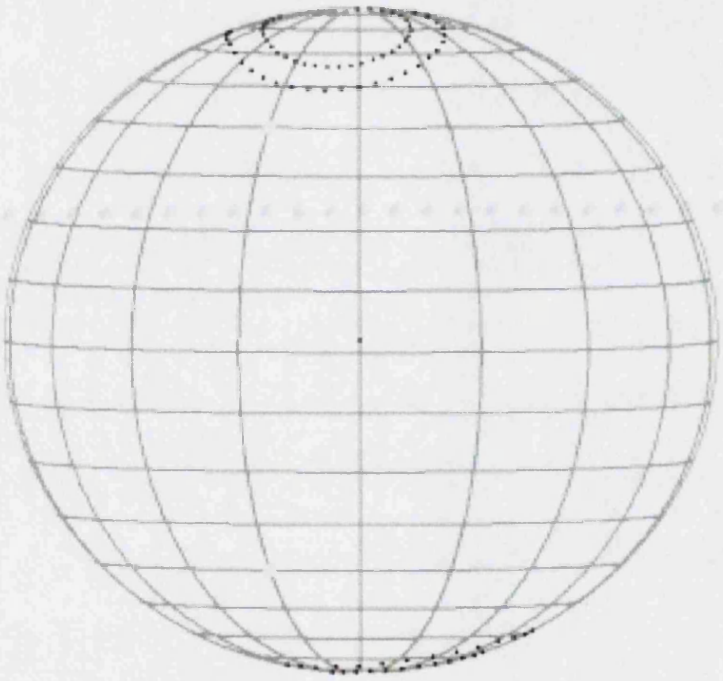

Figure 3-1: The locations of the magnetic latitudes that join to $6R_J$ and $30R_J$ distance in the magnetosphere, according to the VIP4 model

To best determine the conditions of the auroral region, each of the parameters explained in Chapter 2 is described individually.

The fundamental intensity, due to its high signal-to-noise and extensive coverage in images, line-of-sight maps and the profiles themselves, provides a useful way to determine the general morphology of the aurora. Temperature variations allow the conditions of the surrounding thermosphere to be monitored and show the extent of control that auroral heating plays in localised heating. H_3^+ column density then tests the

assumption that this intensity is a good indicator of energy deposition in the aurora. Finally, total emission provides information on auroral energy loss and, in comparison with the temperature and column density, shows the dominant processes which control this.

3.1 Morphology from Intensity

The intensity of the fundamental ν_2 Q(1,0$^-$) line (henceforth the "fundamental intensity") provides a general overview of the morphology of the Jovian auroral region. Using both the spectral profiles and associated images, it is possible to provide a basis from which subsequent environmental conditions can be compared, providing a detailed view of the emission both on the main auroral oval, and in regions at lower and higher latitudes.

The Q(1,0$^-$) line has an Einstein coefficient of ~129s^{-1}, which ensures that the fundamental H_3^+ quickly radiates into the ground state. This results in the fundamental emission effectively providing an instantaneous snapshot of the emission at the time of observation.

There is a general assumption that emission intensity is a strong indicator of the location of energy deposition in the aurora. This assumption will be tested below, but in order to provide a general overview of the morphology, it is enough that the fundamental intensity describes the location of H_3^+ emission across the aurora. Analysis of what this emission means waits upon results given later in this chapter.

3.1.1 General auroral morphology

3.953μm images

The 3.953μm images taken in association with the spectral images clearly show the distribution of the Jovian northern aurora, consisting of the auroral oval and polar cap emission. The image taken for the 11N4 sequence (11sep98_154) (Figure 3-2), which is particularly clear, illustrates the distinctive morphological regions.

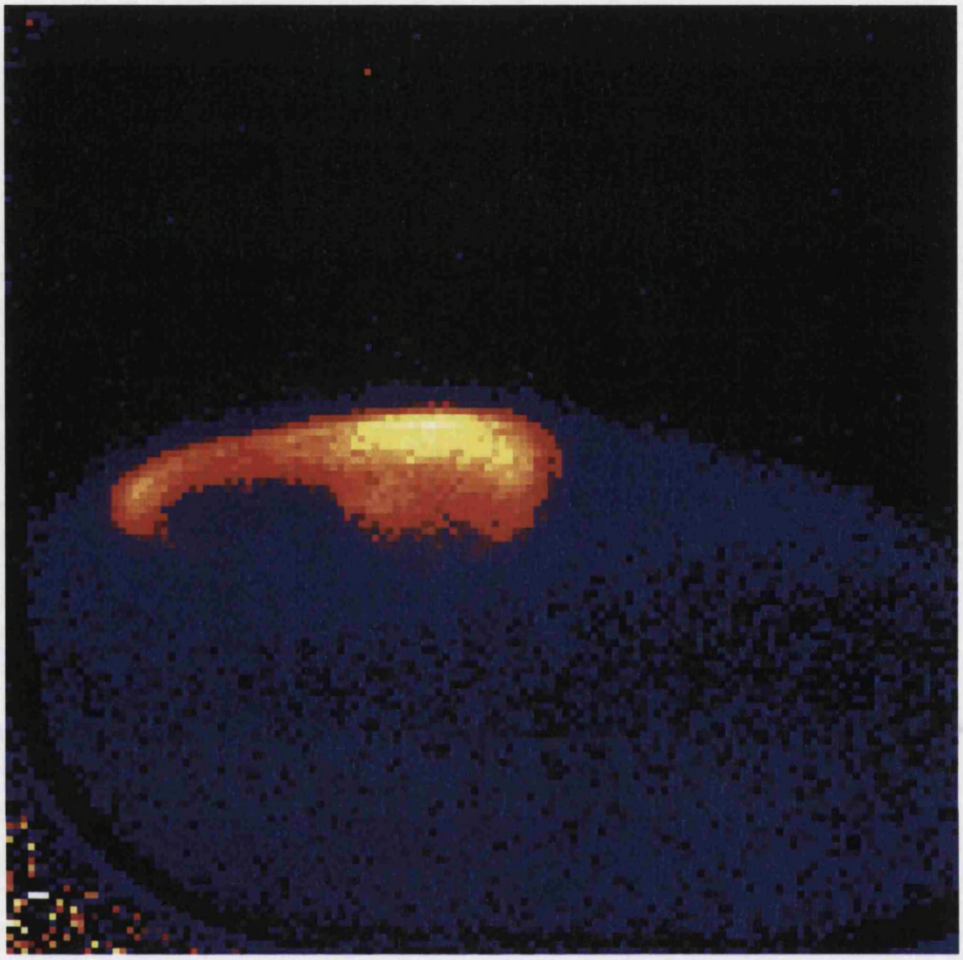

Figure 3-2: 3.953μm image of the Jovian aurora, taken at 159°, on the night of the 11th at 08:34U.T.

The main auroral oval can be clearly seen on most of the images. The oval appears to be sharply delineated, with a rapid intensity decrease away from the oval at lower latitudes. At latitudes above the strongest oval emission, the intensity reduces more gently into the polar region.

Comparing the image with the VIP4 magnetic field model of Connerney *et al.* (1998) at 160° (Figure 3-1), the peak intensity associated with the auroral oval appears to be generally fixed in jovimagnetic co-ordinates. Satoh and Connerney (1999) used 3.953μm images taken with the NSFCAM, the dedicated imaging camera on the IRTF, with superior imaging quality to CSHELL, to model the distribution of H_3^+ emission in jovimagnetic co-ordinates. The results of this modelling closely match the appearance of the CSHELL images.

Satoh and Connerney's work highlights the difficulty involved in pinpointing the exact magnetospheric origin of the auroral oval, though the peak intensities were associated field lines that crossed the (magnetic) equatorial plane at 12-30R_J from the planet, probing the region of the equatorial plasmasheet in the region where corotation tends to break down.

The "polar region" (with the magnetic pole off-axis from the rotational pole directly towards the direction of observation) is clearly complicated. There seem to be two major areas, each with a different emission strength. The dusk side of the polar region (west on the sky*) is bright in intensity, with apparent variations in the strength of emission across this half. The dawn side of the polar region (east on the sky†) is much darker, appearing to be lacking emission any stronger than the main body of the planet below the aurora.

This two-half variation in the polar cap was fitted with a "Yin-Yang" model of emission by Satoh and Connerney (1999). The bright emission, the "Bright Polar Region", was associated with particle precipitation from further out in the magnetosphere than that which gives rise to the auroral oval. The "Dark Polar Region" was a counterpart to this, where no increase in precipitation occurs. This new view of the polar region of the aurora is still somewhat controversial.

The limb of the planet poleward of the aurora is very bright. This small region at the pole is formed where the large increase in line-of-sight associated with the limb is combined with an already raised H_3^+ density from the aurora producing a very high column density, thus resulting in a large emission in the line-of-sight. Within the auroral region, where H_3^+ density remains high, a gradated intensity is apparent, with the intensity decreasing away from the pole as the line-of-sight effect becomes less pronounced.

Fundamental intensity map

The map of intensity (see **2.10 Line-of-sight Maps** for production details) can be compared easily with the image. The map that corresponds to the image described above is shown in Figure 3-3. This was produced using spectral profiles whose positions cover

* right on the image
† left on the image

the limb and auroral regions. Other profiles were not used, because of the difficulty in locating their position on the planet.

Figure 3-3: An interpolated map of the fundamental intensity before the line-of-sight correction, using spectral profiles from 11N4, using a non-linear scale from 0 to 4.2×10^{-12} $Wm^{-2}\mu m^{-1}$ to best show the features within the auroral region; for proper values see the profiles, shown below

While the details are not as clear on the map, because of the linear interpolation process described in Chapter 2, the general form of the auroral region is replicated directly. Some of the streaking associated with the interpolation process (**2.10.1 Implications of line-of-sight mapping**) is apparent along equal lines of longitude. The oval itself is particularly affected by the interpolation because the narrow intensity curves through the map, producing false points of bright and dark with the region of the oval itself.

This means that analysis of the map without reference to both the image and the spectral profiles from which it is produced could be confusing. However, when seen in context with these, it produces a useful link between the two. While some of the variations are due to the interpolation process, some are directly seen in the intensity profiles. The map shows that some variations in the Bright Polar Region can be seen to link together as arcs, rather than individual bright spots.

An advantage in using the interpolated map is that the line-of-sight corrected spectral profiles can be used to produce a second map covering an identical region, but with all the line-of-sight effects removed.

These maps (Figure 3-4 to Figure 3-7) no longer have the bright polar limb, and the brightness is much more even across the whole aurora. The auroral oval is notably brighter on the dusk side, with the bright region of the polar emission also appearing strongly. The dawn side of the auroral oval has diminished in strength significantly, and

the darker emission in the pole appears to be of a reduced intensity compared to the rest of the auroral region.

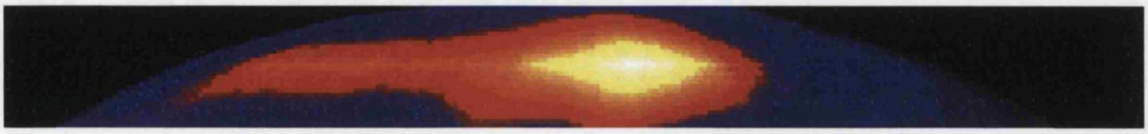

Figure 3-4: The fundamental intensity map made from the 8N5 line-of-sight corrected intensity profiles, using a non-linear scale of 0-6.2×10^{-13} Wm^{-2}μm^{-1}, to best show the features within the auroral region; for proper values see the profiles, shown below

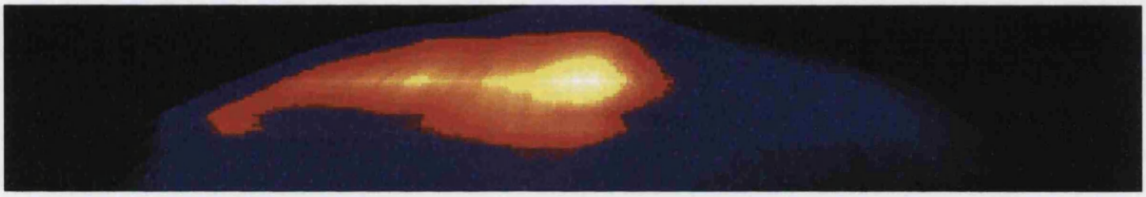

Figure 3-5: The fundamental intensity map made from the 10N5 line-of-sight corrected intensity profiles, using a non-linear scale of 0-5.7×10^{-13} Wm^{-2}μm^{-1}, to best show the features within the auroral region

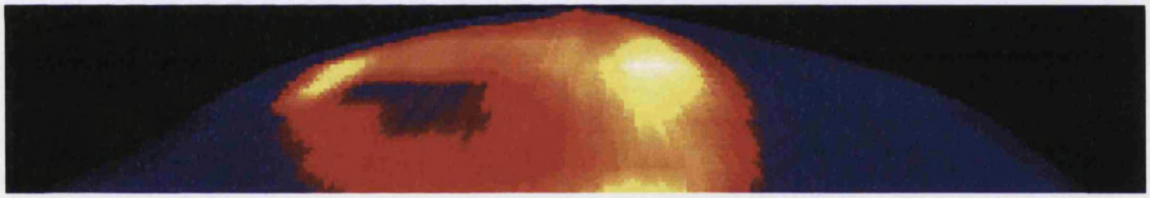

Figure 3-6: The fundamental intensity map made from the 10N6 line-of-sight corrected intensity profiles, using a non-linear scale of 0-4.0×10^{-13} Wm^{-2}μm^{-1}, to best show the features within the auroral region

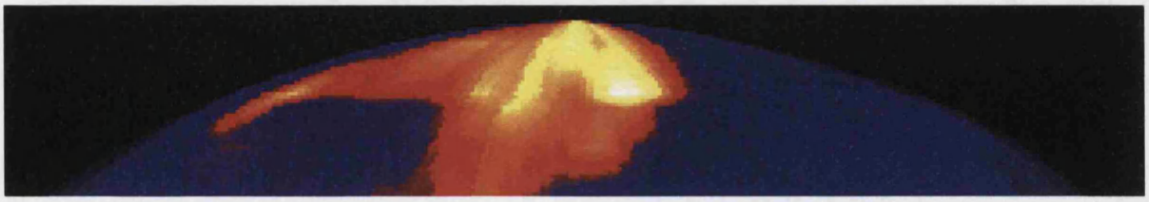

Figure 3-7: The fundamental intensity map made from the 11N4 line-of-sight corrected intensity profiles, using a non-linear scale of 0-4.5×10^{-13} Wm^{-2}μm^{-1}, to best show the features within the auroral region

While there are minor differences between the four intensity maps, mostly attributable to the differences in CML, the general morphology is the same.

Fundamental intensity profiles

The series of profiles which make up a single run (that of 11N4, shown in Figure 3-7) gives an indication of the variation in intensity profiles that can been seen. All the spectral sets consist of four major groups of intensity profile morphology, shown clearly in this example, in order of position on the planet:

1. The sequence begins above the limb of the planet, where noise dominates the first two spectral profiles. Because the method of finding intensity uses the fitted Gaussian height, noise produces a random level above zero, so the values given for the first profile (Figure 3-8) are set at around 1×10^{-14} $Wm^{-2}\mu m^{-1}$. This is not a background level for intensity, since any background is removed once a reliable Gaussian can be fitted, but can be regarded as a minimum value above which recorded intensities can be considered reliable. The second profile (Figure 3-9) has an increase from this minimum in the central region, indicating the slit is positioned such that it is receiving emission from the upper atmosphere of the planet itself. Since the spectra are above the planet, line-of-sight corrections are meaningless.

2. The third spectral profile (Figure 3-10) was the first taken in this sequence; it is positioned directly on the planetary limb. The general form is close to a Gaussian, with no clear morphology, although there is a degree of anisotropy, perhaps due to the width of the slit extending below the limb to pick up variations within the aurora. The strength of the intensity is very high before the correction for limb-brightening, as the line-of-sight is long.

3. As the slit covers lower latitudes, the sequence of spectra cut through the auroral oval itself, and show both the auroral ovals and polar emission. The line-of-sight correction shows the decrease of the dawn side of the oval clearly, so that the dusk dominates the emission. Despite this, both sides of the auroral oval are clearly seen throughout the profiles taken within the auroral region.

   Also clear is both the strength and complexity of the polar emission. The delineation between the bright and dark regions of the polar cap are particularly clear on Figure 3-12 and Figure 3-13, with a strong drop in intensity dividing the two regions. Nonetheless, the "Dark Polar Region" (DPR) of the polar emission can clearly be seen on the intensity profiles to have significant emission between $1\text{-}2\times10^{-13}$ $Wm^{2}\mu m^{1}$, considerably higher than regions outside the auroral oval, which have values around 5×10^{-14} $Wm^{2}\mu m^{1}$. This suggests that, contrary to Satoh and Connerney (1999), this region does consistently contain significant levels of

emission above that caused by the background EUV (Rego *et al.*, 2000), the previously envisaged source of H_3^+ in this region.

The "Bright Polar Region" (BPR) is clearly a highly complex region, with strong emission peaks occurring within the auroral oval. The significant peak showing in this region is, on some profiles (Figure 3-11 and Figure 3-13), actually stronger than the emission that might be associated with the general ring structure. The evidence suggests this stronger emission cannot be from the main oval, in the form of the more complicated structures displayed within it. This strong secondary intensity high consists of two distinct peaks on one profile (Figure 3-12) and changes its shape significantly depending on which profile is being examined.

This diverse morphology is indicative of magnetic field lines connecting to the Jovian ionosphere from the outer (>30R_J) magnetosphere. Rather than individual bright spots, this is an arc or series of arcs that run inside the main oval. While there is very limited published discussion of the Jovian polar region, discussions with researchers working on UV observations of the Jovian aurora (Prangé, R., private communication; connected with Clarke *et al.*, 1998), tied with those made by the Ulysses satellite, suggest a similarity between the UV and H_3^+ emission over the poles.

The Ulysses observations were made from above the planetary rotation axis, providing a unique view of Jovian auroral emission. Recent work studying these observations suggests the presence of emission arcs associated with magnetospheric regions as low as ~20R_J, and that these arcs represent inner rings that mark a fragmentational breaking with corotation, beyond the initial slowing associated with the main auroral oval.

4. At latitudes lower than the auroral region, the intensity quickly drops off, and the profiles become relatively flat (from Figure 3-14 to Figure 3-20). It should be noted that the emission levels are around 6-8×10^{-14} $Wm^2\mu m^1$, greater than the minimum detection levels measured above the limb, evidence of both the EUV and mid-to-low latitude emission discussed in the introduction (**1.3.1 Composition of the ionosphere**). The INTMATCH procedure (**2.8.2 Spatial correction**) used to find the position on the planet for line-of-sight corrections cannot be used at these lower latitudes, because of the difficulty in matching these spectral intensities to the associated image. However, the effective increase in line-of sight effect at these latitudes is minimal, so such a correction is generally unnecessary.

One other interesting feature seen within the intensity profiles of the four sets of spectra chosen is the presence of the "Io spot" on 8N5. This can be seen as a clear peak in Figure 3-22, and a less distinct increase in Figure 3-21. While the footprint of Io is not present on any hotband spectral profiles, from which a temperature could have been calculated, its presence on the fundamental profile is still useful, as the footprint is a direct measure of the link with the magnetosphere, connecting to Io at $5.9R_J$.

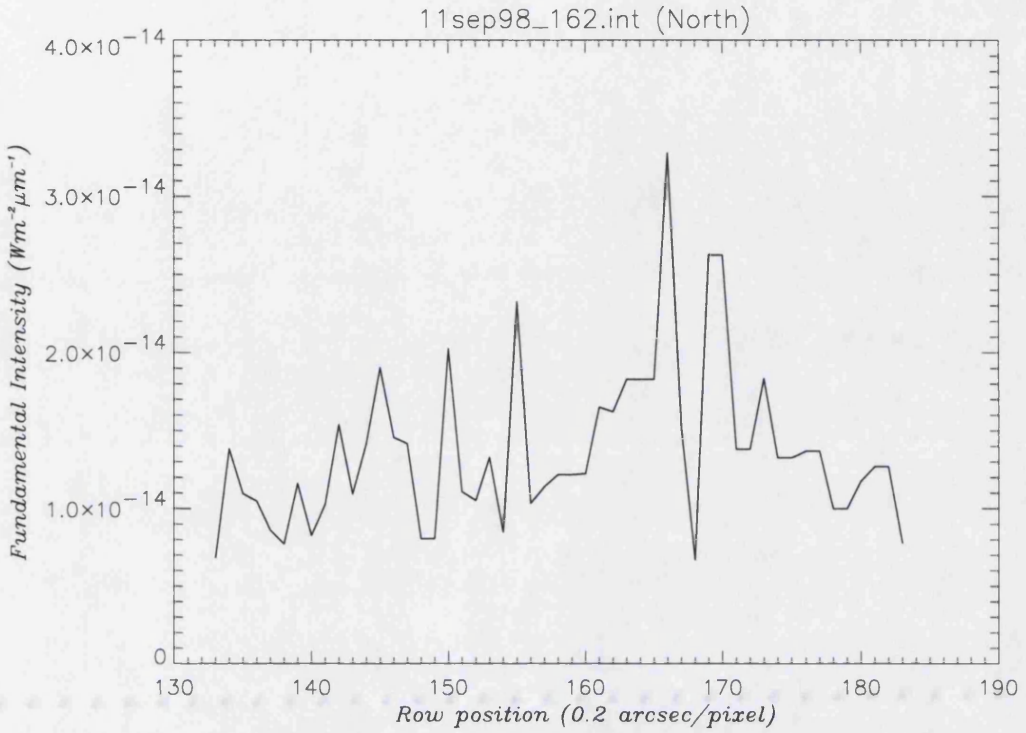

Figure 3-8: The intensity profile, taken above the limb at 08:30U.T., which consists totally of noise, from the 11N4 set of spectra

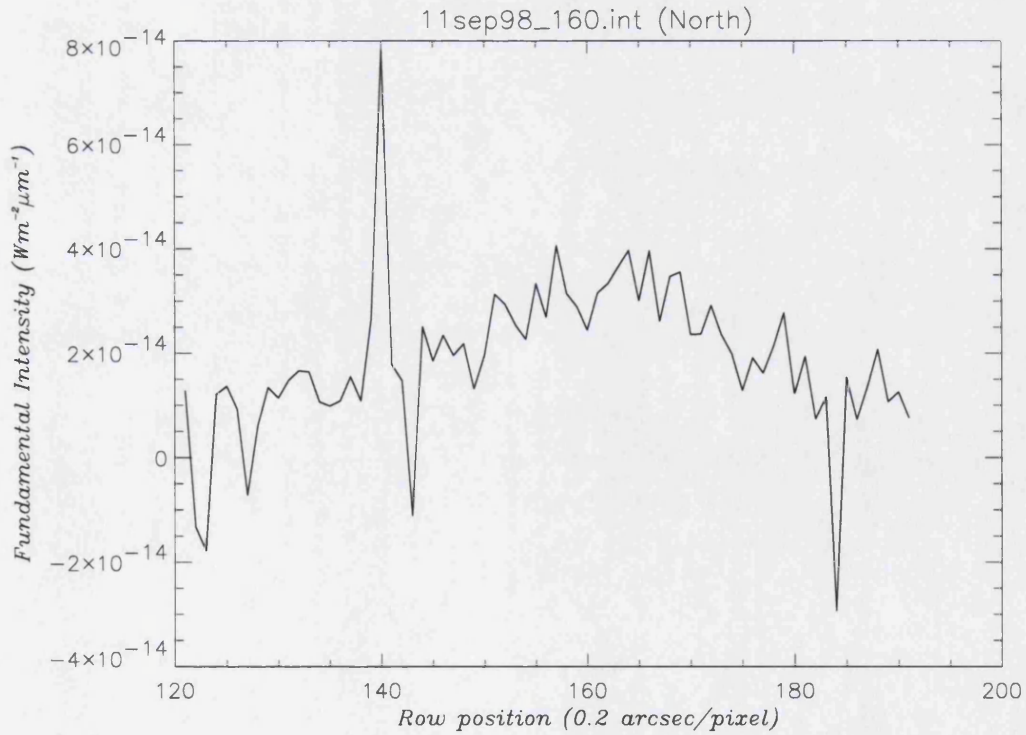

Figure 3-9: The intensity profile, taken above the limb at 08:28U.T., which consists almost totally of noise, from the 11N4 set of spectra

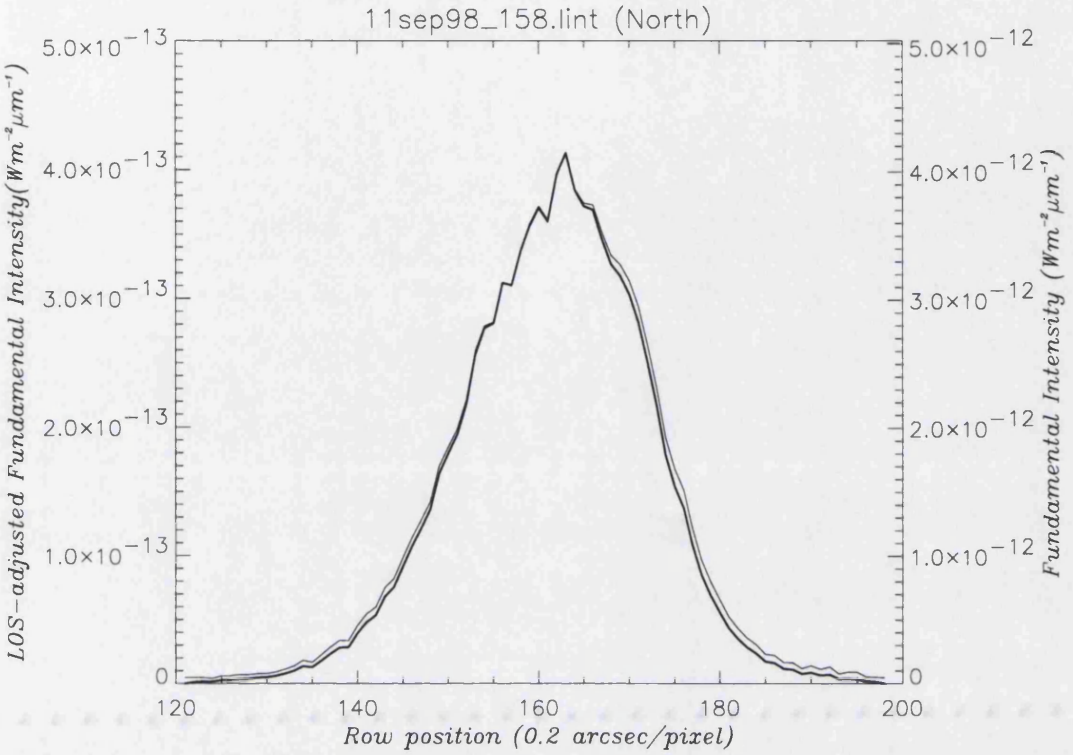

Figure 3-10: The line-of-sight corrected intensity profile, taken at 08:27U.T. with a CML of 155°, from the 11N4 set of spectra

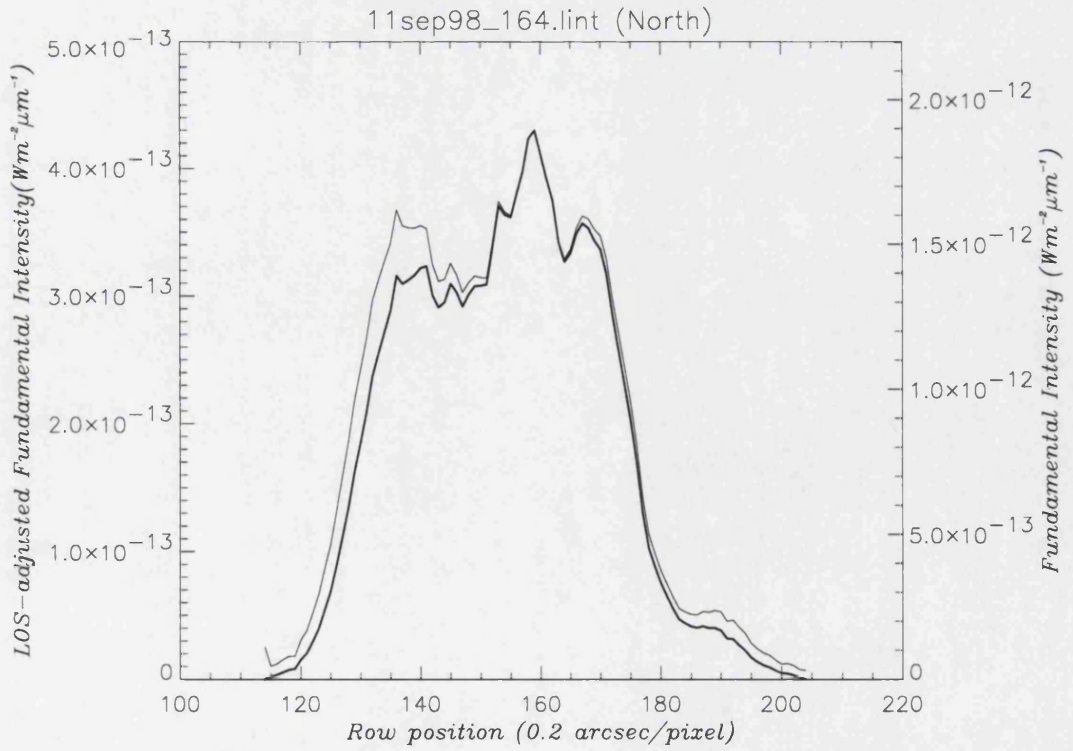

Figure 3-11: The line-of-sight corrected intensity profile, taken at 08:32U.T. with a CML of 158°, from the 11N4 set of spectra

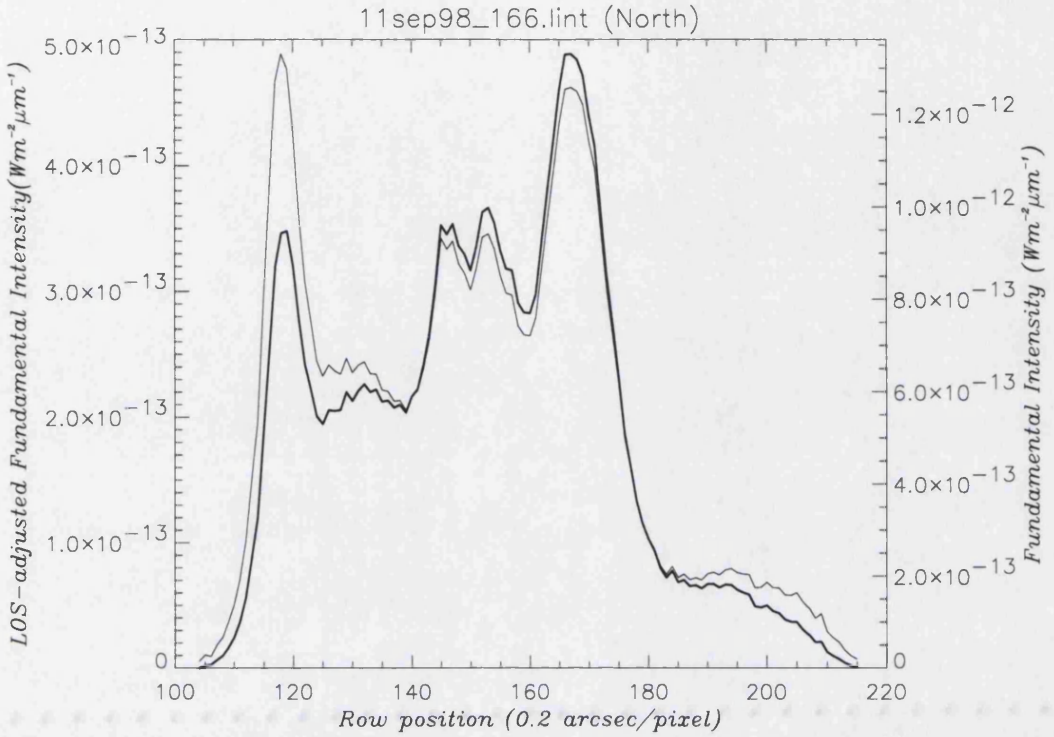

Figure 3-12: The line-of-sight corrected intensity profile, taken at 08:34U.T. with a CML of 159°, from the 11N4 set of spectra

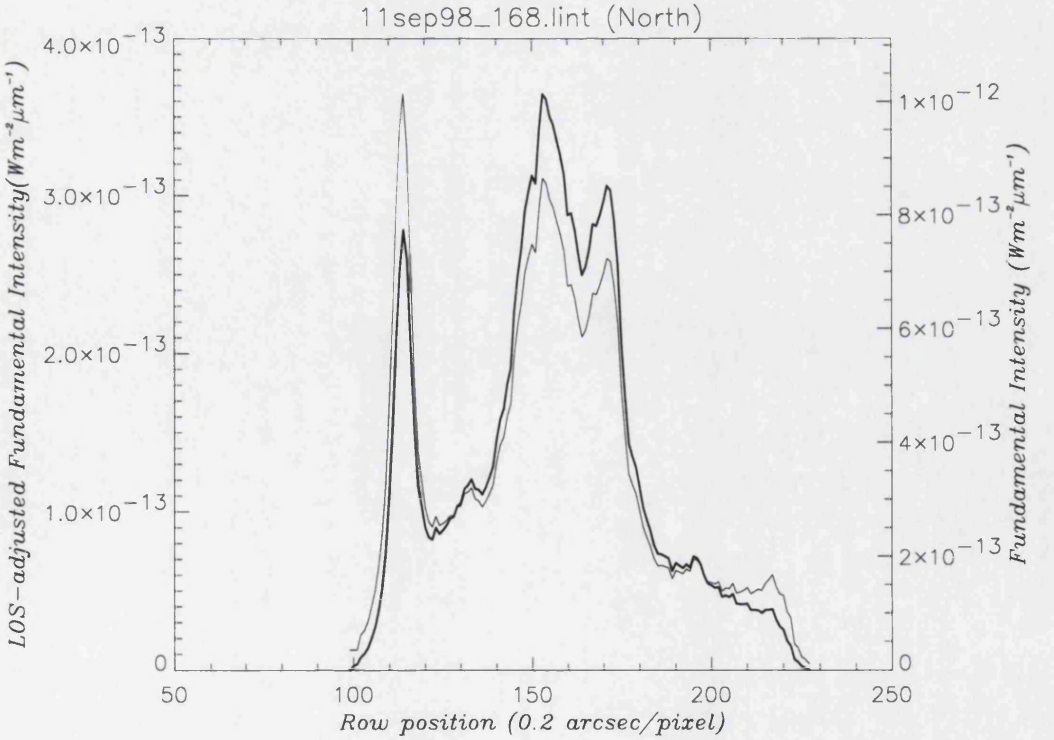

Figure 3-13: The line-of-sight corrected intensity profile, taken at 08:35U.T. with a CML of 160°, from the 11N4 set of spectra

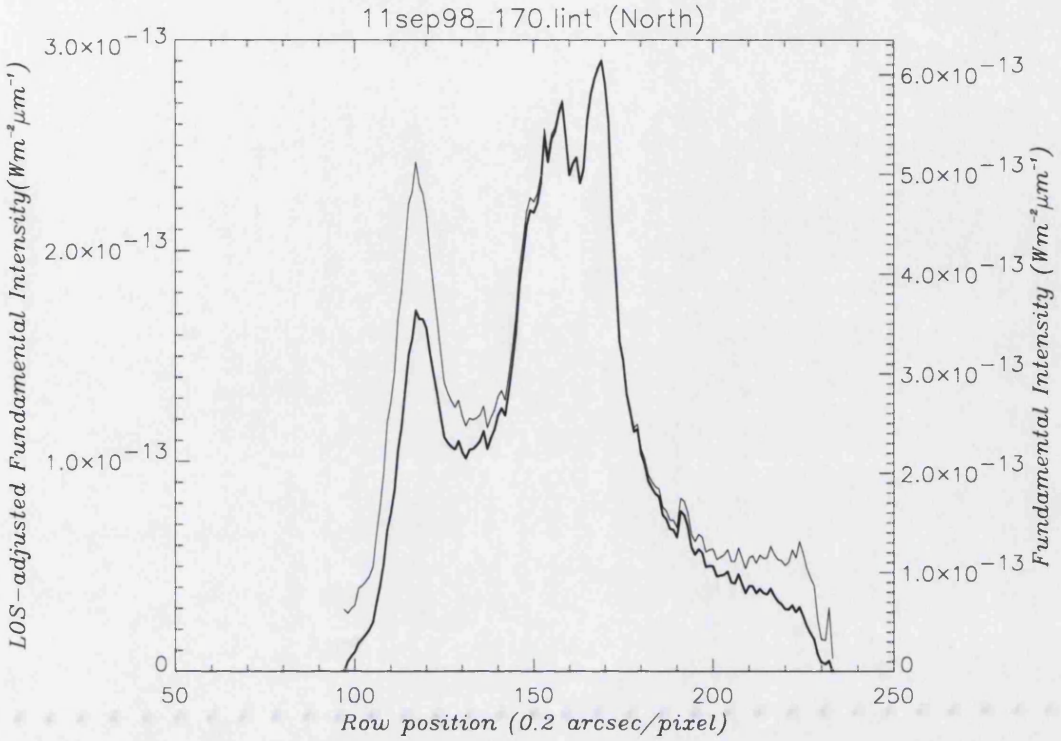

Figure 3-14: The line-of-sight corrected intensity profile, taken at 08:37U.T. with a CML of 161°, from the 11N4 set of spectra

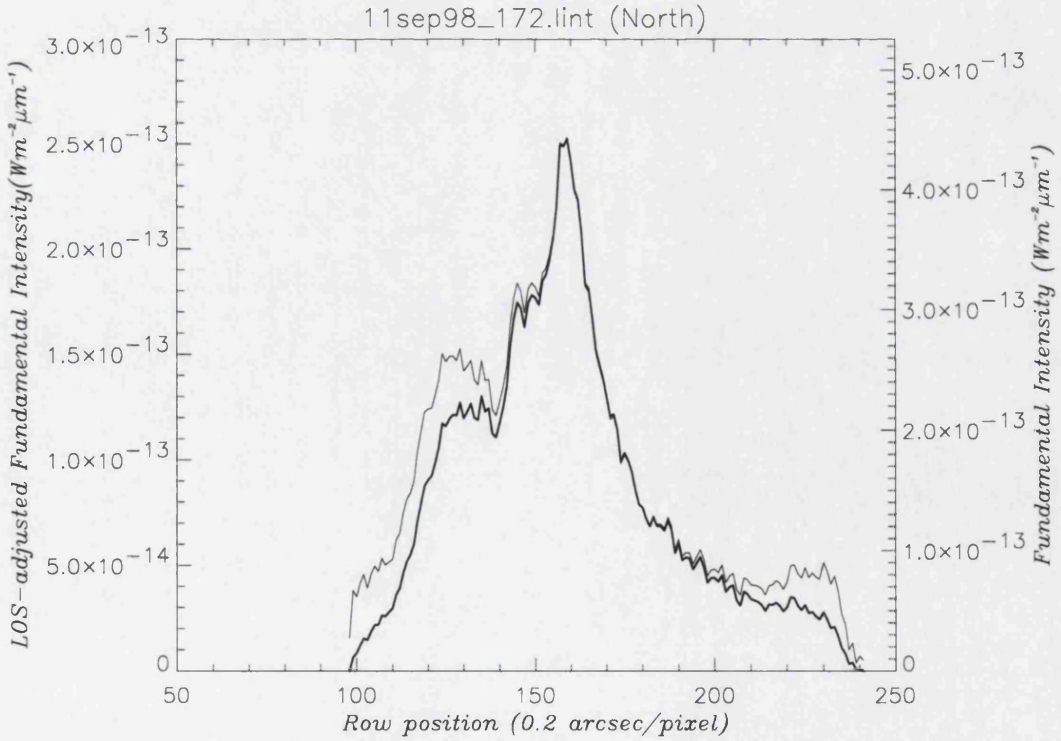

Figure 3-15: The line-of-sight corrected intensity profile, taken at 08:39U.T. with a CML of 162°, from the 11N4 set of spectra

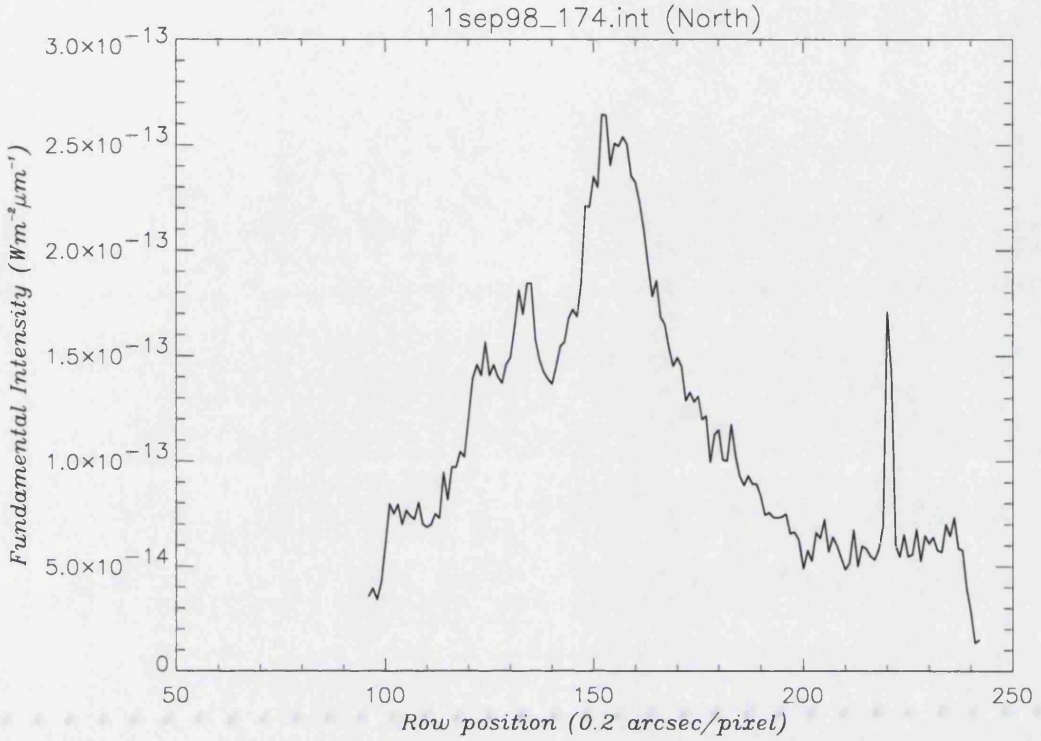

Figure 3-16: The intensity profile, taken at 08:41U.T. with a CML of 163°, from the 11N4 set of spectra

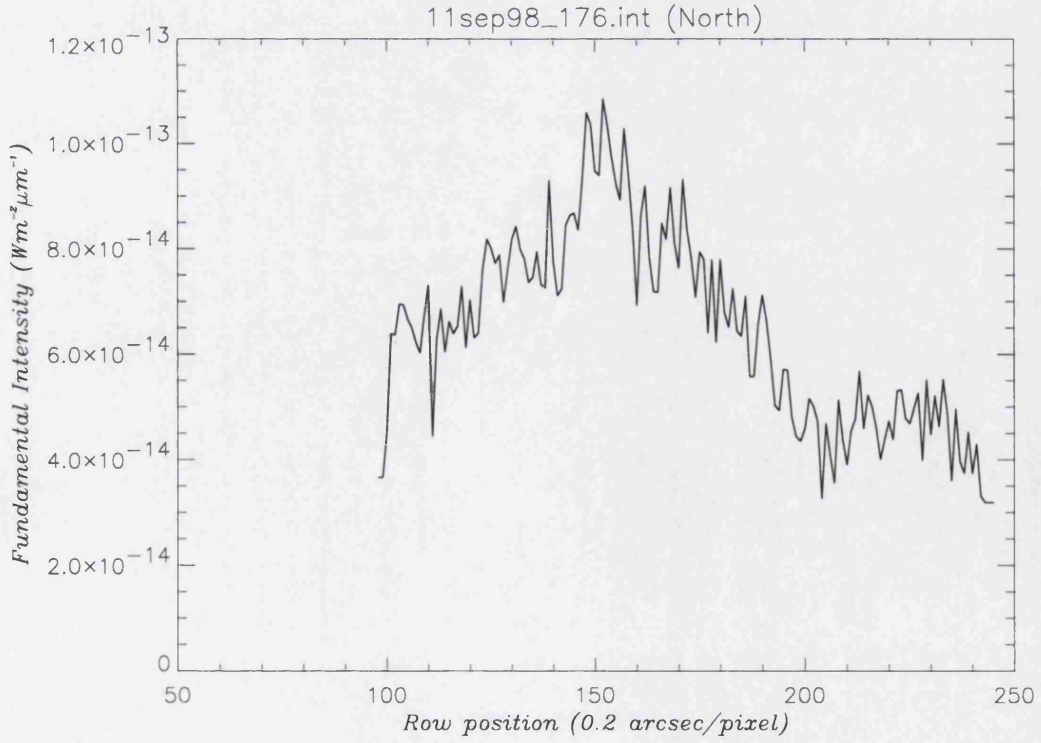

Figure 3-17: The intensity profile, taken at 08:43U.T. with a CML of 165°, from the 11N4 set of spectra

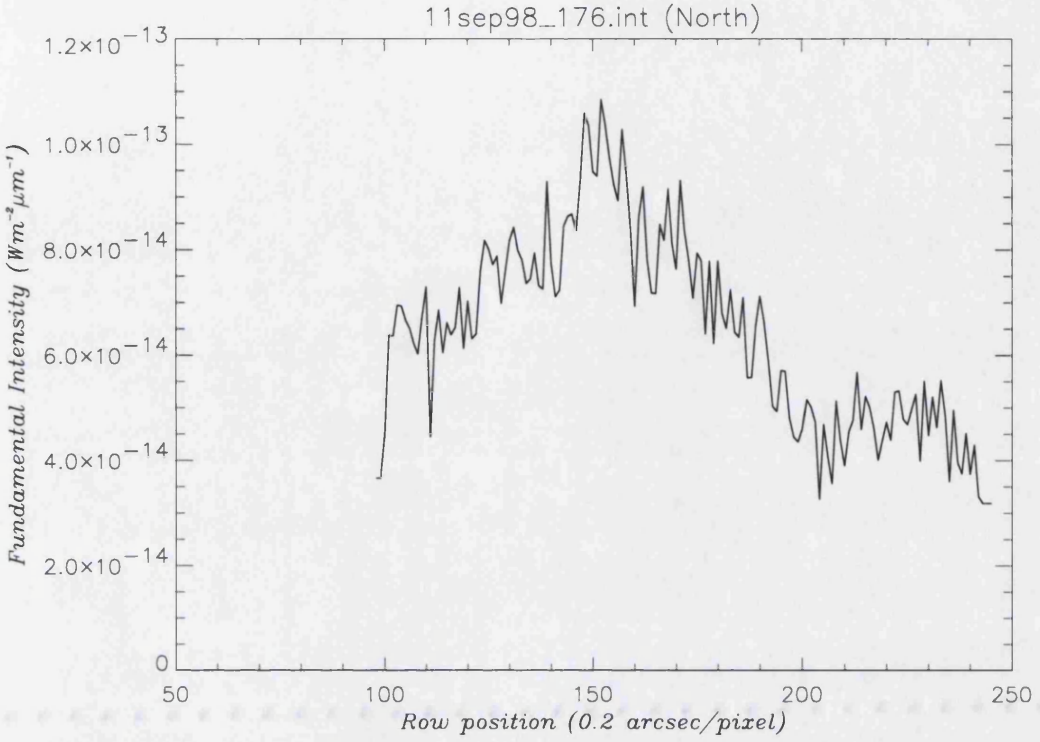

Figure 3-18: The intensity profile, taken at 08:44U.T. with a CML of 166°, from the 11N4 set of spectra

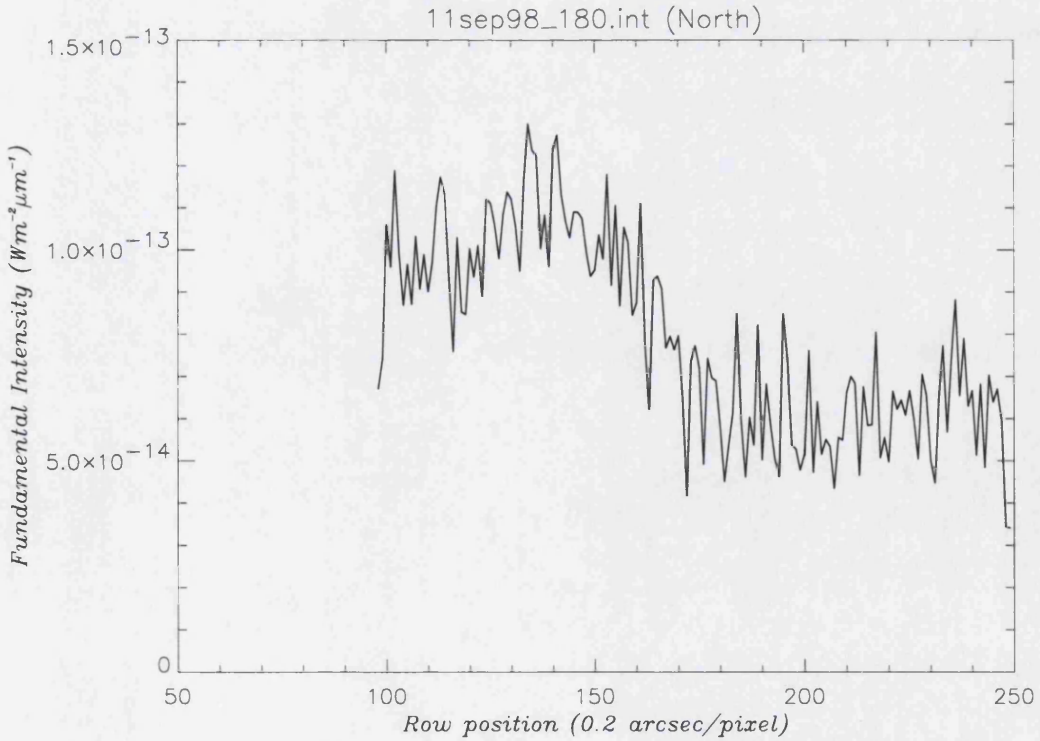

Figure 3-19: The intensity profile, taken at 08:46U.T. with a CML of 167°, from the 11N4 set of spectra

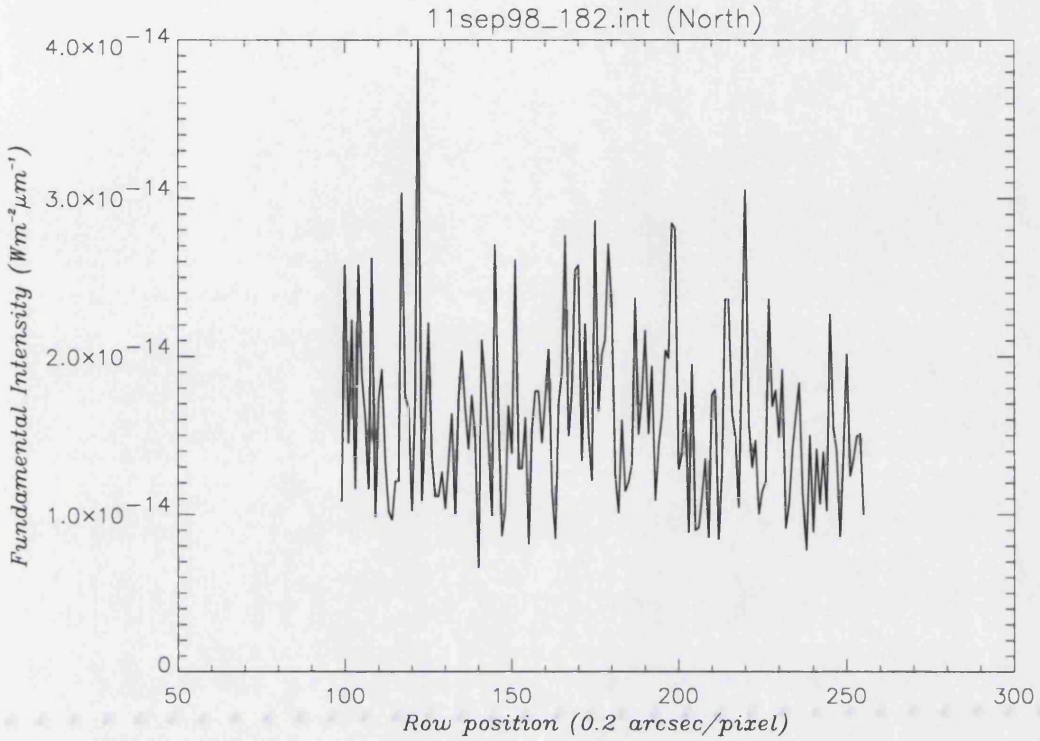

Figure 3-20: The intensity profile, taken at 08:48U.T. with a CML of 168°, from the 11N4 set of spectra

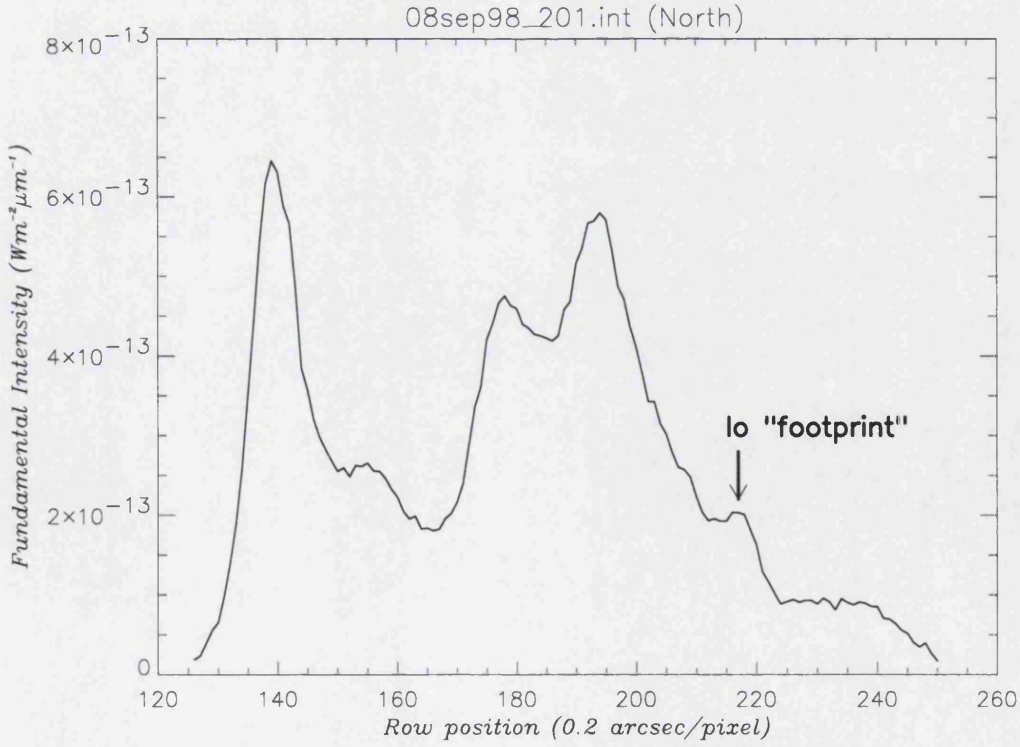

Figure 3-21: The intensity profile which includes an Io footprint trace outside the dusk side of the auroral oval, taken at 10:58U.T. with a CML of 155°, from the 8N5 set of spectra

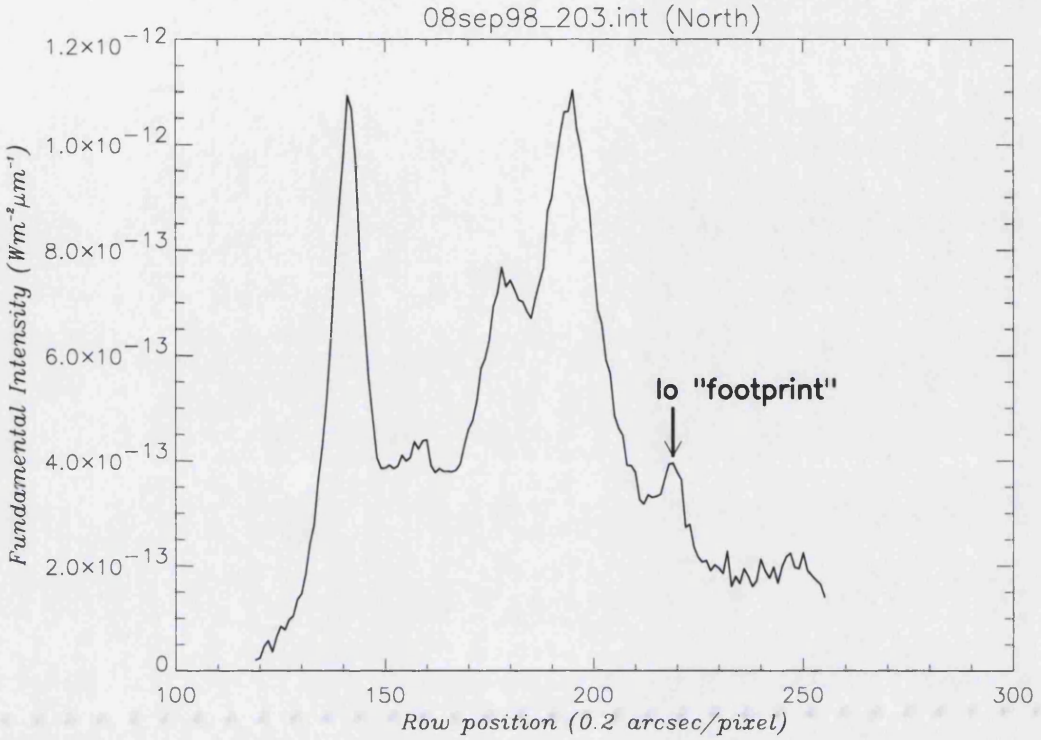

Figure 3-22: The intensity profile which includes a distinct Io footprint outside the dusk side of the auroral oval, taken at 11:00U.T. with a CML of 156°, from the 8N5 set of spectra

3.1.2 Hotband details

The secondary line that we have identified as the $(2\nu_2(0) \rightarrow \nu_2)$ $R(3,4^+)$ hotband, described in **2.4 Secondary Line in the Spectra**, appeared extensively in the auroral regions of Jupiter across all the nights of observation. Only occurring on spectra where the fundamental line is brightest, the hotband was limited solely to the auroral region.

Having identified the hotband as the only plausible cause of the secondary line on the spectral image, the possibility of using it to prove the physical conditions of the aurora was immediately apparent. The comparative properties of the two spectral lines (shown in Table 2-6 on page 94) allowed the direct calculation of the effective vibrational temperature, and hence, assuming quasi-thermal equilibrium, the calculation of the kinetic temperature and both the column density and total emission, as explained in the previous chapter (**2.5.2 Temperature calculation**, **2.6 Column Density** and **2.7 Total Emission**).

3.2 Temperature

In previous observations, the overall temperature of the auroral region has been shown to vary with time, ranging between ~600-1100°K (**1.3.6 Previous measurements of the physical conditions**). The temperature has also been shown to vary across the planet as a whole, with the aurora having a higher temperature than at lower latitudes (apart from a temperature high at the equator). The variation of temperature across the auroral region itself has remained relatively unexplored until now.

The temperatures measured here are the vibrational temperatures, and in order to relate this to the kinetic temperature of neutral atmosphere, the assumption of quasi-thermal equilibrium (QTE) is required (**1.3.3 Local thermal equilibrium**). This demands that even though the ground-state might be overpopulated, the fractional populations of the ($v_2 = 1$) and ($v_2 = 2$) levels can be considered to be populated as might be expected from a Boltzmann distribution at the given kinetic temperature.

If there is a breakdown in this assumption, the non-Boltzmann fractional population of ($v_2 = 1$) and ($v_2 = 2$) becomes significant, as the ($v_2 = 1$) level is appreciably overpopulated, just as the ground state is. This leads to a calculated effective vibrational temperature that under-estimates the kinetic temperature of the atmosphere.

If the fundamental intensity can been shown to directly correlate with energy deposition within the auroral region, comparison between the intensity and the kinetic temperature (assuming QTE) will show the extent to which this energy contribution has caused thermospheric heating. If the temperature profile closely matches the intensity, it will strongly suggest an auroral origin for the majority of the heating.

If the two profiles are dissimilar in parts, these differences can be used to suggest that the underlying temperature of the neutral atmosphere dominates the measured temperature profile, over the heating caused by the energy deposition producing H_3^+. The temperature thus provides a useful tool to uncover physical conditions within the auroral region of the ionosphere.

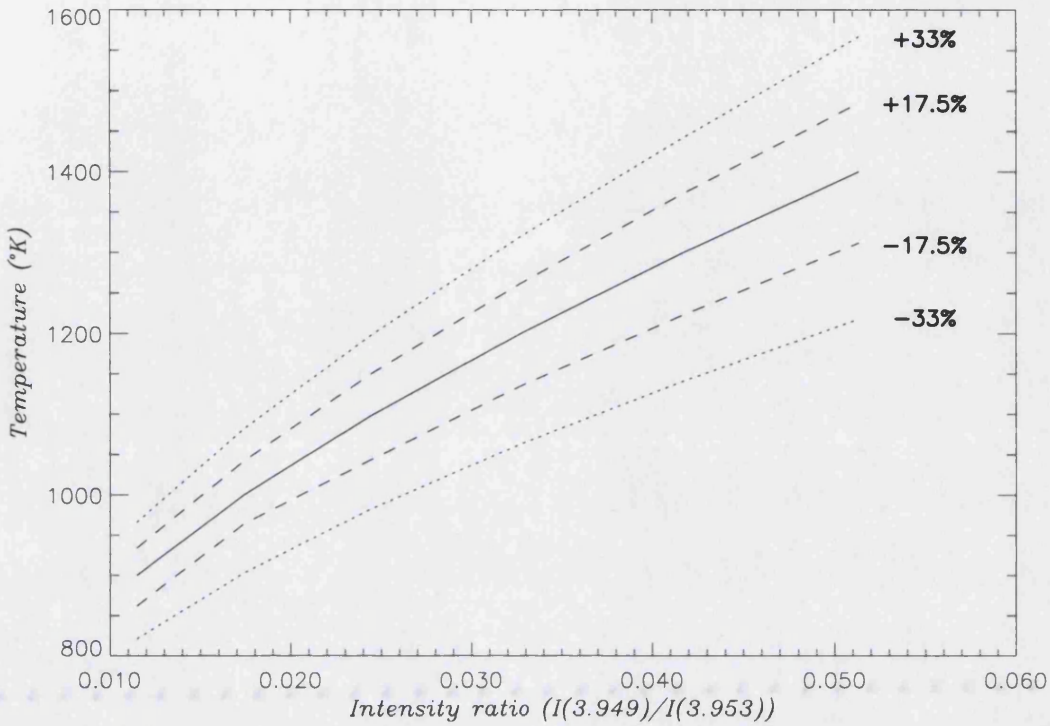

Figure 3-23: The function of temperature with the ratio of the fundamental and hotband intensity; errors of 17.5% and 33% are included for reference

In Figure 3-23, we show the ratio of hotband to fundamental intensity as a function of temperature and the range of errors that result from uncertainties in this ratio of 17.5% and 33%. For our brightest hotband emissions - on the main auroral oval, for example - the lower figure is typical of the uncertainty in this ratio; for the Dark Polar Region, the higher figure represents the outside limit of our uncertainty.

While the pixel-to-pixel variations in temperature are often close to the error limits of the determination of this parameter, the maps and profiles presented show distinct trends over several pixels. These trends show variations that *cannot* be explained solely by errors in the temperature determination process.

3.2.1 Temperature maps

Figure 3-24: The temperature map made using the 8N5 temperature profiles, using a scale ranging from 850°K on the body of the planet to a maximum of 1300°K, which is non-linear to best show the features within the auroral region; for proper values see the profiles, shown below

Figure 3-25: The temperature map made using the 10N5 temperature profiles, using a non-linear scale of 850-1300°K, to best show the features within the auroral region

Figure 3-26: The temperature map made using the 10N6 temperature profiles, using a non-linear scale of 850-1300°K, to best show the features within the auroral region

Figure 3-27: The temperature map made using the 11N4 temperature profiles, using a non-linear scale of 850-1300°K, to best show the features within the auroral region

Maps of the temperature distribution over the auroral region (Figure 3-24 through Figure 3-27), show a complicated structure that only partly correlates with the auroral intensity. In some places the temperatures follow regions of high intensity, but there is a great degree of variation both on and away from the oval.

The 8N5 map (Figure 3-24) is limited in size, because the hotband itself was less bright on that night. Only three spectral images on this particular run contained hotband, so only the brightest fundamental spectra (because of line-of-sight enhancement, those close to the pole) contain a hotband counterpart. This results in only the top half of the auroral

oval being covered by the hotband. However, there is a clear temperature rise close to the auroral region.

The 10N5 (Figure 3-25) map varies in temperature such that the auroral oval is fairly clearly shown as higher in temperature, with a cooler zone in the polar region and outside the aurora. Even on this relatively correlated map, however, the temperature varies considerably, with numerous hot spots. The 10N6 (Figure 3-26) map, taken just 35 minutes later, shows variation in temperature across the auroral region. The temperature appears to be lower on the dusk side of the auroral oval than on the dawn side. The bright polar emission also appears to be relatively hot.

The 11N4 (Figure 3-27) map appears to have a relatively flat temperature distribution, except for hot spots associated with a single spectral profile (Figure 3-37), and an extended region of heating on the eastern limb.

3.2.2 Temperature profiles

Within the maps of temperature distribution, there appears to be only limited correlation of the temperature with the fundamental intensity, and the form the temperature distribution takes appears to vary between the maps. In order to better understand the variations seen, and to better characterise them, it is therefore necessary to look at all of the spectral temperature profiles used in making the maps.

The temperature profiles from different days have been collated so that they appear either in order of position on the planet (from the polar limb, equatorwards), or, where this cannot be clearly determined, in order of CML at the time of exposure. The temperature is plotted against the original fundamental intensity, to show the auroral morphology on any particular profile. It should be noted that temperature profiles were created using a running average of nine pixels (**2.4.4 Hotband Gauss-fitting**), so the relative fundamental intensity would be significantly smoothed over that shown.

Several general trends are evident, which were somewhat obscured at lower latitudes on the map because of the interpolation process. These are associated with the separate

regions already identified in the fundamental intensity profile, as well as one significant variation dependant upon the latitudinal position on the planet.

Spectra on the limb

Temperature variations on the limb differ significantly from spectral profiles located further down on the planet. However, while some show very little variation in temperature across the profile, others have a decrease in temperature towards the Jovian dusk. The temperature seen on the limb, with the exception of one profile (Figure 3-29), with a temperature ~725°K, is within the range of 950-1050°K for all four sequences shown.

Dawn side of the auroral oval

With the exception of a few profiles (Figure 3-39, for example), the fundamental intensity from the dawn half of the auroral oval appears to be universally coincident with an increase in temperature. This increase can sometimes be directly matched by an equivalent temperature peak (Figure 3-40)[1], but is generally spread around the area of the peak intensity, without a pronounced peak (Figure 3-37)[2].

This direct correspondence is a strong indicator that the temperature of the H_3^+ is dominated by the heating caused by auroral energy deposition. The apparent broadening of the temperature peak may be due to localised transferral of heat away from the locality of heating, an issue we will return to in **Chapter 5**.

Dark polar region (DPR)

The reduction in intensity inside the auroral oval often corresponds to a reduction in temperature in the same region. This reduction does not necessarily cover the entire "dark" region, with heated regions often extending in from either side (Figure 3-37)[3], and

[1] a 150°K increase to 1100°K over the adjacent temperature low in the dark polar region

[2] a broad increase of 50°K to 1050°K, covering about 15 pixels or 3" on the planet

[3] about 1" narrowing of the temperature low, compared with the decrease in intensity

the reduction can be minor (Figure 3-45)[4] or sizeable (Figure 3-44)[5]. But the DPR often represents the coolest region in the entire auroral region.

While nearly all the profiles contain cooler areas in the DPR, a significant minority have a combination of cooler and hotter regions (relative to the whole of the aurora). These increases in temperature are usually marked increases, with a strong peak in evidence (Figure 3-42)[6], sometimes being the hottest region in the overall aurora (Figure 3-41)[7]. On careful analysis, the location of these peaks often appears to coincide with minor increases or peaks in the fundamental intensity, though these peaks are not as strong as those seen on the auroral oval.

These peaks can be explained in two ways, in terms of whether or not the assumption of quasi-thermal equilibrium (QTE) still holds.

Given a breakdown in QTE as described in Kim *et al.* (1992), the ($v_2 = 1$) level should be overfilled compared with the ($v_2 = 2$) level, resulting in an underestimation of temperature. The increase in temperature seen in the DPR thus cannot be explained by the more general overfilling of lower energy levels by radiative depopulation, and thus another explanation is required to explain the relative overfilling of higher energy levels. Any non-QTE explanation of this vibrational temperature anomaly needs to account for why such a process appears to dominate the vibrational temperature profile only within certain regions of the DPR, and only on a minority of the spectral profiles.

Assuming that QTE is maintained in the DPR, the general cool trend would indicate lower levels of energy deposition across the whole region, as suggested by the lower fundamental intensities. The sharp increases in temperature could then suggest a localised increase in energy input, leading to increased H_3^+ production. However, the lack of a correspondingly large increase in the fundamental intensity makes this unlikely. The temperature increase is thus more likely to be due to heating of H_3^+ by the surrounding thermosphere, which would require the kinetic temperature to be raised by

[4] a shallow drop of 40-80°K, to 975°K, compared with the temperature of the two sides of the auroral ring
[5] a sharp drop of 200°K, to 825°K, compared with the auroral oval temperatures
[6] a peak temperature of 1030°K, compared with lows on either side of ~950°K
[7] a increase of 250°K over the surrounding dark polar material to 1200°K, compared with an auroral oval temperature of 1050°K

more than just the heating associated with the local aurora. One potential source of this increase could be heat transport within the DPR, though the temperature increase seen is such that the transport process would have to be a significant factor within the aurora. Alternatively, the H_3^+ may have been produced at a higher altitude, since kinetic temperature increases with altitude in the 1-10mbar region.

Bright polar region (BPR)

Generally speaking, the bright polar emission is relatively high in temperature (Figure 3-37)[8]. This temperature is normally not the highest seen within a profile; it is a broad region which is moderately hotter than the average across the aurora. This suggests that this higher temperature is caused by a higher level of energy deposition in the region, associated with the increase in fundamental intensity.

Notable exceptions to this are evident, however, with both high temperature (Figure 3-33)[9] and at least partly cooled regions (Figure 3-36)[10], but these are exceptional. These aberrations could be indicative of a localised breakdown in QTE, or if the assumption of QTE is maintained, through localised transport with neighbouring regions or increases in the local energy input, as seen in the DPR and the dusk side of the auroral oval for increases and decreases in temperature respectively.

Dusk side of the auroral oval

On the majority of the spectral profiles, the region crossed by the dusk side of the auroral limb coincides with cooler temperatures. This drop in temperature varies between a gradual decline in temperature relative to the neighbouring BPR (Figure 3-43)[11] to a sharp temperature trough that is directly coincident with the intensity peak (Figure 3-38)[12].

Nonetheless, there are examples of the auroral oval showing no overall variation from the BPR (Figure 3-40)[13] and even a corresponding hot peak that matches the fundamental

[8] at 1100°K, compared to a peak oval temperature of 1125°K, and a dark polar temperature of 975°K
[9] at 1025°K, about 75°K above the rest of the aurora
[10] about the same temperature as the adjacent dark polar emission, at 1000°K
[11] a decrease from 1000°K to 950°K over 10 pixels, or 2" on the planet
[12] a drop of ~100°K to 900°K, from the surrounding aurora
[13] at 1050°K

peak directly (Figure 3-37)[14]. These latter are much easier to explain than the normal situation, as heating from locally enhanced auroral energy deposition.

However, the majority of the spectral profiles appear to have cooler material in the very region whence the highest H_3^+ emission originates. Since there is a direct anti-correlation between the fundamental intensity and the temperature only within this specific region of the aurora, it suggests that the cause of the apparent temperature drop, whether from a thermal effect or a break with QTE, could well be derived from the conditions within the dusk oval.

An apparent temperature drop could easily be caused by a breakdown in the assumption of QTE, as detailed by Kim *et al.* (1992). Radiative depopulation from higher energy levels leads to an overpopulation of the lower energy levels, which in turn results in an underestimation of the temperature. However, the lack of this effect within the adjacent BPR, as well as the dawn oval, requires that the effect of depopulation is amplified significantly in the dusk oval particularly. This could have been caused by a decrease in the collision rate, thus reducing the excitation that maintains QTE, potentially the product of particle precipitation into a higher altitude, resulting in H_3^+ production within a lower density neutral atmosphere.

If QTE is considered to remain as a reasonable assumption, this temperature anomaly suggests significant variation in the auroral conditions in the region of H_3^+ production. One possibility is that the location of particle precipitation is incident with a cooler surrounding neutral atmosphere, which results in the recently formed H_3^+ being comparatively cooler. This would be the case if the production were occurring deeper into the atmosphere than in the dawn side auroral oval and creating H_3^+ in denser and cooler conditions. An alternative cause of a significantly cooler neutral atmosphere might be through the transport of neutrals either in a neutral wind, or entrained in an ion flow. Once more, we come back to these issues in **Chapter 5**.

[14] a peak of 1120°K, 75°K above the corresponding dawn limb

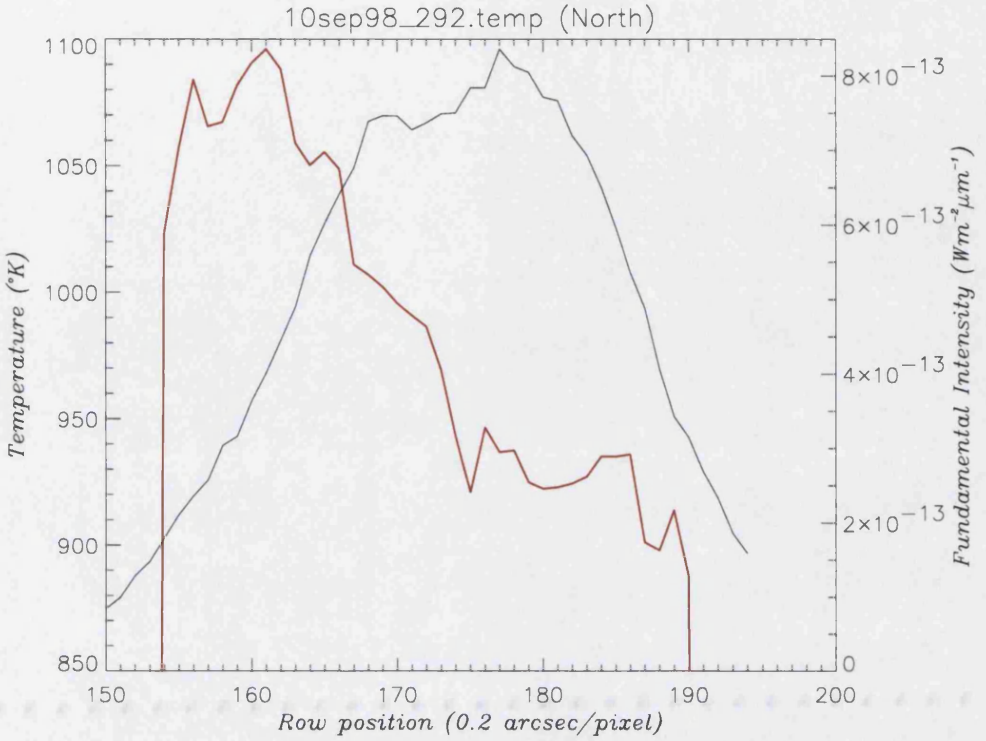

Figure 3-28: The temperature profile (red) plotted with the fundamental intensity profile, taken at 12:22U.T. with a CML of 147°, from the 10N5 set of spectra

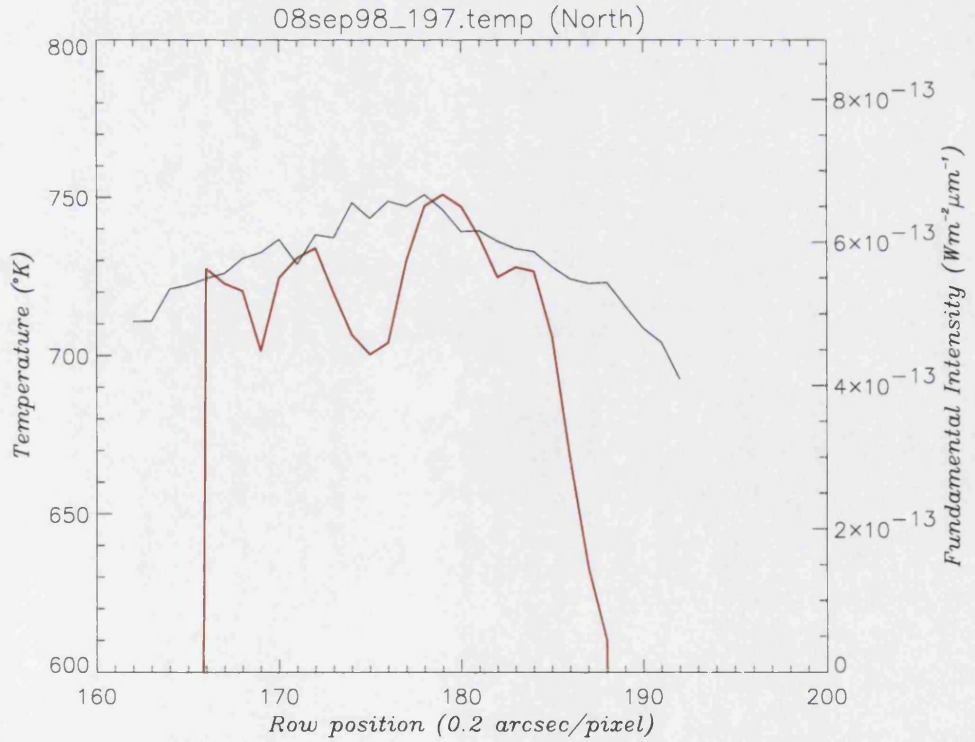

Figure 3-29: The temperature profile (red) plotted with the fundamental intensity profile, taken at 10:54U.T. with a CML of 152°, from the 8N5 set of spectra

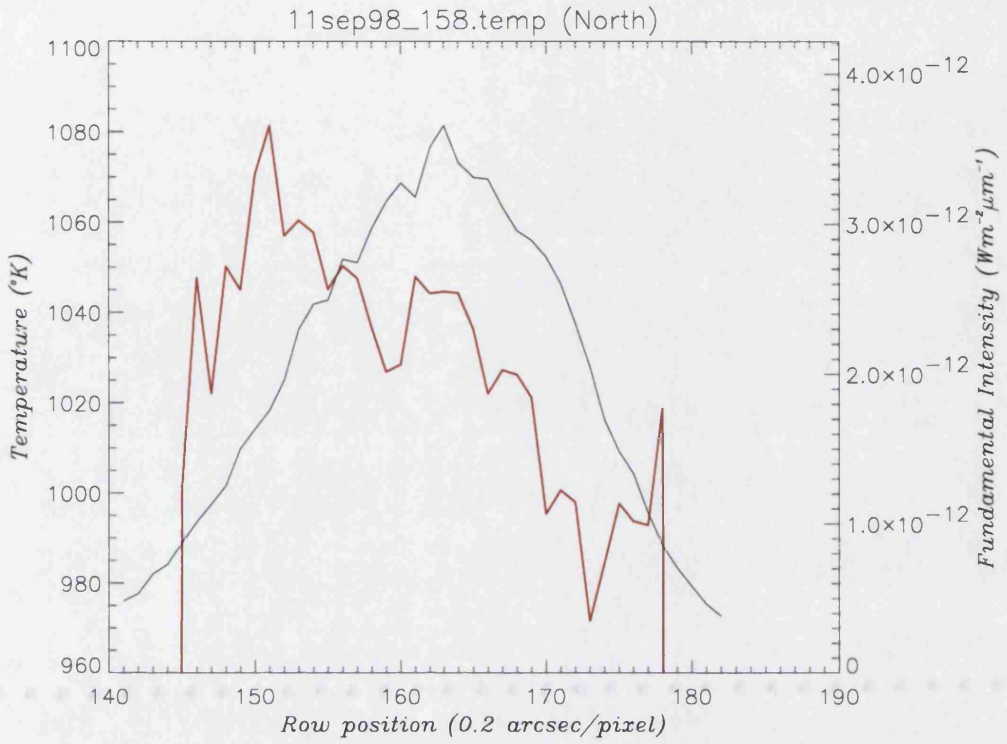

Figure 3-30: The temperature profile (red) plotted with the fundamental intensity profile, taken at 08:27U.T. with a CML of 155°, from the 11N4 set of spectra

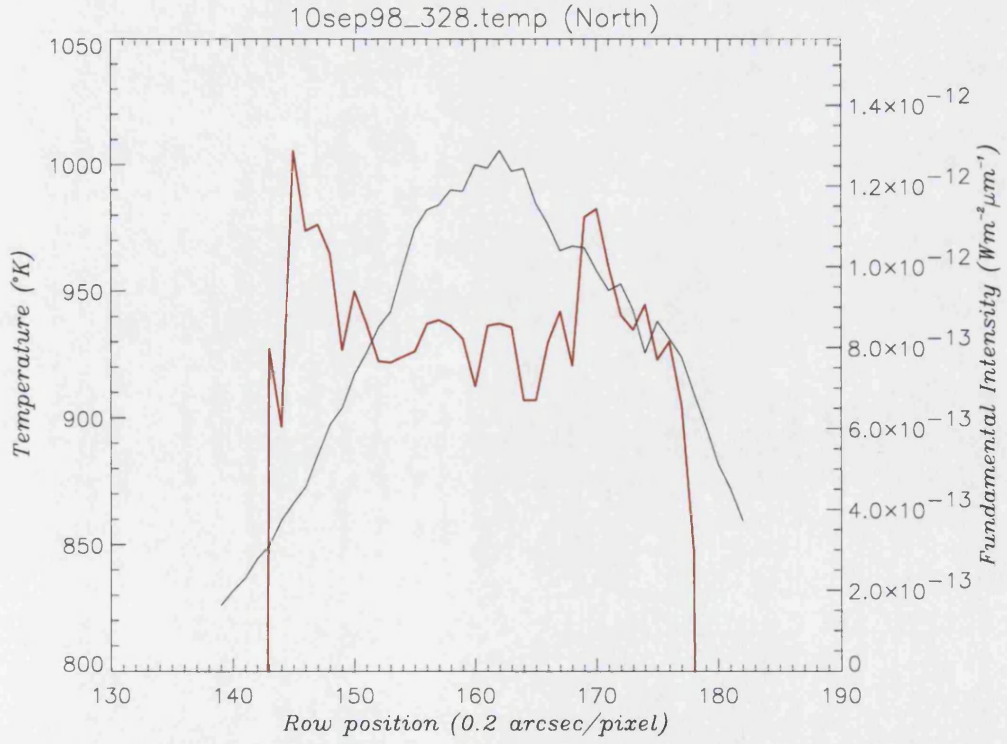

Figure 3-31: The temperature profile (red) plotted with the fundamental intensity profile, taken at 12:58U.T. with a CML of 169°, from the 10N6 set of spectra

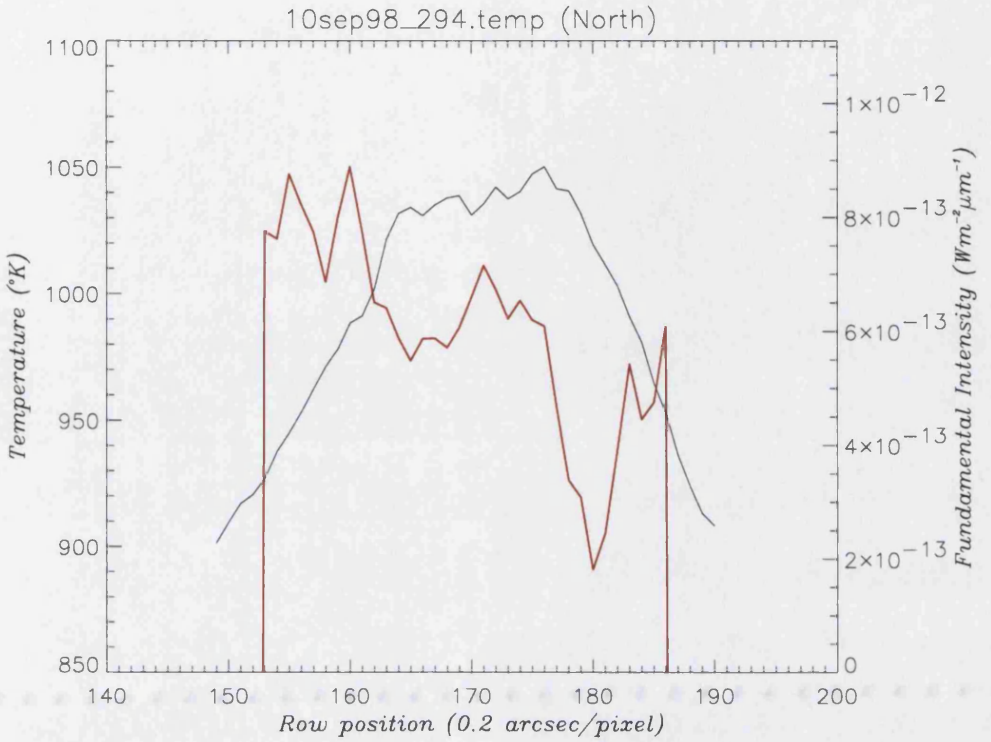

Figure 3-32: The temperature profile (red) plotted with the fundamental intensity profile, taken at 12:24U.T. with a CML of 148°, from the 10N5 set of spectra

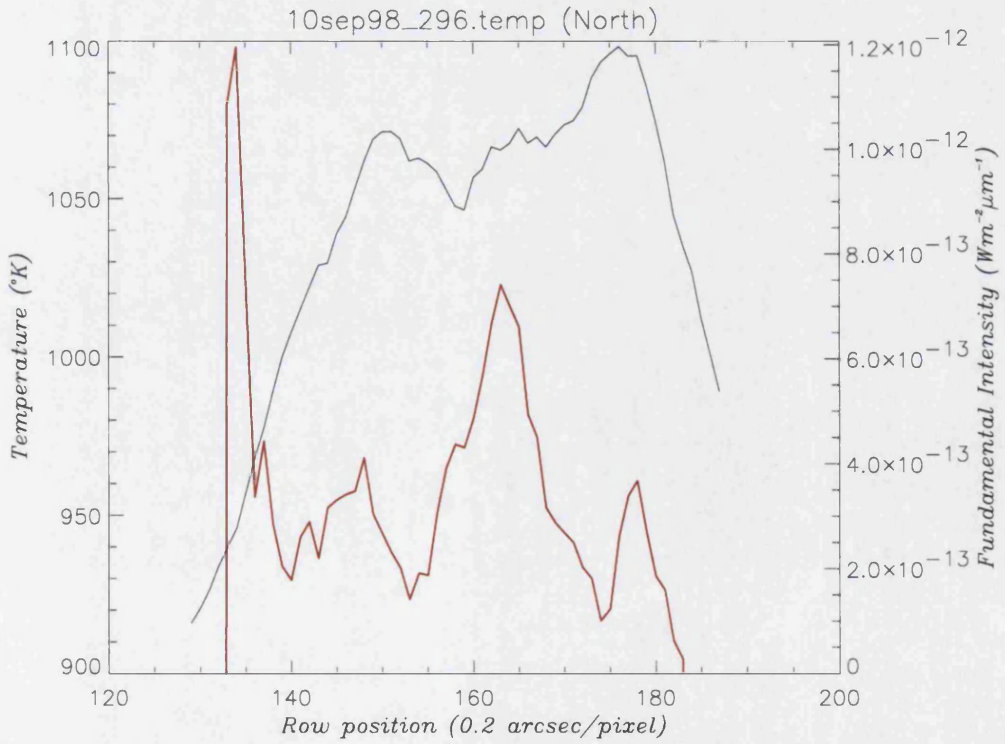

Figure 3-33: The temperature profile (red) plotted with the fundamental intensity profile, taken at 12:26U.T. with a CML of 149°, from the 10N5 set of spectra

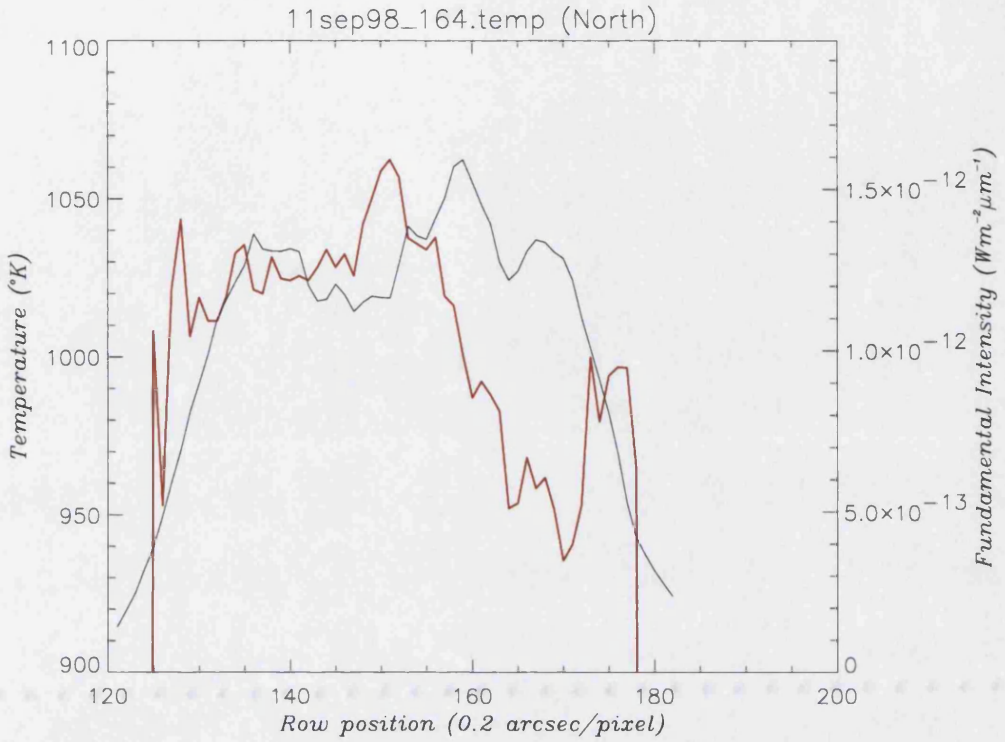

Figure 3-34: The temperature profile (red) plotted with the fundamental intensity profile, taken at 08:32U.T. with a CML of 158°, from the 11N4 set of spectra

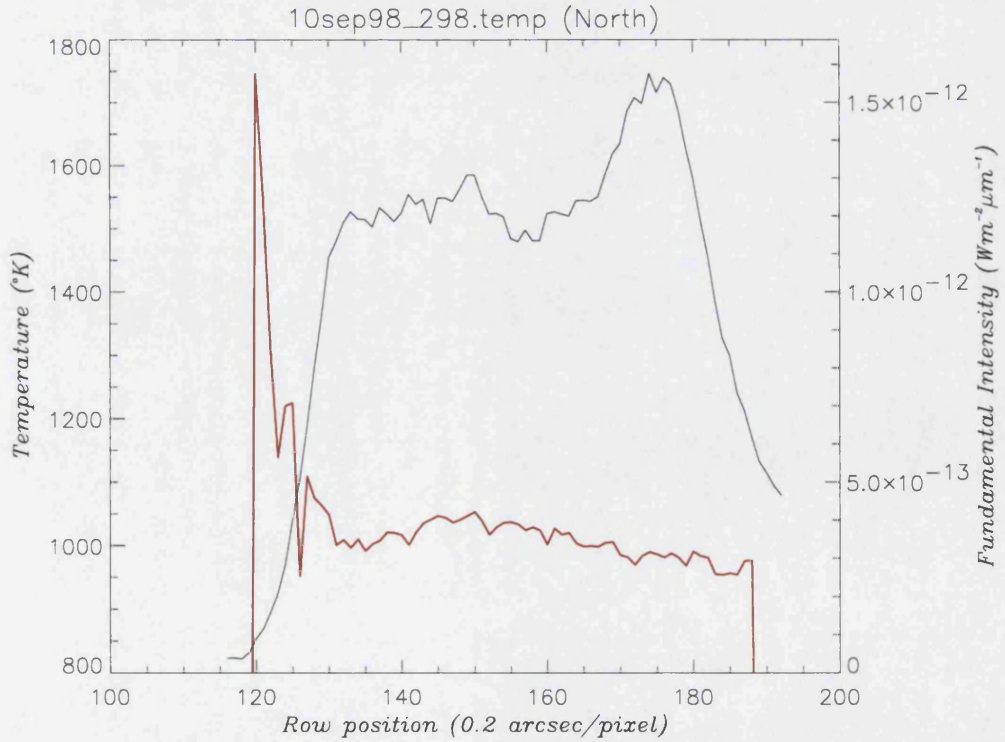

Figure 3-35: The temperature profile (red) plotted with the fundamental intensity profile, taken at 12:28U.T. with a CML of 150°, from the 10N5 set of spectra

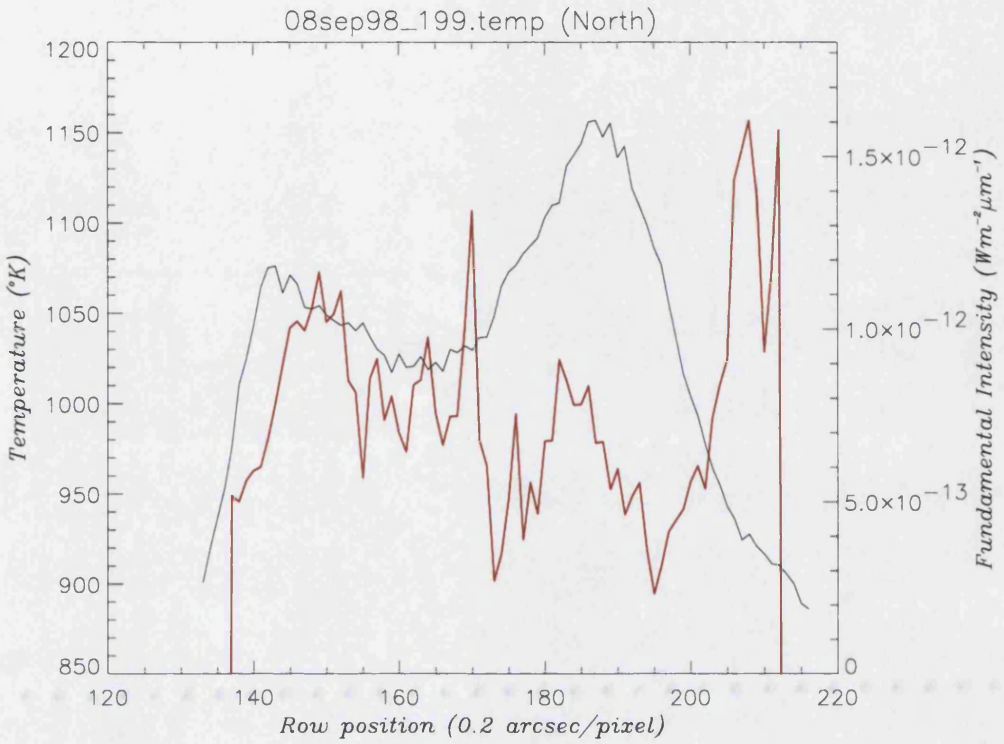

Figure 3-36: The temperature profile (red) plotted with the fundamental intensity profile, taken at 10:56U.T. with a CML of 153°, from the 8N5 set of spectra

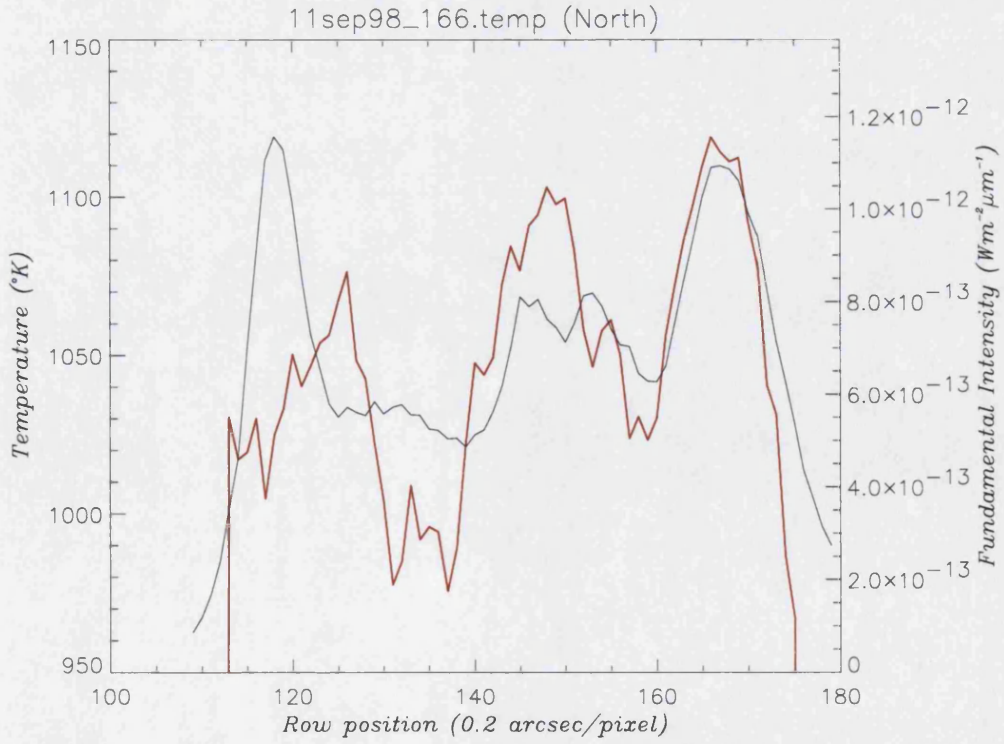

Figure 3-37: The temperature profile (red) plotted with the fundamental intensity profile, taken at 08:34U.T. with a CML of 159°, from the 11N4 set of spectra

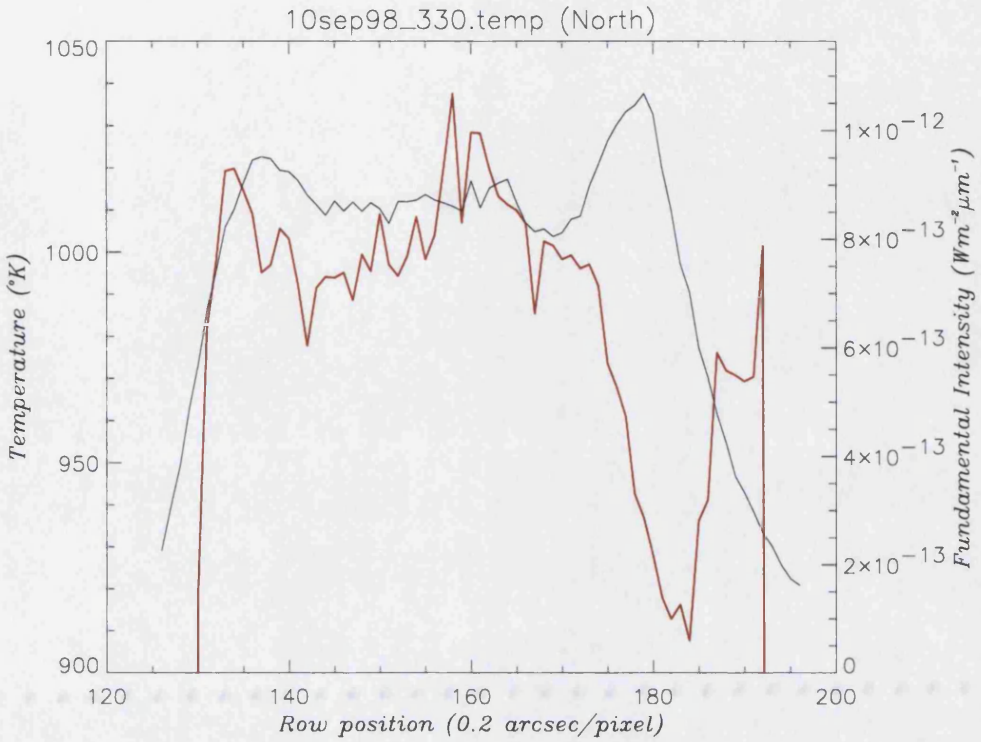

Figure 3-38: The temperature profile (red) plotted with the fundamental intensity profile, taken at 13:00U.T. with a CML of 170°, from the 10N6 set of spectra

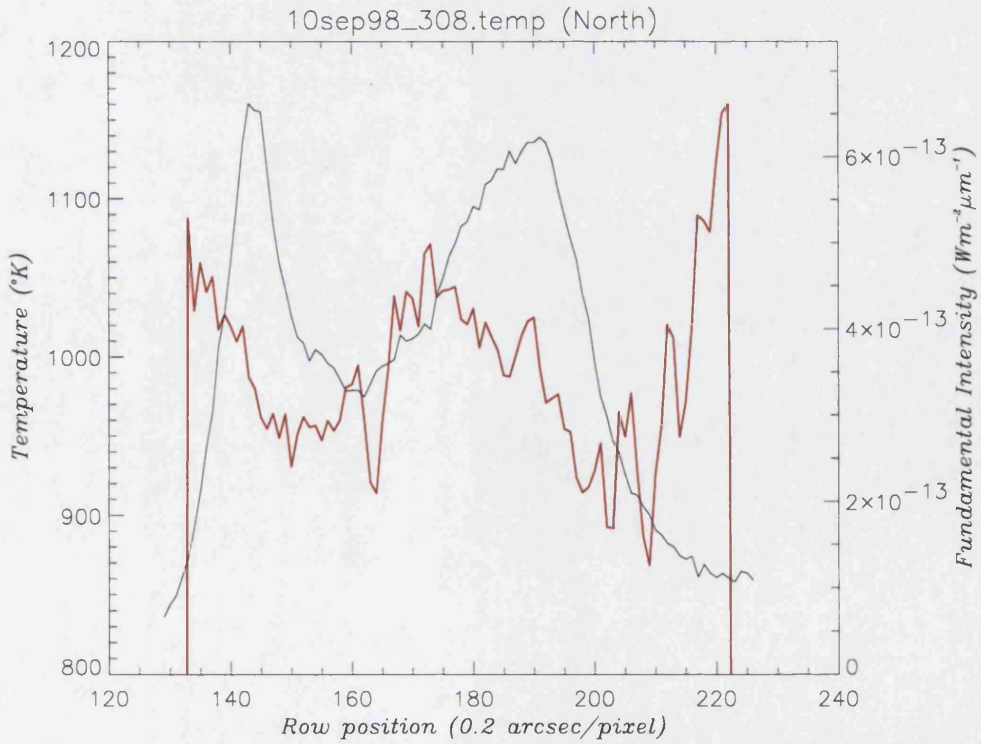

Figure 3-39: The temperature profile (red) plotted with the fundamental intensity profile, taken at 12:38U.T. with a CML of 156°, from the 10N5 set of spectra

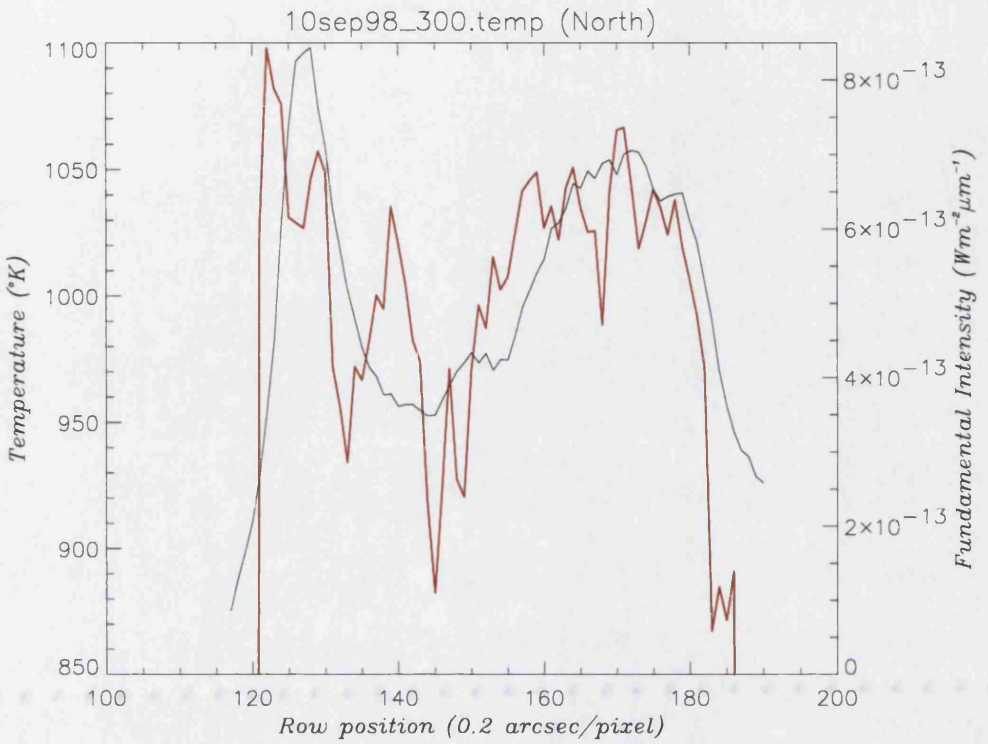

Figure 3-40: The temperature profile (red) plotted with the fundamental intensity profile, taken at 12:30U.T. with a CML of 151°, from the 10N5 set of spectra

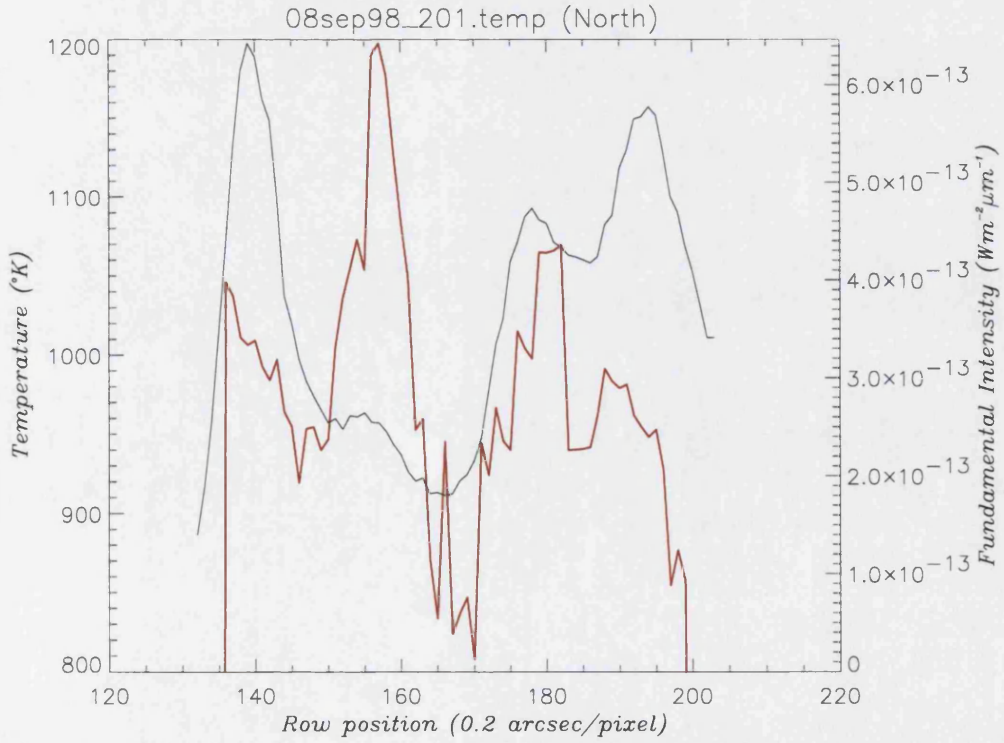

Figure 3-41: The temperature profile (red) plotted with the fundamental intensity profile, taken at 10:58U.T. with a CML of 155°, from the 8N5 set of spectra

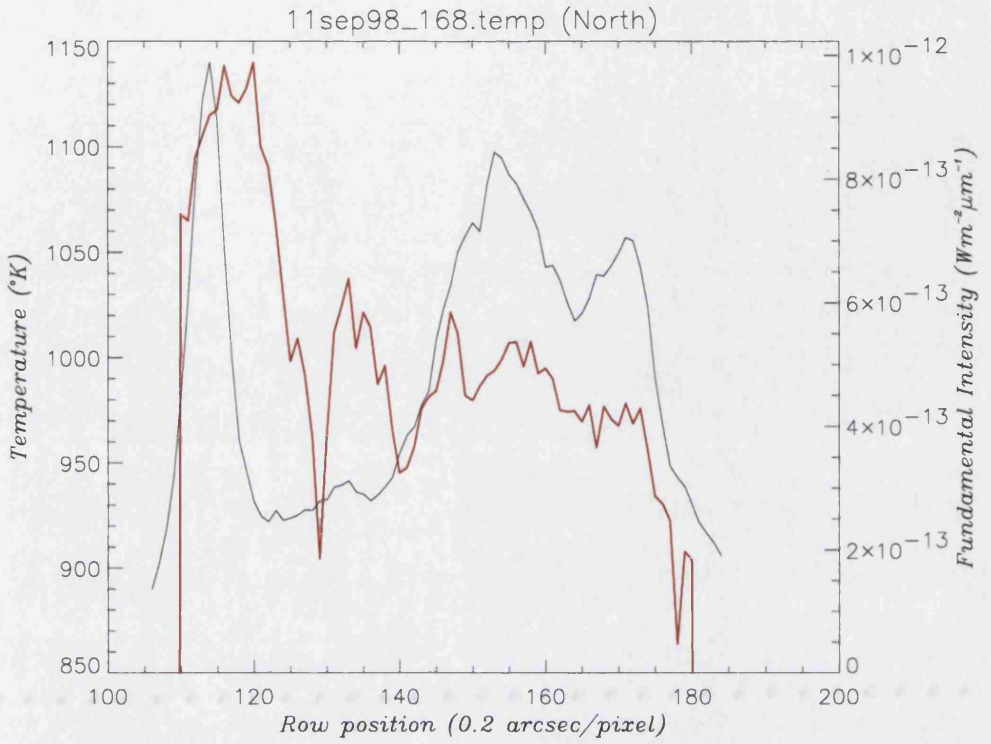

Figure 3-42: The temperature profile (red) plotted with the fundamental intensity profile, taken at 08:35U.T. with a CML of 160°, from the 11N4 set of spectra

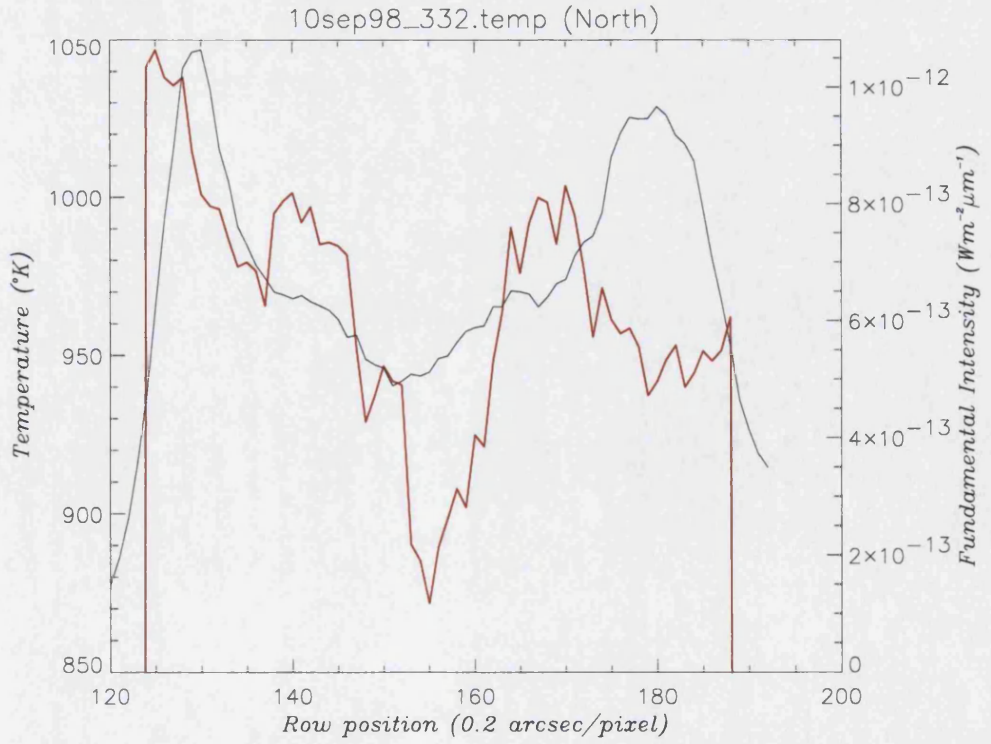

Figure 3-43: The temperature profile (red) plotted with the fundamental intensity profile, taken at 13:02U.T. with a CML of 171°, from the 10N6 set of spectra

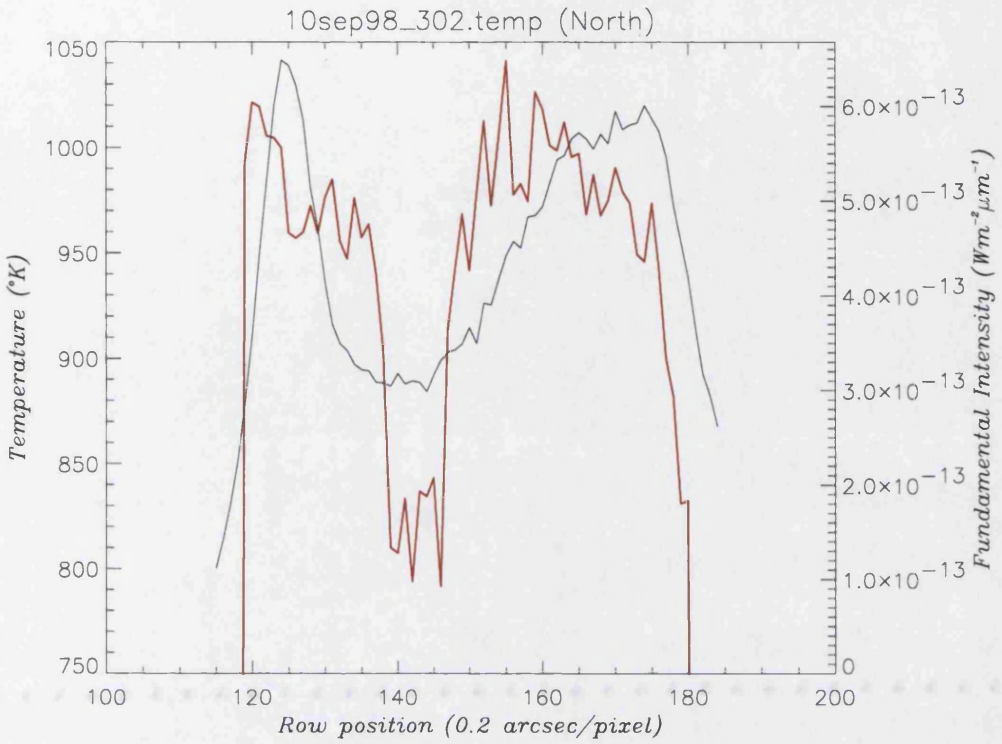

Figure 3-44: The temperature profile (red) plotted with the fundamental intensity profile, taken at 12:32U.T. with a CML of 153°, from the 10N5 set of spectra

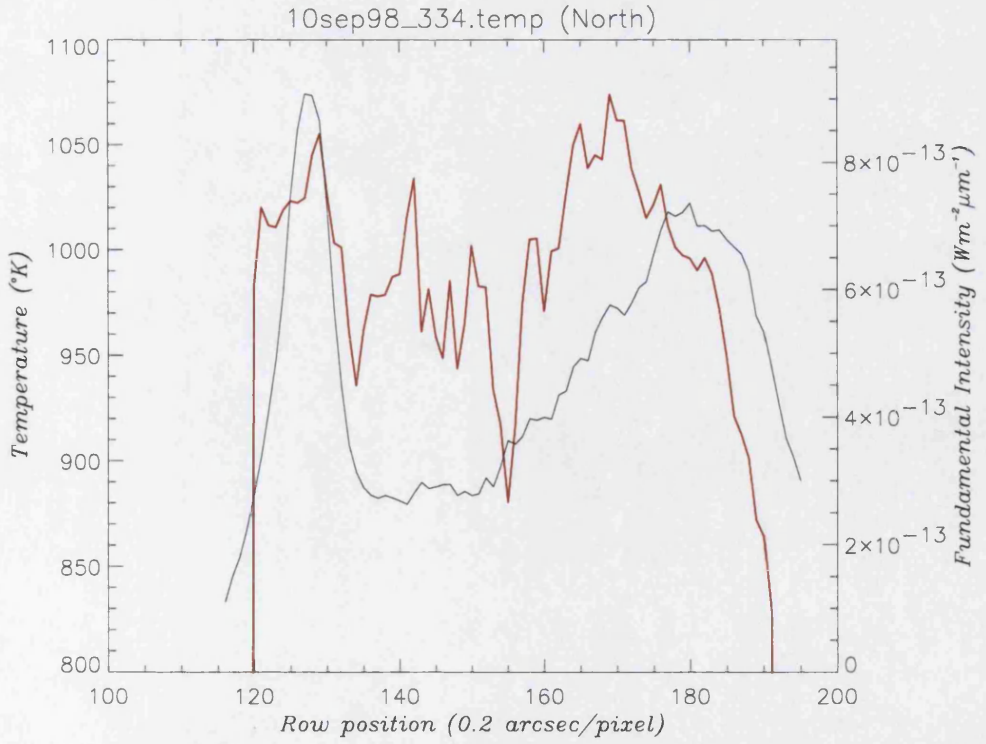

Figure 3-45: The temperature profile (red) plotted with the fundamental intensity profile, taken at 13:04U.T. with a CML of 172°, from the 10N6 set of spectra

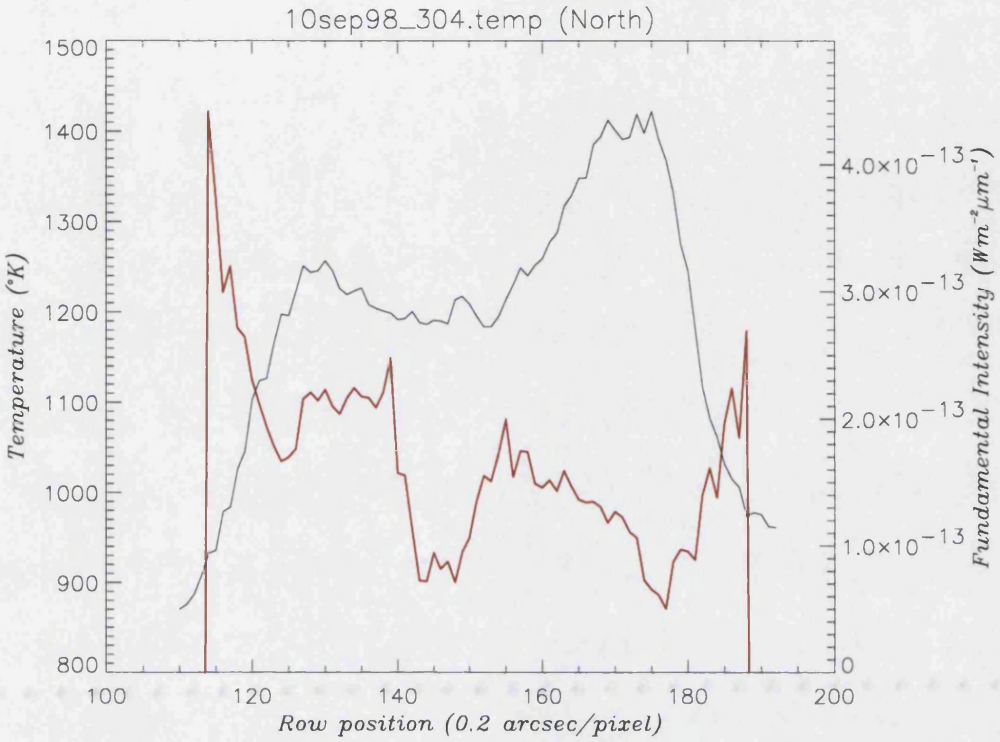

Figure 3-46: The temperature profile (red) plotted with the fundamental intensity profile, taken at 12:34U.T. with a CML of 154°, from the 10N5 set of spectra

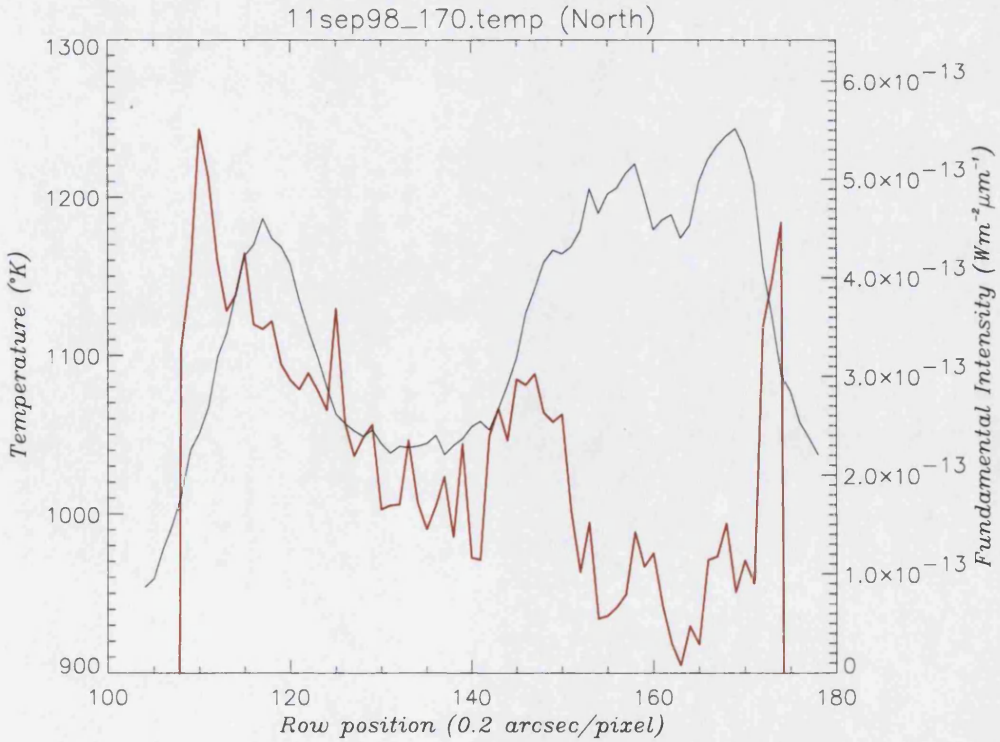

Figure 3-47: The temperature profile (red) plotted with the fundamental intensity profile, taken at 08:37U.T. with a CML of 161°, from the 11N4 set of spectra

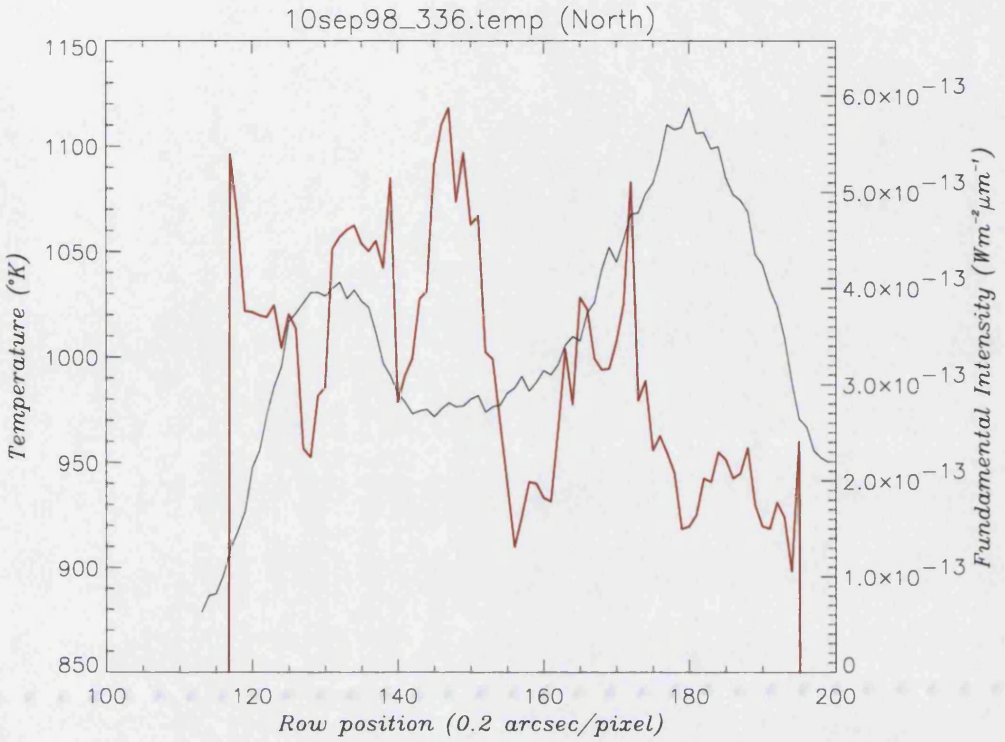

Figure 3-48: The temperature profile (red) plotted with the fundamental intensity profile, taken at 13:06U.T. with a CML of 173°, from the 10N6 set of spectra

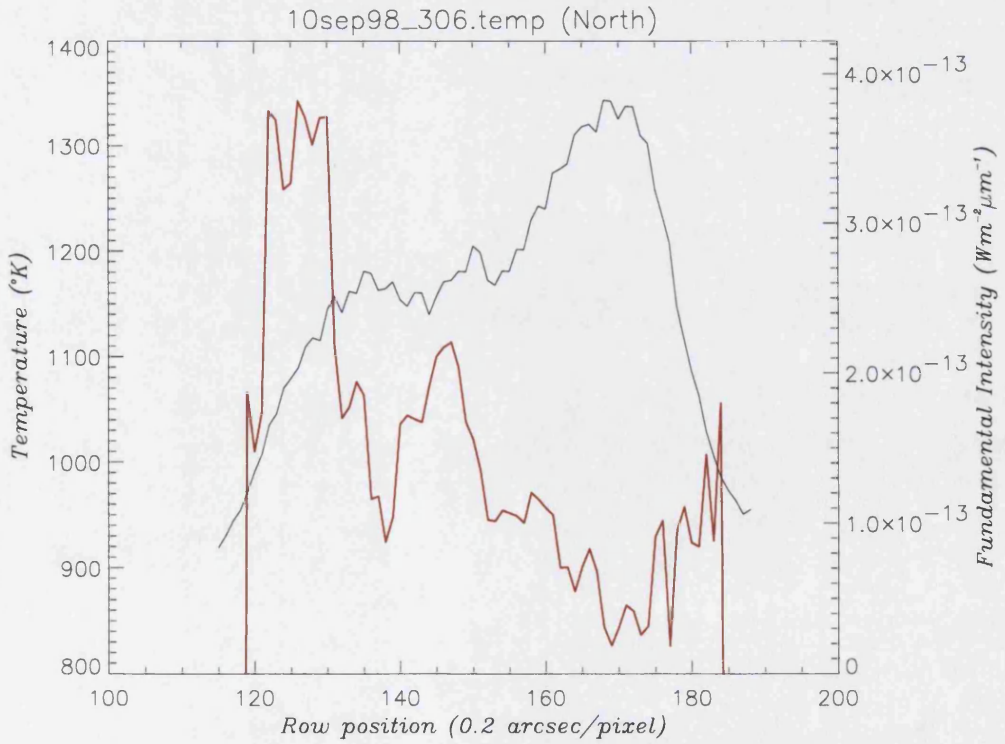

Figure 3-49: The temperature profile (red) plotted with the fundamental intensity profile, taken at 12:36U.T. with a CML of 155°, from the 10N5 set of spectra

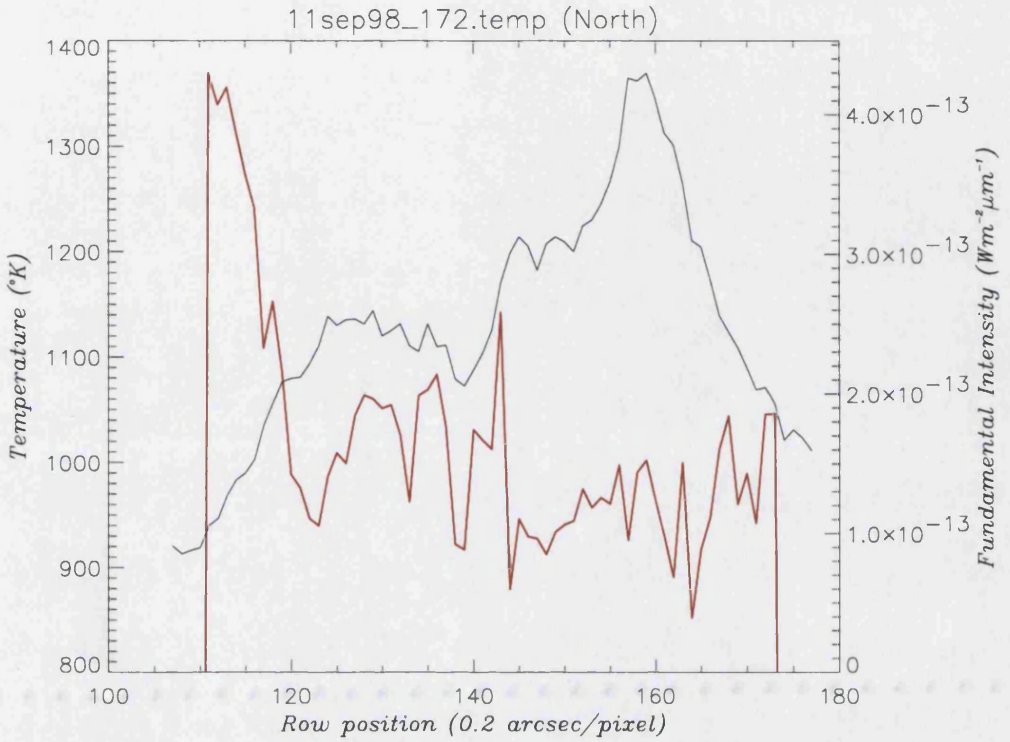

Figure 3-50: The temperature profile (red) plotted with the fundamental intensity profile, taken at 08:37U.T. with a CML of 161°, from the 11N4 set of spectra

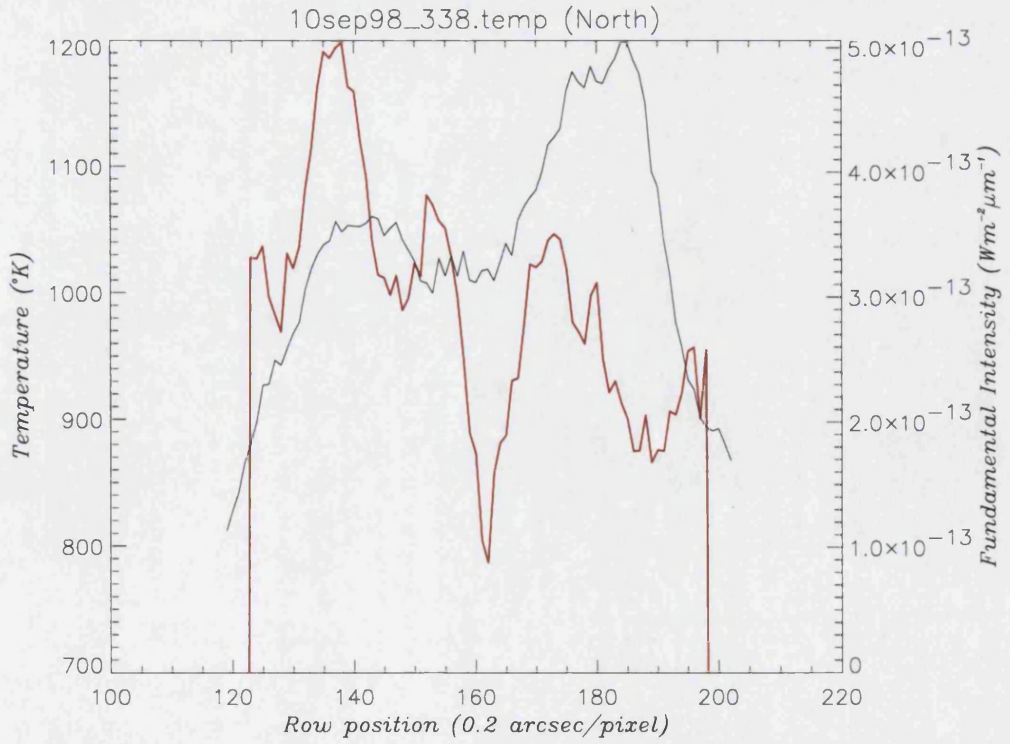

Figure 3-51: The temperature profile (red) plotted with the fundamental intensity profile, taken at 13:08U.T. with a CML of 174°, from the 10N6 set of spectra

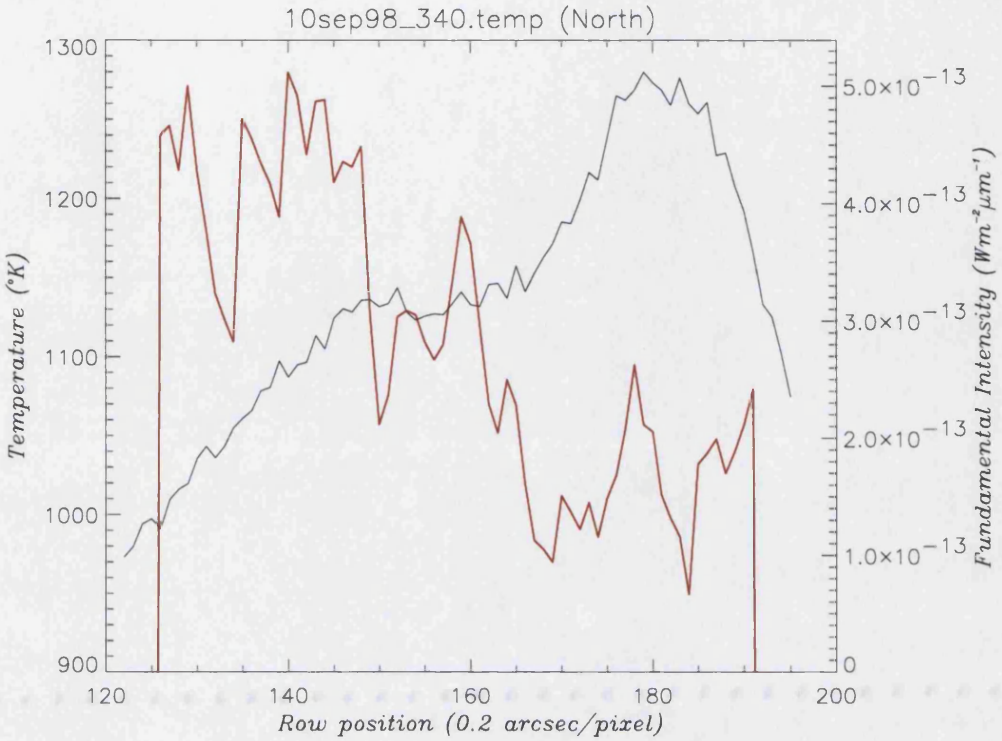

Figure 3-52: The temperature profile (red) plotted with the fundamental intensity profile, taken at 13:10U.T. with a CML of 176°, from the 10N6 set of spectra

3.2.3 Average temperatures

The average vibrational temperatures, described in **2.5.2 Average spectral temperature**, have been produced to detect any systematic variation with planetary CML or with day-to-day variations.

Assuming that the assumption of QTE holds, and that effective vibrational temperature is analogous with kinetic temperature, the variations in the average temperatures are attributable to the physical conditions across the auroral oval and polar cap region. Each spectral image in any given sequence was taken at a separate latitude from the others in that sequence. The analysis of time and CML variations should thus take into consideration the change in temperature with varying latitude.

The variation in temperature with time is shown in Figure 3-53. While average temperatures vary considerably over the spectra measured from the first three nights, there is a general trend of increasing temperature towards the end of our observing run.

Between the 9th and the 11th there is an increase of at least 100°K, resulting in a temperature high in the range of 1050-1100°K. In addition to this night-by-night increase, the night of the 10th shows an apparent increase in temperature throughout the night itself, resulting in a rise from ~1000°K to ~1050°K.

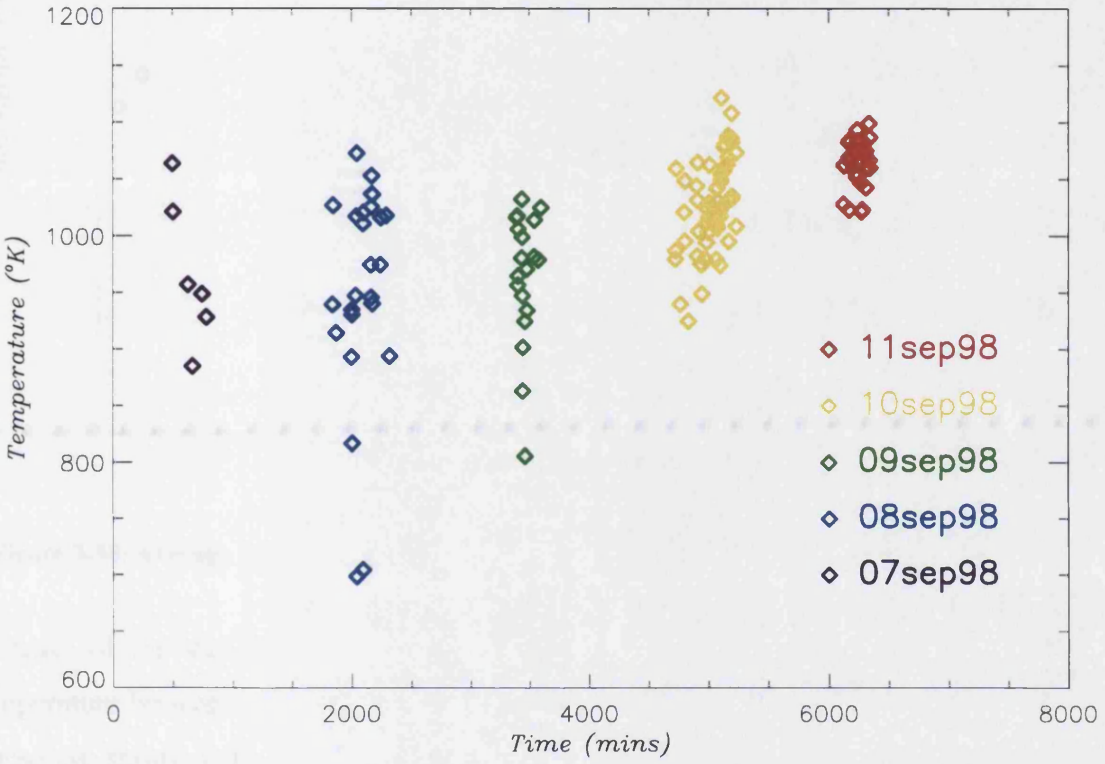

Figure 3-53: Average temperature for each spectral image, plotted against the time from 0:00hrs U.T. on 7th Sept, 1998.

The variation of temperature with CML is shown in Figure 3-54. The temperature shows no significant variation with CML across the range where the aurora is fully displayed (~120°-220°). As the amount of aurora displayed decreases, the resulting temperature decreases slightly, as do the number of available spectral images with a hotband signature. However, this variation is not beyond the range of values found within spectral sequences taken with the aurora fully displayed, and is thus not significant. The increase in temperature over the last two nights can be clearly identified, with identical CMLs being hotter on the 10th and 11th than on the previous three nights.

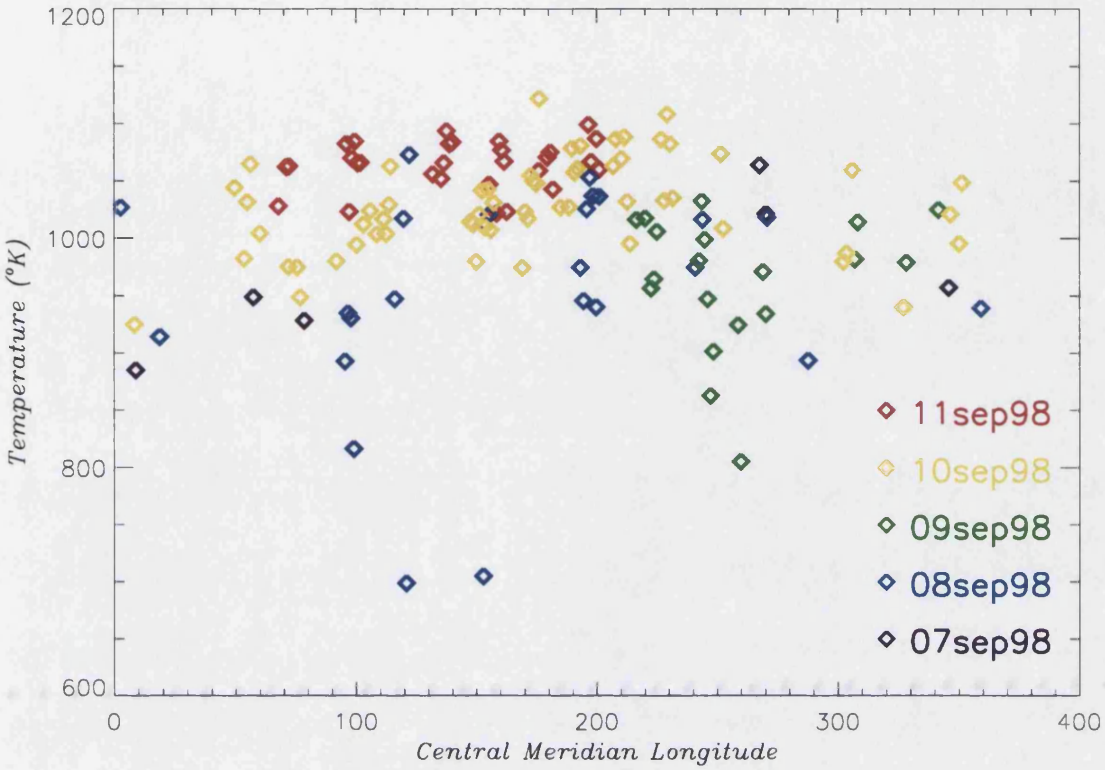

Figure 3-54: Average temperature for each spectral image, plotted against the CML at the time of observation

Because of the variation within the data, a more direct indicator of the variation in temperature between each night is the average temperature of *all* the spectra in each day. These are shown below, with the integrated signal-to-noise values calculated, assuming temperature is independent on a point-to-point basis, using:

$$\int (S/N) = \left(\frac{\text{mean}\,(S/N)}{\sqrt{\text{no. of spectra}}} \right)$$

Table 3-2: The average temperature across each night

Night	Average Temp	Integrated Hotband S/N
07th Sept '98	981	38
08th Sept '98	940	65
09th Sept '98	973	45
10th Sept '98	1021	102
11th Sept '98	1065	78

These temperatures show very clearly the steady increase in temperature over the final two nights. These temperatures are comparable with those shown in earlier publications, although they are all towards the high end of the range of temperatures seen before. The increase in temperatures across the last two nights stretches this towards the very highest previous recorded temperatures, which are ~1100°K recorded in Drossart *et al.* (1989). That the aurora can be considered "hot" in these observations is consistent with the lack of hotband spectral lines in any previous observations (see **3.1.2 Hotband details**).

3.3 H_3^+ Column Density and Production

Studies of H_3^+ play an important role in the understanding of the Jovian system as a result of the sensitivity of this ion to energy deposition into the ionosphere. There has often been a tacit assumption of a one-to-one correlation between the emission intensity and the location of energy deposition within previous research (*e.g.*, Satoh and Connerney, 1999).

Although this assumption may be a good one for the auroral region as a whole, it has never been tested using both a spatial and spectral resolution high enough to see local variations within the aurora itself.

Assuming that quasi-thermal equilibrium (QTE) holds, a truer measure of H_3^+ production, and thus energy deposition, is the measured H_3^+ column density, for the following reasons. The average molecular lifetime of H_3^+ is ~10 seconds (**1.2.1 The H3+ lifecycle**), so assuming a maximum thermal velocity in the atmosphere of 2.5 km/s, the maximum distance that H_3^+ can travel before destruction is only 25 km, a fraction of the minimum pixel size (at the equator) of 575 km used in this study.

This means the H_3^+ column density of any particular pixel will always have an almost one-to-one correlation with the extent of H_3^+ production. The assumption that H_3^+ emission represents energy deposition in the aurora thus requires there to be a direct correlation between H_3^+ column density and H_3^+ emission intensity. If the assumption does not hold, then only the column density can provide information on energy deposition into the aurora.

The calculation of column density is described in **2.6 Column Density**. Previous observations, looking at a general auroral column density, have produced values in the range of $1\text{-}10\times10^{16}m^{-2}$. Consistent with these values, our data produce values in the range of $0.5\text{-}1.5\times10^{16}$, for the auroral oval, and $0.4\text{-}0.8\times10^{16}$, for the polar cap regions.

3.3.1 Column density maps

Figure 3-55: The column density map made using the 8N5 line-of-sight corrected column density profiles, using a non-linear scale of $0\text{-}2.4\times10^{16}$ m^{-2}, to best show the features within the auroral region; for proper values see the profiles, shown below

Figure 3-56: The column density map made using the 10N5 line-of-sight corrected column density profiles, using a non-linear scale of $0\text{-}2.55\times10^{16}$ m^{-2}, to best show the features within the auroral region

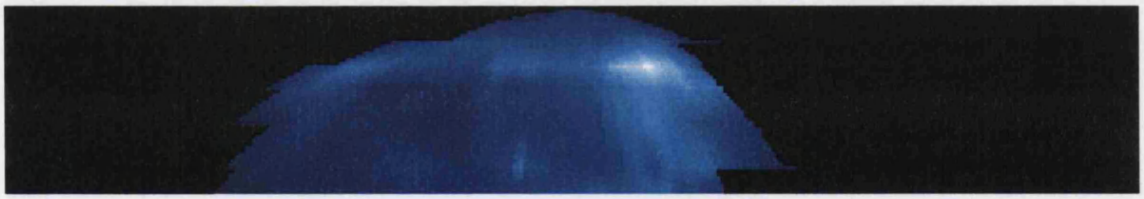

Figure 3-57: The column density map made using the 10N6 line-of-sight corrected column density profiles, using a non-linear scale of $0\text{-}1.55\times10^{16}$ m^{-2}, to best show the features within the auroral region

Figure 3-58: The column density map made using the 11N4 line-of-sight corrected column density profiles, using a non-linear scale of $0\text{-}1.45\times10^{16}$ m^{-2}, to best show the features within the auroral region

We have produced line-of-sight maps of the column density for the four sets of spectra. These maps (Figure 3-55 through Figure 3-58), when compared to those of fundamental

intensity (Figure 3-4 through Figure 3-7 on page 144), show that the two parameters correspond closely. While the column density maps cover only the regions in which the hotband was observed, this shows nearly the entire aurora on all four maps to have a general concurrence between intensity and column density.

All four column density maps show considerable similarities. The column density follows the auroral oval strongly, with significantly high densities on the dusk side of the oval and in the adjacent Bright Polar Region. This suggests the column density remains stable for the given CML position over the period of the observations, although temperatures seem to vary.

3.3.2 Column density profiles

The degree of similarity seen in the column density maps for different days means that only a single set of spectra showing the line-of-sight corrected column density (that of 11N4 in Figure 3-58) will be analysed in detail, since it is exemplary of all our data. Within this sequence, the correlation between the fundamental intensity and the column density is even more apparent than for the maps. Peaks in each match well in both position and relative intensity.

The only point where there is evidence of anti-correlation between the profile of temperature and column density is within the dark polar region (Figure 3-42 on page 171, and Figure 3-62 below), where a sharp drop in temperature is offset by a column density peak, which has no significant comparable intensity peak (The strength of this column density peak is, however, relatively small in comparison with that of the auroral oval and bright polar emission). This indicates that, for our data set, we are determining temperature and column density more independently than was the case for Lam *et al.* (1997).

Column densities appear to vary from $5\times10^{15}m^{-2}$ in the dark polar region to $1.5\times10^{16}m^{-2}$ on the auroral oval, with some variation in these values between each profile. These values are repeated across the spectral images of all four maps shown. This correlates well with previous studies (Lam *et al.*, 1997; Miller *et al.*, 1997a; and **1.3.6 Previous**

measurements of the physical conditions), which find column densities that reached a maximum of ~1.0-1.5×$10^{16}m^{-2}$ after line-of-sight correction. Both these earlier papers used the CGS4 spectrometer on the United Kingdom InfraRed Telescope. This uses a pixel size of ~3" square, significantly smearing out the intensity variations shown using CSHELL. However, the CGS4 results correlate well with the values for column density measured here, where the column densities were produced with an effective pixel size of 1.8" × 0.5" (see **2.4.4 Hotband Gauss-fitting**).

As the ground state of H_3^+ is overfilled due to radiative depopulation from higher energy levels (see Kim *et al.*, 1992; and **1.3.3 Local thermal equilibrium**), the true value of the column density will be higher than the values given here. The spatial resolution used was also significantly more than the predicted width of the auroral oval, as well as the detailed structure within the polar emission, measured using the unsmoothed fundamental intensity. This reduction in resolution will have effectively smeared out the peak density values. These considerations mean that the column densities given should be considered the minimum possible values for the true column density. However, if the assumption of QTE breaks down, then the overfilling of the fundamental energy level will result in an underestimation in the calculation of temperature, which will in turn extend to an overestimation of the column density.

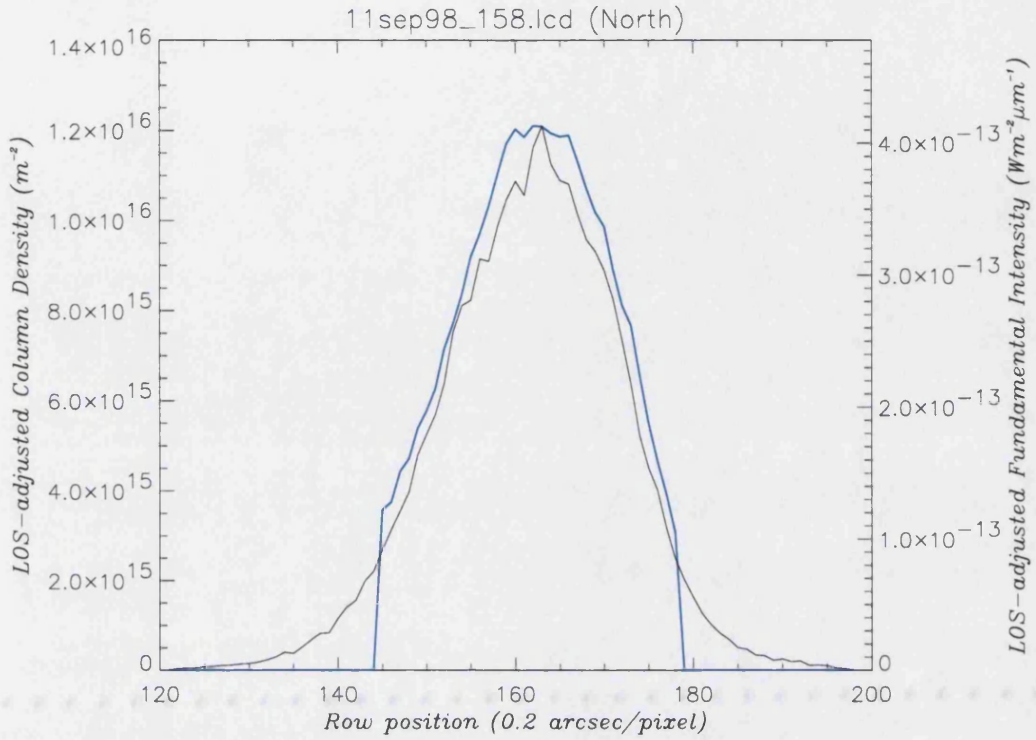

Figure 3-59: The line-of-sight corrected column density profile (blue) plotted with the fundamental intensity, taken at 08:27U.T. with a CML of 155°, from the 11N4 set of spectra

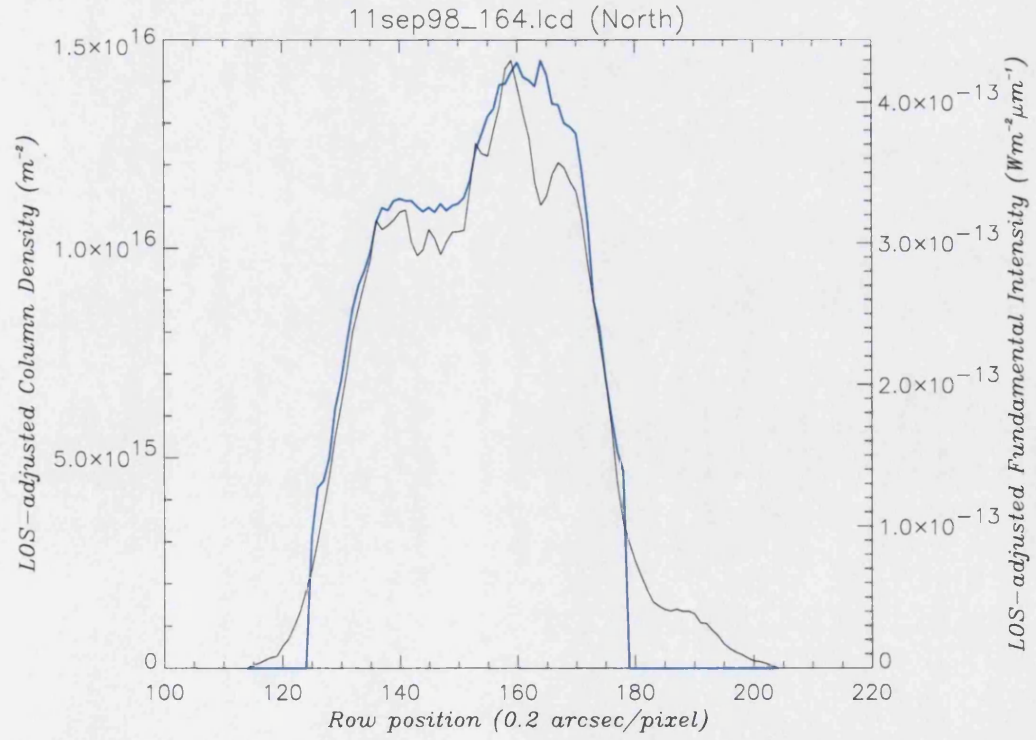

Figure 3-60: The line-of-sight corrected column density profile (blue) plotted with the fundamental intensity, taken at 08:32U.T. with a CML of 158°, from the 11N4 set of spectra

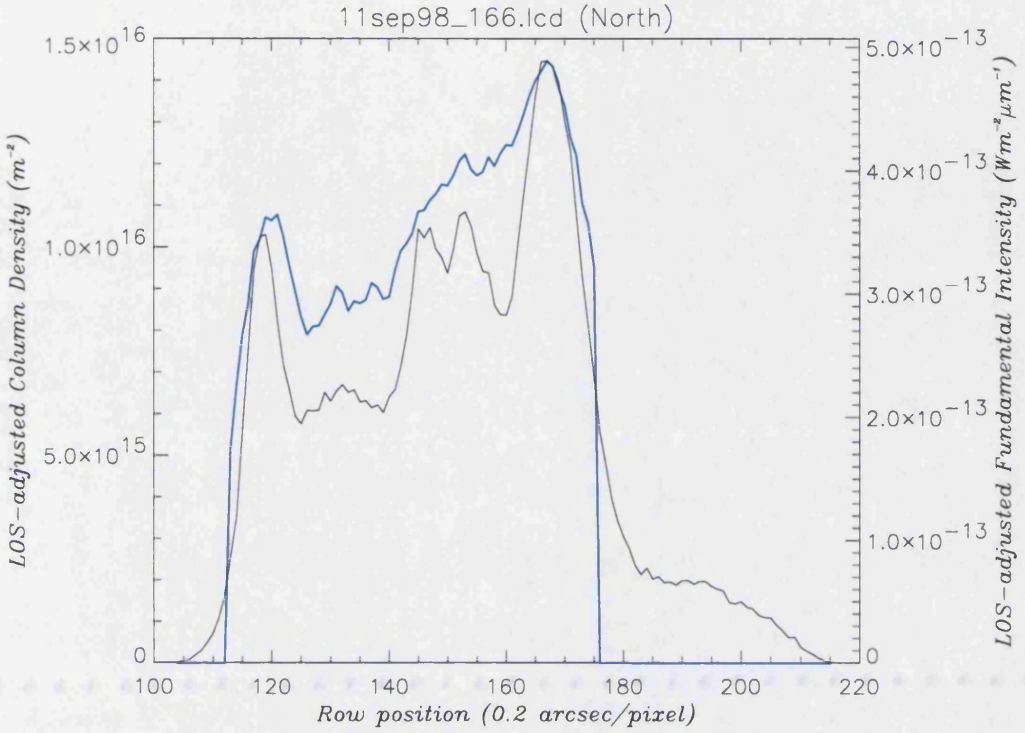

Figure 3-61: The line-of-sight corrected column density profile (blue) plotted with the fundamental intensity, taken at 08:34U.T. with a CML of 159°, from the 11N4 set of spectra

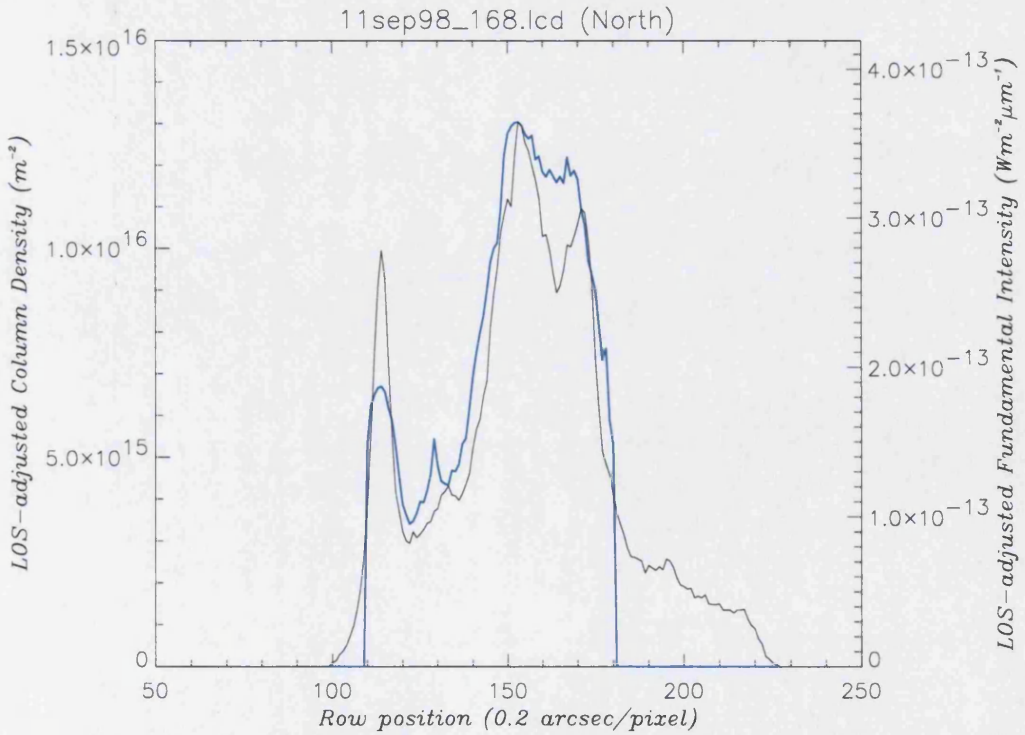

Figure 3-62: The line-of-sight corrected column density profile (blue) plotted with the fundamental intensity, taken at 08:35U.T. with a CML of 160°, from the 11N4 set of spectra

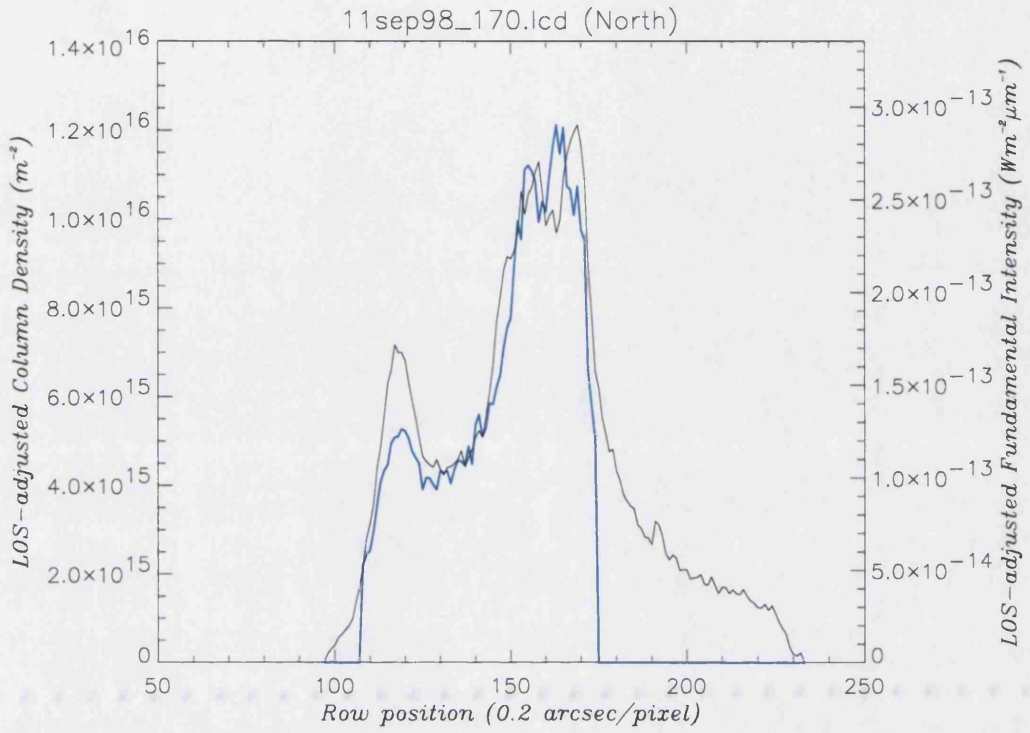

Figure 3-63: The line-of-sight corrected column density profile (blue) plotted with the fundamental intensity, taken at 08:37U.T. with a CML of 161°, from the 11N4 set of spectra

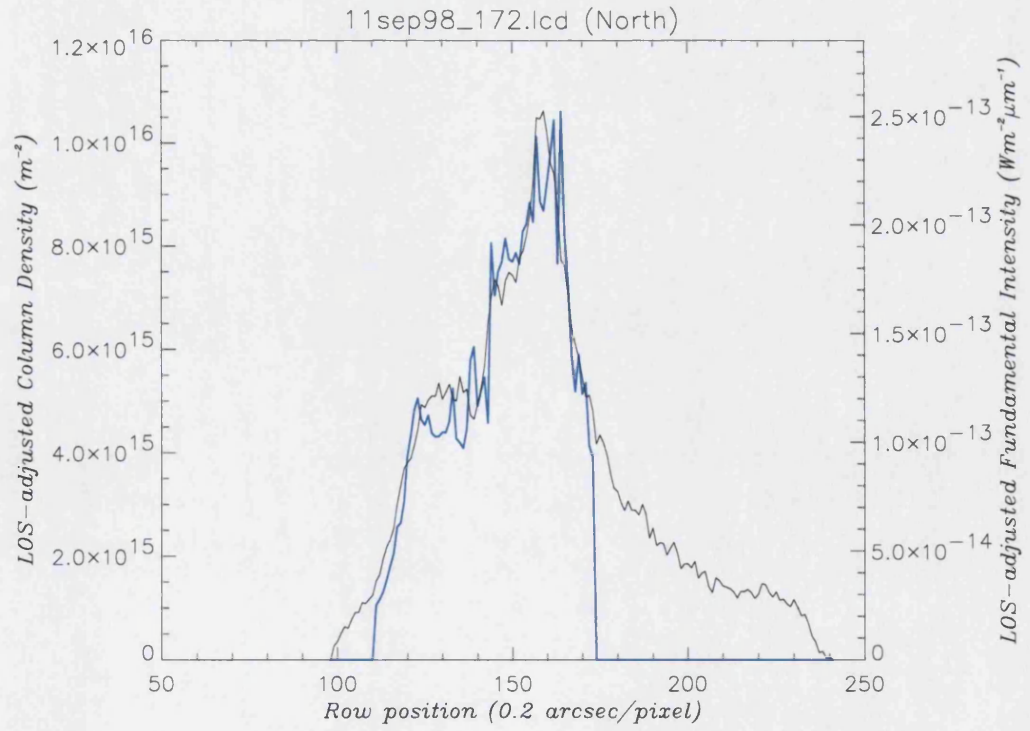

Figure 3-64: The line-of-sight corrected column density profile (blue) plotted with the fundamental intensity, taken at 08:39U.T. with a CML of 162°, from the 11N4 set of spectra

3.4 Total Emission

The total emission parameter, $E(H_3^+)$, is defined as the emission of H_3^+ across all the allowed energy transitions at a given temperature. It was first suggested as a method of combining the anticorrelated temperature and column densities seen in Lam *et al.* (1997), as described in **1.3.5 Total emission**. Typical $E(H_3^+)$ values are in the order of $1\text{-}4\times10^{-3}$ Wm^{-2} in the aurora. Although the temperature/column density anticorrelation does not seem significant within this data set, this parameter is useful in its own right: the distribution of H_3^+ total emission shows the regions in which heat loss occurs.

The calculation of $E(H_3^+)$ requires the assumption of quasi-thermal equilibrium (QTE) to hold, so that the population of the energy levels follows that which would be expected by a Boltzmann distribution (**1.3.3 Local thermal equilibrium**). The requirement that the ground state is overfilled does not effect the value of calculated $E(H_3^+)$ because the ground state does not emit. If the assumption of QTE breaks down, as predicted by Kim *et al.* (1992), then lower energy levels will become overfilled in comparison with upper levels. However, this has a minimal effect in the calculation of $E(H_3^+)$, because the resultant underestimation of temperature is balanced by an overestimation of column density. This comparative stability of the calculated value of $E(H_3^+)$ was shown in Lam *et al.* (1997) to be accurate generally to within 10%, increasing to ~5% over the auroral region itself. Thus, unless the assumption of QTE breaks down completely, beyond that predicted by Kim *et al.*, the value of $E(H_3^+)$ can still be found relatively accurately.

The variation in fundamental intensity and total emission is directly related, and they differ from each other only in the variation in emission per molecule with temperature for the $Q(1,0^-)$ line and across all the lines respectively. This variation is shown in Figure 2-38 and Figure 2-43. Using the measured temperature range in the auroral region, between 900-1200°K, produces a variation in total emission per molecule that is three times higher than the variation in emission from the $Q(1,0^-)$ line. Thus, although the column density dominates the form of the fundamental intensity, temperature variations may have a more notable control over the form of the total emission.

The degree of correlation between either the temperature or the column density and the total emission will provide insights into the way in which H_3^+ plays a role in controlling the cooling from the planet.

Since models show the H_3^+ column density correlates with energy deposition, a close relationship between the total emission and column density would provide evidence of H_3^+ stabilising the temperature structure of the atmosphere *in situ*. The H_3^+ hot spots would then be a product of secondary energy transport. However, if the total emission were to correlate with the temperature, which itself does not correlate well with either fundamental intensity or the column density, this would suggest that energy transport processes are distributing the heat away from the region of energy deposition before H_3^+ can stabilise the temperature.

These results will prove very important for future modelling of the coupled Jovian ionosphere/magnetosphere system, since the effect of H_3^+ cooling has been largely ignored by current models (one exception of this being the model of Waite *et al.* (1997)).

3.4.1 Total emission maps

As with the column density, the maps of total emission (Figure 3-65 through Figure 3-68) match closely with those of fundamental intensity, with high levels of total emission corresponding with the auroral oval and bright polar region, and a significantly lower value within the dark polar emission.

Figure 3-65: The total emission map made using the 8N5 line-of-sight corrected total emission profiles, using a non-linear scale of 0-2.8×10^{-3} Wm^{-2}, to best show the features within the auroral region; for proper values see the profiles, shown below

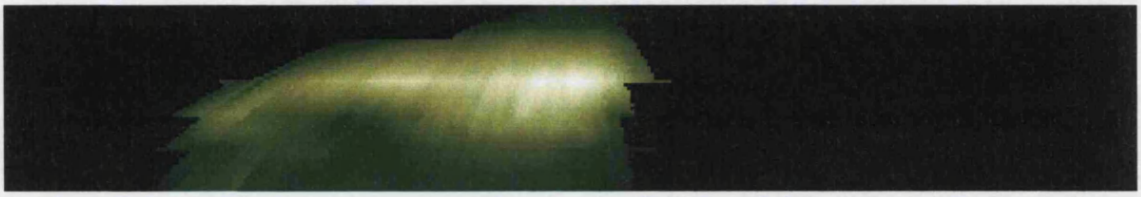

Figure 3-66: The total emission map made using the 10N5 line-of-sight corrected total emission profiles, using a non-linear scale of 0-2.6×10^{-3} Wm^{-2}, to best show the features within the auroral region

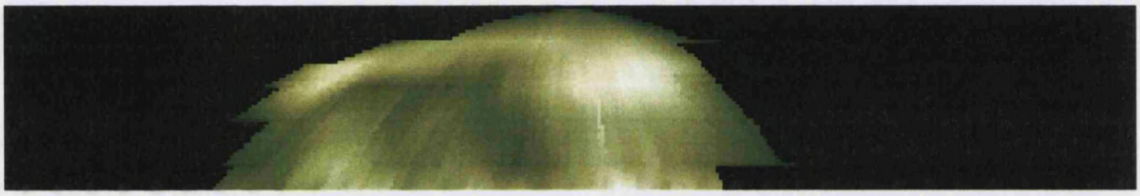

Figure 3-67: The total emission map made using the 10N6 line-of-sight corrected total emission profiles, using a non-linear scale of 0-1.8×10^{-3} Wm^{-2}, to best show the features within the auroral region

Figure 3-68: The total emission map made using the 11N4 line-of-sight corrected total emission profiles, using a non-linear scale of 0-3.1×10^{-3} Wm^{-2}, to best show the features within the auroral region

3.4.2 Total emission profiles

Line-of-sight total emission profiles are shown from 11N4 (Figure 3-68). The total emission, once corrected for line-of-sight effects, generally has a value of ~1.0-1.5×10^{-3} Wm^{-2}, with this range of variation being seen between the low-emission Dark Polar Region and the auroral oval. In some cases this value increases as high as 3×10^{-3} Wm^{-2} (Figure 3-71), where the total emission is enhanced by the coincident peaks of temperature and intensity.

Fundamental intensity correlates well with the general structure of total emission, with the position of the peaks of emission and intensity almost universally coincident, so that the majority of the H_3^+ cooling in the Jovian aurora is produce from the dusk side of the aurora. Temperature has a secondary effect, producing broadening in total emission peaks or increasing the strength of peaks depending on the degree of coincidence between fundamental intensity and temperature, and in general affecting the overall value of the total emission.

The values for total emission are comparable with those in Lam *et al.* (1997), Miller *et al.* (1997a), and Satoh and Connerney (1999). These give peak values for total emission in the auroral region of the order of 1.0×10^{-3} Wm^{-2}. But their values are slightly lower than that recorded here, probably as a direct consequence of the lower temperatures measured in these papers (**1.3.5 Total emission**).

The relative lack of correlation between variations in temperature and variations in total emission provides some justification for the simplification made by Satoh and Connerney (1999), who assume a constant temperature of 800°K across the whole auroral/polar cap region to produce values for H_3^+ cooling. The resultant values for total emission range between $2\text{-}5\times10^{-3}$ in the auroral region, agreeing generally with the results presented here, although the form this variation takes across the auroral region differs significantly. This difference in morphology of total emission originates from Satoh and Connerney's modelled intensity, which has no significant emission on the dusk side of the auroral oval.

What these results show best is the role H_3^+ plays as a stabilising agent within the Jovian aurorae. Variations in energy deposition do not result in large-scale temperature variations, at least on the localised scale. The column density varies as H_3^+ is created by the energy deposited, and this results in a variation in the total emission, countering the energy input with H_3^+ cooling. This prevents extreme variations in temperature within the thermosphere, despite the potentially large variations in energy input intrinsic to particle precipitation.

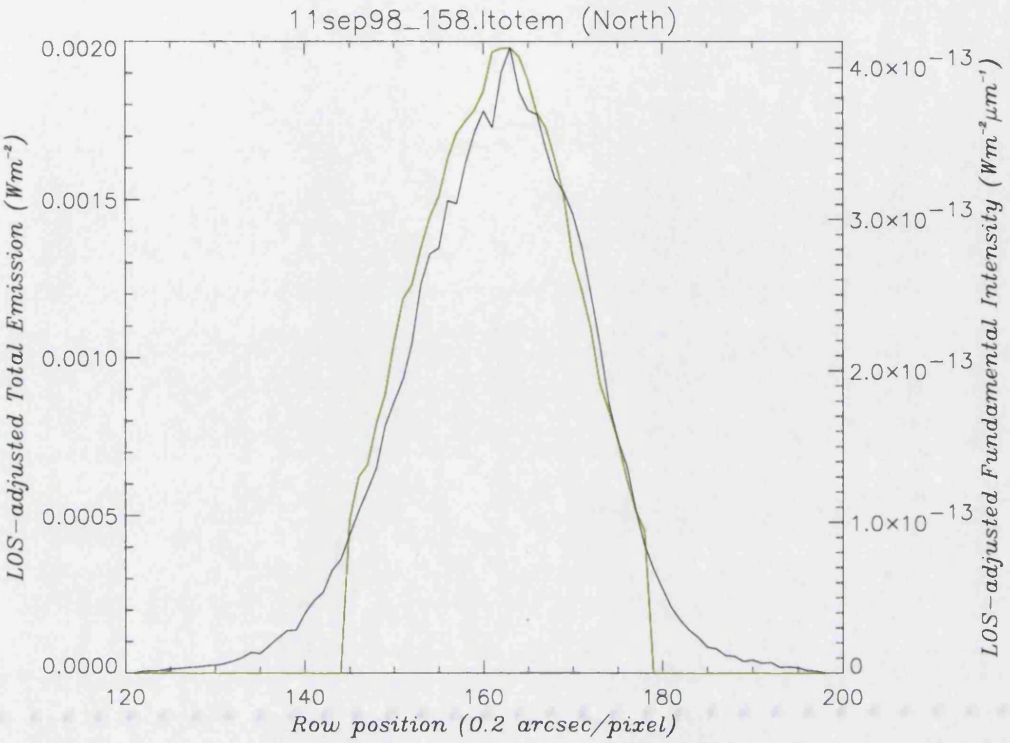

Figure 3-69: The line-of-sight corrected total emission profile (blue) plotted with the fundamental intensity, taken at 08:27U.T. with a CML of 155°, from the 11N4 set of spectra

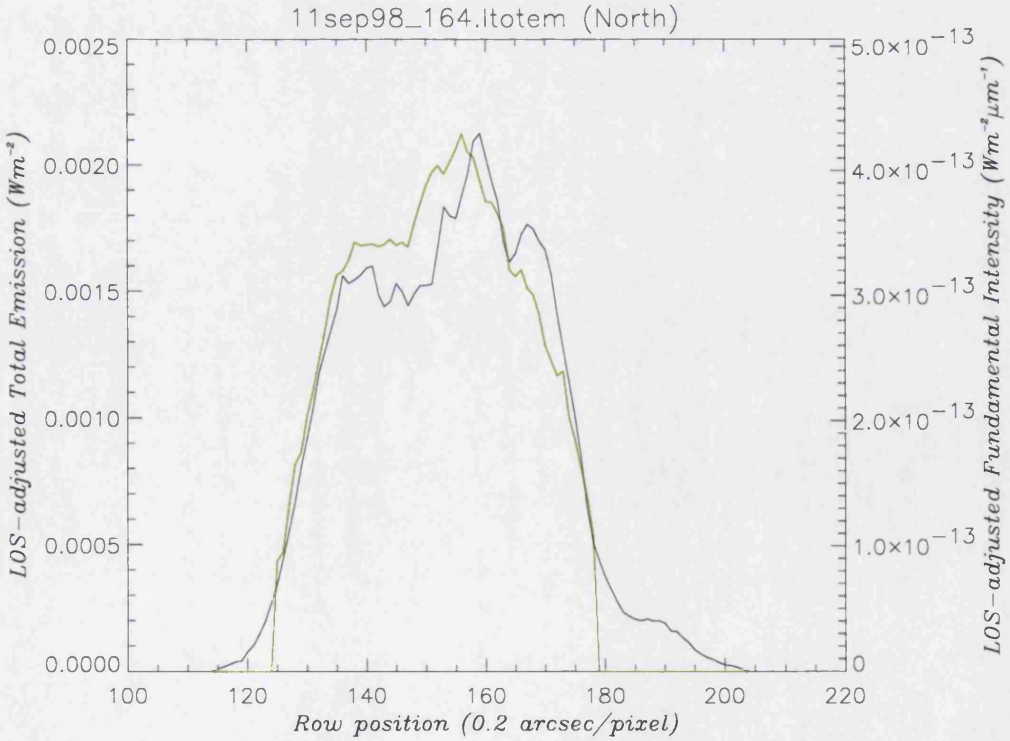

Figure 3-70: The line-of-sight corrected total emission profile (blue) plotted with the fundamental intensity, taken at 08:32U.T. with a CML of 158°, from the 11N4 set of spectra

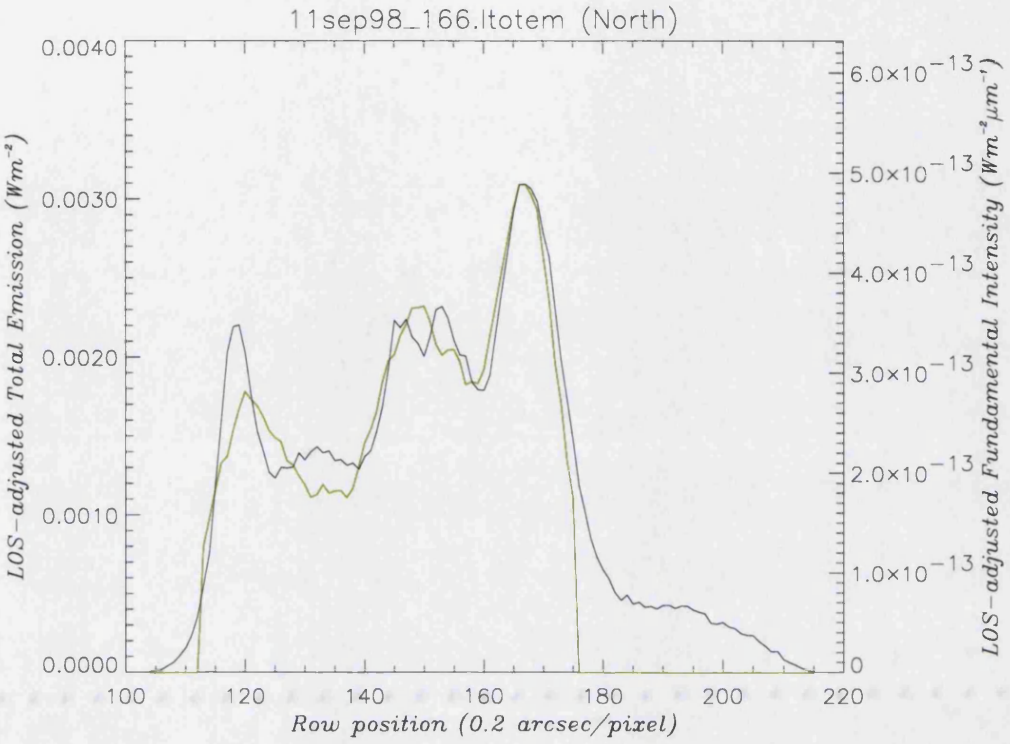

Figure 3-71: The line-of-sight corrected total emission profile (blue) plotted with the fundamental intensity, taken at 08:34U.T. with a CML of 159°, from the 11N4 set of spectra

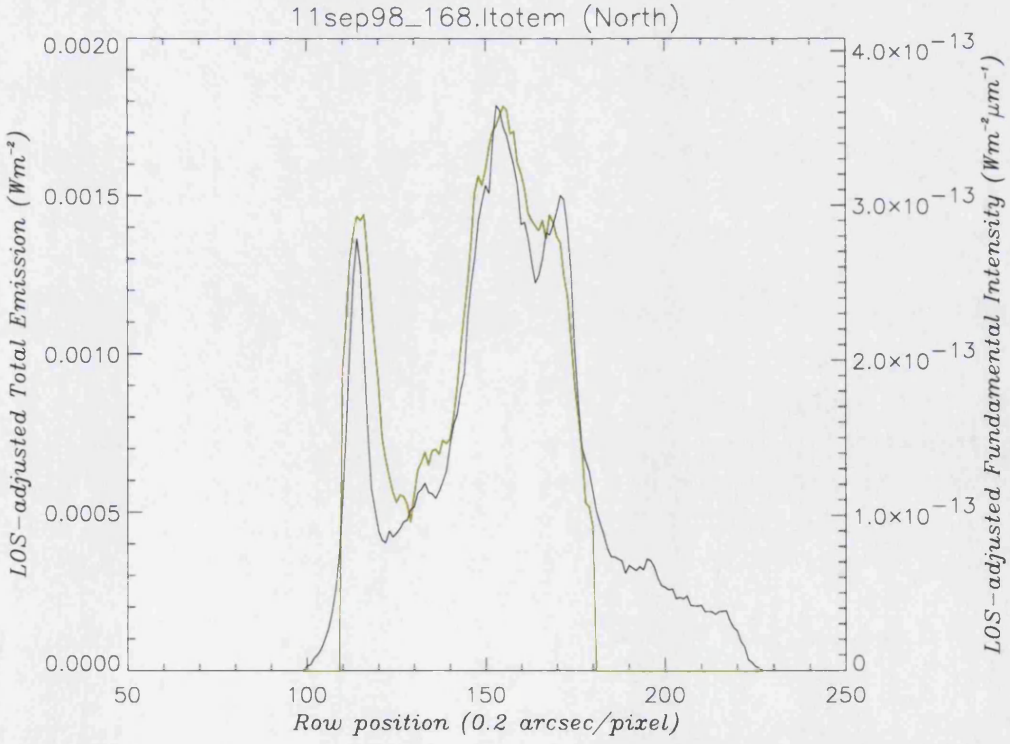

Figure 3-72: The line-of-sight corrected total emission profile (blue) plotted with the fundamental intensity, taken at 08:35U.T. with a CML of 160°, from the 11N4 set of spectra

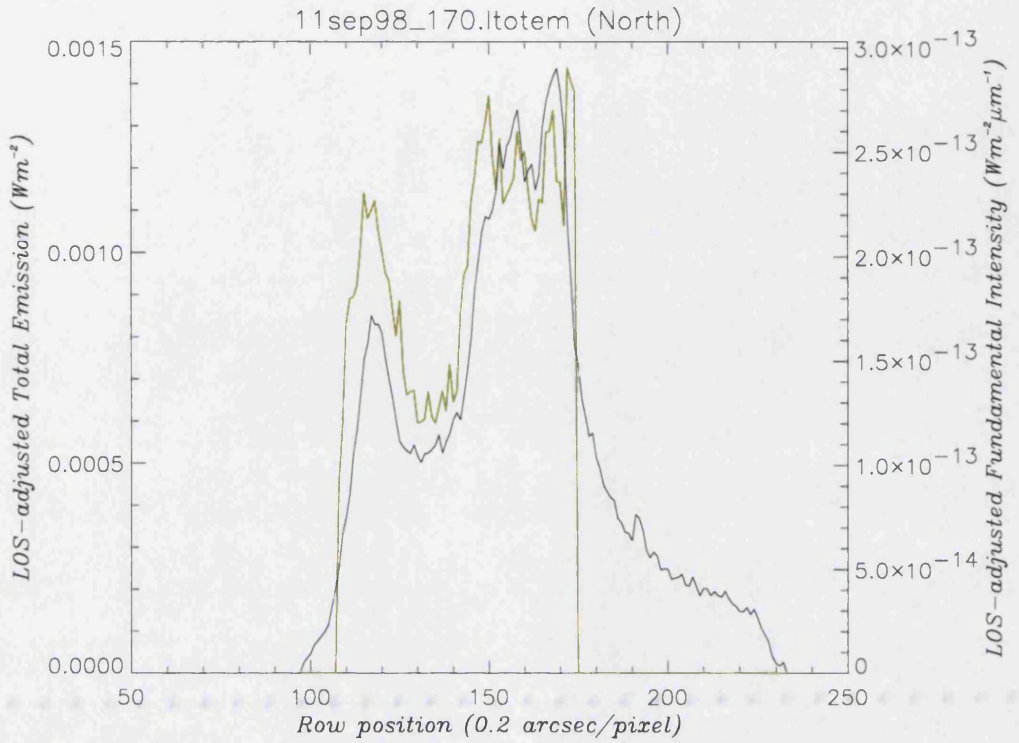

Figure 3-73: The line-of-sight corrected total emission profile (blue) plotted with the fundamental intensity, taken at 08:37U.T. with a CML of 161°, from the 11N4 set of spectra

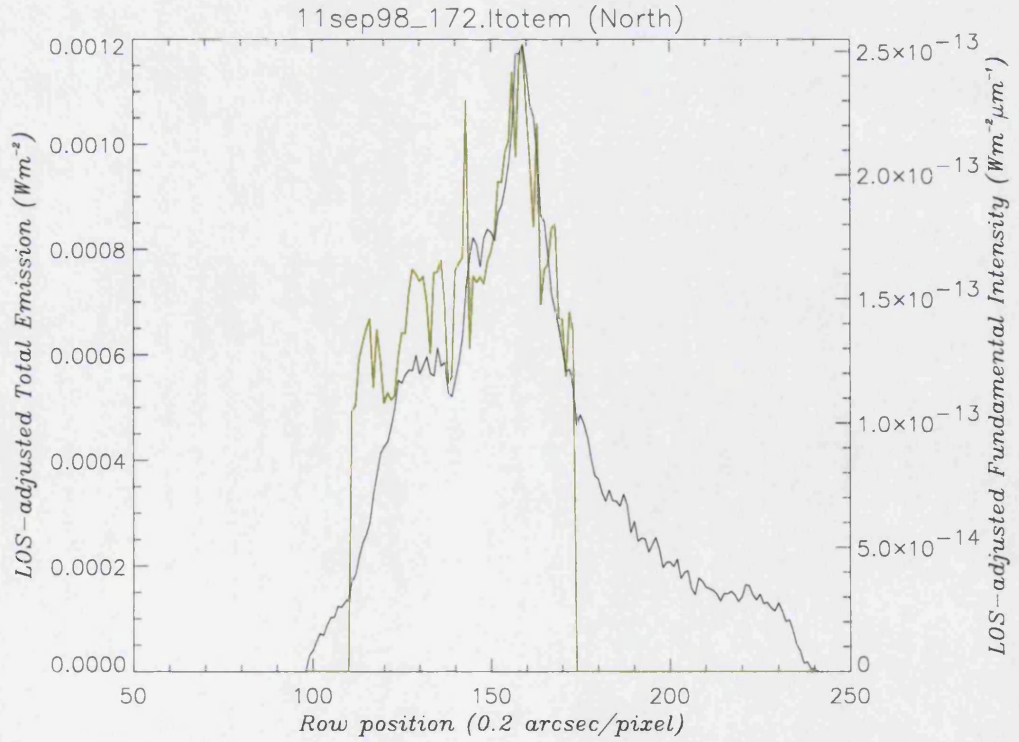

Figure 3-74: The line-of-sight corrected total emission profile (blue) plotted with the fundamental intensity, taken at 08:39U.T. with a CML of 162°, from the 11N4 set of spectra

Chapter 4 : Dynamics of the Jovian Auroral Region

The aurora of Earth has been shown to contain an electrojet, a current system that flows in the anti-rotational direction. This current system is formed through the greater collisional deceleration of the ions compared to the electrons, both equally accelerated through $\mathbf{E} \times \mathbf{B}$ Hall drift. A similar electrojet system has been proposed for the Jovian aurorae, where collisions between H_3^+ ions and the neutral thermosphere are thought to significantly slow, but not halt, the ion component of the $\mathbf{E} \times \mathbf{B}$ Hall drift (see Achilleos *et al.*, submitted; and **1.3.8 Dynamics of the Jovian aurorae**).

The ion winds associated with the electrojet have been postulated as a means of redistributing auroral energy to the rest of the planet, playing an important part in thermospheric temperatures (Waite *et al.*, 1983). The $\mathbf{E} \times \mathbf{B}$ Hall drift that forms the electrojet is powered by the Pedersen current across the auroral region, which is linked through Birkeland (field-aligned) currents to the plasmasheet (Hill, 1979). This current system and the electrojet it produces are essential for keeping the plasmasheet in corotation with the planet. The detection of a continuous electrojet on Jupiter is thus an important step in the understanding of both the entire thermosphere/ionosphere region, and the ionosphere/magnetosphere interaction.

Although there have been several observations linked to possible electrojet activity, the first direct detection was made by Rego *et al.* (1999), who measured the Doppler shift in H_3^+ caused by the $\mathbf{E} \times \mathbf{B}$ Hall drift. This detection was "accidental", and considered to have occurred during an "auroral event", which resulted in high velocity (~1-3 km/s) winds. It was seen during a short period of significantly high auroral activity and ideal line-of-sight viewing conditions, but it raised the possibility of routinely finding winds in

the ionosphere, using H_3^+ as a marker for Doppler shifts, and of determining a prevailing "wind structure". The observations made for this thesis were a direct consequence of this initial detection, made with the specific objective of locating the ion winds that pertain to the electrojet, and studying the variation in H_3^+ velocity across both the auroral oval and polar regions.

This data has been processed by techniques used to remove "non-velocity" effects from the original output of the SPECTRA procedure, described in full in **2.3.1 Gauss fitting**. The data was analysed through a four-stage process to obtain the true line-of-sight velocity profile as reliably as possible:

a) Removal of planetary rotational effect $V_r(y)$;

b) Removal of effects due to array distortion (by using lamp lines) $\Delta V_d(y)$;

c) Removal of effects due to uneven illumination of the slit resulting from the genuine spatial variation in Jupiter's H_3^+ emission (discussed in **Chapter 3**), making use of the 3.953μm images $\Delta V_s(y)$;

d) Assuming an absolute zero on the body of the planet, and applying a correction to adjust for this V_0.

Steps a) and b) are relatively straightforward, and so this chapter discusses data once these two processes have been completed, as well as final velocity profiles which result from the completion of all the processes. This means we are looking at data *pre-spatial* effect removal ("pre-spatial" velocities, $V_{ps}(y)$;) and *post-spatial* effect removal ("actual" velocities, $V_a(y)$;).

The data set collected for this thesis is of an exceptional quality and quantity. The quality of the spectral images has already been demonstrated in **Chapter 3** - where auroral structure is clearly seen even within the hotband intensity profiles, some 50 times weaker than the fundamental line we used for this chapter. The signal-to-noise ratio (S/N) measured for the fundamental line in the auroral region is excellent, often in the range of 80-100.

The quantity of data collected provides extensive coverage of Jupiter, with a large range of CMLs, especially those with the northern aurora displayed, re-observed on a number of nights. The recurrence of similar CMLs over different nights makes comparative studies possible, in addition to the confirmation of general regional trends.

However, in order to carry out the removal of spatial effects, good quality images are required to properly predict the intensity variation across the slit. On the night of the 10^{th} and early on the 11^{th}, a "double effect" described fully in **2.3.5 Bounce feature on images** makes such spatial correction extremely difficult, and we have not attempted it in this thesis.

To go beyond velocities determined in the line-of-sight of the observations, requires making some very fundamental assumptions about the structure of H_3^+ emission and the dynamics of the Jovian auroral/polar regions - the very quantities we are trying to determine empirically, rather than postulate *a priori*. Even to properly understand these line-of-sight velocities, a strong understanding of their exact location on the planet is needed, so we need the auroral/polar cap regions well displayed on the planet. This was the case for the northern aurora, for certain CMLs, but the southern aurora was always poorly displayed.

Therefore, the strategy used to analyse the data set of this chapter is:

a) To select data wholly from the northern auroral/polar cap regions where the auroral oval is well displayed on the planet. This means choosing data obtained between CMLs 140 to 180;

b) To compare sequences of "pre-spatial" velocity profiles from nights where similar CMLs were obtained. This enables us to investigate the extent to which the underlying velocity structure is stable or variable - assuming that the intensity variation as a function of planetary location is "stable", which was reasonably shown in **3.1.1 General auroral morphology**;

c) Then to use the data for which "good" 3.953μm images are obtained to determine the underlying "actual" velocity structure, using the spatial correction discussed in **2.8.2 Velocity calibration.**

The data that will be studied in detail within this chapter consists of the same four set of spectra chosen for Chapter 3, shown again below. These sets of spectra match the criteria given above, being centred around a CML of ~160° and taken from three separate nights. Using the same sets of spectra as in the last chapter will also allow for easier comparison of the data in **Chapter 5 : Summary, Discussion and Conclusions**. The morphology of the H_3^+ emission on these sets is described in full in **3.1.1 General auroral morphology**.

Table 4-1: The sets of spectra analysed for velocity

Name of sequence	CML at start of sequence	U.T. at start of sequence
8N3	150	10:46
10N5	144	12:13
10N6	164	12:48
11N4	154	08:19

As noted above, we will look at both pre-spatial and post-spatial velocities in this chapter. The pre-spatial velocities are important because they show the extent of conformity or divergence between separate nights, and allow the results of actual velocity profiles to be referred to nights where spatial correction was not possible, *e.g.*, on the 10th September.

To better understand the effects of the spatial effect in the calibration process, it is also important to compare the profiles of spatial effect against the pre-spatial velocity, which are the actual velocity, without the spatial and absolute zero correction. This provides a better understanding of the influence of the spatial effect in the pre-spatial velocities, and the variations in the true dynamical effects within the atmosphere, across all four sets of spectra studied. Once the effects of the spatial component are better understood, analysis of the actual velocities for 8N3 and 11N4 can be placed in context of the relative velocities from the 10th, either through the similarities or significant variations across the nights.

4.1 Pre-spatial Velocities

When the initial Gaussian fitting was performed on the spectral images (**2.3.1 Gauss fitting**), three important outputs were produced: peak intensity, peak width and peak position. The peak position was automatically converted into an effective relative

velocity in kilometres per second. In order to produce the final "actual" velocities shown below, extensive calibrations specific to each spectral profile were required (**2.8.2 Velocity calibration**).

However, without considering the spatial effects on the velocity, calibration becomes far less complicated. Thus it becomes an easily performed removal of the array and rotation effects that can be automated into output procedures. This means that calculation of the "pre-spatial velocities" is possible for every spectral image that has been processed using the SPECTRA procedure.

The resultant pre-spatial data set that has been produced thus covers several hundred spectral images. Within a single set of spectra, there is a limit to the number of velocity profiles that are useful, since many are made on regions where the fundamental intensity is relatively weak (*e.g.*, towards the equator), or even non-existent (above the limb). Removing those profiles which consist of noise, the four sets of spectral data become more manageable, if of a slightly larger size than those seen in the last chapter. These can then be shown as individual profiles in order.

To better understand the variations in the actual velocities across all four sets of spectra, it is best to analyse all of them together, rather than in their individual sets. By ordering the spectral profiles in terms of position on the planet (determined by the morphology of the fundamental intensity as in the case of our temperature data in **3.2.2 Temperature profiles**), the extent of correspondence between similar latitudes on separate sets of spectra can be judged.

4.1.1 Pre-spatial velocity profiles

The pre-spatial velocity profiles not only appear to correlates well across the four sets of spectra, but also follow a continuous development of form with varying latitude. The profile morphology of the velocity appears to have consistency across the all of the spectral images. While the morphology appears to vary continuously with latitude, the general form can be divided into specific groups, which describe the appearance of variations in the profile morphology, spanning from the limb to the equator.

Above-limb profiles

On spectral images taken above the limb of the planet, the velocity profile contains no structure. Even close to the limb, where a small peak in the intensity can be seen, no variation in the velocity profile can be seen above the overriding noise (Figure 4-1). This lack of velocity structure further confirms the validity of associating the velocity variations with the planet itself, rather than any instrumental or terrestrial artefacts.

Limb profiles

Once the slit is moved onto the planet, and a definite intensity peak is produced, the noise associated with the velocity reduces to much lower levels (~0.25 km/s or less on the peak), and velocity structure within the profile becomes apparent.

The first significant feature that appears in the velocity profile is a linear slope across the planet (from Figure 4-2 to Figure 4-5), showing increasing blue-shifting towards the dusk limb (west on the sky). The slope begins relatively flat, with an effective variation of about 2 km/s across the planet. However, as the profiles continue across the limb region, the linear slope changes form, appearing to curve to a flat velocity on either end of the noise-reduced region, with the appearance of an inclined S-shape of 2-4 km/s, which appears to curve greatest over the emission peak (from Figure 4-6 to Figure 4-9).

High-auroral latitude profiles

As the intensity peak begins to broaden onto the body of the planet, the velocity profile progresses from an S-shape into a simple curve (Figure 4-10 and Figure 4-11). This peaks near the dusk side peak in the intensity profile and shows a strong decrease on the dawn side (3-6 km/s) crossing the main emission peak, and a gentler one (1-3 km/s) over the body of the planet, which is now starting to be seen in intensity.

As the intensity profiles broaden and variations in intensity appear within the auroral region, blue-shift peaks occur on the velocity profiles, corresponding with the peaks in intensity (Figure 4-13). The curve also flattens on the top, so that over the auroral emission a red-shift of ~2 km/s forms, from the dusk peak to the dawn peak. Beyond the

dawn peak, the velocity falls away sharply over the limb, as expected, dominated by spatial effects.

Mid-auroral latitude profiles

Once the aurora is displayed clearly, more small-scale variations in apparent velocity appear over the general form of the previous simple curve. These consist of peaks of blue-shift coinciding with the peaks of the auroral oval and a series of peaks and troughs across the polar region, with no shift over the Dark Polar Region, and a 1-2 km/s shift over the Bright Polar Region (from Figure 4-16 to Figure 4-19).

The combination of velocity variation across the DPR and BPR means that the difference between the dawn and dusk auroral oval is also 1-2 km/s, which appears to be a consistent trend from its first appearance here all the way down across the aurora.

However, as the profiles continue to lower latitudes, a red-shift trough located in the dark polar region of the velocity profile becomes continually redder and more dominant (from Figure 4-20 onwards).

At still lower latitudes, another feature appears, with a double blue-shift peak appearing on the dawn auroral oval (east on the sky), with the internal velocity peak generally coincident with the corresponding intensity peak (for example, Figure 4-22, Figure 4-23 and Figure 4-25).

Low-auroral latitude profiles

The velocity profile appears to smooth out at lower latitudes, as features remain but broaden considerably. The form of the velocity profiles continues to smooth into the background, as the noise increases and the variations decrease, when the intensity profile becomes a single peak corresponding to the slit just cutting across the auroral oval. The progressing velocity profiles return to a noisy but essentially flat profile, as they continue out from the auroral region onto the body of the planet towards the equator (Figure 4-34).

Overall distribution

The pre-spatial velocity variation follows a basic trend: both limbs show significant levels of relative red-shifting, the dawn auroral oval is slightly red-shifted, the dark polar region has a red-shift that increases with decreasing latitude, the bright polar region remains fairly neutral or with slight blue-shifting, the dusk auroral limb appears to be relatively blue-shifted, and the body of the planet is neutral, but tails off into a red-shift as it nears the limb.

There appears to be little variation between the four sets and, unless the spatial correction dominates the form of the actual velocity profiles, results from the 8^{th} and 11^{th} can be translated back to the 10^{th}. In addition, it may be possible to draw further conclusions from the variations seen between pre-spatial velocities.

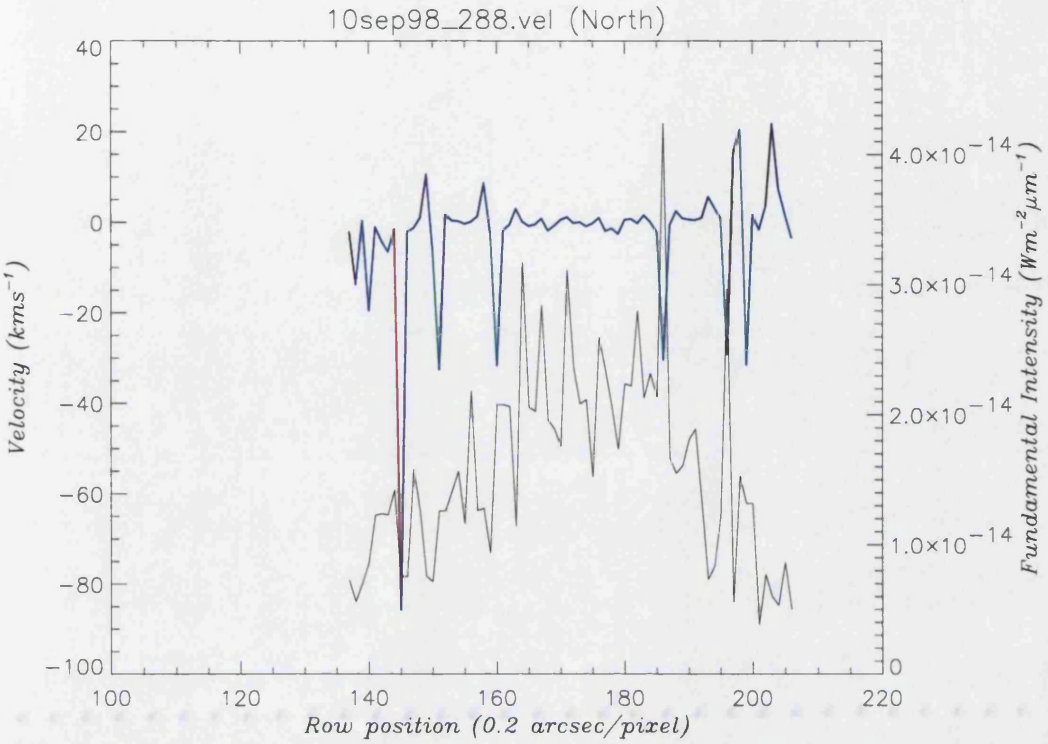

Figure 4-1: The pre-spatial velocity profile (an individually scaled non-linear blue-red shift colour scale, used for clarity) plotted with the fundamental intensity, taken above the limb of the planet at 12:18U.T., from the 10N5 set of spectra

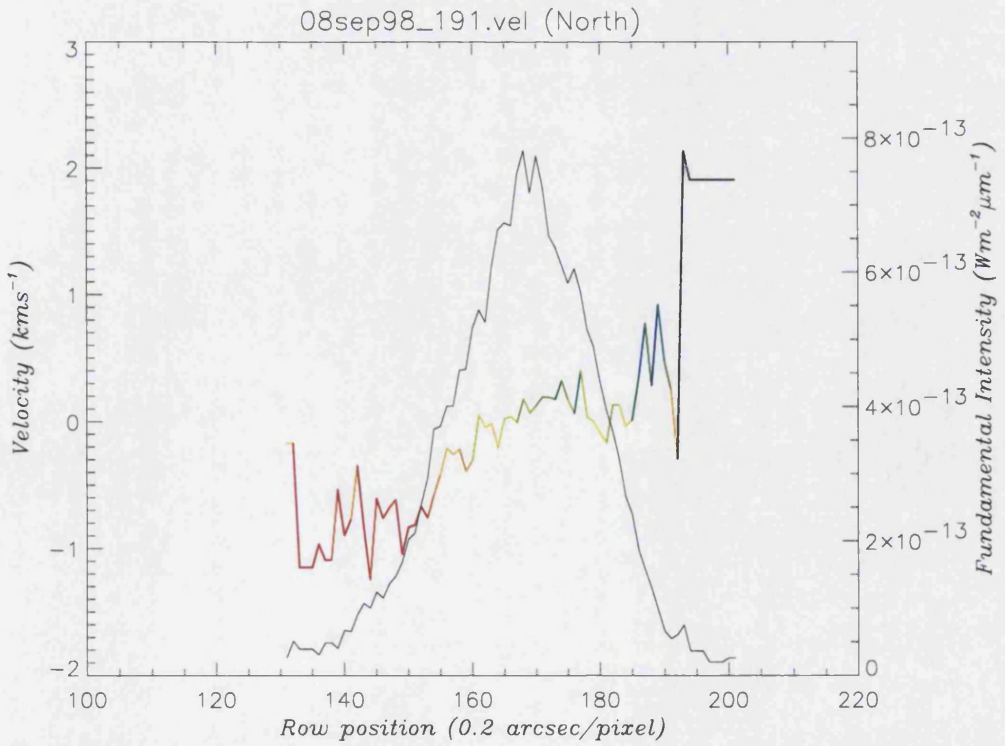

Figure 4-2: The pre-spatial velocity profile (blue-red shift) plotted with the fundamental intensity, taken at 10:49U.T. with a CML of 149°, from the 8N5 set of spectra

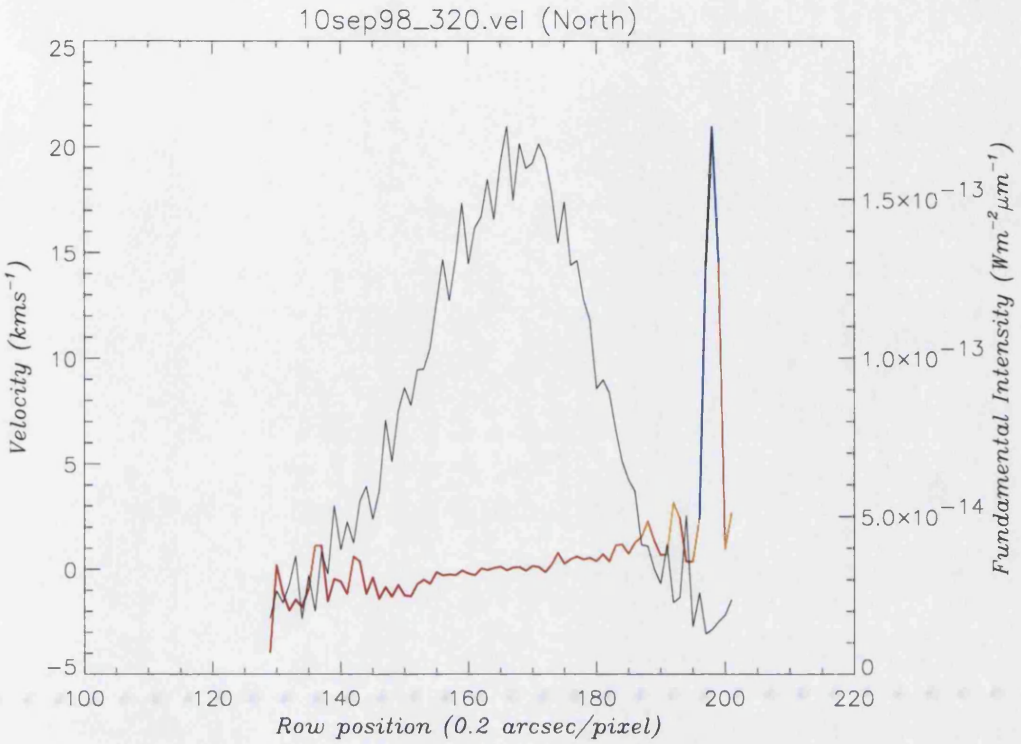

Figure 4-3: The pre-spatial velocity profile (blue-red shift) plotted with the fundamental intensity, taken at 12:51U.T. with a CML of 164°, from the 10N6 set of spectra

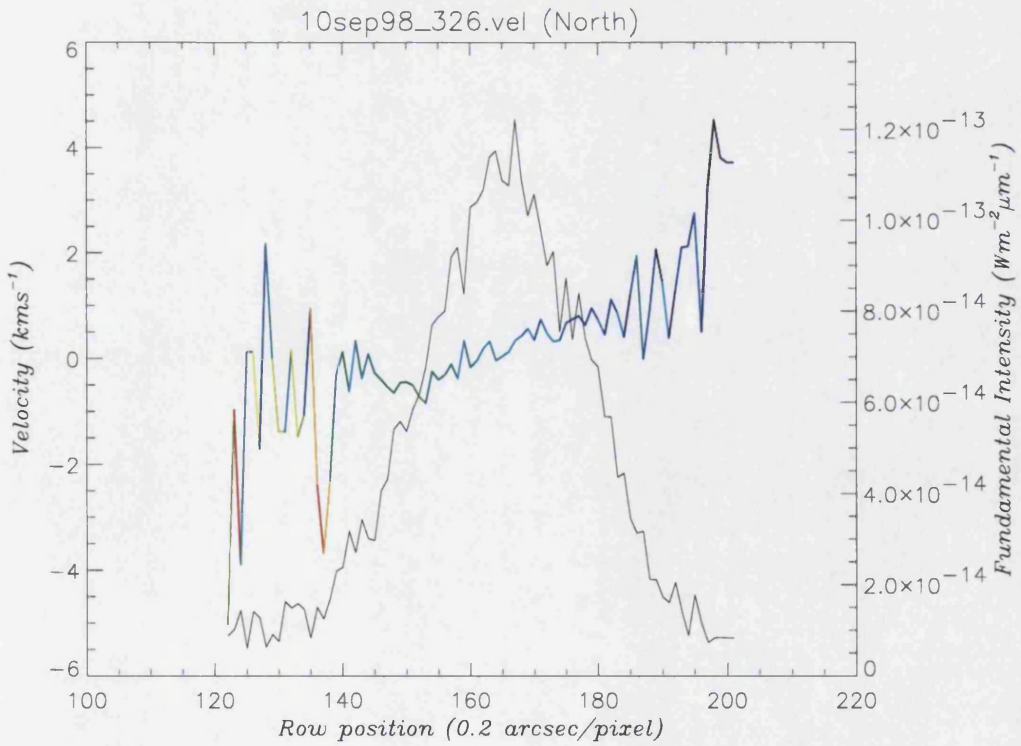

Figure 4-4: The pre-spatial velocity profile (blue-red shift) plotted with the fundamental intensity, taken at 12:56U.T. with a CML of 167°, from the 10N6 set of spectra

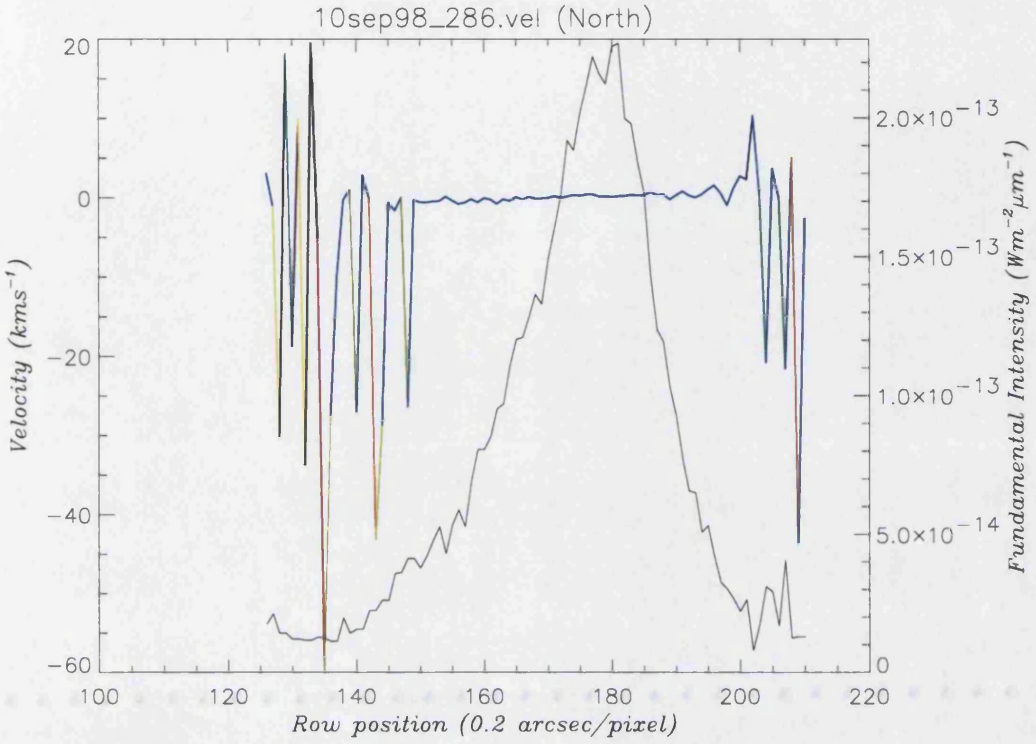

Figure 4-5: The pre-spatial velocity profile (blue-red shift) plotted with the fundamental intensity, taken at 12:17U.T. with a CML of 143°, from the 10N5 set of spectra

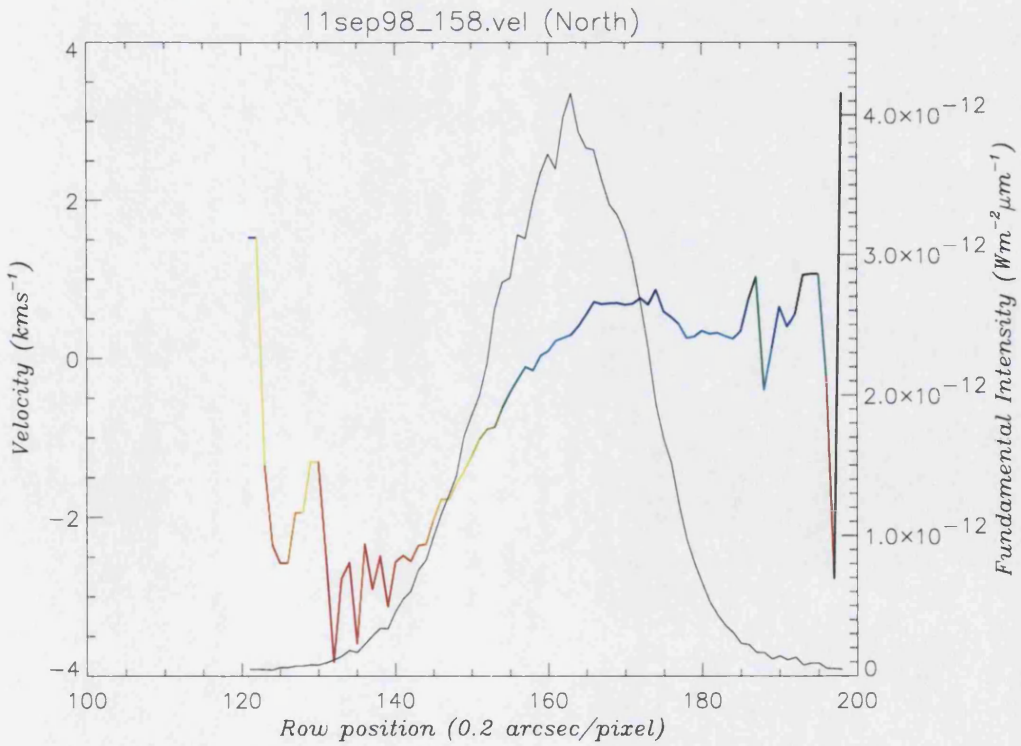

Figure 4-6: The pre-spatial velocity profile (blue-red shift) plotted with the fundamental intensity, taken at 08:27U.T. with a CML of 155°, from the 11N4 set of spectra

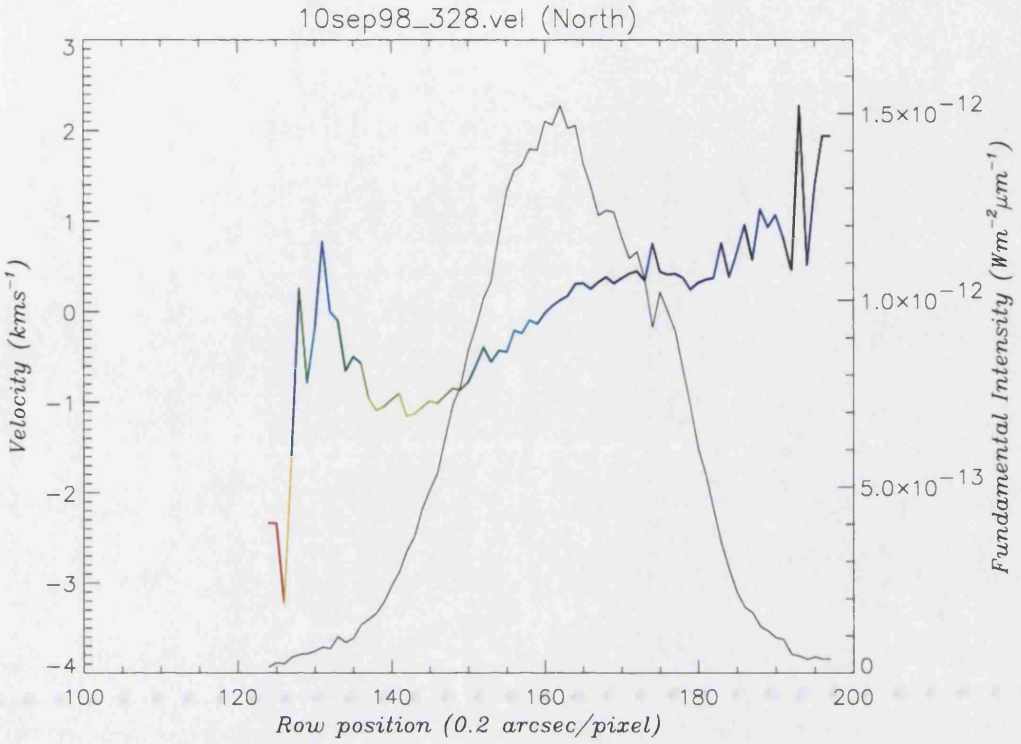

Figure 4-7: The pre-spatial velocity profile (blue-red shift) plotted with the fundamental intensity, taken at 12:58U.T. with a CML of 169°, from the 10N6 set of spectra

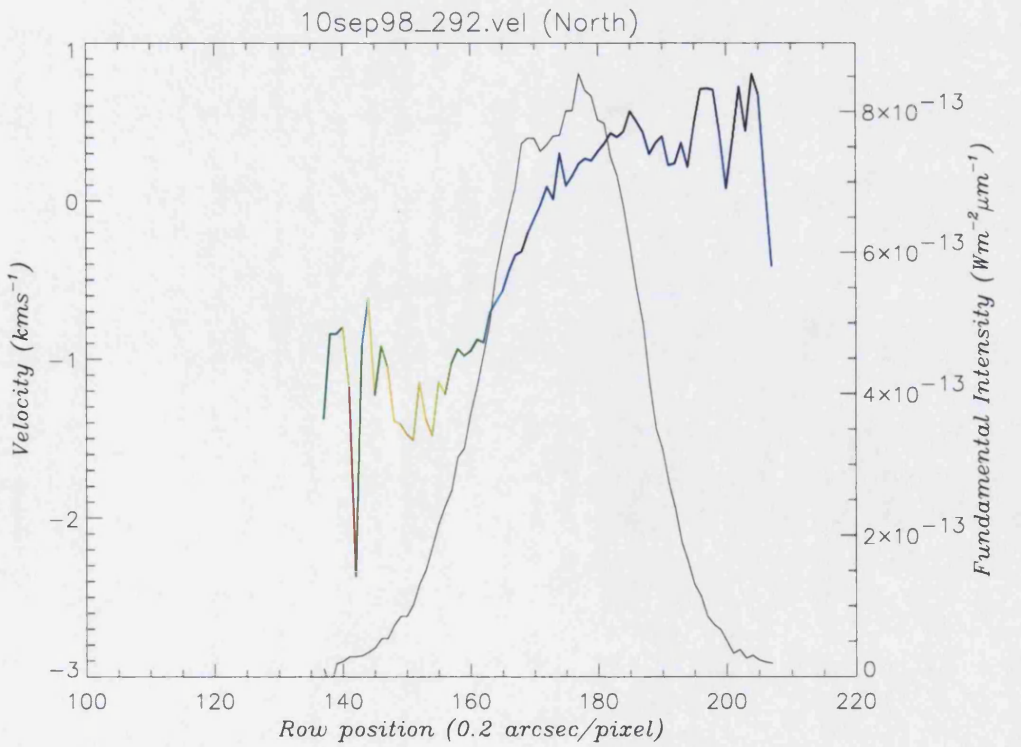

Figure 4-8: The pre-spatial velocity profile (blue-red shift) plotted with the fundamental intensity, taken at 12:22U.T. with a CML of 147°, from the 10N5 set of spectra

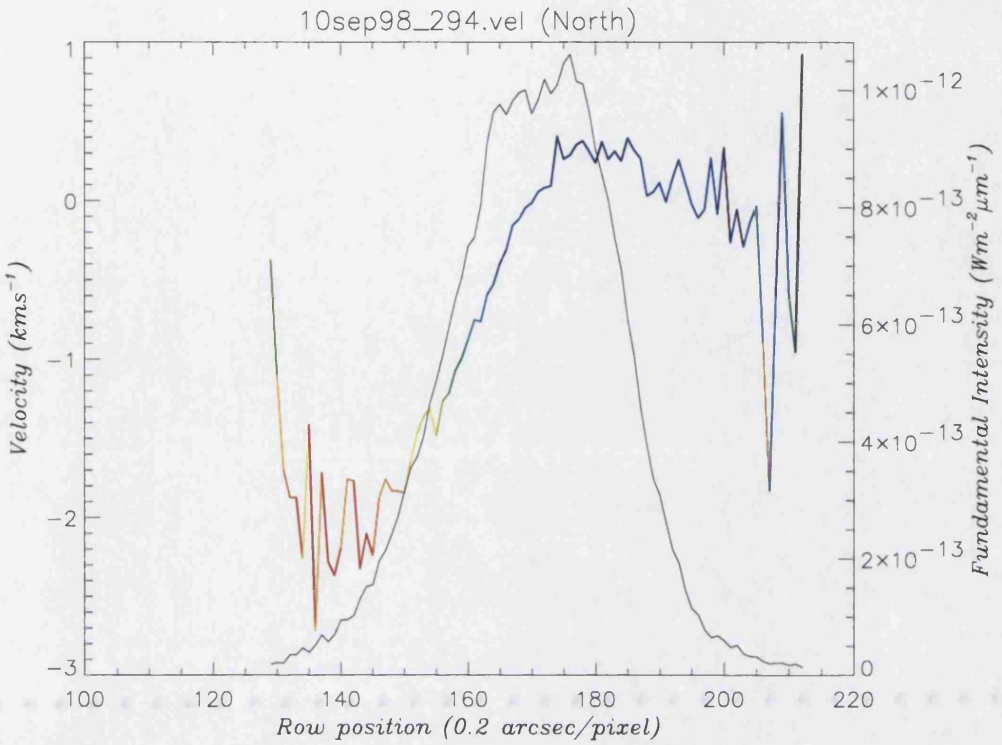

Figure 4-9: The pre-spatial velocity profile (blue-red shift) plotted with the fundamental intensity, taken at 12:24U.T. with a CML of 148°, from the 10N5 set of spectra

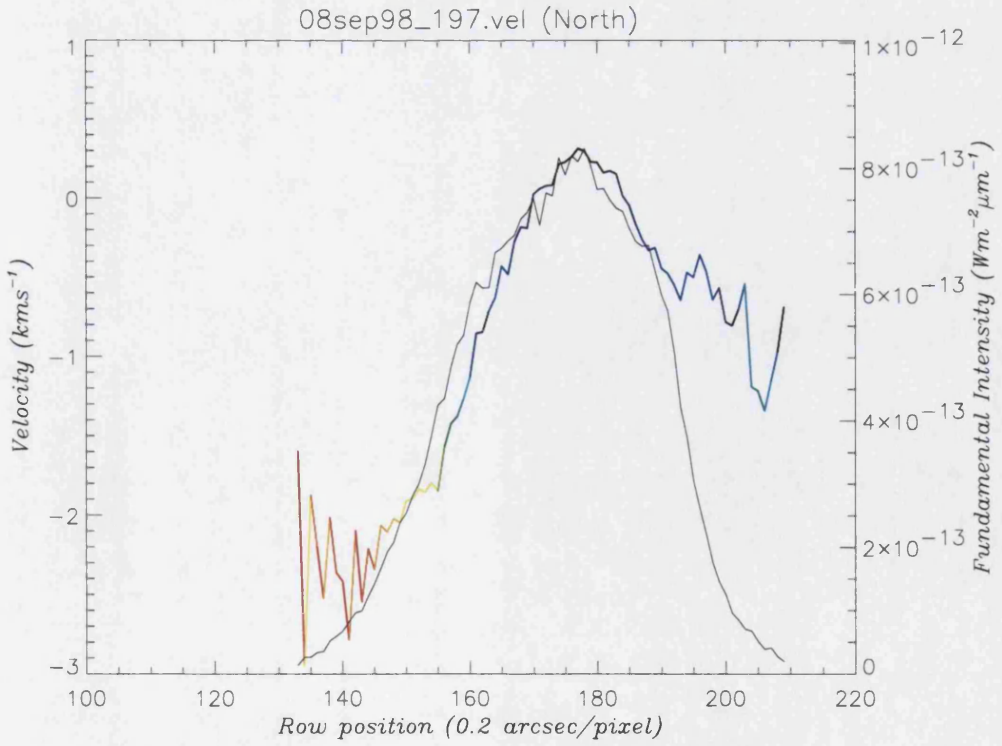

Figure 4-10: The pre-spatial velocity profile (blue-red shift) plotted with the fundamental intensity, taken at 10:54U.T. with a CML of 152°, from the 8N5 set of spectra

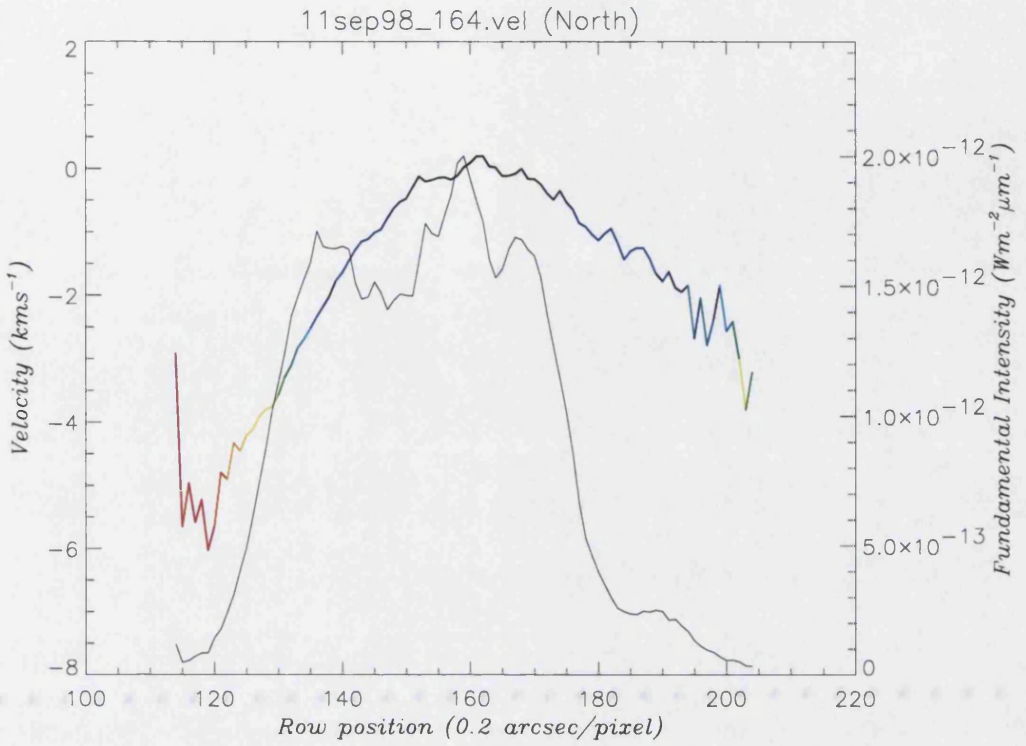

Figure 4-11: The pre-spatial velocity profile (blue-red shift) plotted with the fundamental intensity, taken at 08:32U.T. with a CML of 158°, from the 11N4 set of spectra

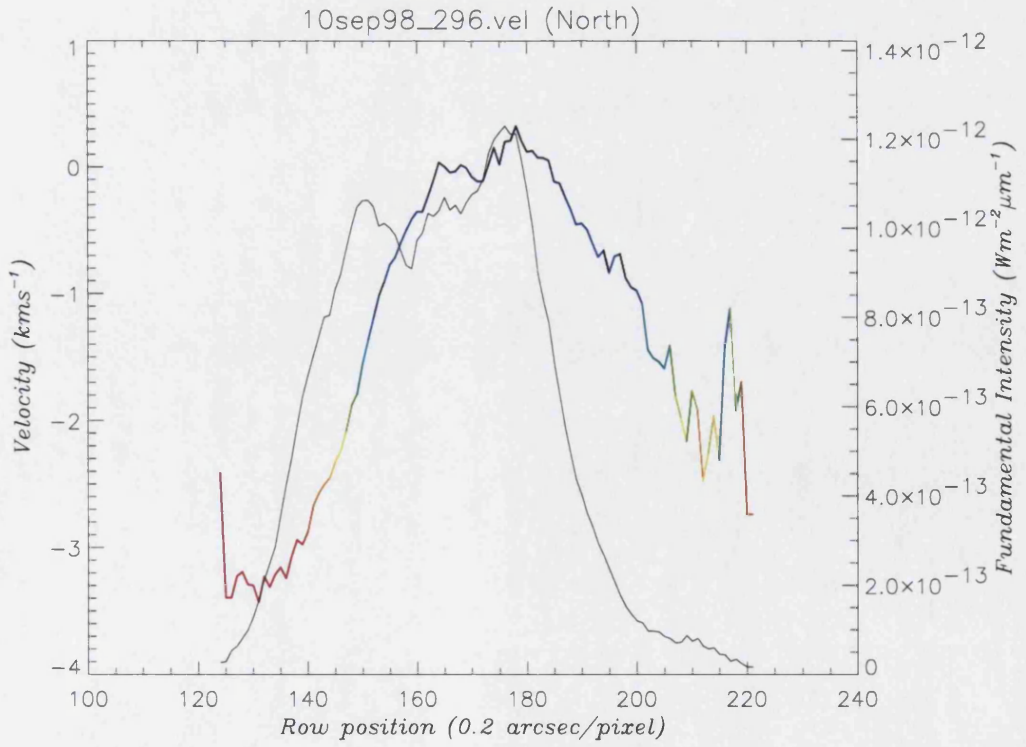

Figure 4-12: The pre-spatial velocity profile (blue-red shift) plotted with the fundamental intensity, taken at 12:26U.T. with a CML of 149°, from the 10N5 set of spectra

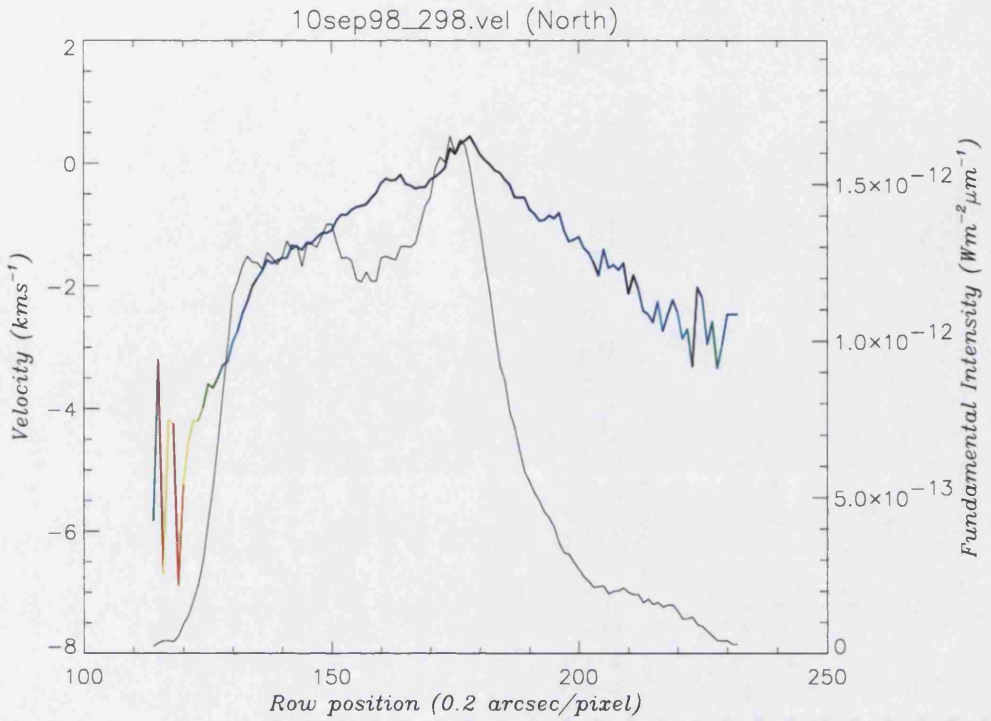

Figure 4-13: The pre-spatial velocity profile (blue-red shift) plotted with the fundamental intensity, taken at 12:28U.T. with a CML of 150°, from the 10N5 set of spectra

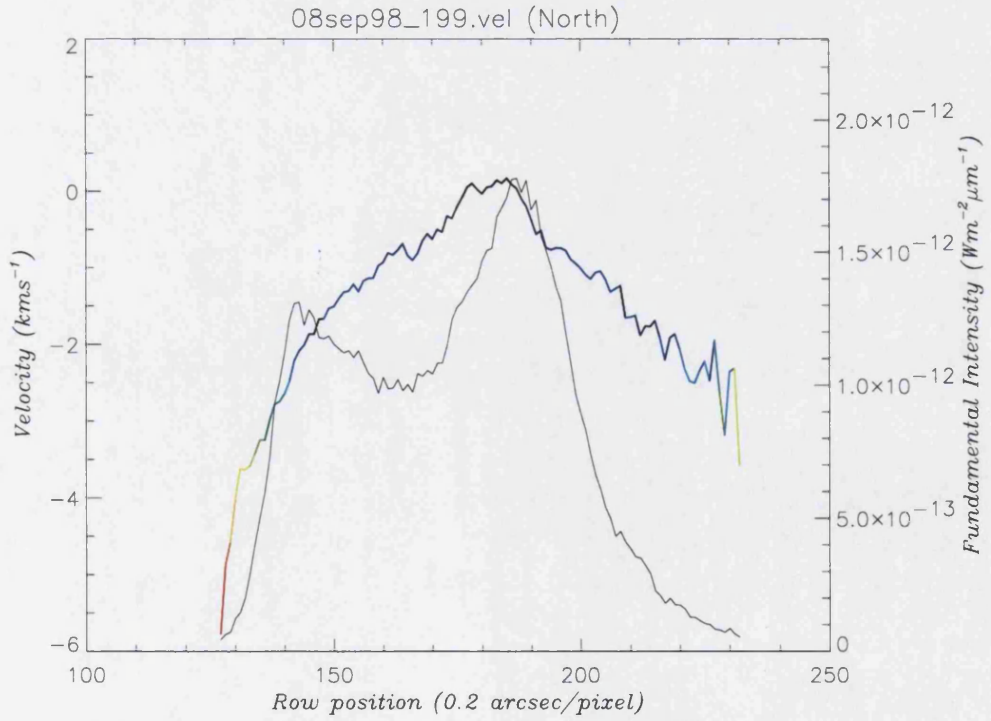

Figure 4-14: The pre-spatial velocity profile (blue-red shift) plotted with the fundamental intensity, taken at 10:56U.T. with a CML of 153°, from the 8N5 set of spectra

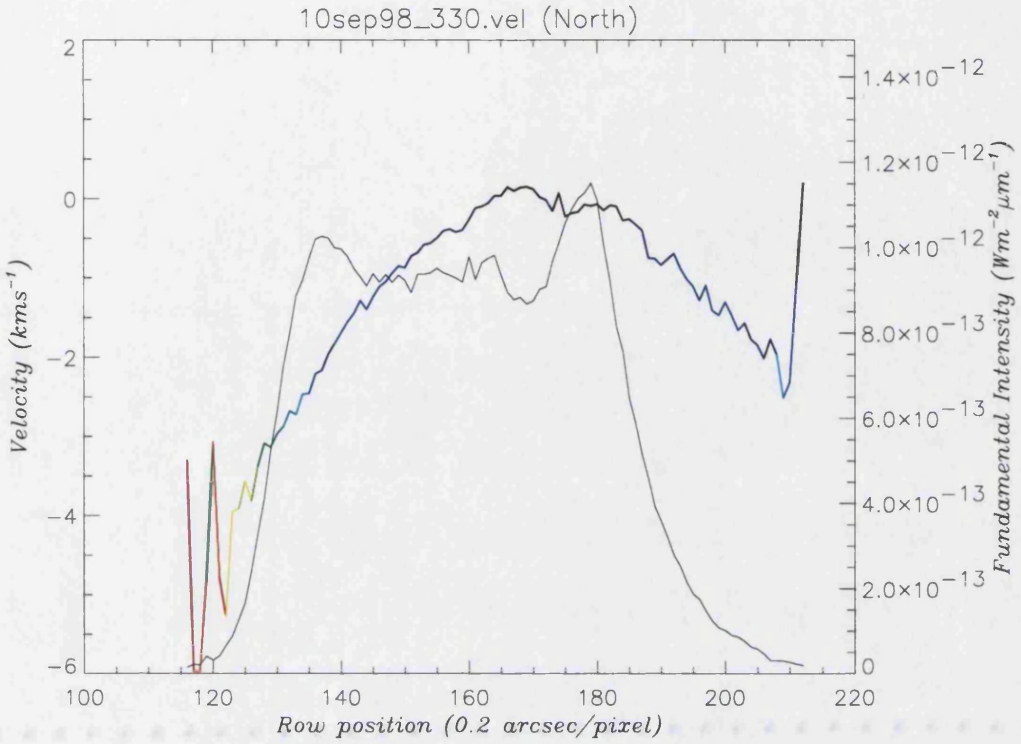

Figure 4-15: The pre-spatial velocity profile (blue-red shift) plotted with the fundamental intensity, taken at 13:00U.T. with a CML of 170°, from the 10N6 set of spectra

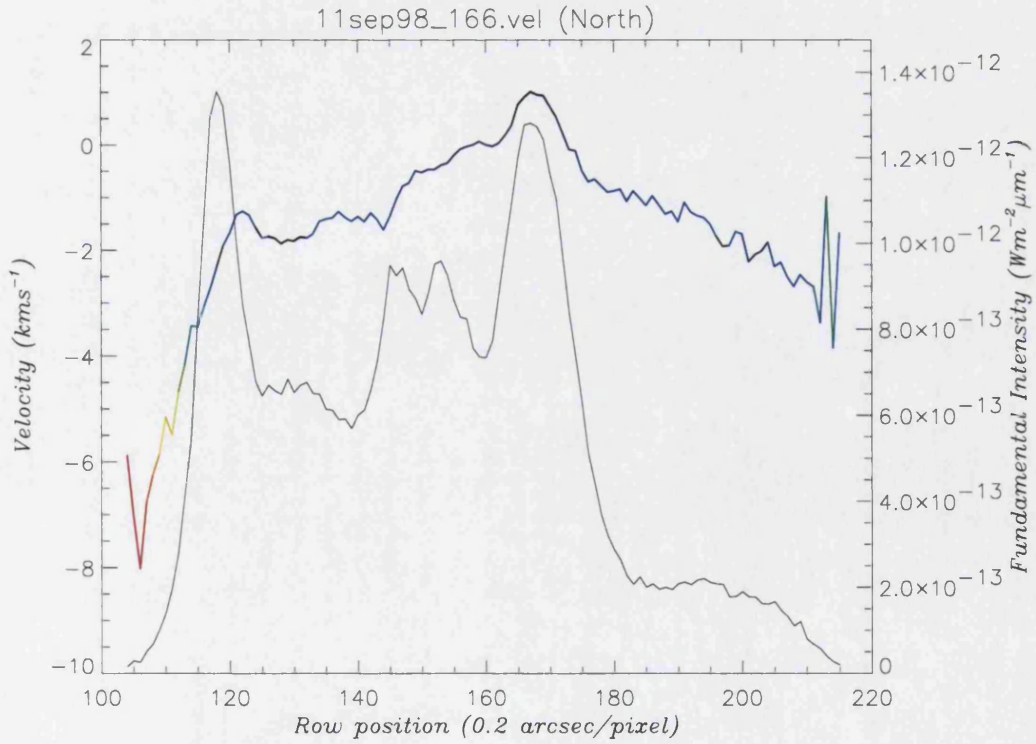

Figure 4-16: The pre-spatial velocity profile (blue-red shift) plotted with the fundamental intensity, taken at 08:34U.T. with a CML of 159°, from the 11N4 set of spectra

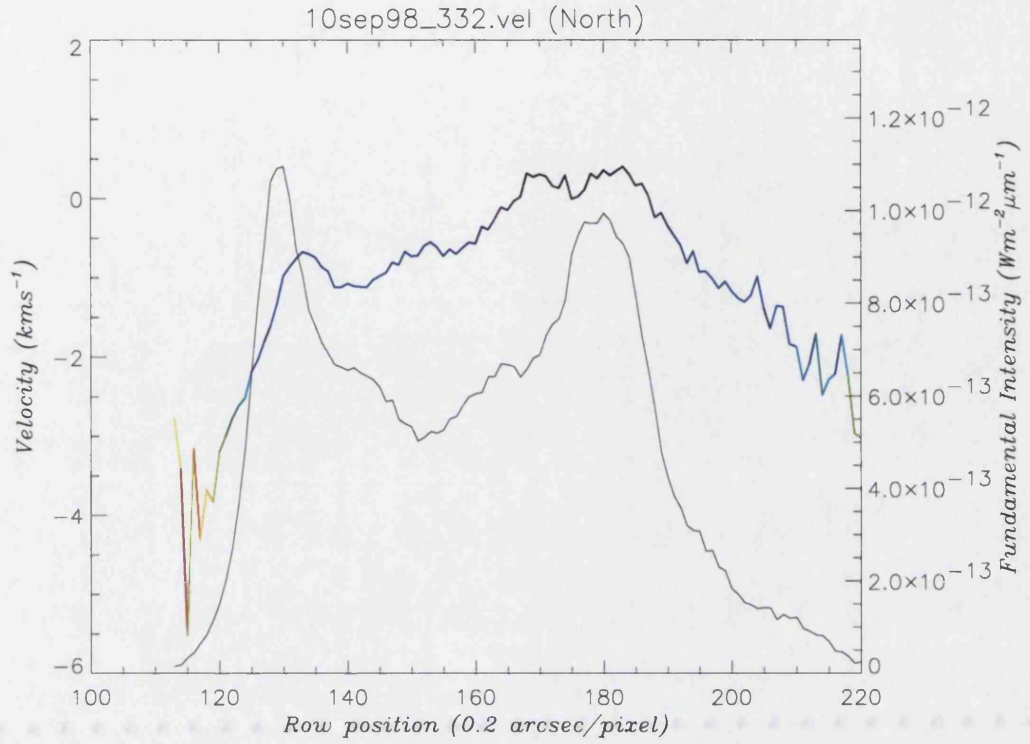

Figure 4-17: The pre-spatial velocity profile (blue-red shift) plotted with the fundamental intensity, taken at 13:02U.T. with a CML of 171°, from the 10N6 set of spectra

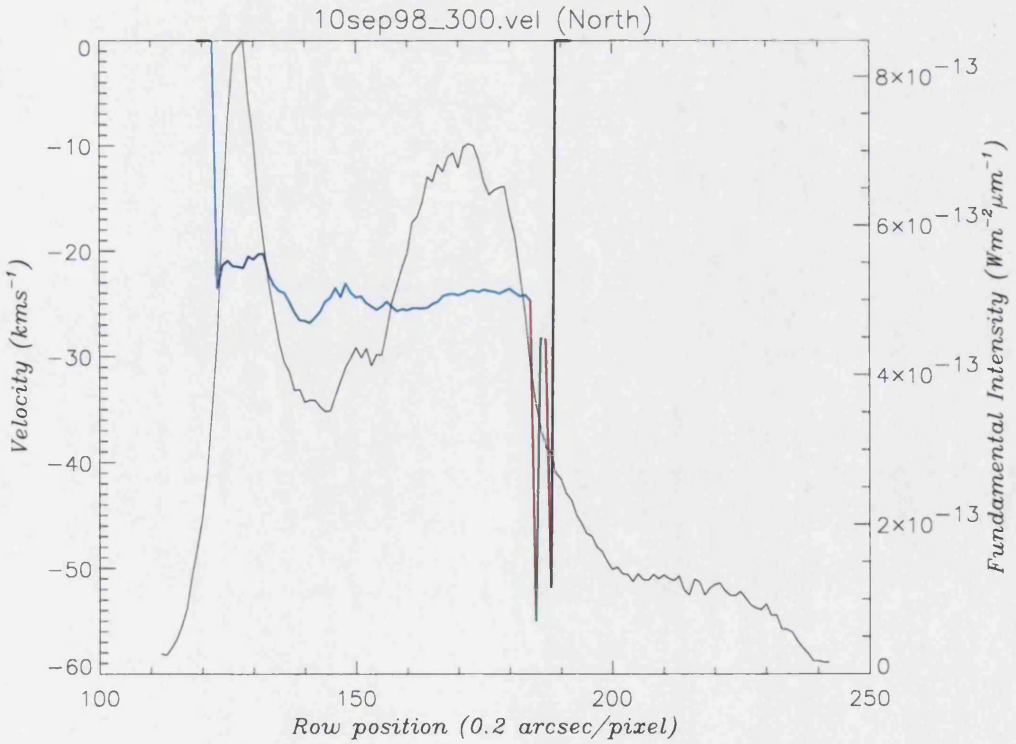

Figure 4-18: The pre-spatial velocity profile (blue-red shift) plotted with the fundamental intensity, taken at 12:30U.T. with a CML of 151°, from the 10N5 set of spectra

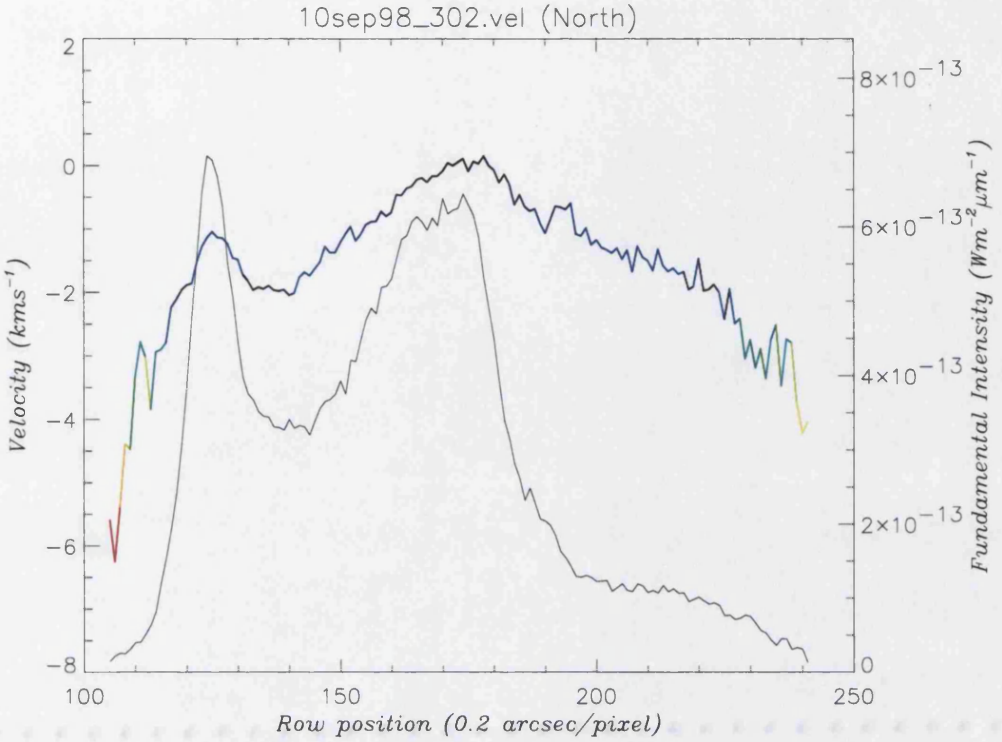

Figure 4-19: The pre-spatial velocity profile (blue-red shift) plotted with the fundamental intensity, taken at 12:32U.T. with a CML of 153°, from the 10N5 set of spectra

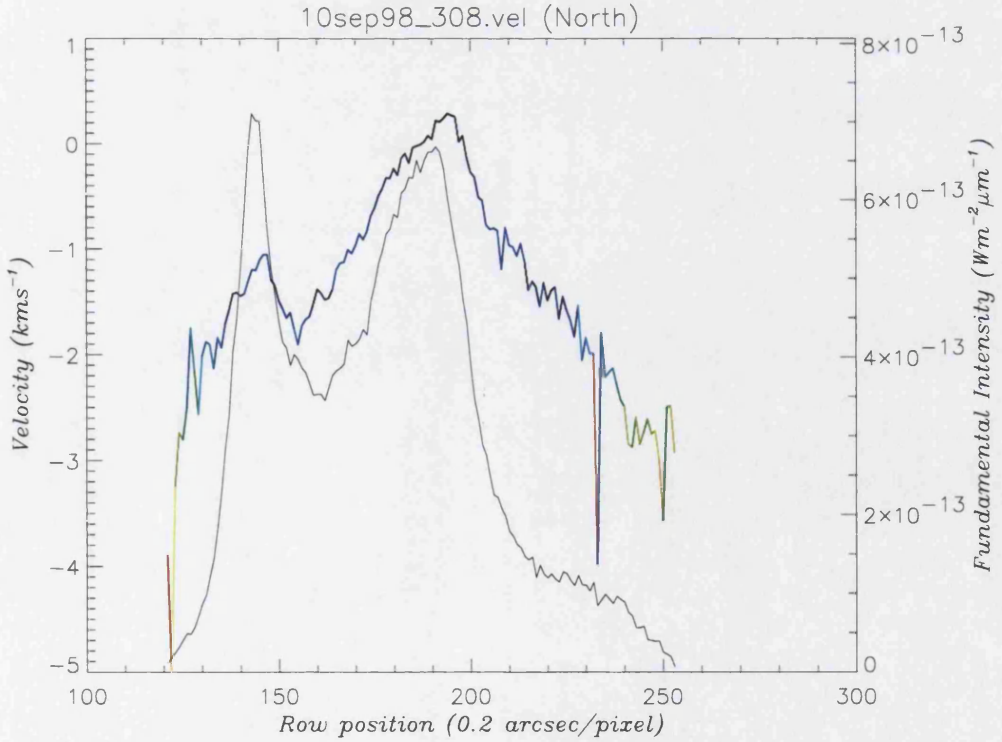

Figure 4-20: The pre-spatial velocity profile (blue-red shift) plotted with the fundamental intensity, taken at 12:38U.T. with a CML of 156°, from the 10N5 set of spectra

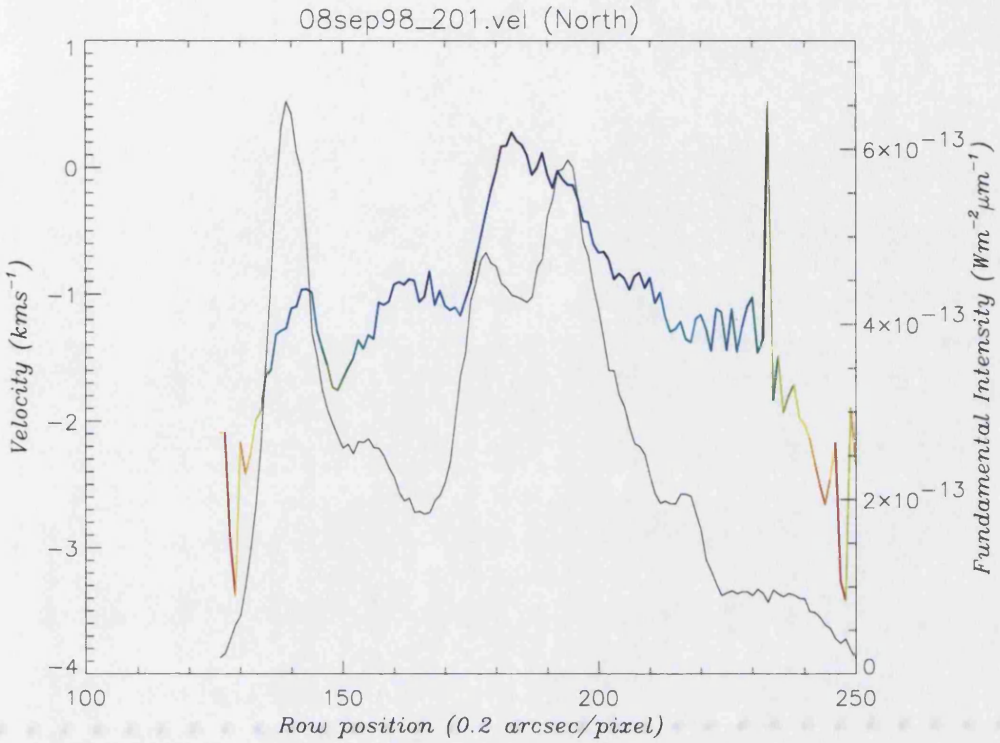

Figure 4-21: The pre-spatial velocity profile (blue-red shift) plotted with the fundamental intensity, taken at 10:58U.T. with a CML of 155°, from the 8N5 set of spectra

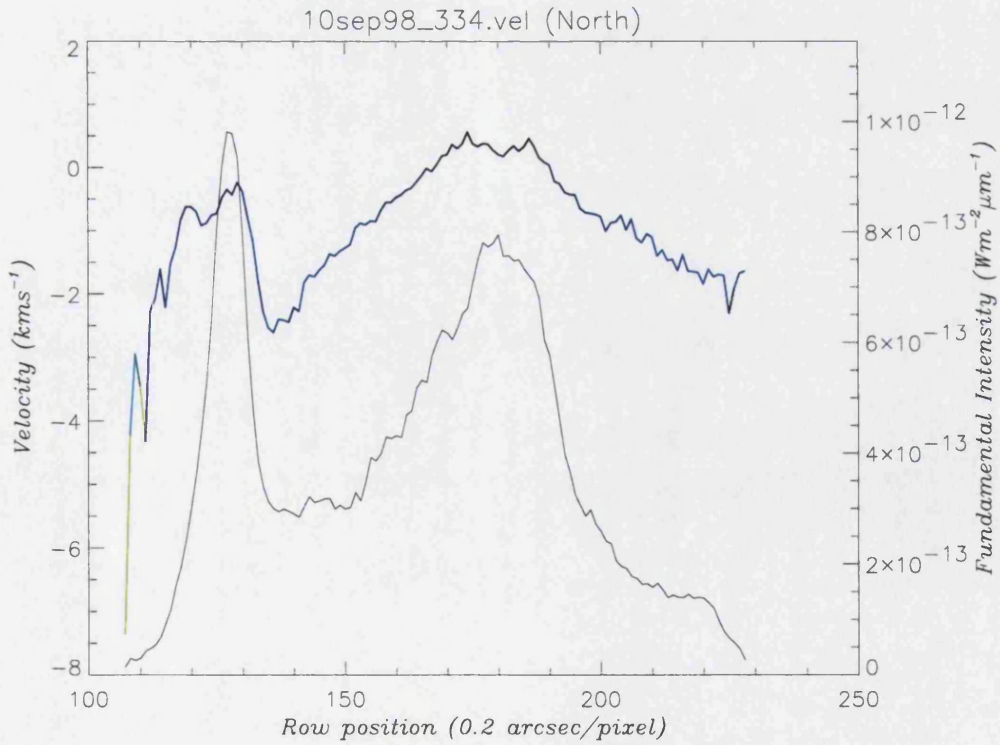

Figure 4-22: The pre-spatial velocity profile (blue-red shift) plotted with the fundamental intensity, taken at 13:04U.T. with a CML of 172°, from the 10N6 set of spectra

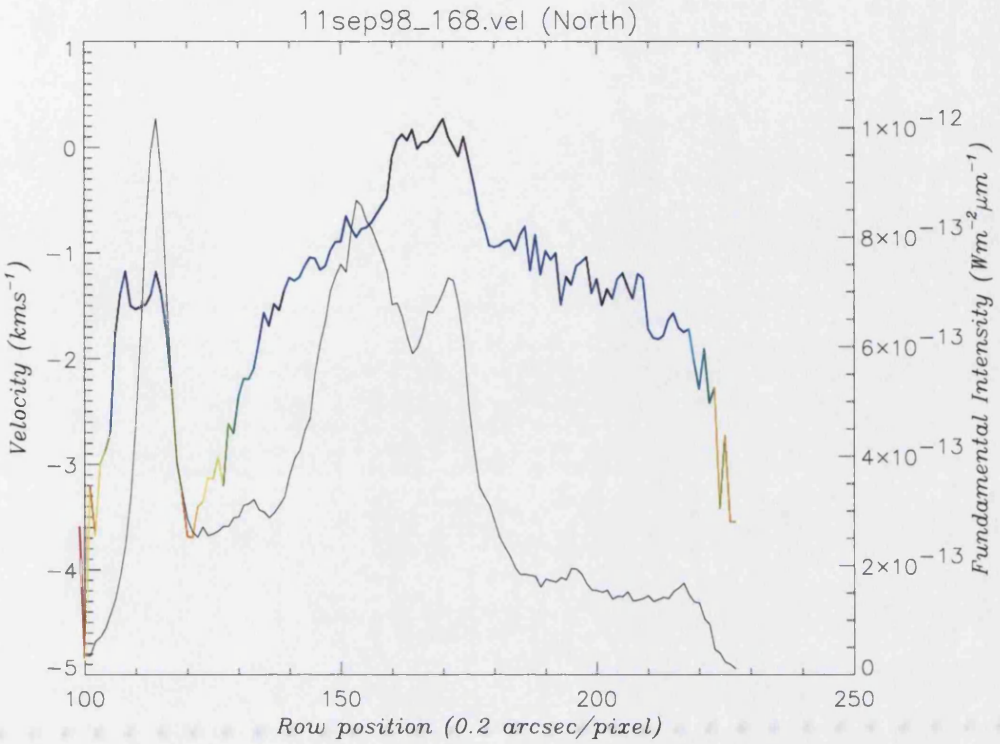

Figure 4-23: The pre-spatial velocity profile (blue-red shift) plotted with the fundamental intensity, taken at 08:35U.T. with a CML of 160°, from the 11N4 set of spectra

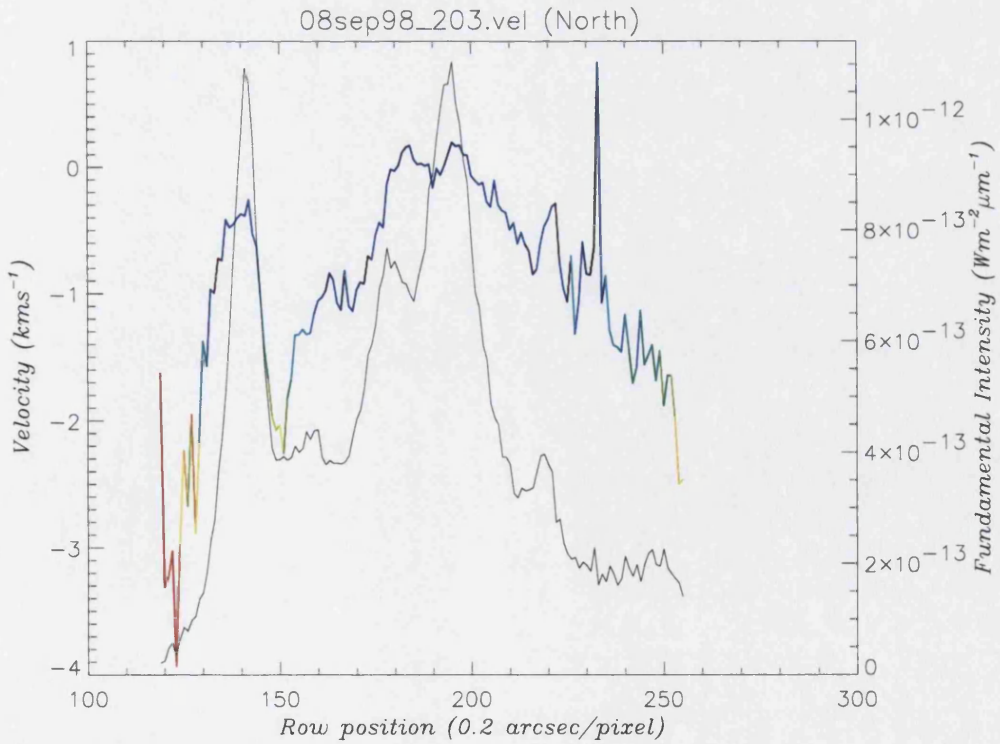

Figure 4-24: The pre-spatial velocity profile (blue-red shift) plotted with the fundamental intensity, taken at 11:00U.T. with a CML of 156°, from the 8N5 set of spectra

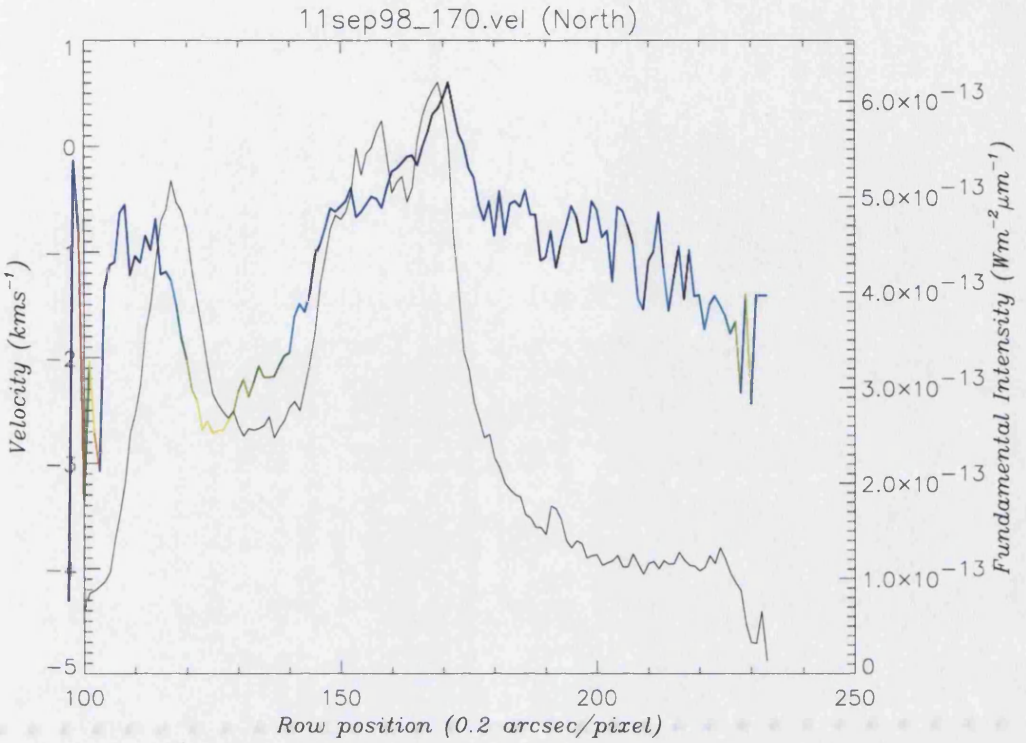

Figure 4-25: The pre-spatial velocity profile (blue-red shift) plotted with the fundamental intensity, taken at 08:37U.T. with a CML of 161°, from the 11N4 set of spectra

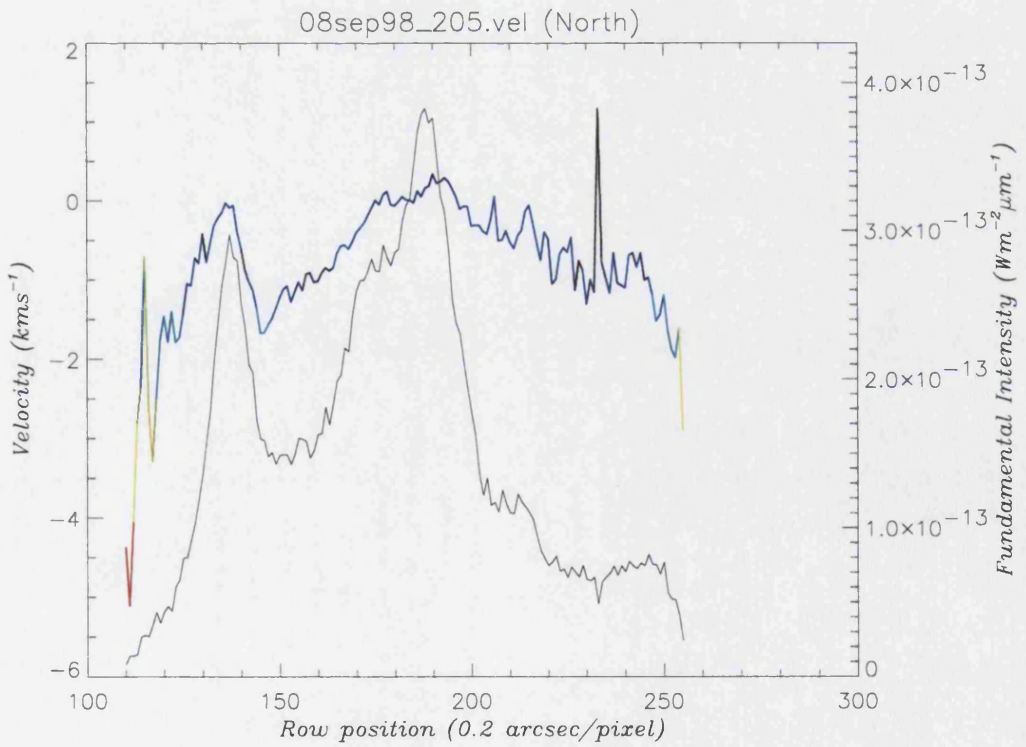

Figure 4-26: The pre-spatial velocity profile (blue-red shift) plotted with the fundamental intensity, taken at 11:02U.T. with a CML of 157°, from the 8N5 set of spectra

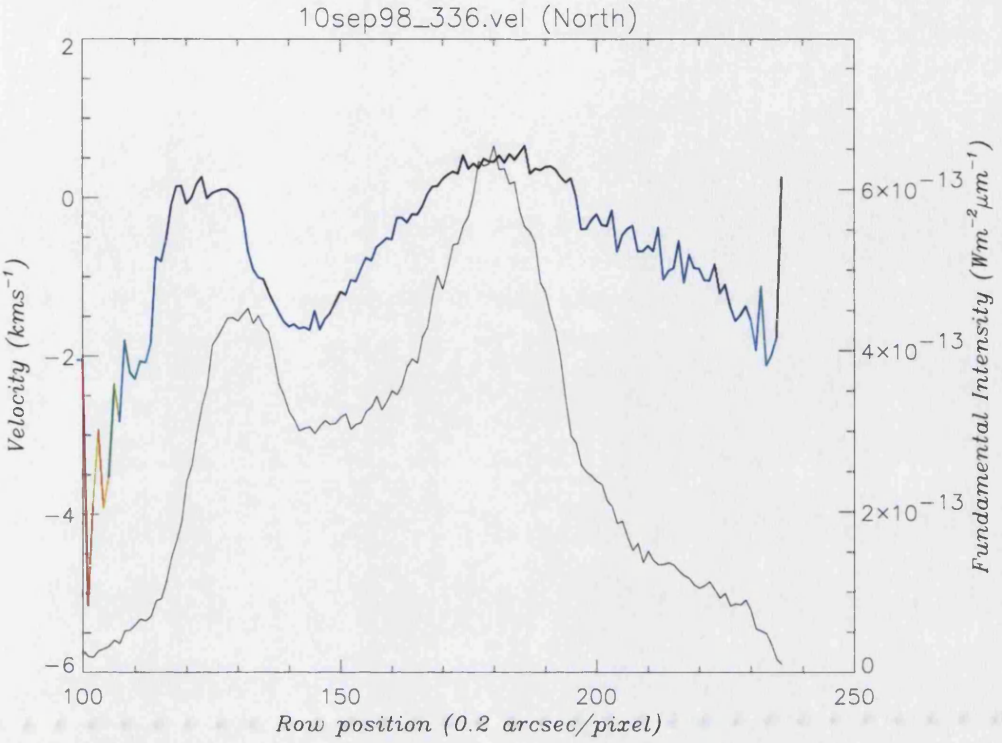

Figure 4-27: The pre-spatial velocity profile (blue-red shift) plotted with the fundamental intensity, taken at 13:06U.T. with a CML of 173°, from the 10N6 set of spectra

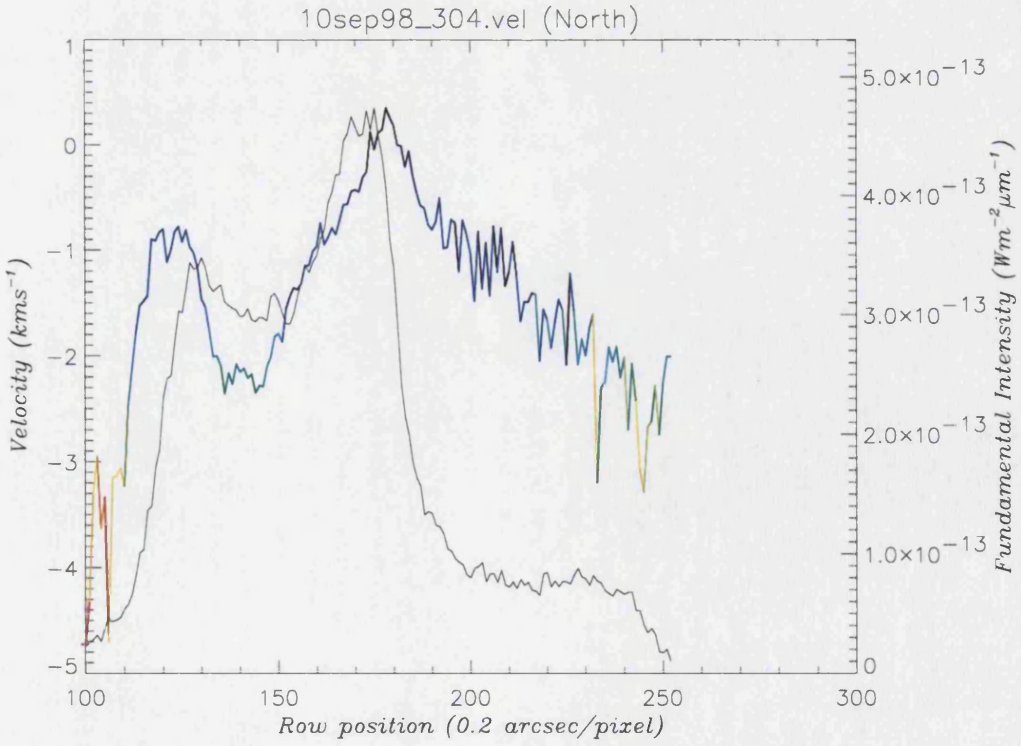

Figure 4-28: The pre-spatial velocity profile (blue-red shift) plotted with the fundamental intensity, taken at 12:34U.T. with a CML of 154°, from the 10N5 set of spectra

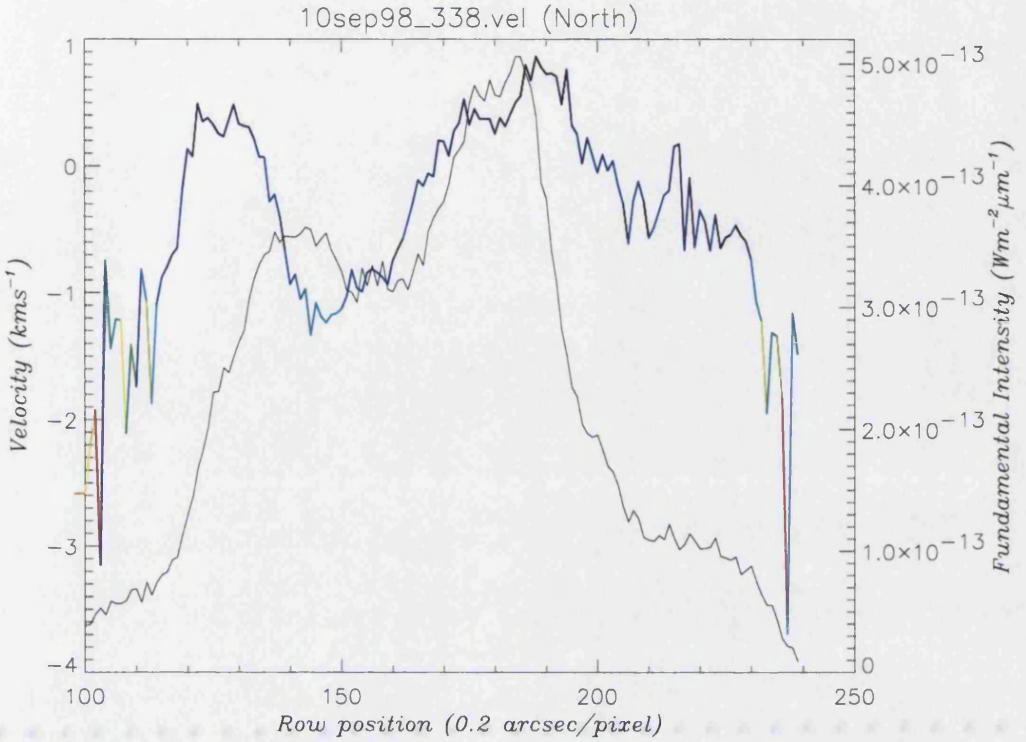

Figure 4-29: The pre-spatial velocity profile (blue-red shift) plotted with the fundamental intensity, taken at 13:08U.T. with a CML of 174°, from the 10N6 set of spectra

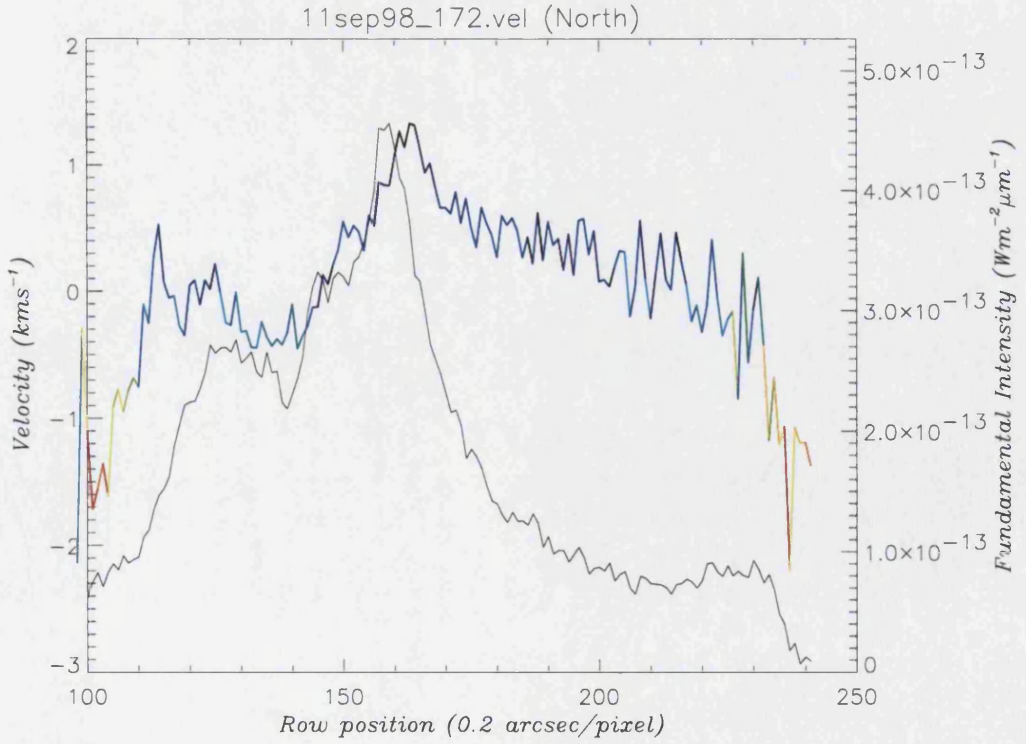

Figure 4-30: The pre-spatial velocity profile (blue-red shift) plotted with the fundamental intensity, taken at 08:39U.T. with a CML of 162°, from the 11N4 set of spectra

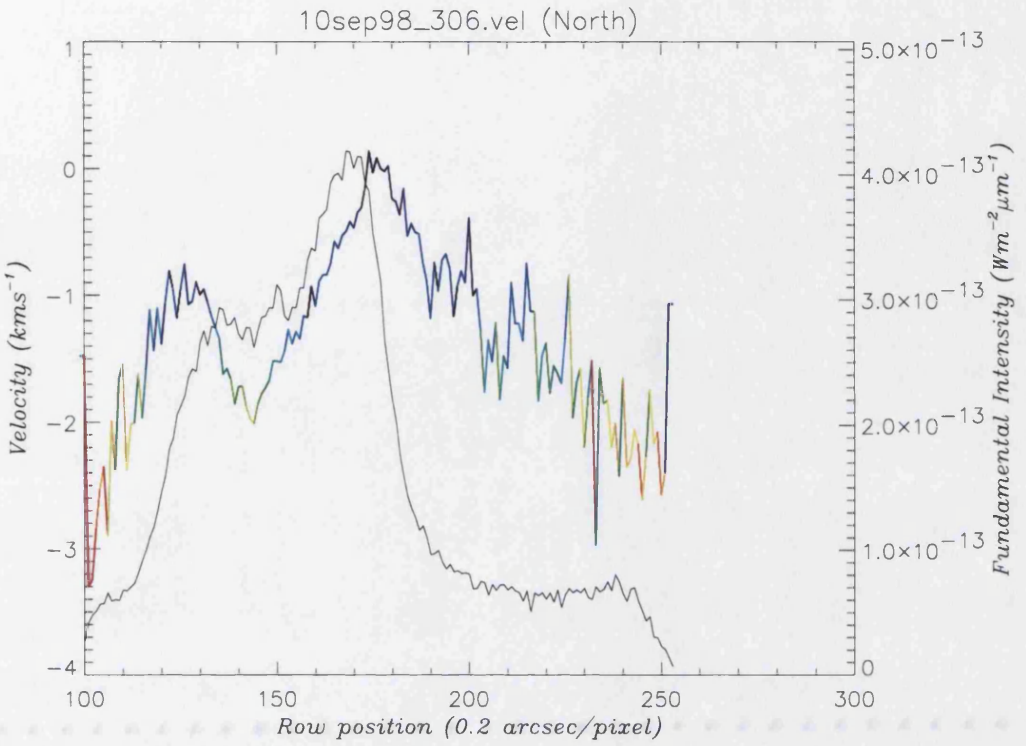

Figure 4-31: The pre-spatial velocity profile (blue-red shift) plotted with the fundamental intensity, taken at 12:36U.T. with a CML of 155°, from the 10N5 set of spectra

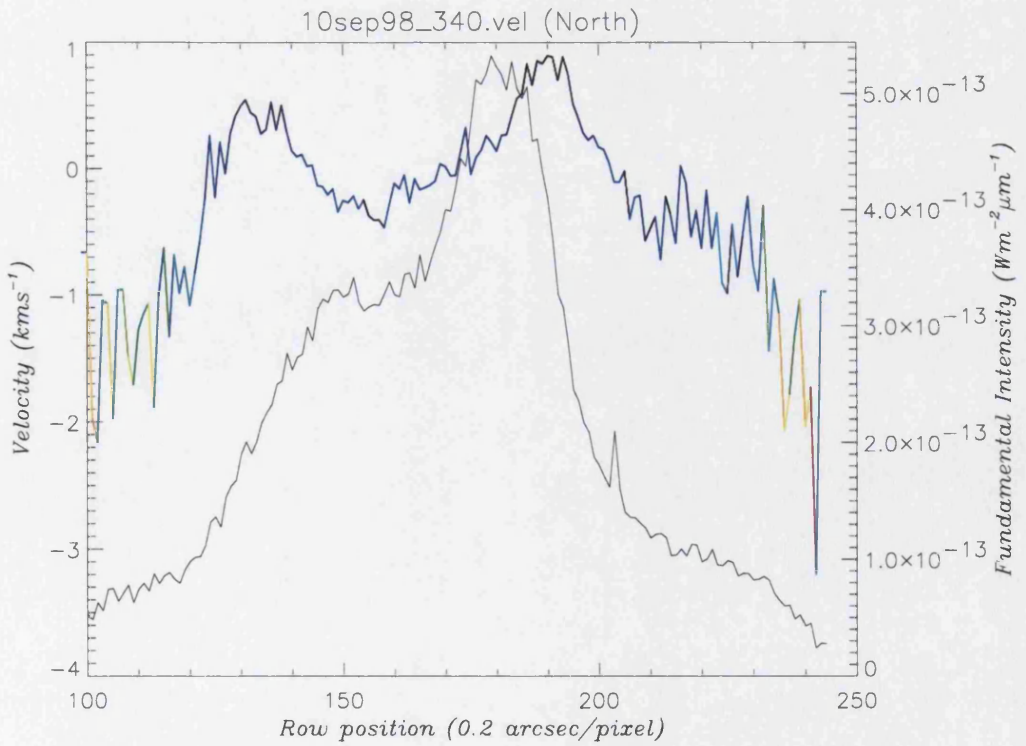

Figure 4-32: The pre-spatial velocity profile (blue-red shift) plotted with the fundamental intensity, taken at 13:10U.T. with a CML of 176°, from the 10N6 set of spectra

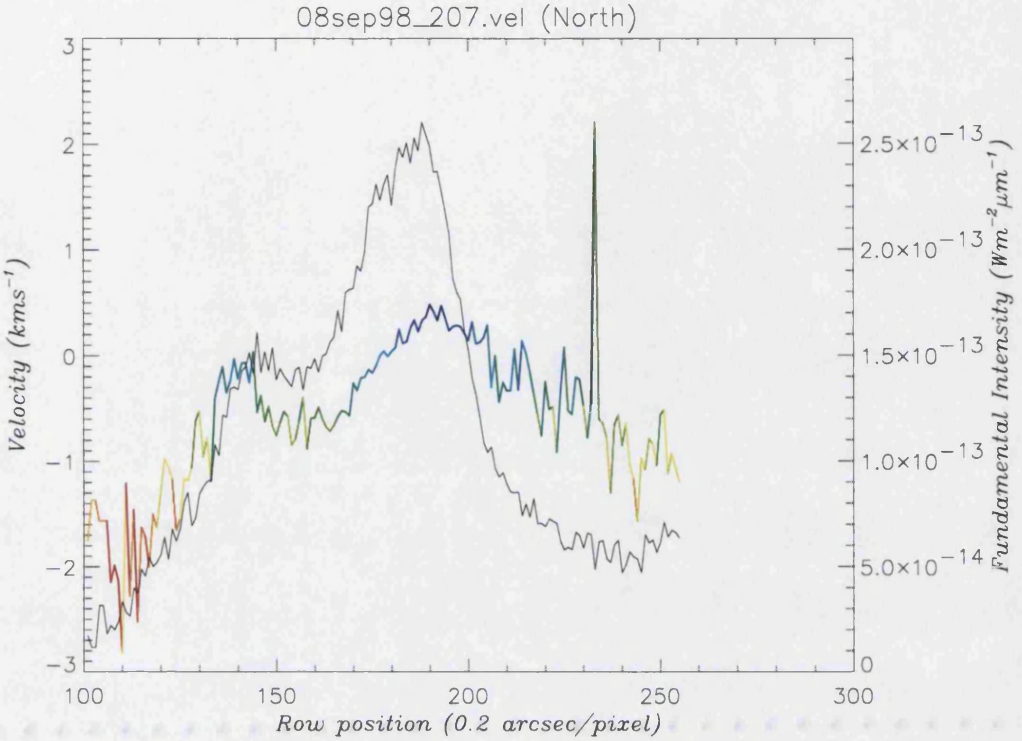

Figure 4-33: The pre-spatial velocity profile (blue-red shift) plotted with the fundamental intensity, taken at 11:04U.T. with a CML of 158°, from the 8N5 set of spectra

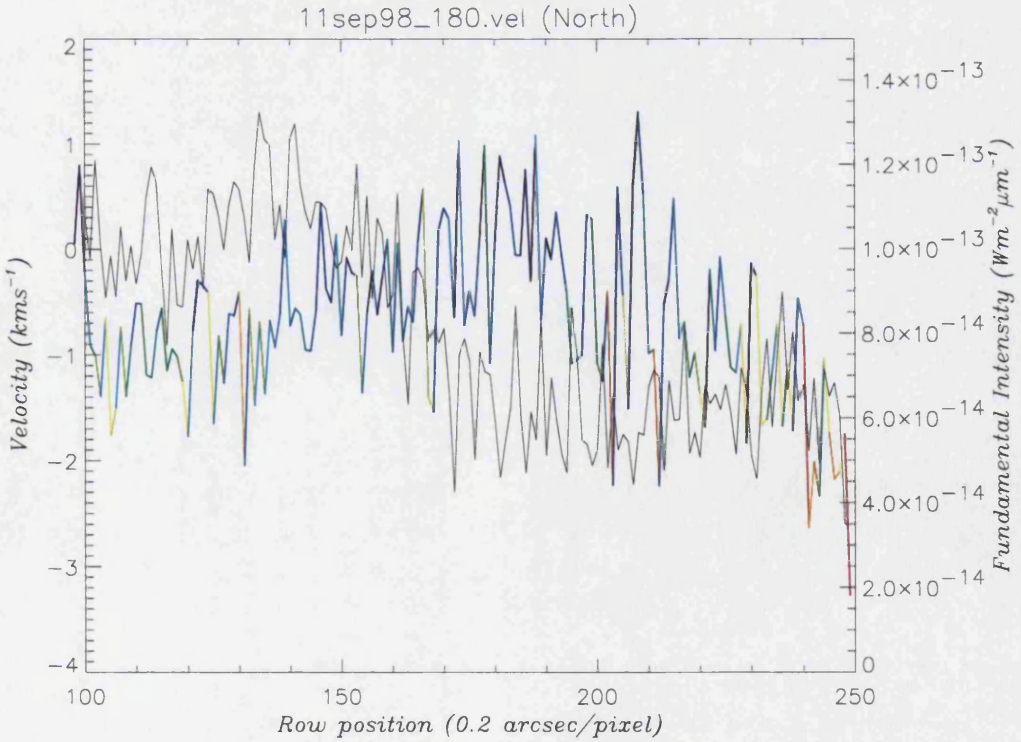

Figure 4-34: The pre-spatial velocity profile (blue-red shift) plotted with the fundamental intensity, taken below the aurora at 08:46U.T., from the 11N4 set of spectra

4.2 Actual Velocities

Accounting for the effects of the spatial distortion of the spectral line within the instrument is essential before an understanding of the true dynamics within the auroral region can be obtained. The removal of this effect allows a direct measure of true relative velocities and, assuming a zero velocity on the body of the planet below the aurora, the "actual" line-of-sight velocities as well.

The quality of the spectral images is extremely good, and the ability to use Gaussian fitting to find the relative intensity peak position has been shown to be highly accurate. This means that the limitations are not in the spectral image itself, but in the accompanying image of Jupiter used to calculate the spatial effect. It is thus important in the analysis of actual velocity profiles to consider the effects of spatial correction, and the extent to which it influences the structure of features in terms of relative velocity.

4.2.1 Velocity profiles for 8N5 and 11N4

Image quality for the 8th and 11th

The CSHELL instrument is primarily a spectrometer, and its ability as an imaging camera is usually of secondary concern. Despite this, by leaving the slit wheel open, it is possible to take images at the same spatial resolution as the spectral profiles. This function is provided by CSHELL for the purpose of positioning the telescope accurately on the desired object, which was the reason for producing the images taken with each set of spectra. The quality of the images is thus considerably less than that of the spectral images that they accompany, with a total exposure time of just 8 seconds compared with the 50 seconds used for each spectral image.

The images taken on the night of the 10^{th} are all affected by the "double bounce" effect described in **2.3.5 Bounce feature on images**, making them effectively unusable for the calculation of a spatial effect. This leaves only two of the four sets of spectra detailed above for further analysis: 8N5 and 11N4.

The 3.953μm images from 8N5 and 11N4 (Figure 4-35), show a wide difference in quality. The image from the 8th clearly shows the general features discussed in **3.1.1 General auroral morphology**, with the form of both the auroral oval and the polar bright and dark regions discernible. However, the level of detail present is not as good as that within the image from 11N4, which shows finer-scale structures across the aurora. The spatial corrections for 8N5 are potentially less accurate than those of 11N4, and must therefore be regarded with care in the analysis below.

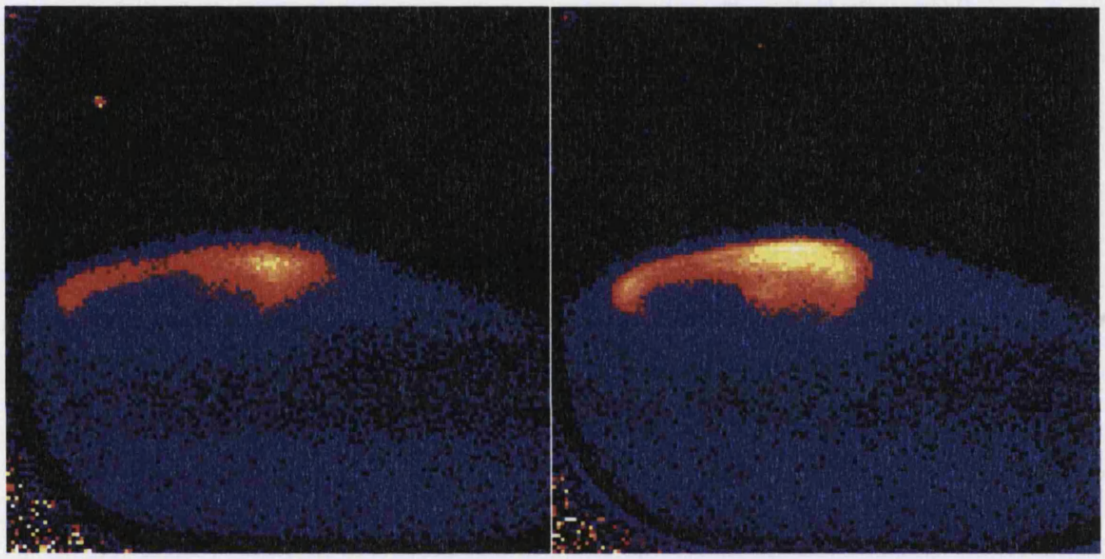

Figure 4-35: 3.953μm images from the 8th (on the left) and the 11th (on the right)

Actual velocity profiles

Given the difficulty in removing spatial effects from the velocity profiles, we need to constantly check their reliability as measures of true wind speeds in the Jovian frame of reference. In assessing the reliability of our actual velocity profiles, one indicator can be the extent to which features seen in these profiles are also present in the pre-spatial profiles. Thus we consider features - particularly relative trends - which are seen in both pre-spatial and spatially corrected profiles to be especially reliable. Features which tend to show up *post*-spatial processing have to be viewed with some caution.

The spatial correction ($\Delta V_s(y)$) appears to consistently remove the general curved shape seen within the pre-spatial velocity, accounting for the effect of intensity variations on both the limbs and on the body of the planet. The calculated spatial correction appears to

vary consistently from profile to profile, but the sign of this effect within the auroral region is reversed, the morphology of the spatial correction profile mirrored on either side of where the auroral oval reaches its maximum width, an effect caused by the reverse in anisotropy of light in the slit either side of the widest extent of the oval (for example, see the spatial correction on Figure 4-41 and Figure 4-43).

Since the pre-spatial velocity is consistent across latitudinal position in the aurora, this means that profiles taken in the higher-latitude aurora have different features enhanced or removed than those in the lower-latitude aurora. With a few notable exceptions, both the auroral oval and the polar region contain the same red-shift to blue-shift velocity divergence between dawn and dusk.

Deviation from this general trend occurs both on the limb (Figure 4-49) and in the lower-latitude auroral region below the point where the spatial effect reverses its sign (Figure 4-55), removing the auroral oval variation, but maintaining the polar region velocity gradient. That this only appears on 8N5 strongly suggests that it is caused by the poor image quality on the 8th, resulting in a poorly calculated spatial correction.

That the large majority of profiles show the same general trends suggests that the pre-spatial velocities, while being unable to directly measure actual line-to-site velocities, are a reasonable measure of the relative form of the internal auroral velocity.

Fine-scale variations in velocity can also be seen within the auroral region. But comparison with the pre-spatial profiles shows that some of these variations are artefacts of the spatial correction.

Taking the example of the spectral profile 08sep98_199 (the actual velocity in Figure 4-52, and the spatial correction and pre-spatial velocity in Figure 4-53), the extent of the variability seen in the spatial effect is not evident in the pre-spatial velocity, which varies smoothly. This suggests that the calculated spatial effect may be producing some false fine-scale structure into the actual velocity structure. However, while the spatial correction is sometimes overlarge, it is rarely if ever large enough to distort the general trends in velocity, specifically the strong red-shift in the dark polar region and the red/blue-dawn/dusk velocity divergence.

Importantly, some spectral profiles - *e.g.*, Figure 4-40, where the spatial effect and pre-spatial velocity profiles show very similar size and shape of fine-scale features - appear to have a very good correspondence between the scale of the spatial effect and features seen within the pre-spatial effect, suggesting the actual velocity profile produced is accurate.

Many of the spectral profiles fall between these two extremes, with spatial correction following the pre-spatial velocities reasonably well even in fine-scale features, but possibly creating some minor velocity variations. This shows the significance of checking the final velocity structure against the spatial correction and pre-spatial velocity when examining fine scale features, to ascertain the origin of such features.

In the case of Figure 4-40, the spatial correction adds to the existing pre-spatial velocity profile within the aurora. This shows fine-scale structure within the polar region that is potentially less clear on other spectral profiles where the poorer quality of calculated spatial correction is overriding the true velocity profile. This profile shows small variations in the bright polar region potentially connected with the variations in fundamental intensity, as well as a significant reduction of 1 km/s within the dark polar region, narrow enough to suggest a possible significant change in direction of the flow of ionic material.

There appears to be a strong correlation between the features seen in the actual velocity profiles and the regions already delineated by the fundamental intensity (**3.1.1 General auroral morphology**). While the degree of this correlation varies both between nights and individual profiles, the same general velocity structure is apparent within most of the relevant profiles. This general morphology is shown clearly in Figure 4-40, and is repeated not only within those profiles shown here (for example, Figure 4-42, Figure 4-52 and Figure 4-54), but also within most sets of spectra from the 8^{th}, 9^{th} and 11^{th} where the spatial correction can be made, for which we do not present a detailed analysis.

The auroral oval, identifiable from the intensity profile, shows a significant difference in velocity between the dawn and dusk sides. This variation is generally seen on all the profiles, and is notable because the dawn side of the oval is relatively red-shifted, and the dusk side is relatively blue-shifted. The magnitude of this difference varies with latitude

(and thus presumably the line-of-sight effects), but appears to peak at about a 2 km/s difference between the two intensity peaks (Figure 4-40), with each peak consisting of 1 km/s in a different direction. If we assumed we were observing along the auroral ansa, at a latitude ~60°N and that the H_3^+ is flowing parallel to the planetary "surface", this would correspond to an ion jet of ~1.15 km/s.

The polar cap region contains a similar velocity variation, with the Dark Polar Region containing a relative red-shift in velocity, and the Bright Polar Region a relative blue-shift. The extent of this variation is different from that associated with the auroral oval. The DPR appears to have a strong red-shift directly associated, which has a similar velocity to the 1 km/s of the dawn side of the auroral oval (Figure 4-44), but in many cases can be significantly stronger (Figure 4-42), with associated red-shift velocities of 2-3 km/s. The BPR has blue-shifted velocities generally similar to, or less than, the dusk auroral oval.

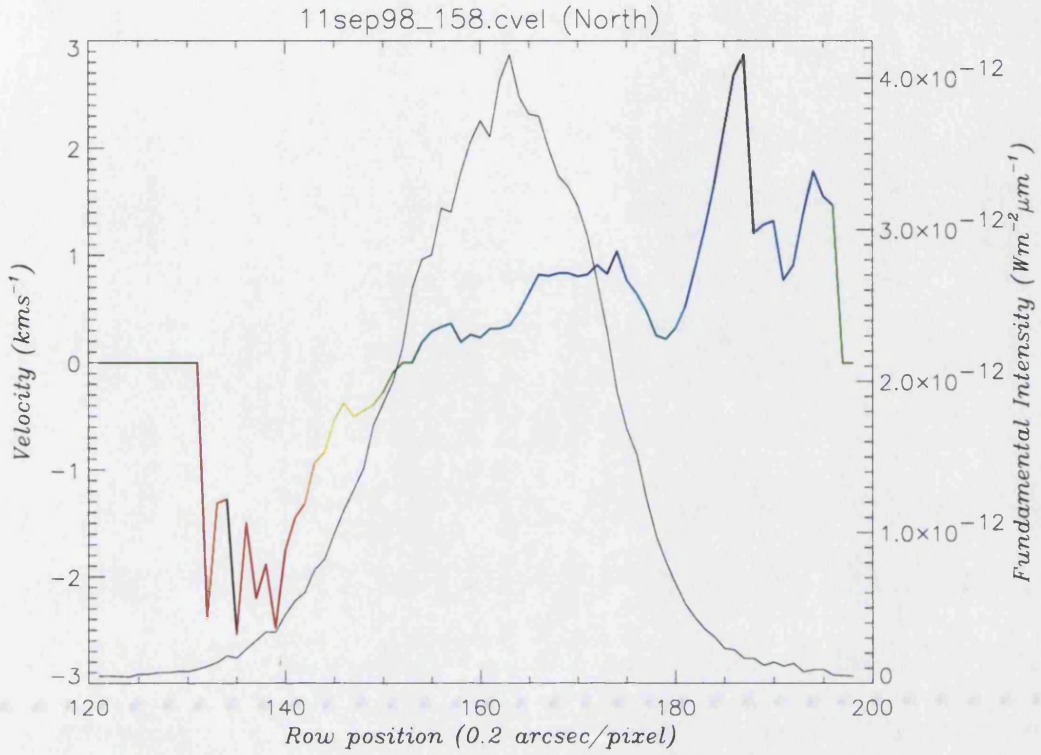

Figure 4-36: The actual velocity profile (an individually scaled non-linear blue-red shift colour scale, used for clarity) plotted with the fundamental intensity, taken at 08:27U.T. with a CML of 155°, from the 11N4 set of spectra

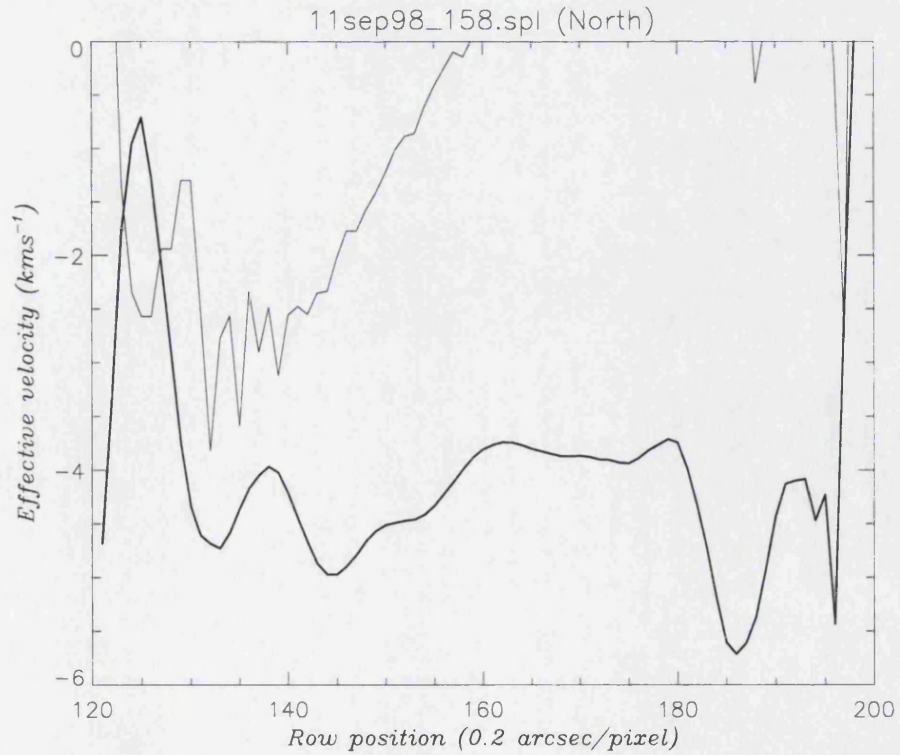

Figure 4-37: The spatial correction that corresponds to the profile taken at 08:27U.T. with a CML of 155°, from the 11N4 set of spectra

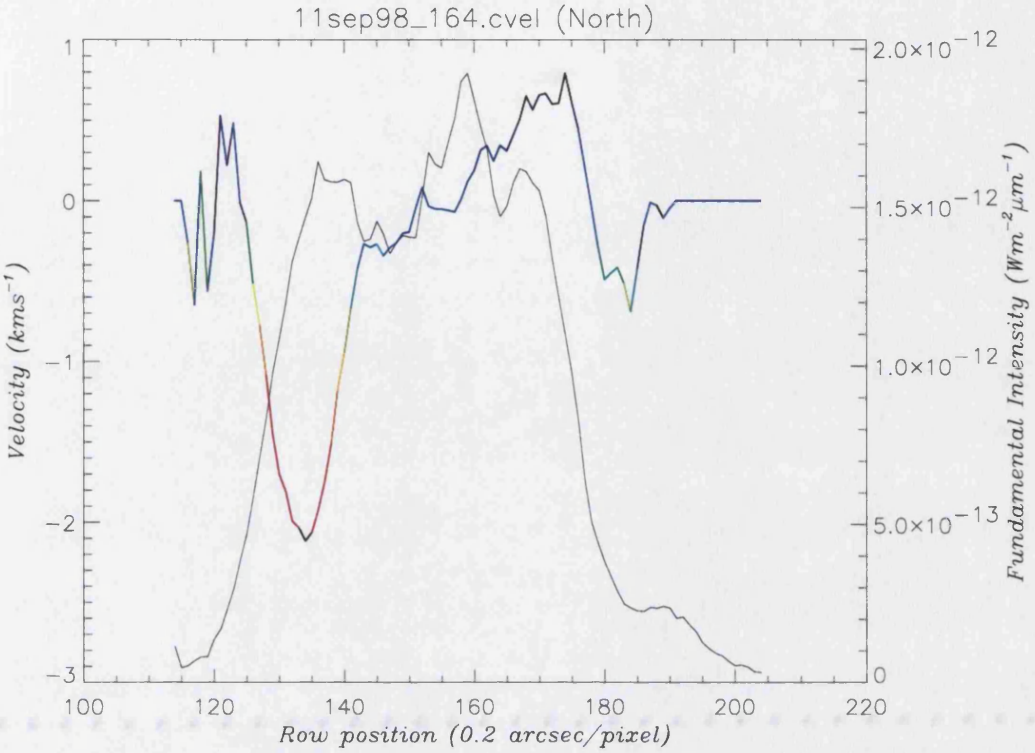

Figure 4-38: The actual velocity profile (blue-red shift) plotted with the fundamental intensity, taken at 08:32U.T. with a CML of 158°, from the 11N4 set of spectra

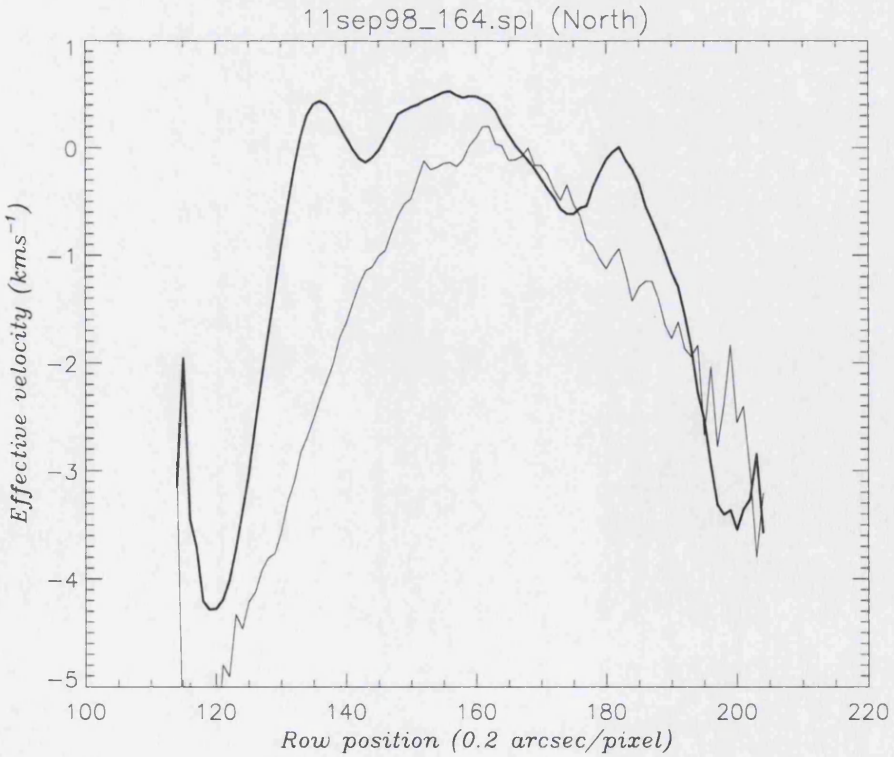

Figure 4-39: The spatial correction that corresponds to the profile taken at 08:32U.T. with a CML of 158°, from the 11N4 set of spectra

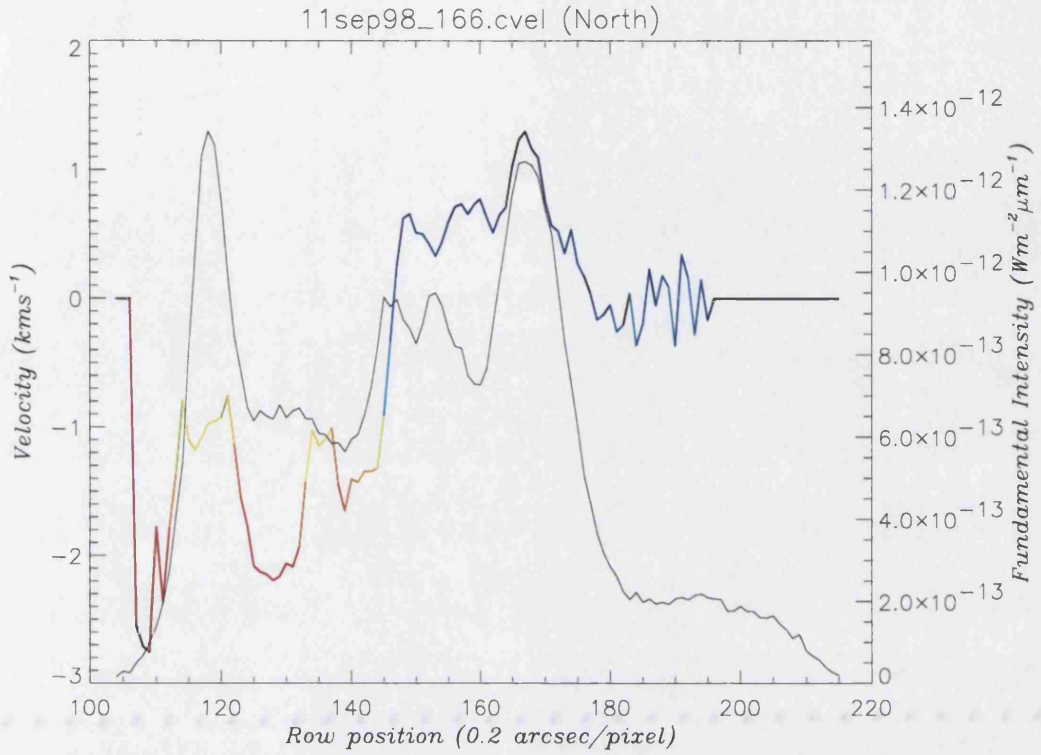

Figure 4-40: The actual velocity profile (blue-red shift) plotted with the fundamental intensity, taken at 08:34U.T. with a CML of 159°, from the 11N4 set of spectra

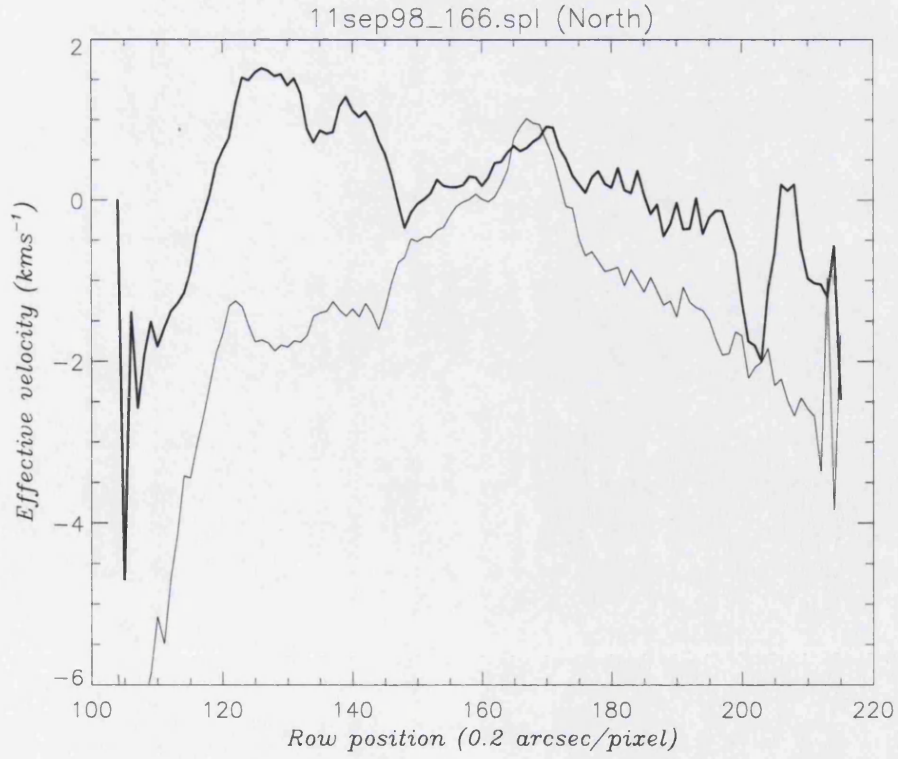

Figure 4-41: The spatial correction that corresponds to the profile taken at 08:34U.T. with a CML of 159°, from the 11N4 set of spectra

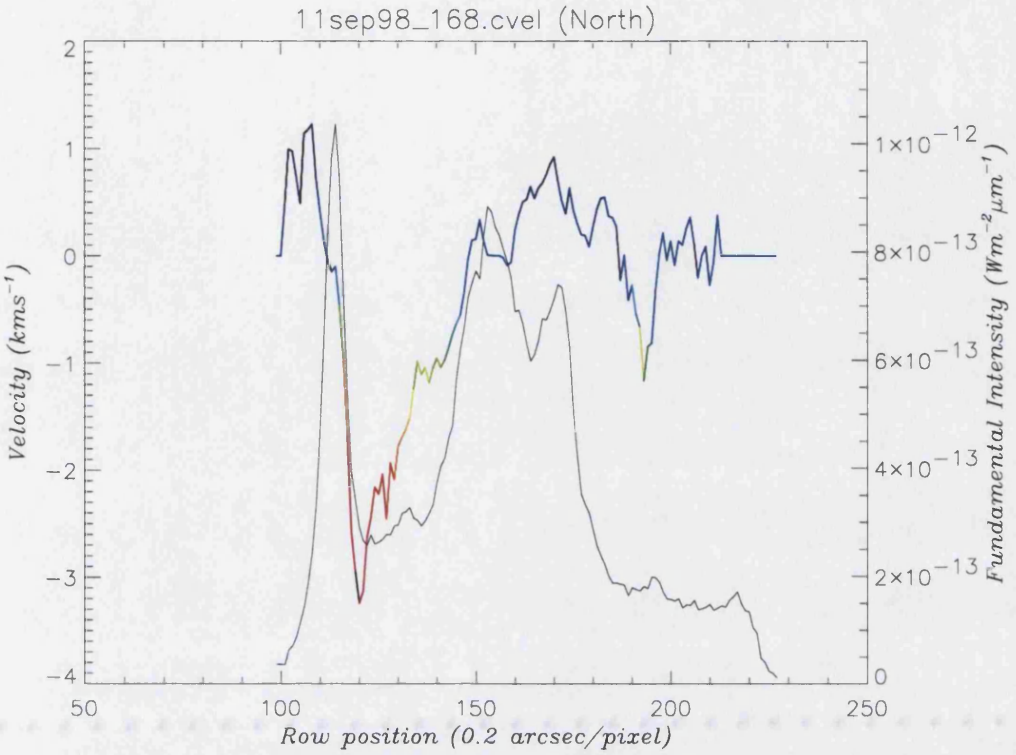

Figure 4-42: The actual velocity profile (blue-red shift) plotted with the fundamental intensity, taken at 08:35U.T. with a CML of 160°, from the 11N4 set of spectra

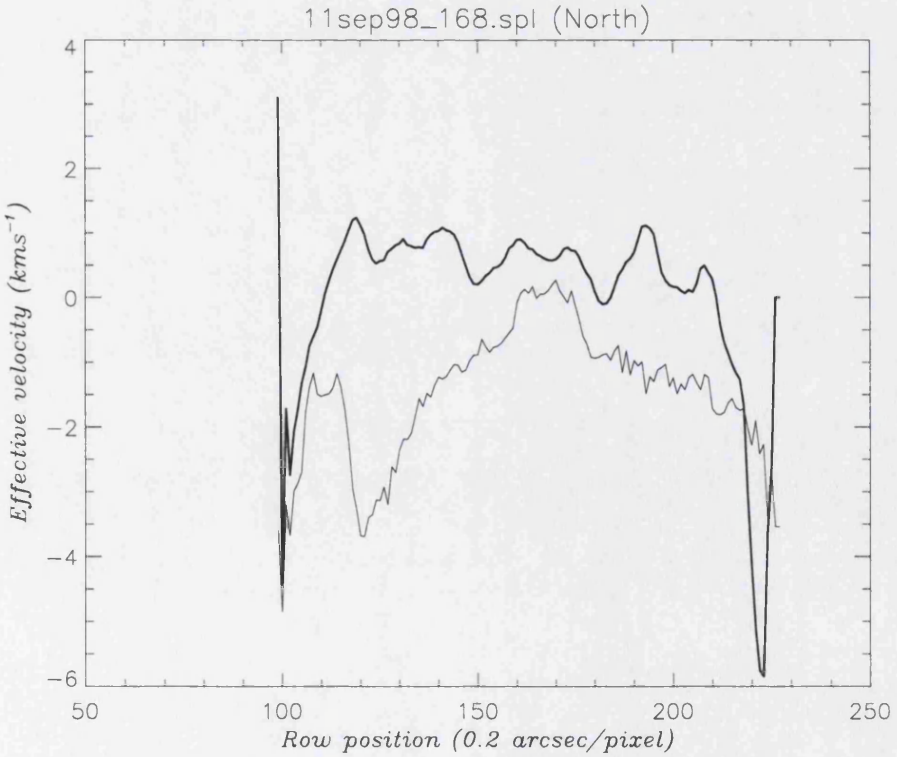

Figure 4-43: The spatial correction that corresponds to the profile taken at 08:35U.T. with a CML of 160°, from the 11N4 set of spectra

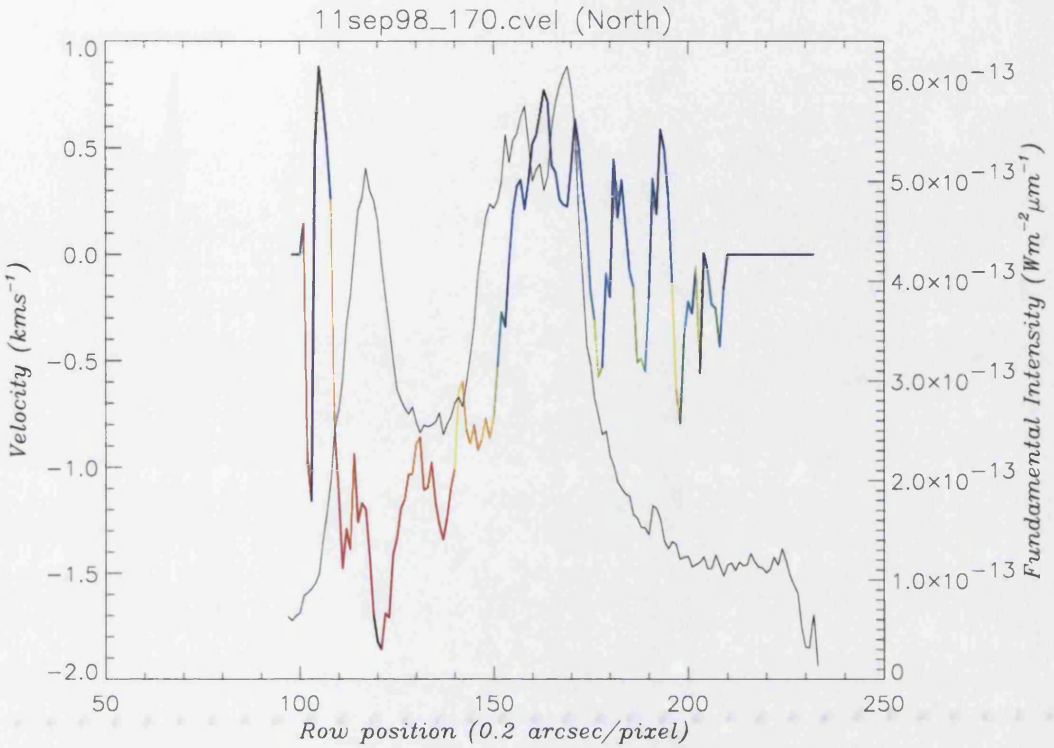

Figure 4-44: The actual velocity profile (blue-red shift) plotted with the fundamental intensity, taken at 08:37U.T. with a CML of 161°, from the 11N4 set of spectra

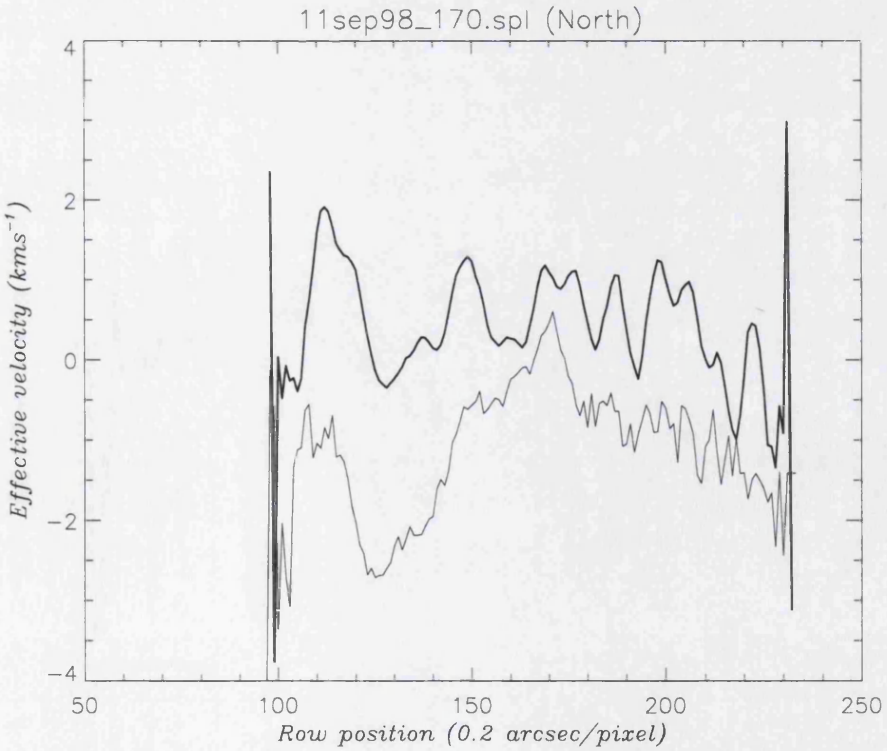

Figure 4-45: The spatial correction that corresponds to the profile taken at 08:37U.T. with a CML of 161°, from the 11N4 set of spectra

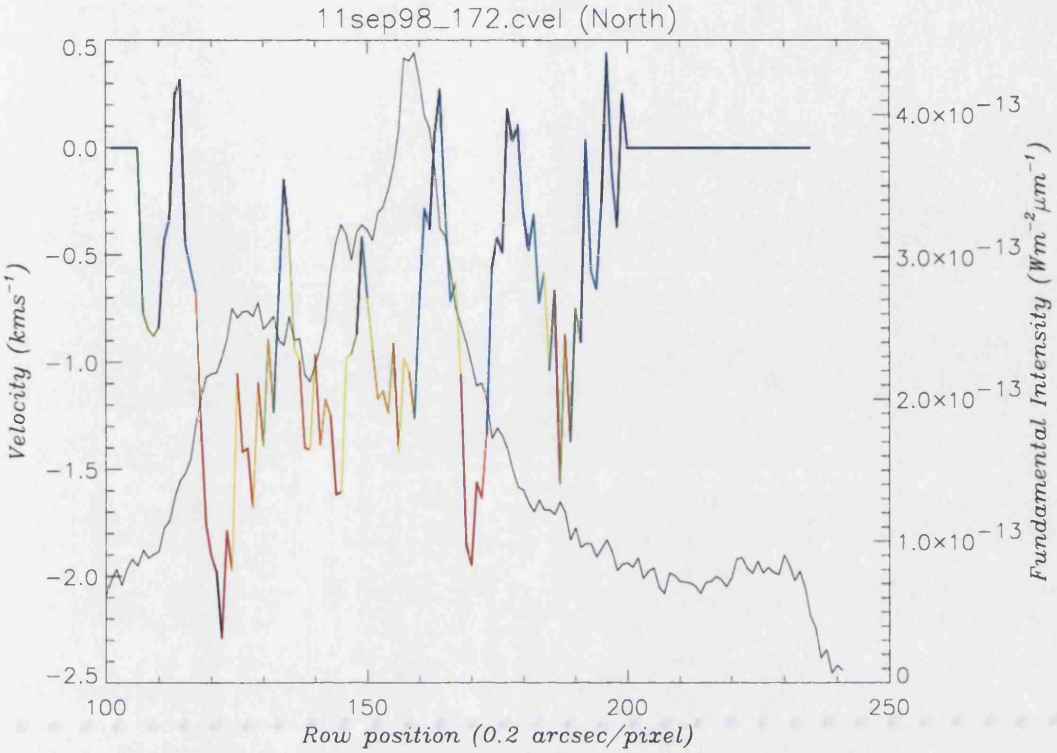

Figure 4-46: The actual velocity profile (blue-red shift) plotted with the fundamental intensity, taken at 08:39U.T. with a CML of 162°, from the 11N4 set of spectra

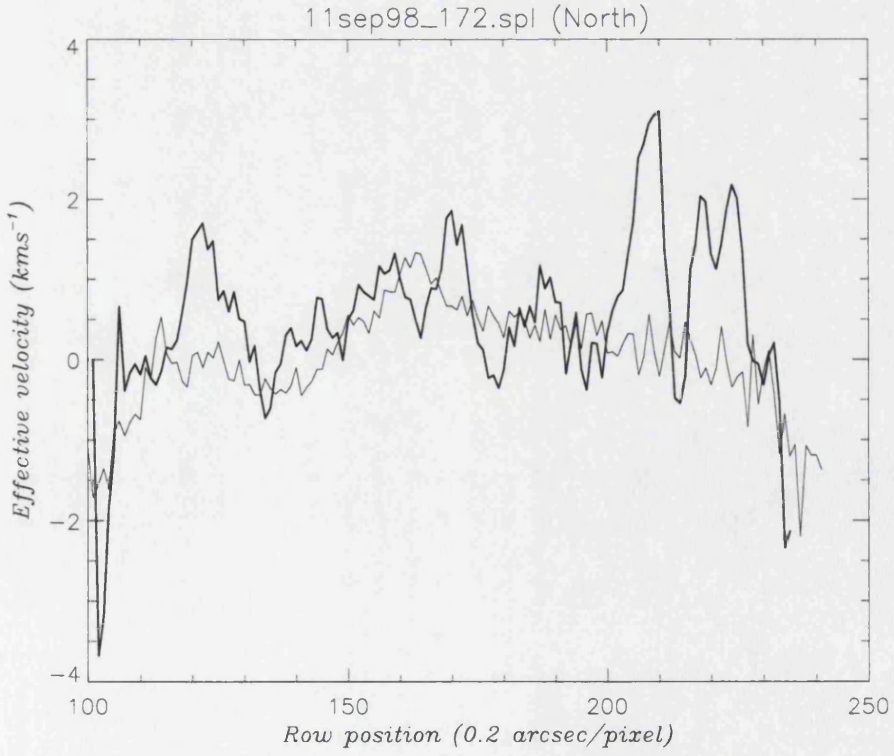

Figure 4-47: The spatial correction that corresponds to the profile taken at 08:39U.T. with a CML of 162°, from the 11N4 set of spectra

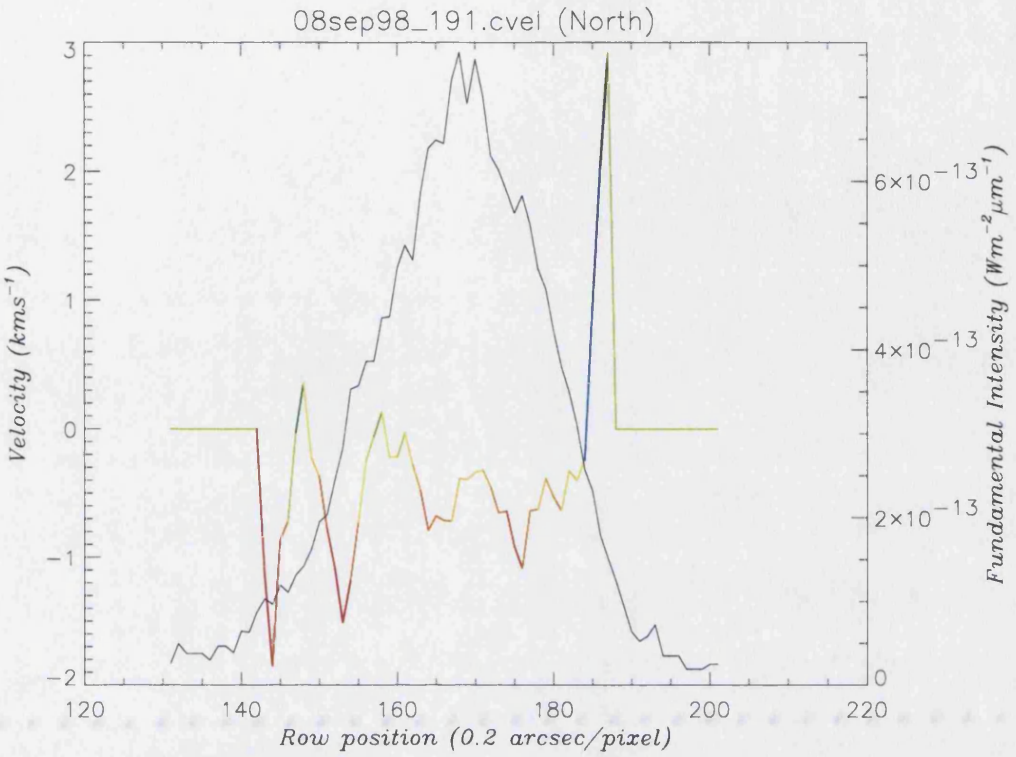

Figure 4-48: The actual velocity profile (blue-red shift) plotted with the fundamental intensity, taken at 10:49U.T. with a CML of 149°, from the 8N5 set of spectra

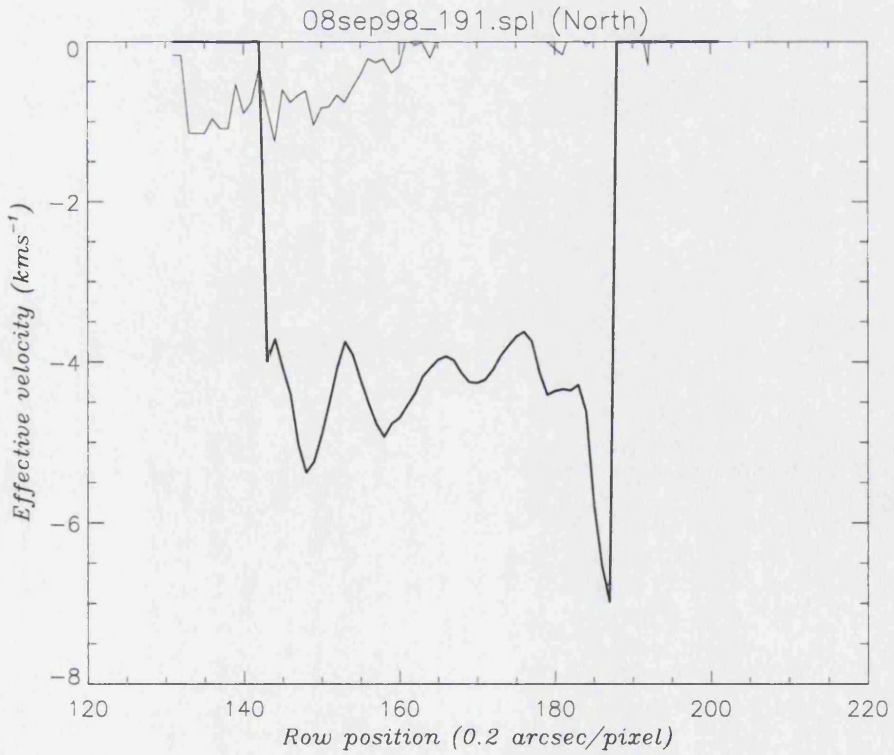

Figure 4-49: The spatial correction that corresponds to the profile taken at 10:49U.T. with a CML of 149°, from the 8N5 set of spectra

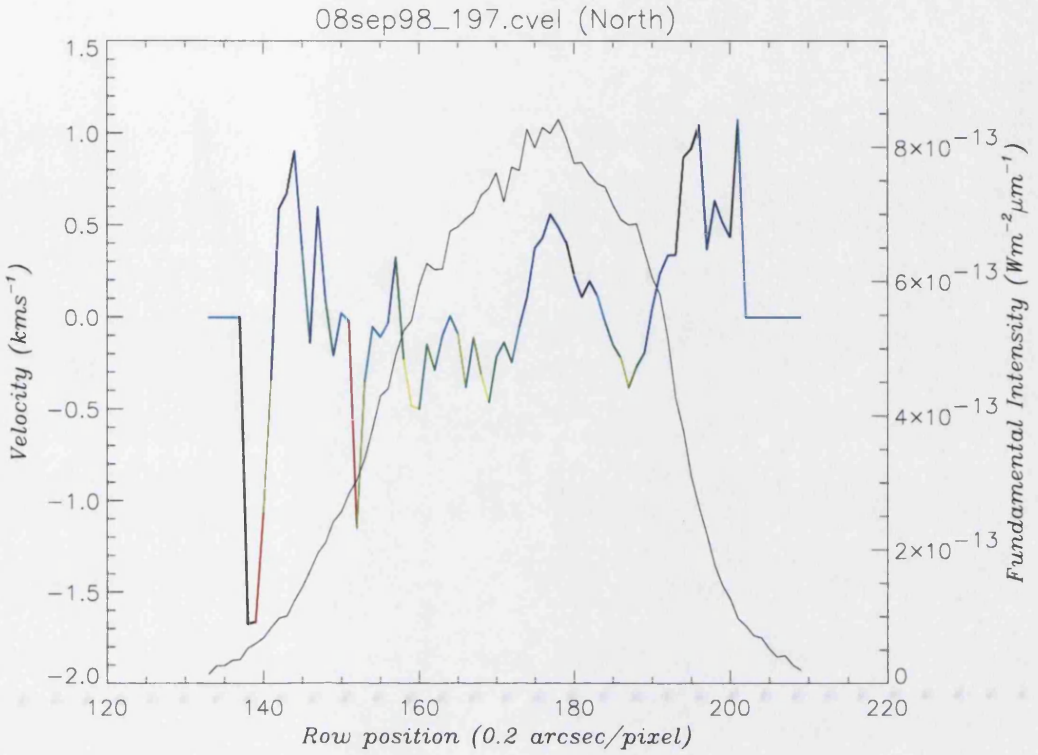

Figure 4-50: The actual velocity profile (blue-red shift) plotted with the fundamental intensity, taken at 10:54U.T. with a CML of 152°, from the 8N5 set of spectra

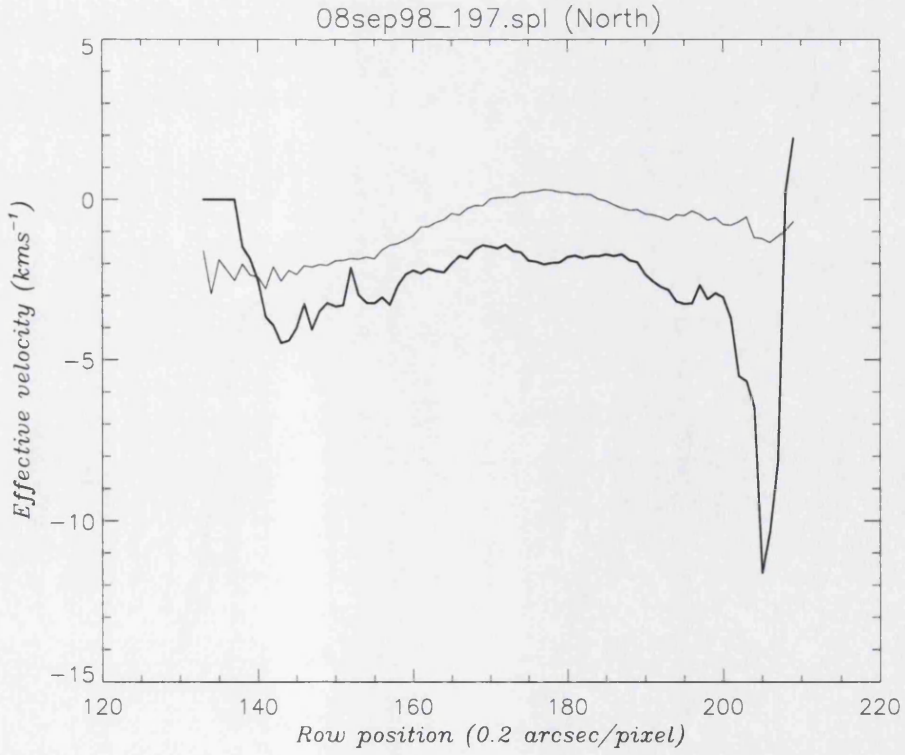

Figure 4-51: The spatial correction that corresponds to the profile taken at 10:54U.T. with a CML of 152°, from the 8N5 set of spectra

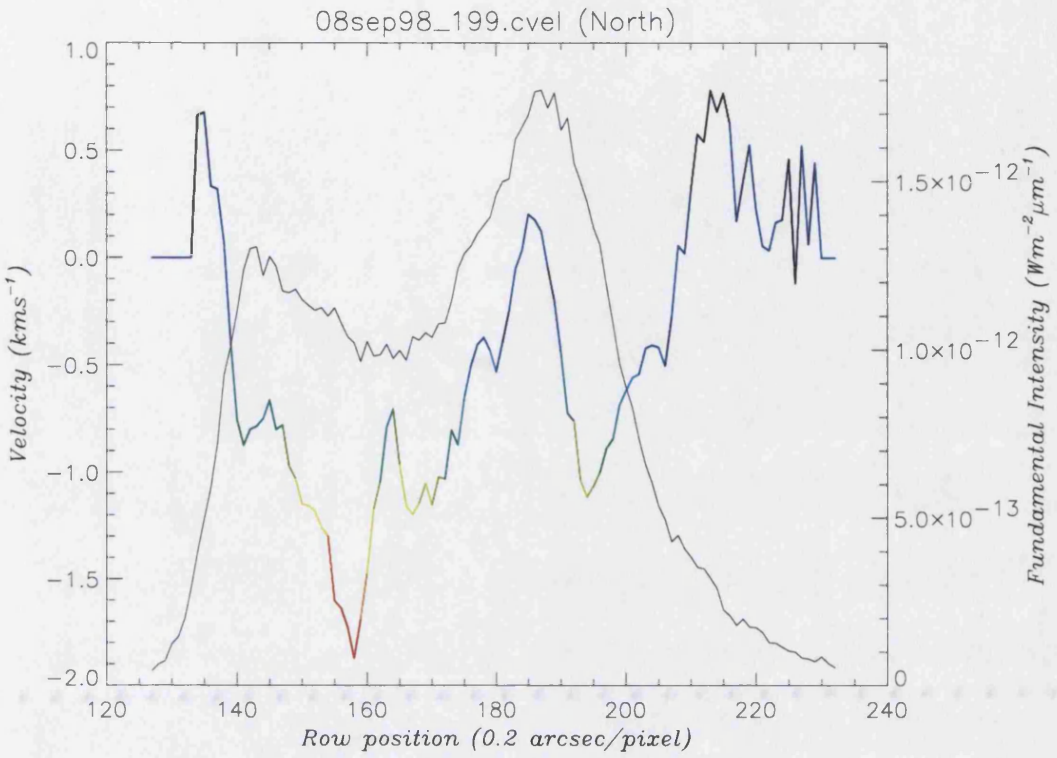

Figure 4-52: The actual velocity profile (blue-red shift) plotted with the fundamental intensity, taken at 10:56U.T. with a CML of 153°, from the 8N5 set of spectra

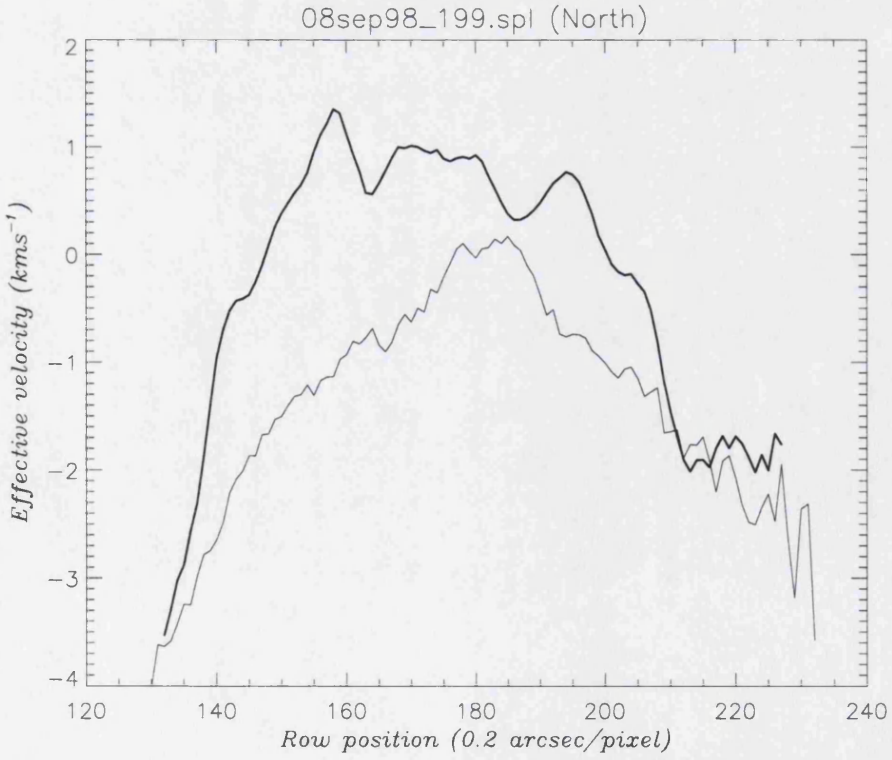

Figure 4-53: The spatial correction that corresponds to the profile taken at 10:56U.T. with a CML of 153°, from the 8N5 set of spectra

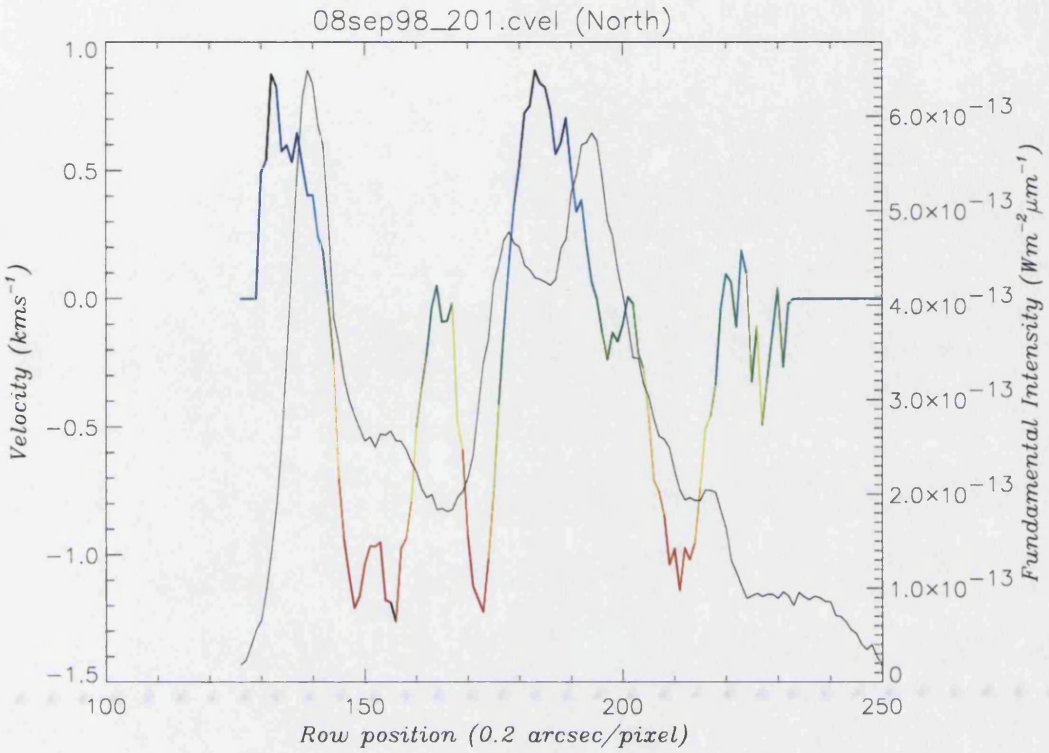

Figure 4-54: The actual velocity profile (blue-red shift) plotted with the fundamental intensity, taken at 10:58U.T. with a CML of 155°, from the 8N5 set of spectra

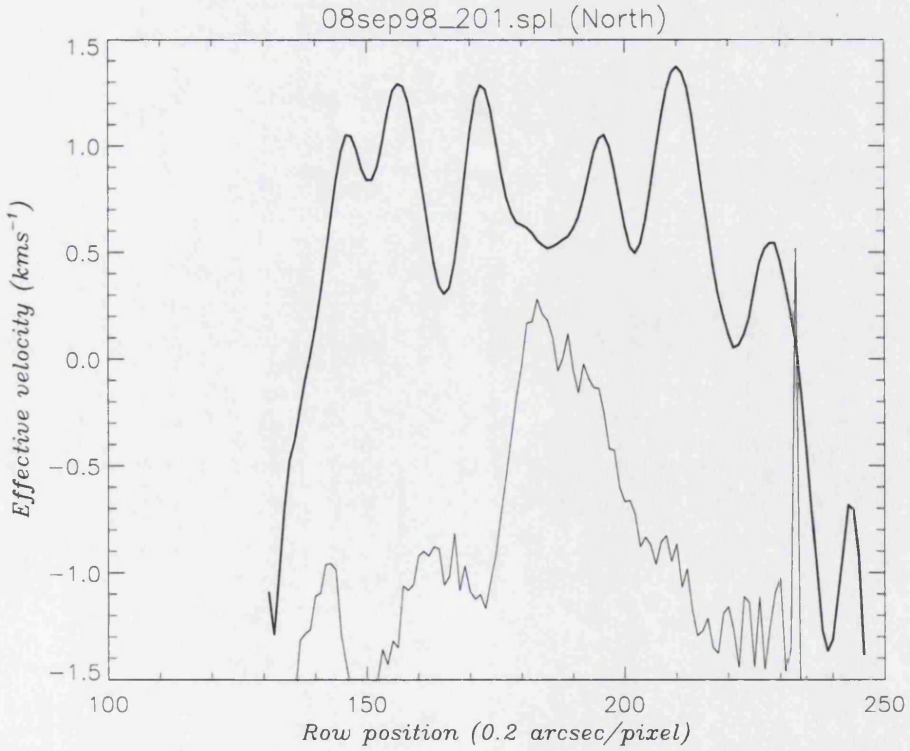

Figure 4-55: The spatial correction that corresponds to the profile taken at 10:58U.T. with a CML of 155°, from the 8N5 set of spectra

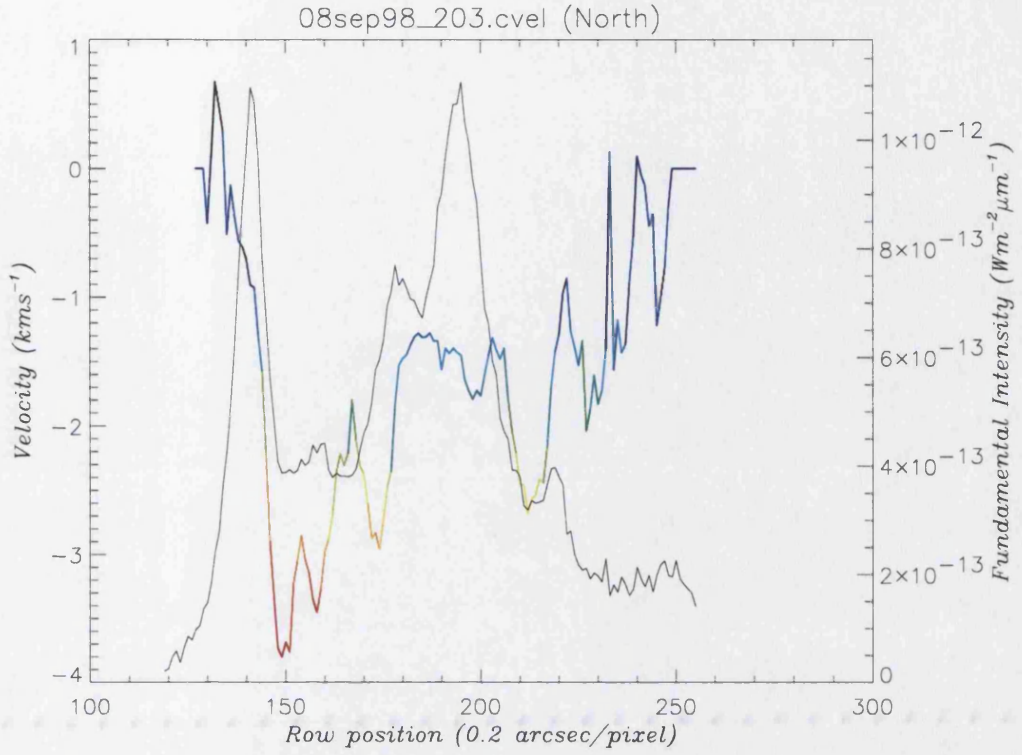

Figure 4-56: The actual velocity profile (blue-red shift) plotted with the fundamental intensity, taken at 11:00U.T. with a CML of 156°, from the 8N5 set of spectra

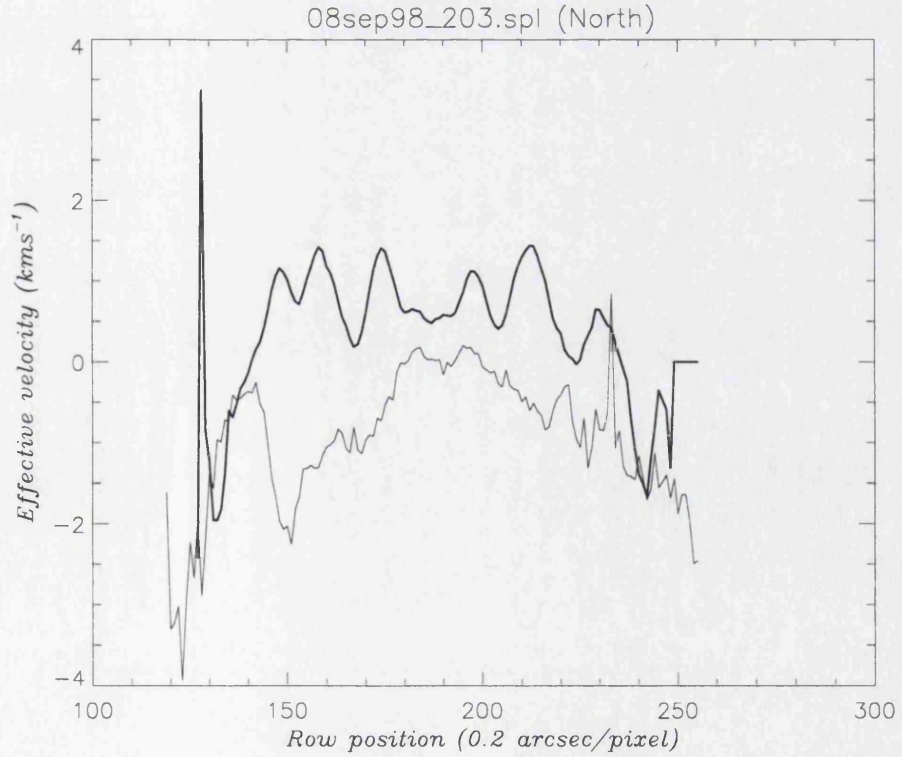

Figure 4-57: The spatial correction that corresponds to the profile taken at 11:00U.T. with a CML of 156°, from the 8N5 set of spectra

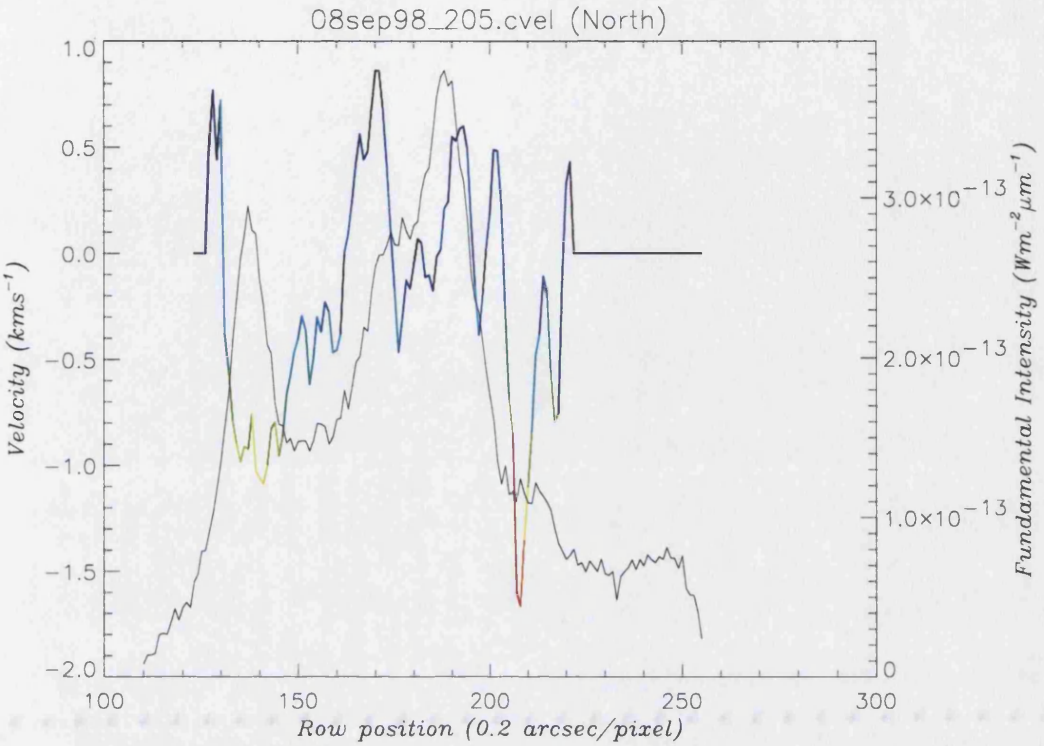

Figure 4-58: The actual velocity profile (blue-red shift) plotted with the fundamental intensity, taken at 11:02U.T. with a CML of 157°, from the 8N5 set of spectra

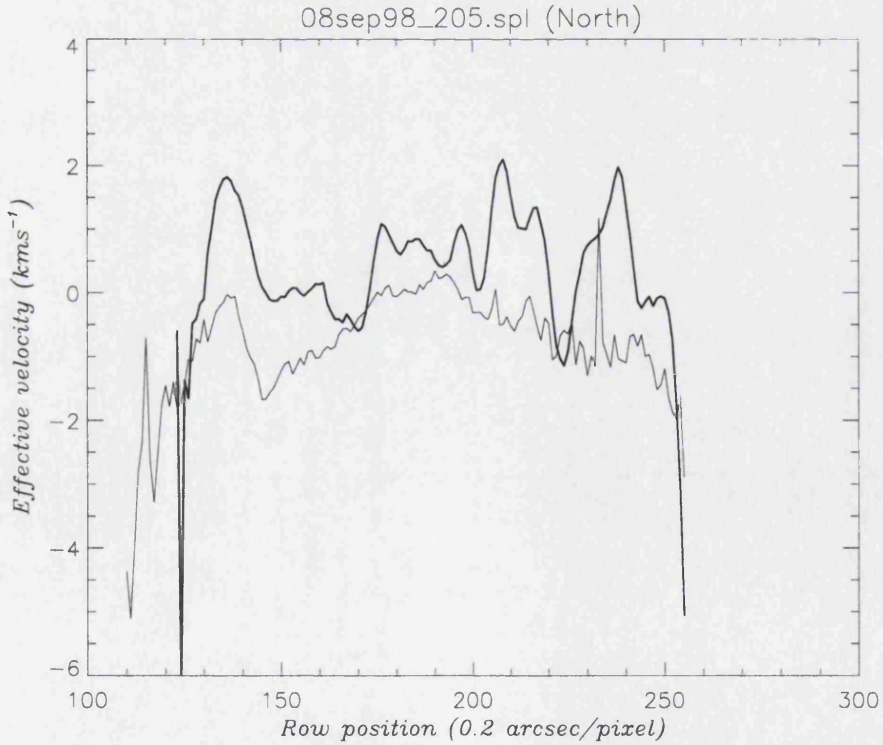

Figure 4-59: The spatial correction that corresponds to the profile taken at 11:02U.T. with a CML of 157°, from the 8N5 set of spectra

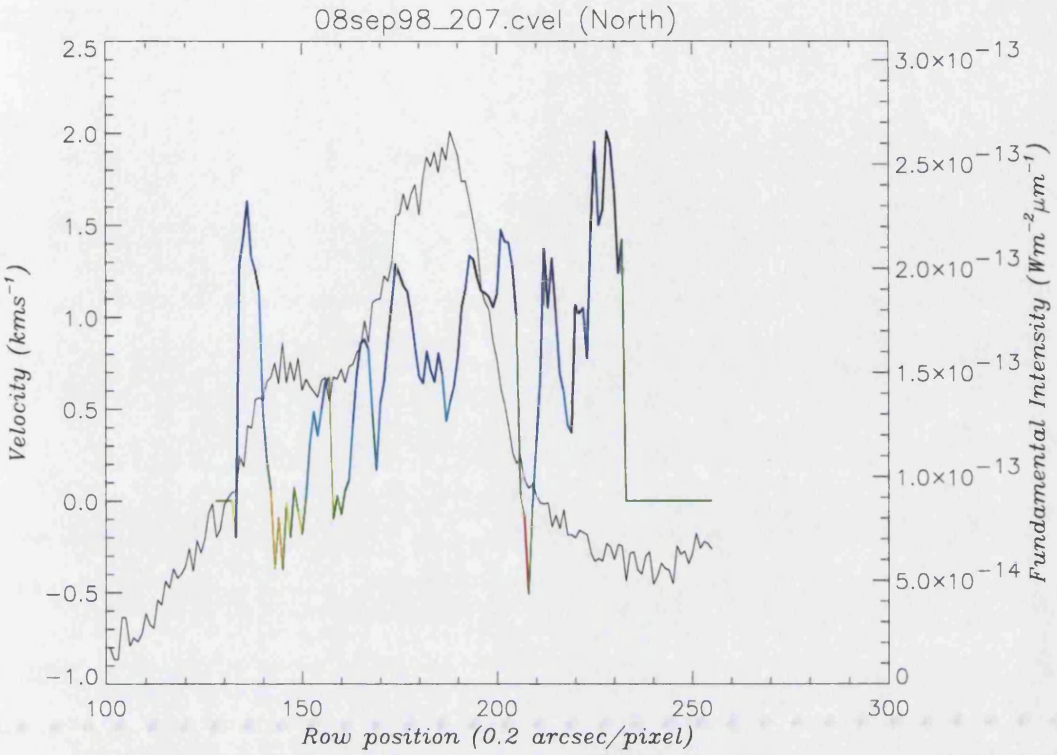

Figure 4-60: The actual velocity profile (blue-red shift) plotted with the fundamental intensity, taken at 11:04U.T. with a CML of 158°, from the 8N5 set of spectra

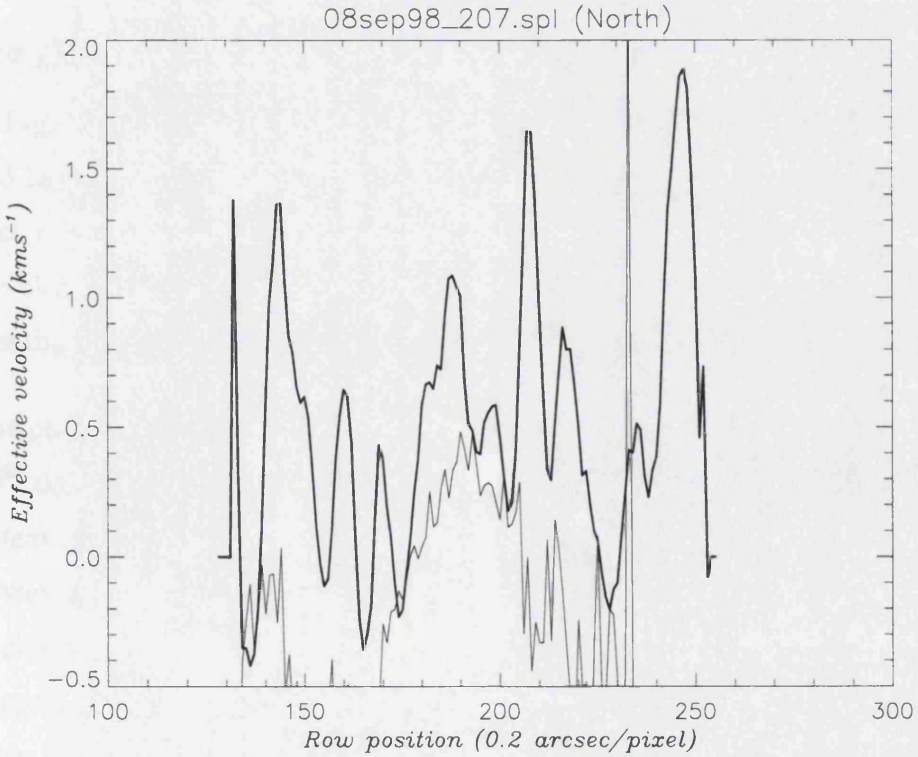

Figure 4-61: The spatial correction that corresponds to the profile taken at 11:04U.T. with a CML of 158°, from the 8N5 set of spectra

4.2.2 Variation in velocity with time

Calculation

The variation in velocities seen over the four sets of spectra can be assessed by taking an average velocity for each set. Two basic types of velocity can be viewed:

1. The electrojet velocity, which is defined here as half the difference between the velocities on the peak emission for each side of the oval;

2. The polar velocity, which is defined as the difference between the strongest shift in the dark polar emission and the zero point of the electrojet shift, between the two oval extremes.

To find the variation for each set of spectra, these velocities are measured for three or four spectra in each set, to produce an average value. This is done for both the actual velocity and pre-spatial velocity where possible, to allow further comparison between all four spectral sets.

Analysis

In Figure 4-62, the electrojet increases in velocity across the four nights between the first and last spectral set recorded. The actual and pre-spatial velocities agree generally with each other, showing that the spatial correction does not appear to affect the appearance of the electrojet on pre-spatial velocities. The increase is at least a factor of 2, suggesting that the Pedersen current across the auroral oval has increased significantly.

The polar wind does not produce as clear a picture, since the pre-spatial velocities on the 10^{th} are not aligned with a linear increase of the velocity over the four nights, which is potentially caused by an incorrect spatial correction. The velocities of the 8^{th} and 11^{th} do, however, suggest a general agreement between the pre-spatial and actual velocities. In addition, the differing viewing angles of the two sets of spectra from the 10^{th} would suggest that the spatial effect, if incorrect, would vary more between these than from the other nights.

If the polar velocity variation is a true indication of the variation seen on Jupiter, it shows an increase between the 10th and 11th, decreasing before this, which suggests that the electrojet and dark polar velocities are not directly associated.

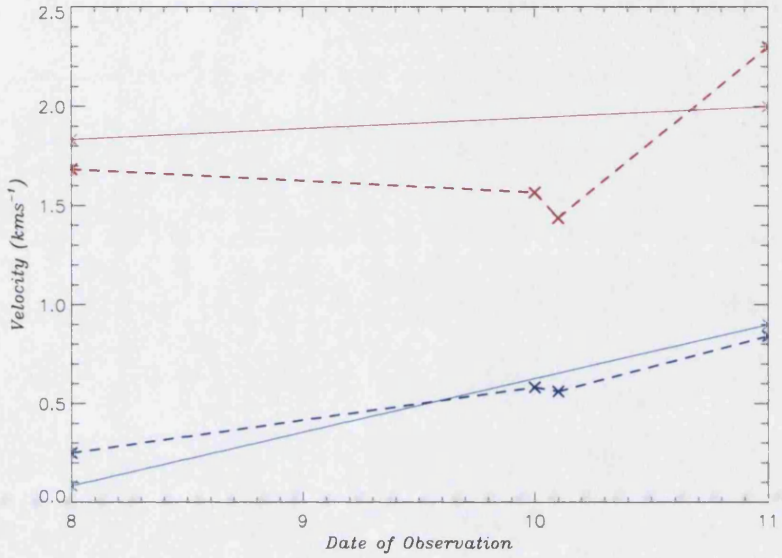

Figure 4-62: The variation in average velocity for the electrojet (blue) and the dark polar wind (red); given in both actual and pre-spatial (dotted) velocities

4.2.3 Causes of the dynamics in the auroral region

Auroral electrojet

The initial impetus for making the observations seen in this thesis was the search for a continuous electrojet, furthering the initial detection made in Rego *et al.* (1999) (see **1.3.8 Direct evidence of the electrojet**). The spectral sequences shown here give very strong evidence of the existence of an electrojet. The calculated velocity profiles show a matching pair of red-shift and blue-shift components on either side of the auroral oval. These are consistent with an electrojet with a true velocity in the range of 1-1.5 km/s.

Within the sequences themselves, there is proof of the existence of an electrojet that occurs on the 8th and 11th. The data set as a whole shows the detection of an electrojet across the majority of sets of spectra that could be processed to a final "actual" velocity. The actual velocity profile within the auroral region is not overly affected by spatial effects. The pre-spatial velocities show a general red-shift to blue-shift dawn-to-dusk

velocity variation across all the nights studied. This shows that there was an auroral electrojet in operation for the entire period of observation.

This is the first time that the existence of a long-term electrojet has been proved to exist within the solar system. The existence on Jupiter of such a perpetual electrojet illustrates the effects of an internal plasma source within the Jovian magnetosphere, which, unlike the Earth system, continually feeds the ionosphere with charged material.

Velocity in the polar region

The velocity of material within the polar region of the aurora is suggestive of a generally similar velocity effect as is seen on the auroral oval. However, there are problems with attributing the velocity effects to one driven by the continuous supply of material from the plasmasheet.

Most easily seen within the velocity structure is the disparity between the bright and dark polar regions. While the auroral oval appears to have a similar values for red-shift and blue-shift in velocity on either side of the oval, there is a very strong difference between the values seen within the auroral polar region.

The Dark Polar Region has a consistently strong red-shift associated with it, commonly stronger than the auroral oval. This is considerably stronger than the counterpart blue-shift in the Bright Polar Region, which is often weaker and seldom stronger than the auroral oval. Clearly, for the velocity within these regions to be produced by the same process, the conditions within the contemporaneous thermosphere and the effects on the ionic velocity due to collision should be significantly different.

A secondary challenge to the connection between the polar velocity disparity and the electrojet of the ovals is the variation in fundamental intensity across the polar region. Within **3.3 H3+ Column Density**, it has been shown conclusively that the fundamental intensity represents the location of energy input into the aurora. The relatively low levels of emission within the DPR, when compared to the rest of the aurora, is suggestive of a different energy source than the BPR, or at least a less powerful energy input.

Chapter 5 : Summary, Discussion and Conclusions

5.1 Temperatures, Column Densities and Total Emission

This thesis presents the detection of the H_3^+ ($2\nu_2(0) \rightarrow \nu_2$) R(3,4$^+$) hotband at 3.949μm, the first time a hotband of H_3^+ has ever been reported outside the laboratory. Not only was the hotband detected, but the strength of the line was such that the variation in intensity could be measured across the entire aurora. Using the ratio of the hotband intensity to that of the H_3^+ ($\nu_2 \rightarrow 0$) Q(1,0$^-$) fundamental line, it was possible to calculate temperature, and from that column densities and total emission, across the auroral region. The use of the hotband allowed an improved sensitivity to temperatures than with studies using lines taken from the same vibrational manifold.

The spectra were taken using a better spatial resolution than has ever been used before. The orientation of the slit, east-west on the planet, also allowed a better view of the cross-section of the aurora than has been previously available. The effective vibrational temperature distribution over the auroral region shows a complicated structure that only partly correlates with the fundamental intensity across the aurora. Assuming quasi-thermal equilibrium (QTE) (**1.3.3 Local thermal equilibrium**), these effective vibrational temperatures equate with kinetic temperatures. The temperature range seen in these observations (950-1200°K) is above the average seen in previous work (between 800-1000°K; see **1.3.6 Previous measurements of the physical conditions**).

On the dawn side of the auroral oval, the temperature is generally relatively high compared to the rest of the aurora, in the range of 1050°K and 1100°K. This elevated

temperature region matches the position of the auroral oval well, though the temperature peak is often broader than that of the emission. This indicates that, here, the temperature of the H_3^+ is probably dominated by the heating caused by auroral energy deposition.

The Dark Polar Region (DPR) is a relatively cool region of the aurora, with temperatures dropping as low as 850°K. A significant minority of the profiles examined have a small region in the DPR that have hotter temperatures associated with them, ranging between 1050°K and 1200°K. Generally, therefore, the DPR is associated with lower levels of energy deposition. The high temperature peaks could be the result in a complete breakdown in QTE, beyond the overfilling of lower energy levels described in Kim *et al.* (1992). Alternately, if the assumption of QTE remains valid, the rise in kinetic temperature could be caused by the heating of H_3^+ by the surrounding thermosphere.

The Bright Polar Region (BPR) is, with a few notable exceptions, relatively high in temperature, at about 1100°K. This is probably the result of a higher level of energy deposition in the region, associated with the increase in fundamental intensity.

The dusk side of the auroral oval coincides, in most cases, with cooler temperatures ranging between 900°K and 1000°K. This is an unexpected result, since the line-of-sight corrected intensity on this side of the oval is significantly brighter than the dawn side (by up to a factor of 2). The energy input into this region would suggest an increase in temperature, so it is possible that this is indicative of the overfilling of the lower energy levels associated with a breakdown in QTE, as discussed by Kim *et al.* (1992). It could, if the assumption of QTE holds, be caused by a cooler surrounding thermosphere causing the kinetic temperature to drop.

The correlation between the fundamental intensity and the column density, assuming QTE, is well defined. Peaks in each match well in both position and relative intensity. This suggests that the temperature has only a secondary role in the column density variations, and that the two are reasonably well determined as individual parameters. The line-of-sight corrected column densities appear to vary across the aurora, between $\sim 5\times10^{15} m^{-2}$ in the dark polar regions to $\sim 1.5\times10^{16} m^{-2}$ on the auroral oval. This correlates well with previous studies (Lam *et al.*, 1997; Miller *et al.*, 1997a; and **1.3.6 Previous**

measurements of the physical conditions), which find column densities that reached a maximum of ~1.0-1.5×10^{16} after line-of-sight correction. Previous studies have covered the auroral region in only a few spatial pixels, but our study is able to discriminate features within the aurora, to spatially pick out the true locations of higher density.

As with the column density, the total emission matches closely with the fundamental intensity, with high levels of total emission corresponding with the auroral oval and the BPR, and a significantly lower value within the DPR. The total emission, once corrected for line-of-sight effects, generally has a value of ~1.0-1.5×10^{-3} Wm^{-2}, with this range of variation being seen between the DPR and the auroral oval; in some cases this value increases as high as 3×10^{-3} Wm^{-2}. These can be assumed to be accurate to within 10%, even under the breakdown in QTE described in Kim *et al.* (1992).

This means that the majority of the H_3^+ cooling in the Jovian aurora is produced in regions of high H_3^+ column density, with temperature structure of the auroral region having only a secondary effect; H_3^+ is a thermally stabilising agent within the Jovian aurora. The column density varies as H_3^+ is created by the energy deposited, and this generally results in a variation in the total emission balancing the energy input with H_3^+ cooling. This means that variations in energy deposition do not result in large-scale temperature variations within the thermosphere, despite the potentially large variations in energy input intrinsic to particle precipitation.

The values for total emission are also comparable with those in Lam *et al.* (1997), Miller *et al.* (1997a), and Satoh and Connerney (1999). These give peak values for total emission in the auroral region in the range of 1.0×10^{-3} Wm^{-2}. These values are slightly lower than those recorded here, probably in direct consequence of the lower temperatures measured in those papers.

5.2 Winds in the Jovian Auroral and Polar Regions

5.2.1 Electrojet

Following the first ever direct detection of the Jovian **E** × **B** Hall drift, and thus the electrojet, by Rego *et al.* (1999), this thesis used observations with a west-east orientated slit to attempt to relocate the Doppler shift seen in an "auroral event" over an extended period. This provided the first ever detection of a sustained electrojet, seen with similar features over a period of four nights of observations - seven Jovian days. In addition to the electrojet, ion drift was also seen inside the polar region of the aurora, where no motion had previously been postulated. This has shown the dynamics of the Jovian aurora to be far more complex than previously described, and our study provides a unique view into the conditions within the magnetosphere.

The actual velocity of the ion drift was measured across the 8N5 and 11N4 sets of spectra. These showed that the velocity seen varied with the latitude of the individual spectrum, presumably because of local and line-of-sight effects.

The ion drift connected with the electrojet appears clearly on the auroral oval. From the actual velocity profiles it has measured velocities of up to 1 km/s on each side of the auroral oval, which suggests a ring velocity of up to 1.5 km/s after accounting for the line-of-sight effects. The pre-spatial velocities suggest that this electrojet ion drift is seen consistently across all the data, and that the electrojet increases linearly in velocity across the nights observed, from an initial value of ~0.5 km/s on the 8^{th} up to 1 km/s measured on the 11^{th}.

The only previous measurement of the electrojet velocity was made by Rego *et al.* (1999), giving a velocity along the oval of ~2 km/s. It is likely that the higher velocity in the Rego *et al.* paper is due to the "auroral event" that these authors identified. There was some evidence, in the conditions after the "event", of a lower velocity electrojet of the order ~1 km/s in the north, close to the measurements made here.

5.2.2 Polar cap

The ion drift in the polar region is less easily characterised. Like the electrojet-associated ion drift, there is a corresponding red-shift and blue-shift between the dawn and dusk sides of the aurora. However, the velocities seen do not "zero out" as well as they do on the auroral oval, unless one assumes a velocity zero different from that of the planet as a whole.

The DPR has a strong red-shift associated with it, which increased from a value of ~1.5 km/s on the 8^{th} and the 10^{th}, to 3 km/s on the 11^{th}, with some profiles showing velocities as high as 3.5 km/s. This drift can be clearly identified across the majority of both the actual and pre-spatial velocity profiles, suggesting a continuous and stable flow of ions across the pole, from day to night. In contrast with this, the blue-shifted ion drift associated with the bright polar region showed velocities of only 0.5-1.0 km/s at its strongest. The velocity appears to follow that of the dusk side of the auroral oval, though usually with a lesser extent. The BPR also shows more structure within the variations seen than the DPR.

The velocity of material within the polar region is suggestive of a generally similar velocity effect as is seen on the auroral oval, but there is a disparity in the velocity magnitude between the Bright and Dark polar regions. The DPR has a consistently strong red-shift associated with it, commonly stronger that the auroral oval, whereas the blue-shift in the BPR is often weaker and seldom stronger than the auroral oval. This suggests that, while the velocity variations in the BPR might have a similar origin to the electrojet, the DPR is unlikely to have a similar direct association.

5.3 Magnetosphere/Ionosphere/Thermosphere Interconnection

5.3.1 The auroral oval

The detection of the auroral electrojet on Jupiter provides a direct link between the region from which precipitating material originates in the magnetosphere and the resultant aurora within the ionosphere. The correlation between the H_3^+ emission and H_3^+ column density means that the location of emission is a direct indicator of energy deposition. The energy source for the auroral oval is tied to particle precipitation from the breakdown in corotation, by the formation of the electrojet.

The presence of the electrojet on the auroral oval also provides a direct mapping into the magnetosphere. Although this mapping is not as exact as the footprints of satellites, since the location of corotation breakdown is not well known, it does confirm that the location of the IR (and UV) auroral oval is likely to be located in the range of 12-20R_J, rather than 30R_J.

Given that the energy source of the auroral oval is particle precipitation, it is perhaps a surprising result that the dusk side of the oval appears to be not just generally cooler than the adjacent BPR, but has a definite temperature low directly associated with it. This can be explained in the context of the maintenance or breakdown in QTE, but whatever the cause, it must be directly associated with the auroral oval itself.

Given a breakdown in the assumption of QTE as described in Kim *et al.* (1992), the lower fundamental ($v_2 = 1$) energy level is overfilled compared with the upper hotband ($v_2 = 2$) level. This is caused by the radiative depopulation exceeding the collisional excitation rate, leading to a breakdown in the thermalisation of upper levels. Thus, for the assumption of QTE to hold in other regions, this suggests that the collisional excitation rate is lower in the dusk auroral oval. One way the collision rate could be reduced is if the particle precipitation occurs at a higher altitude, with a corresponding lower density in the neutral atmosphere.

Under conditions where QTE is maintained, cooling from the surrounding thermosphere has already been implicated as a cause of lower effective H_3^+ vibrational temperatures. It is possible that the H_3^+ in the dusk side of the oval is created at lower altitudes, because of higher energy impacting particles. UV images show that the dawn and dusk sides of the auroral oval do appear to be different in basic morphology, and that the dusk side is often associated with diffuse emission, which might have a consequential effect on the depth of H_3^+ production. The higher line-of-sight column density seen on the dusk side of the oval could be an indicator of a deeper origin, where higher atmospheric pressure allows more H_3^+ to be produced.

However, an alternative is that the thermospheric source of cooler neutral material is potentially the collisionally accelerated neutral atmosphere moved from cooler regions of Jupiter. The electrojet is not rapid enough to carry neutrals over the limb from the dark side of Jupiter, since the rotational velocity is greater than the velocity variation from the Hall drift (Figure 2-47 shows this clearly). However, the dayside of Jupiter has a temperature gradient across it, hottest at the equator, due to the incident angle with the sun. The electrojet could be transporting neutrals between higher and lower latitudes; the equatorward flow on the dusk side cooling the ions. This does, however, fail to explain why the BPR has a significantly raised temperature over the adjacent dusk oval.

5.3.2 Auroral polar cap region

The mechanisms determining conditions in the polar cap regions are relatively uncharacterised in comparison with the main auroral oval. Where the polar cap maps to the magnetosphere is still a matter of great debate, and no real consensus on the matter has been managed. The "Yin-Yang" bright and dark regions in the IR are directly correlated with the polar region of the UV, which appears to be dominated by diffuse polar emission which occurs only on the dusk side.

An important connection made in this thesis is that the DPR is not completely inactive, having a significantly raised emission compared with the non-auroral body of the planet, only a factor of 2-3 times lower than the peak oval values. This follows through with column density, and so the DPR has emission due to particle precipitation. It is thus

likely that the UV aurora also has a significant minor component of emission in this dark region, which has been overlooked in the both the UV and IR images.

The presence of some temperature peaks in the middle of the DPR, which appear with no corresponding H_3^+ emission, are suggestive of a change from the normal conditions in the DPR. The apparent temperature increase could be due to a complete breakdown the assumed QTE, with the hotband being overfilled relative to the fundamental level. The conditions for this are not explained by the breakdown in QTE discussed in Kim *et al.* (1992), and requires a localised variation in energy level population not seen elsewhere. The reason for such an overpopulation of the upper energy level remains unexplained.

Given the maintenance of the assumption of QTE, the kinetic temperature peak is potentially caused by a collisionally accelerated neutral atmosphere carrying thermal energy with it into a normally cool ionospheric region. This provides additional evidence for the interconnection between the ionosphere and thermosphere through auroral dynamics.

The wind system detected within the polar region has not been previously predicted. It thus provides a vital new source of information about the effects of magnetospheric/ionospheric coupling in the polar region. Interpreting the wind system detected is difficult, because so little is currently known about coupling from the ionosphere out to the magnetosphere. The origins of the bright and dark regions are not necessarily the same, and the inability to distinguish these two sources adds to the difficulty of interpretation.

The DPR has, until now, had very little variation detected in it other than sporadic "dawn storms", and so discussion over its origin is scarce. On the other hand, the BPR with the analogous UV diffuse emission, and the "dawn storms" themselves, have been discussed more extensively. Interpretation of the velocity system depends greatly on the assumed origin, so the two main theories of the magnetosphere origin will be discussed in terms of the possible resultant interpretation of the dynamics presented within this thesis.

The two main theories for the origin of the BPR result from calculating the location on the planet, and extrapolating this out to the corresponding location in the magnetosphere.

The first explanation places the origin far out in the magnetotail, through particles carried in the convective system driven by the solar wind, similar to the magnetosphere of Earth. The second suggested origin is the Jovian middle magnetosphere, beyond the point where corotation has broken down (reflecting fast rotational dynamics, connected to the edge of the current sheet).

Magnetotail convection

The Jovian magnetosphere is substantially dominated by the Io fed current sheet to distances as far out as $125R_J$ (Kane *et al.*, 1995). But the solar wind must have effects at some point within the magnetosphere, in the tail where the influence of the corotating plasma is much less. Return flows in the tail have been deduced from *in-situ* measurements (Cowley *et al.*, 1993, 1996; Hawkins *et al.*, 1998). However, the Ulysses spacecraft failed to detect any clear field-aligned current signatures in the polar region (Dougherty *et al.*, 1993). The UV dawn storms have been interpreted as being analogous to "substorms" on Earth, the manifestations of which include the down-tail ejection of a significant portion of the plasmasheet (see **1.1.3 The outer magnetosphere**).

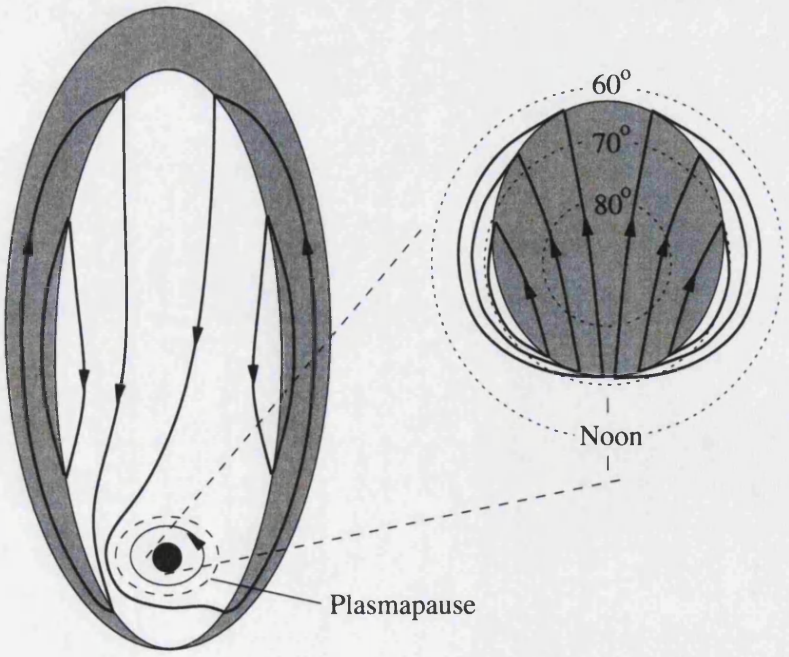

Figure 5-1: The Earth's magnetospheric tail convection, and resultant ionospheric dynamics, based on diagram in Hill and Dessler (1991)

To understand how the features we have noted in the Jovian polar regions are formed, it is useful to refer briefly to the Terrestrial situation. The effects of the solar wind dominate the Earth's magnetosphere (see Figure 5-1). One of the effects of this domination, first described in the Dungey model (1961), is a convection pattern in the magnetotail driven by the viscous interaction at the magnetopause, in turn powered by magnetic tension developed along "open" magnetic field lines that link the solar wind directly to the Earth's polar caps.

If this were the case for Jupiter, then the entire polar cap of the Jovian aurora would emulate the situation across Earth's pole (Figure 5-2). The solar wind, connecting with open field lines over the pole, stream past the planet at high speed, pulling the field lines with them. This causes the plasma on the flux tube to sense an electric field (through the motion of the magnetic field line relative to the plasma, $\mathbf{E} = \mathbf{u} \times \mathbf{B}$), which in turn drives an antisunward motion of plasma in the high-latitude ionosphere. This is compensated by a sunward return flow at lower latitudes, associated with the reconnection of the field lines in the magnetotail.

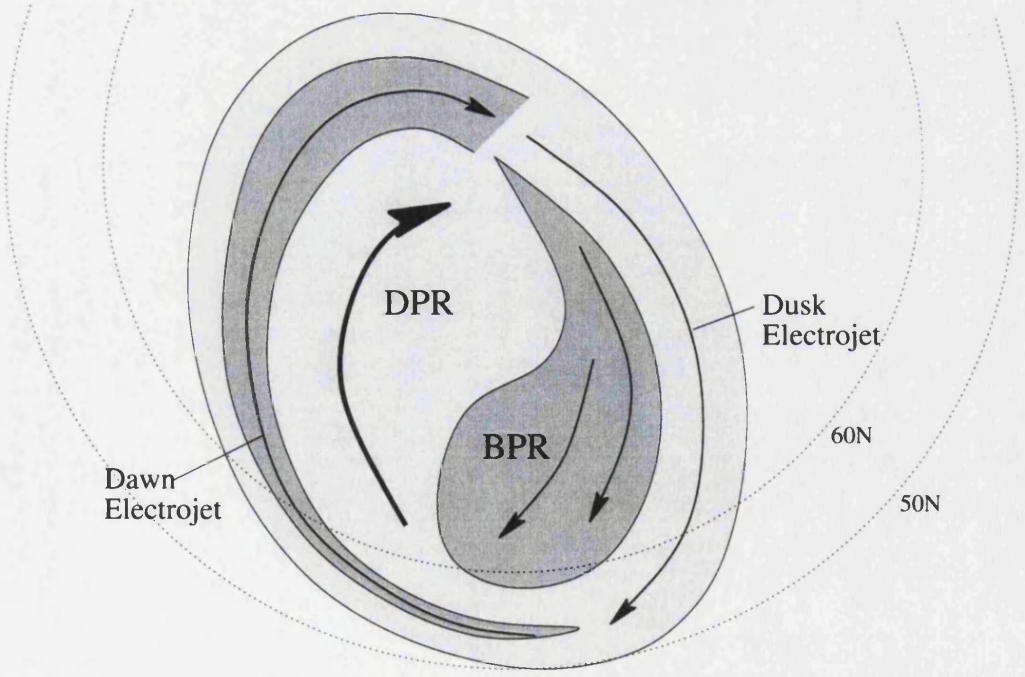

Figure 5-2: The suggested whole polar cap convection based on the observations presented here, in context with the Earth's ionospheric pole cap (Figure 5-1), overlaid on a representation of the H_3^+ emission model of Satoh and Connerney (1999)

As in the case of the Earth, this process would depend on conditions in the solar wind, and these are by no means constant. For the convection to occur at all, it needs the interplanetary magnetic field to have a northward component (the reverse direction to that required by Earth), so that the "open" field lines can connect to the interplanetary field. In addition, the return flow (the Earth's "substorms"), just above the auroral oval, may be intrinsically sporadic even if the flow imposed on the dayside is constant (Erikson and Wolf, 1980).

The sporadic nature does explain the velocity differences seen between the dark polar region, containing a strong and constant antisunward flow, and the bright polar region, with a less determinate return flow. The major problem with this polar configuration is that there appears to be only a dusk side sunward flow, with very little evidence of IR "dawn storms". Additionally, the antisunward flow on the dark polar cap does not vary a great deal, and yet reversals in the interplanetary magnetic field can occur on a short timescale in comparison with the period of observations, when fast solar wind and slow solar wind meet, although the slow wind reversals do occur over a timescale long enough to theoretically not affect the observations taken here.

In this configuration, the solar wind has a significant effect upon the Jovian ionosphere and magnetosphere that has not previously been expected, and the DPR interconnects directly with the solar wind. This potentially explains the occurrence of high speed ionospheric winds, without any apparent particle precipitation.

Plasmasheet disruption

There is significant evidence within this thesis that the bright polar emission and dark polar emission have occurred from different sources; they contain very different temperature, column density and total emission environments, as well as an imbalance in the associated velocities. Observations by Ulysses have suggested that the bright polar region is connected with regions in the magnetosphere just beyond the breakdown in corotation, or even as the breakdown occurs (Prangé, private communication), and notably that the BPR is separate from the DPR, which does not connect to these regions. In UV observations, the appearance of "dawn storm" emission along the reference oval

has been implicated as evidence that the origin of the storm is the middle magnetosphere (Clarke *et al.*, 1998).

If the BPR is connected with the plasmasheet beyond the breakdown in corotation, then the processes involved in linking the ionosphere with the magnetosphere must explain the lower velocities seen in the profiles within this thesis. The temperature and column density of the BPR are similar to those of the dawn auroral oval; temperatures in the BPR are often higher than in the dusk oval. This does suggest that their origin within the magnetosphere may be similar to that of the auroral oval itself, with a significant influx of particles for the ionisation process.

A continuance of the sequential breakdown in corotation could be involved as a potential driver of the H_3^+ velocity, which is similar to or less than that seen on the oval itself. Since the breakdown in corotation is not thought to be a smooth decay, sudden regions of slowing can be expected beyond the point of initial breakdown. The location where this occurs is, unlike the initial breakdown, determined by the chaotic processes within the partially unstable disk. This scenario might also account for the arc-like features often seen in UV emission in the BPR (Clarke *et al.*, 1996; Ballester *et al.*, 1996; Prangé *et al.*, 1998), features that appear in our data as intensity peaks inside the main auroral oval.

The DPR has to be considered separately, since the processes in control of this region appear to be very different from the rest of the aurora. The generally low temperatures and low column densities are suggestive of a lower energy regime, and yet the associated velocities are the largest seen within the aurora.

It is possible that the solar wind control described above is limited to the DPR alone. This would have an appearance somewhat distorted in comparison with the Earth's antisunward polar wind, having to move around the BPR which is connected to the middle magnetosphere; a representation of what this could appear as is given in Figure 5-3.

The same problem with a lack of evidence for a return of flow is self evident, but the location of UV "dawn storms" in the proximity of the dark polar region is perhaps evidence that sudden surges of input can occur in an otherwise quiescent region.

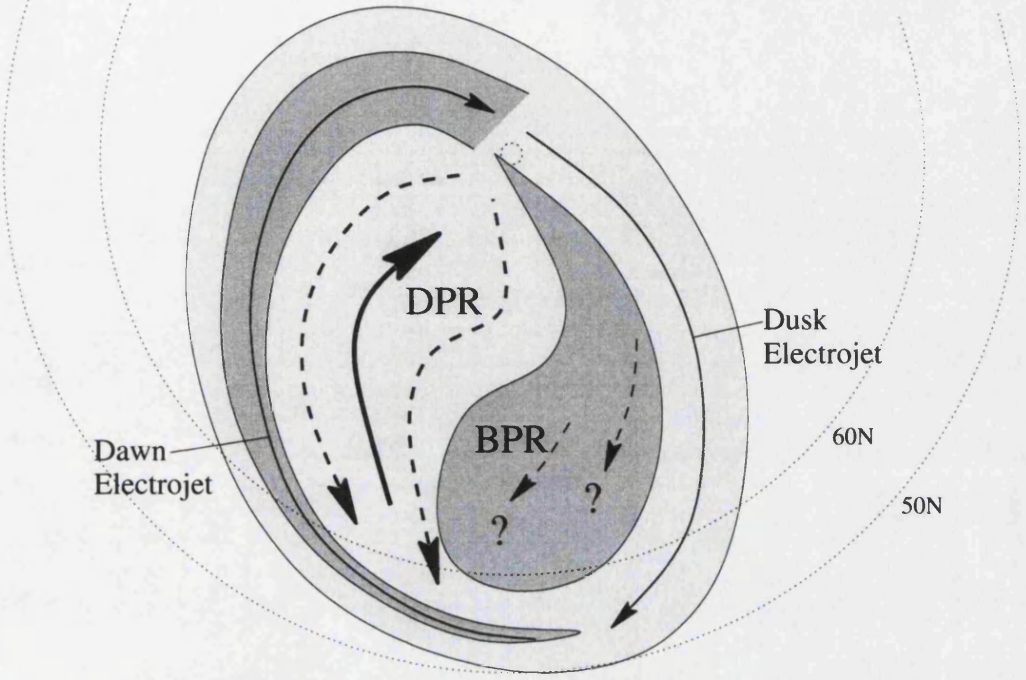

Figure 5-3: The sectional polar cap, with solar wind controlled dark polar region, and middle magnetosphere controlled bright polar region, overlaid on a representation of the H_3^+ emission model of Satoh and Connerney (1999)

If a solar wind origin for the antisunward flow is ruled out, and without the large scale energy inputs that would cause H_3^+ production, then non-magnetospheric origin has to be considered. The transpolar winds on Earth are in part caused by the day/night temperature differential. However, if the magnetic field in this region is closed, there would be a significant magnetic friction to the flow of ions across the pole, which in turn requires a thermal wind significantly larger than 3 km/s in order to collisionally accelerate the H_3^+ ions to the velocities measured. We therefore consider this scenario to be unlikely.

5.3.3 Sub-auroral latitudes

While the observations made in this thesis centred on the aurora, rather than lower latitudes in the ionosphere, the detection of a continuous auroral electrojet has important implications for these lower latitudes. Examples of possible evidence of the underlying thermosphere being collisionally accelerated by the H_3^+ ions has already been shown in this chapter, and the electrojet has previously been implicated as a significant energy

redistribution method in the ionosphere, providing lower latitudes with auroral energy (see **1.3.8 Indirect evidence of the electrojet**).

By using the electrojet velocities taken from this thesis in the Jovian Ionosphere Model (JIM, Achilleos *et al.*, 1998), it is possible to model the effect that the acceleration process would have on the lower latitudes. Achilleos *et al.* (submitted) suggests that for an electrojet that produces velocities in excess of 1 km/s - beyond the current velocity limit of the model - there would be significant transferral of momentum to the thermosphere. In Figure 5-4, the electrojet is clearly defined as a strong antirotational velocity, and its effects on the thermosphere can be seen in Figure 5-5. This clearly shows that not only does the motion of H_3^+ produce a significant degree of collisional acceleration, but also that this results in the neutral atmosphere flowing at lower latitudes.

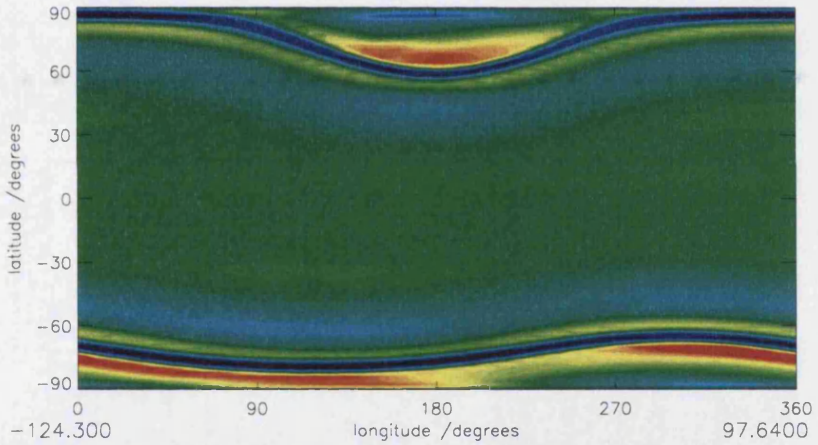

Figure 5-4: JIM calculated H_3^+ velocities at 0.1μm, in a rotational frame; antirotational motion in blue, and superrotational motion in red, ranging on a linear scale between -124.3 to 97.6 m/s

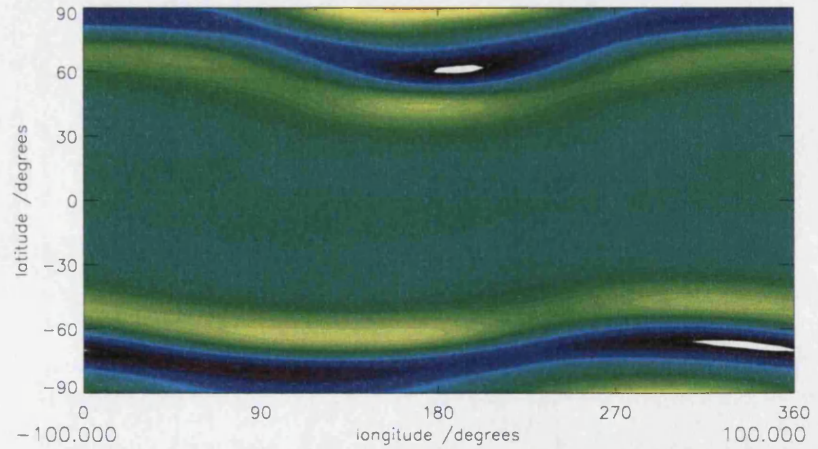

Figure 5-5: JIM calculated neutral atmosphere velocities at 0.1μm; antirotational motion in blue, and superrotational motion in red, ranging on a linear scale between -100 and 100 m/s. Note that the velocity of the neutrals is a significant percentage (>40%) of the electrojet velocity in Figure 5-4

5.4 Future Work

This thesis has provided a new method of measuring the interconnected ionosphere/magnetosphere, providing a new "ground truth" to plasma detection experiments on spacecraft within the Jovian magnetosphere. The preliminary results of this, presented within this thesis, suggest a highly dynamic system that links from different regions within the magnetosphere to the entire auroral region of Jupiter. A major task in the future will be explaining the results shown in this thesis in the context of the dynamic magnetosphere.

The major question still unanswered within this thesis is the origin for auroral emission within the polar region, because the emission cannot be distinguished between local-time brightening or that fixed in the rotational frame, as with the auroral oval. The confusion comes because ground-based observations can only look at the Jovian aurora in a small range of configurations, with a CML of 100-220°.

In collaboration with the Galileo mission, the Cassini flyby in December 2000 will allow significant advances in our understanding of the magnetosphere. Solar wind data will be obtained during the encounter, and the imaging experiments will acquire spectral and morphological data on Jovian auroral emissions at local times not observable from Earth. This will help distinguish local time events associated with the solar wind from the longitudinal effects produced through the Jovian plasmasheet.

In the longer term, the INSIDE Jupiter mission, a proposed NASA "Discovery" mission, will also provide an important advance in the understanding of the Jovian system, if it is accepted. This spacecraft will orbit over Jupiter at high latitudes, in order to allow it to map the gravity and magnetic fields close in.

A second possible "Discovery" mission currently in discussion is the Jupiter Polar Orbiter. This mission includes an imaging spectrograph, which will allow very high resolution infrared and ultraviolet images of the auroral processes from above and behind the planet. If this mission were to carry a spectrometer, the dynamics of the polar region

could also be investigated in unparalleled detail, which would provide a direct measure of the magnetospheric effects within the aurora.

5.5 Conclusions

This thesis provides a comprehensive review of the observations, methods of processing and analysis of a data set that provides an unprecedented level of detail on the processes within the Jovian H_3^+ aurora.

Using the previously astronomically undetected H_3^+ ($2\nu_2(0) \rightarrow \nu_2$) R(3,4$^+$) hotband, a detailed view of the temperature, column density and total emission within the auroral region has been produced. Using the position of the H_3^+ ($\nu_2 \rightarrow 0$) Q(1,0$^-$) fundamental line, along with a new method of processing CSHELL data, the actual H_3^+ line-of-sight velocities have been calculated for the entire auroral region.

Table 5-1 shows the characterisation of the auroral region into the four regions discussed in this thesis; the two sides of the auroral oval and the bright and dark segments of the polar cap. Typical values for the calculated parameters across these regions are also given, in order to characterise the prevailing conditions; the Jovian aurora is highly variable and has been shown to diverge significantly from this general overview.

Table 5-1: General attributes of the Jovian auroral region

	Dawn Oval	**Dark Polar Region**	**Bright Polar Region**	**Dusk Oval**
T [°K]	1050-1100	900-950	1000-1100	900-1000
$N(H_3^+)$ (line-of-sight) [10^{16} m^{-2}]	5-11	4-8	10-13	12-15
$E(H_3^+)$ (line-of-sight) [10^{-3} Wm^{-2}]	1.1-1.7	0.5-1.1	1.2-2.2	1.3-3.1
$V_a(y)$ [kms^{-1}]	0.5-1.0	2-3	0-1.0	0.5-1.0
Magnetospheric Origin	~20R_J	Solar wind?	30-50R_J?	~20R_J

Analysis of data has shown that H_3^+ plays a dominant role in stabilising the temperature of the aurora in regions of particle precipitation, that H_3^+ emission intensity is as good an indicator of energy deposition as UV observations at the spatial resolution used in this

work, and that the whole auroral region, including the Dark Polar Region, has a significantly raised emission level.

It has also shown that the Jovian electrojet is a continuous feature, and that additional dynamical structure occurs in the auroral polar regions, and has highlighted the instrumental problems facing future observers of planetary-based Doppler shifts. The importance of the electrojet and polar wind systems to both the thermosphere and magnetosphere are also explored, highlighting the role that the understanding of Jovian ionospheric processes can play in future work on the Jovian magnetosphere.

Appendix A : Tables of Observation

A.1 Introduction

On every night of observations, the data was collected using a basic methodology, as described in **2.2.2 Early evening set-up observations**, **Star observations** and **Jovian observations**. These were performed across much of the night, except when the weather conditions were too poor for observations to be taken, or when Jupiter was too low in the sky.

This appendix contains the sequence of macros that was run for each night, along with the U.T. time, the airmass, and the CML for Jovian observations. For reference, the set of spectra name is given, as well as the beginning "file number"; the array output for each spectral image is recorded in a file with the name **<date>_<file_number>.idl** (*e.g.*, the spectral image number 166, recorded on the 11th September 1998, is given as 11sep98_166.idl).

A.2 Observation Sequence from the 7th

U.T.	Sequence Name	Type of run	No of start frame	CML	Airmass	Notes
04:37		Arc Lamp sequence	2	n/a	n/a	
06:33		Stellar sequence	11	n/a	1.86	
07:56	07N1	North Jupiter sequence	21	262	1.571	
09:45		Stellar sequence	50	n/a	1.122	
10:14	07N2	North Jupiter sequence	56	340	1.111	
11:01	07S1	South Jupiter sequence	80	7	1.091	
11:58		Stellar sequence	102	n/a	1.298	
12:17	07N3	North Jupiter sequence	108	47	1.163	
13:00	07S2	South Jupiter sequence	130	79	1.275	

Table A-1: The sequence of macros run on the 7th

A.3 Observation Sequence from the 8th

U.T.	Sequence Name	Type of run	No of start frame	CML	Airmass	Notes
04:10		Arc Lamp sequence	2	n/a	n/a	
04:45		Arc Lamp sequence	8	n/a	n/a	
05:44		Stellar sequence	14	n/a	2.622	
06:31	08N1	North Jupiter sequence	22	1	2.75	
07:10	08S1	South Jupiter sequence	50	?	1.992	
07:49		Stellar sequence	78	n/a	1.321	
08:13	08N2	North Jupiter sequence	85	57	1.435	
08:51		Stellar sequence	113	n/a	1.17	
09:11	08N3	North Jupiter sequence	120	92	1.212	
09:51	08N4	North Jupiter sequence	152	116	1.134	
10:30		Stellar sequence	180	n/a	1.134	
10:46	08N5	North Jupiter sequence	187	150	1.092	
11:19	08N6	North Jupiter sequence	215	170	1.098	
11:50	08N7	North Jupiter sequence	243	118	1.128	
12:30	08N8	North Jupiter sequence	277	213	1.201	
13:05	08N9	North Jupiter sequence	307	234	1.311	
13:46		Stellar sequence	335	n/a	2.195	
14:01	08N10	North Jupiter sequence	341	268	1.621	
14:34	08S2	South Jupiter sequence	371	285	1.961	

Table A-2: The sequence of macros run on the 8th

A.4 Observation Sequence from the 9th

U.T.	Sequence Name	Type of run	No of start frame	CML	Airmass	Notes
04:03		Arc Lamp sequence	1	n/a	n/a	
07:53		Stellar sequence	7	n/a	1.301	2 spectral sequences
08:28	09N1	North Jupiter sequence	20	216	1.344	
09:03	09N2	North Jupiter sequence	50	237	1.224	
09:37	09S1	South Jupiter sequence	80	259	1.148	
09:55	09S2	South Jupiter sequence	94	269	1.123	
10:35		Stellar sequence	122	n/a	1.141	
10:52	09N3	North Jupiter sequence	129	303	1.092	
11:26	09S3	South Jupiter sequence	159	324	1.107	
11:55	09N4	North Jupiter sequence	183	342	1.141	
12:29	09S4	South Jupiter sequence	213	1	1.209	

Table A-3: The sequence of macros run on the 9th

A.5 Observation Sequence from the 10th

U.T.	Sequence Name	Type of run	No of start frame	CML	Airmass	Notes
03:59		Arc Lamp sequence	1	n/a	n/a	
05:53		Stellar sequence	7	n/a	2.258	
06:31	10N1	North Jupiter sequence	27	302	2.534	
07:22	10S1	South Jupiter sequence	61	327	1.742	
07:54	10N2	North Jupiter sequence	87	347	1.496	
08:29	10S2	South Jupiter sequence	119	8	1.332	
09:21		Stellar sequence	145	n/a	1.128	
09:38	10N3	North Jupiter sequence	153	50	1.141	
10:14	10S3	South Jupiter sequence	183	72	1.102	
10:45	10N4	North Jupiter sequence	209	92	1.092	3 fund. Images
11:22	10S4	South Jupiter sequence	245	112	1.108	
11:57		Stellar sequence	272	n/a	1.34	
12:13	10N5	North Jupiter sequence	280	144	1.183	2 fund. Images
12:48	10N6	North Jupiter sequence	316	164	1.28	
13:22	10N7	North Jupiter sequence	350	185	1.427	
13:58	10N8	North Jupiter sequence	382	207	1.673	
14:32	10N9	North Jupiter sequence	414	227	2.054	
15:05	10N10	North Jupiter sequence	446	249	2.734	2 fund. Images

Table A-4: The sequence of macros run on the 10th

A.6 Observation Sequence from the 11th

U.T.	Sequence Name	Type of run	No of start frame	CML	Airmass	Notes
04:16		Arc Lamp sequence	1	n/a	n/a	
05:15		Stellar sequence	8	n/a	3.146	
05:35		Stellar sequence	16	n/a	2.556	corrupt
06:00	11N1	North Jupiter sequence	34	32	3.41	
06:39	11N2	North Jupiter sequence	71	57	2.266	
07:23		Stellar sequence	105	n/a	1.388	
07:45	11N3	North Jupiter sequence	116	132	1.534	
08:23	11N4	North Jupiter sequence	154	154	1.331	
08:58	11N5	North Jupiter sequence	188	197	1.215	
09:33	11N6	North Jupiter sequence	224	229	1.142	

Table A-5: The sequence of macros run on the 11th

Appendix B : In-house IDL Procedures

B.1 Introduction

In the course of producing this thesis, it has been necessary to produce a wide variety of different procedures for use with the IDL program. The procedures presented here are those referenced within the thesis, but the full catalogue produced in the making of this thesis extends to over 200 different procedures.

The procedures are accessed from within the IDL environment, using the command prompt. Those shown here are listed with the procedural input and output values, the procedures called that have been custom built for the thesis, and a general description. Additional information may be taken in or out in the form of user interfacing, screen or postscript plots, or saved files.

B.2 Loading, Saving and Plotting

B.2.1 buildata[1-2]

Inputs

```
date_of_observation, spectra_number (,number_of_images)
```

Outputs

```
output_image (, output_image2)
```

Procedures Called

```
readfits
```

Description

Using the date and number of the spectra, `buildata` finds the directory and then either loads the specific file for `buildata1`, or using the given number of spectral images, `buildata2` loads the number of object and sky frames.

These files are converted using the *readfits* procedure provided by the Institute of Astronomy in Hawaii. This is then displayed and output by `buildata1`.

In `buildata2`, each image is constructed by removing the sky frame from the image frame using the equation (from **2.3 Data Reduction**):

$$\frac{(o_{xy} - s_{xy})}{s_{xy} / |s|_{ave}} \times (\text{total number of pixels})$$

where, o is the value of the pixel on the object frame;
and, s is the value of the pixel on the sky frame.

This is then displayed and output.

B.2.2 bulkrun.pro

Inputs

`none`

Outputs

`none`

Procedures Called

`ps_primer_*`

Description

This procedure was written to allow the plotting of the large data set recorded for this thesis quickly and easily. The information needed to be able to access the correct files is stored in a variety of files. The hardwired values are changed in the procedure depending on the choice for the run.

`Bulkrun` then works out which spectra need to be accessed, and all the other values that are needed by the particular plot. It then opens a postscript file and runs the particular `ps_primer` needed to set up the values properly to print out the plot.

This allows an entire set of data for a particular parameter (velocity, for example) to be plotted quickly.

B.2.3 loadvel.pro

Inputs

`filename`

Outputs

`profile_array`

Procedures Called

`none`

Description

Originally designed to load velocity profiles, this procedure allows the user to load any of the outputs from `spectra` or `writevel`. It simply loads and outputs the chosen file as an array. For the file format, see `writevel`.

B.2.4 map.pro

Inputs

none

Outputs

map_array

Procedures Called

limb, map_lrow, intmatch, map_interp, map_conv

Description

On running map, the procedure requests information to allow it to located the files for the K-image, 3.953μm image and all the spectra to be used in the map. It uses limb to find the position of the limb on the K-band image, and then loads each spectrum using map_lrow (which in turn uses loadvel).

It then finds the relative position of each spectrum using intmatch, and puts each spectrum into a specific row on a rectangle array. It accesses map_interp to fill the gaps between each spectrum in the array with a linear interpolation.

The procedure then calls map_conv, which uses map_calc to calculate the relative size of each line to reshape the array to appear as a planetary surface. This array is then output.

There are separate versions of this procedure for the north (map) and south (map_s) poles.

B.2.5 ps_primer_*.ps

Inputs

```
date_of_observation, spectra_number, north/south_pole
```

Outputs

```
none
```

Procedures Called

```
loadvel, ps_twoplot_*
```

Description

These procedures are set-up procedures for the `ps_twoplot` set of procedures. They allow the `ps_twoplot` procedures to input values from pre-recorded files rather than directly from arrays within IDL itself, and to output postscript plots.

It first loads the profiles needed in `ps_twoplot_*`, sets up the environment, and then opens into a postscript file ready for recording. It then feeds the profiles through to the `ps_twoplot_*` procedure, which plots them out.

B.2.6 ps_twoplot_*.ps

Inputs

`date_of_observation, number_extension, north/south_pole`

Outputs

`none`

Procedures Called

`none`

Description

This procedure takes two different profiles and plots them on the same graph, using two different y-axes so they both fill the graph as much as possible.

It scales one profile to the scale of the other, and plots them on the same graph. This graph has two y-axes, one automatically calculated by IDL, and the second carefully scaled so it corresponds directly with the re-scaled profile.

The `ps_twoplot_vel*` procedures also calculate the colour scale to use depending upon the values of the velocity profile, so the values range between red and blue, from negative to positive. The `ps_twoplot_vel` procedure, used for .cvel files, also calculates the position of the zero and changes the Gauss of the colour scale so zero always appears as green.

B.2.7 writevel.pro

Inputs

`profile_array`

Outputs

`filename`

Procedures Called

`none`

Description

A counterpart to the `loadvel` procedure, this allows the user to save files using the `spectra` format. A simple file type, it saves the array as a two-column ASCII file, with a two-line header. The first line contains the number of rows in the array, and the second is zeroed, originally used by spectra to record the absolute position of the centre of the recorded line.

B.3 Data Processing

B.3.1 avtemp.pro

Inputs

`date_of_observation, spectra_number`

Outputs

`average_temp`

Procedures Called

`avtemp_in, gauss1, avtemp_out`

Description

This procedure is based on the spectra procedure, except that it calculates the temperature for an entire spectrum, rather than for individual spatial rows.

Using the date and number of the spectra, `avtemp` finds the directory and loads the spectral image. The user then delineates the region of the hotband, and the wavelength position of both the hotband and fundamental line, using `avtemp_in`.

The procedure then coadds all the spatial rows for each spectral line to produce two high signal-to-noise lines. The `gauss1` procedure is then used to fit these with Gaussian, and the resultant intensity peaks are ratioed to produce a temperature.

The `avtemp_out` procedure then saves the particular temperature to the end of a file designated by the date of observations, so by processing the data in order for each day, a file is produced with the temperatures ranked by spectral number. The temperature is then output.

B.3.2 colden.pro

Inputs

`date_of_observation, spectra_number, north/south_pole`

Outputs

`column_density, fluxcalibrated_intensity`

Procedures Called

`loadvel, fluxcalibration, writevel`

Description

This procedure is used to calculate the column density profile for a chosen spectrum, shown in **2.6 Column Density**.

The procedure starts by loading the intensity, half-width maximum and temperature with `loadvel`, using the date and number of the spectra to find the specific files. The intensity and half-width are then smoothed to match the temperature in spatial resolution, and then cropped to match it in size. `Colden` then calibrates the intensity, using `fluxcalibration`, and the half-width into microns.

The $E_{H_3^+}(\lambda, T)$ was then calculated and, from this, the column density profile was produced. This was written to file using `writevel`, and printed to a postscript file using `ps_twoplot_cd`. The column density profile and flux calibrated intensity are then output.

B.3.3 hbtemp.pro

Inputs

`date_of_observation, spectra_number`

Outputs

`temperature_profile`

Procedures Called

`loadvel, hbtemp_temp, writevel, ps_twoplot_temp`

Description

This procedure calculated the temperature profile for a given fundamental and hotband intensity profile pair, as described in **2.5.2 Temperature calculation**.

Using the date and number of the spectra, `hbtemp` finds the directory and then loads the fundamental and hotband intensities using `loadvel`. It resizes the arrays, and smoothes the fundamental to match the resolution of the hotband, then shifts the fundamental intensity so the intensities match in spatial position.

It then uses `hbtemp_temp` to use the ratio of the two intensities to calculate the temperature profile. It saves this as a file using `writevel`, and prints it into a postscript file using `ps_twoplot_temp`.

B.3.4 intmatch.pro

Inputs

```
date_of_observation, image_number, spectra_number
```

Outputs

```
y_position
```

Procedures Called

```
loadvel
```

Description

Using the date and number of the spectra, `intmatch` finds the directory and then loads the 3.953μm images and using `loadvel` the corresponding spectral intensity profile is also loaded.

Having resized and rotated the image, the intensity profile is then plotted against the specific row selected using the mouse position over the image. This allows the position of the spectra to be found relative to the image, and this position is output.

B.3.5 limb.pro

Inputs

`date_of_observation, spectra_number`

Outputs

`limb_value`

Procedures Called

`none`

Description

Using the date and number of the spectra, `limb` finds the directory and loads the correct K-band spectral image. Then it automatically crops the image to the correct size, rotates it so the top of the planet faces upwards, and displays it using a specific colour scale selected to provide a clear view of the planetary limb.

It then allows the user to select the limb by eye, and outputs the value of the selected limb position.

B.3.6 los.pro

Inputs

`date_of_observation, k-band_image_number,`
`3.953μm_image_number, spectra_number`

Outputs

`los_corrected_array`

Procedures Called

`los_lat, los_long, loadvel, savevel, ps_profile_los`

Description

The `los` procedure is used to correct for the line-of-sight effect of the atmosphere (see **2.9 Line-of-sight Corrections**). It first opens `los_lat`, which uses the limb and `intmatch` procedures to find the position of the chosen spectrum on the planet. Using this, it calculates the latitudinal correction needed.

The `los_long` procedure then opens the chosen profile (using `loadvel`) and corrects the profile for the longitudinal line-of-sight effect. When the profile is returned to `los`, the latitudinal effect is also accounted for.

The resultant profile is then plotted into a postscript file using `ps_primer_los` and written to a file using `writevel`, before being output.

B.3.7 spectra.pro

Inputs

```
arrayname, save_filename
```

Outputs

```
velocity, intensity, halfwidth
```

Procedures Called

```
spectrain, gauss2, spectraout
```

Description

This procedure takes in a spectral image and allows the user to select the location of the line to be examined using `spectrain`.

Once the extent of the line is known, the region selected is inputted into `gauss2`, which feeds each individual spatial row into `gauss1`. This fits the individual spectral line with a Gaussian, and `gauss2` outputs an array containing the parameters of the Gaussian fits for all the spatial rows back into `spectra`.

The velocity is then calculated from the relative positions of the peak heights across the spatial extent of the selected region. The intensity, velocity and half-width calculated are then fed into `spectraout`, which saves the values in a text file and creates a plot of each in postscript files.

B.3.8 totem.pro

Inputs

`date_of_observation, spectra_number, north/south_pole`

Outputs

`total_emission`

Procedures Called

`loadvel, writevel, ps_twoplot_totem`

Description

This procedure is used to calculate the total emission profile for a chosen spectrum, shown in **2.7 Total Emission**.

The procedure starts by loading the intensity, temperature and column density with `loadvel`, using the date and number of the spectra to find the specific files. The intensity is then cropped to match the temperature in size.

The procedure then uses the temperature to find the $E_{H_3^+}^{Total}(T)$, which when used with the column density produces the total emission profile. This is saved to file using `writevel`, and printed to a postscript file with the intensity using `ps_twoplot_totem`. The total emission profile is itself then output.

B.4 Calibration and Fitting

B.4.1 calc_gaussacc.pro

Inputs

none

Outputs

none

Procedures Called

gauss1

Description

The procedure was used to calculate the accuracy of the intrinsic IDL Gaussian fitting procedure `gauss_fit`, accessed from the `gauss1` procedure. The methodology used for this is given in **2.3.1 Fitting accuracy**, and the output accuracy is printed to the screen.

B.4.2 fluxcalibration.pro

Inputs

```
input_intensity, star_flux
```

Outputs

```
output_intensity
```

Procedures Called

```
none
```

Description

This simple procedure takes in an intensity profile, and for a given flux value measured, will flux calibrate the intensity using the values for BS8647. The resultant profile is then output (see **2.3.3 Star slope calibration**).

B.4.3 lamp.pro

Inputs

`date_of_observation`

Outputs

`array_correction`

Procedures Called

`loadvel, writevel`

Description

This procedure opens the lamp lines from either side of the 3.953μm line for the particular night chosen using `loadvel`, and then calculates the gradient between these for each spatial position on the array.

Using this gradient and the known location of the H_3^+ line, it can then calculate the array adjustment that is needed for the velocity profiles from that particular night, writes this to a file (using `writevel`) and outputs the result.

B.4.4 spatialcali.pro

Inputs

`date_of_observation, image_number, spectra_number`

Outputs

`actual_velocity`

Procedures Called

`loadvel, intmatch, writevel`

Description

This procedure does all the calculations to determine and calibrate the spatial correction required for the velocity profiles. This process is a complex one, covered properly in **2.8.2 Spatial correction**, and cannot be given in a procedure description.

It is important to note that `spatialcali` was the original procedure used in calculating the spatial effect and includes all the code for calculating the scaling factor between the spatial effect and the velocity, but this is cumbersome and unwieldy once a value for this scaling has been decided.

In response to this, a sister procedure `actual_vel` has been written as a stripped down version of `spatialcali`. `Actual_vel` was used in the processing of the data, and produces postscript output using its own code, and saves both the actual velocity and the calculated spatial effect using `writevel`.

B.4.5 velofit.pro

Inputs

```
load_filename, save_filename, polynomial_values
```

Outputs

```
fit_plot, fit_values
```

Procedures Called

```
loadvel, writevel
```

Description

Used to fit polynomials to profiles, this procedure reads in the profile with `loadvel`, expands it with a linear interpolation to allow a better fit, and then fits to the require polynomial using the intrinsic IDL procedure `poly_fit`.

It then displays the original profile against the fitted curve. If prompted, it will also save the curve profile, and then outputs the curve profile and the curve values.

Appendix C : Examples of Programming Code

This thesis was controlled to a great extent by the programming involved in both the collection and analysis of the data. The telescope was controlled through a combination of the telescope operator directing the general positioning, and fine-tuning of the position on the object by macros written to interact with the XUI Guider.

With the data recorded, every subsequent stage of reduction, analysis and presentation of the data was done within the IDL programming language environment. IDL is interactive, and so short programs can be written at the command prompt, but longer procedures are executed from previously saved files.

C.1 CSHELL macros

This macro runs in the Guider XUI software, to record the spectral images for the northern aurora of Jupiter. The code in *italics* sets up the initial conditions for the observations within the CSHELL instrument. Below this the tcs command moves the telescope by an x and y value - these should be x = 0 and y = 1, but have been altered to correct for the problems with tracking. The wait command is used to allow the instrument to reset having completed a telescope movement.

```
Obsmode 1
PVoltages -3.700 -3.375
observer Miller
Object Jupiter
Comment Macro for N pole
FileName Jup
filter 0
Slit 0.5
InstMode S
ITIME 50.000
Coadd 01
Cycles 01
AutoSaveXUI On
tcs 1    0.0   0.0 -1 C.SCN
WAIT 2
go
tcs 1 -0.4 0.9    1 C.SCN
wait 2
go
tcs 1 -0.8 1.8    1 C.SCN
wait 2
go
tcs 1 0.4 -0.9    1 C.SCN
wait 2
go
tcs 1 0.8 -1.8    1 C.SCN
wait 2
go
tcs 1 1.3 -2.7    1 C.SCN
wait 2
go
tcs 1 1.7 -3.6    1 C.SCN
wait 2
go
tcs 1 2.1 -4.6    1 C.SCN
wait 2
go
tcs 1 2.6 -5.5    1 C.SCN
wait 2
go
tcs 1 3.0 -6.4    1 C.SCN
wait 2
go
tcs 1 3.4 -7.3    1 C.SCN
wait 2
go
tcs 1 3.8 -8.2    1 C.SCN
wait 2
go
tcs 1 10.0 -20.9 1 C.SCN
wait 2
go
```

C.2 IDL procedures

This is the stripped down code used for the **B.3.7 spectra.pro** procedure.

```
pro spectra,arrayname,velocity,intensity,halfwidth,filename
                        ; opening command line in IDL

spectrain,arrayname,startx,endx,starty,endy,Yc
                        ; calls the input procedure

Yc=(endy+starty)/2
endby=endy
diffx = (endx-startx)+1
diffy=(endy-starty)+1 ; sets up the scaling factors

gauss2,arrayname,startx,endx,starty,endy,matrixa,matrixy
                        ; fits the rows with gaussian, use gauss2b
                        to use nine-pixel running averages
print,'stage1 complete...'

abpos=startx+matrixa(1,0)    ; define an arbitary reference point

;;;;; rotation correction ;;;;;;
slope=-0.101388
rotation = fltarr(2,diffy)
for i=starty,endy do rotation(0,i-starty)=i
for i=0,diffy-1 do rotation(1,i) = slope*(i-Yc+starty)
;;;;;;;;;;;;;;;;;;;;;;;;;;;;;;;;

velocity = fltarr(2,diffy)
for i=starty,endy do velocity(0,i-starty)=i
velocity(1,*) =((matrixa(1,*)+startx-abpos)*(2.998e5/103750.)*(-
1))-rotation(1,*)
                        ; calculate velocity output

intensity = fltarr(2,diffy)
for i=starty,endy do intensity(0,i-starty)=i
intensity(1,*) = matrixa(0,*)*matrixy(*)
                        ; calculate intensity output

halfwidth = fltarr(2,diffy)
for i=starty,endy do halfwidth(0,i-starty)=i
halfwidth(1,*) = matrixa(2,*)
                        ; calculate halfwidth output

spectraout,velocity,intensity,halfwidth,diffy,abpos,filename
return                  ; calls output procedure
end                     ; saves results and closes the procedure
```

Bibliography

Achilleos, N., S. Miller, J. Tennyson, A.D. Aylward, I. Mueller-Wodarg, and D. Rees, JIM: A time-dependent, three-dimensional model of Jupiter's thermosphere and ionosphere, *J. Geophys. Res.*, **103**, 20089-20112, (1998)

Achilleos, N., S. Miller, R. Prangé and M. Dougherty, A dynamic model of Jupiter's auroral electrojet, *New J. Phys.*, submitted, (2000)

Acuña, M.H., and N.F. Ness, The main magnetic field of Jupiter, *J. Geophys. Res.*, **81**, 2917-2922, (1976)

Acuña, M.H., K.W. Behannon, J.E.P. Connerney, Jupiter's magnetic field and magnetosphere, in *Physics of the Jovian Magnetosphere*, ed. A.J. Dessler, Cam. Plan. Sci. Series, Cambridge University Press, 1-49, (1983)

Atreya, S.K. and T.M. Donahue, Model ionospheres of Jupiter, in *Jupiter (Studies of the interior, atmosphere, magnetosphere and satellites)*, ed. T. Gehrels, Tuscon: University Arizona Press, 304-310, (1976)

Atreya, S.K., T.M. Donahues, B.R. Sandel, A.L. Broadfoot and G.R. Smith, Jovian upper atmosphere temperature measurements by the Voyager 1 UV spectrometer, *Geophys Res Lett*, **6**, 795-798, (1979)

Atreya, S.K., *Atmospheres and Ionospheres of the Outer Planets and their Satellites.* Heidelberg: Springer-Verlag, 139-143, (1986)

Ballester, G.E., S. Miller, J. Tennyson, L.M. Trafton, and T.R. Geballe, Latitudinal temperature variations of Jovian H_3^+, *Icarus*, **107**, 189-194, (1994)

Ballester, *et al.*, Time-resolved observations of Jupiter's far-ultraviolet aurora, *Science*, **274**, 409-413, (1996)

Baron, R.L., R.D. Joseph, T. Owen, J. Tennyson, S. Miller, and G.E. Ballester, Imaging Jupiter's aurorae from H_3^+ emission in the 3-4μm band, *Nature*, **353**, 539-542, (1991)

Baron, R.L., T. Owen, J.E.P. Connerney, T. Satoh, and J. Harrington, Solar wind control of Jupiter's H_3^+ aurorae, *Icarus*, **120**, 437-442, (1996)

Boström, R., *J. Geophys. Res.*, **69**, 4983-4999, (1964)

Caldwell, J., A.T. Tokunaga, and F.C. Gillett, Possible infrared aurora on Jupiter, *Icarus*, **44**, 667-675, (1980)

Caldwell, J., A.T. Tokunaga, and G.S. Orton, Further observations of 8-μm polar brightenings of Jupiter, *Icarus*, **53**, 133-140, (1983)

Clarke, J.T., G.R. Gladstone and L. Ben Jaffel, Jupiter day-glow H Lyman alpha emission line profile, *Geophys. Res. Lett.*, **18**, 1935-1938 , (1991)

Clarke, J.T., *et al.*, Far-ultraviolet imaging of Jupiter's UV aurora and the Io 'footprint', *Science*, **274**, 404-409, (1996)

Clarke, J.T., *et al.*, Hubble Space Telescope imaging of Jupiter's UV aurora during the Galileo orbiter mission, *J. Geophys. Res.*, **103**, 20217-20236, (1998)

Connerney, J.E.P., Doing more with Jupiter's magnetic field, in *Planetary Radio Emissions III*, eds. H.O. Rucker, S.J. Bauer, M.L. Kaiser, Proc. Of 3rd Int. Workshop Held in Graz (Austria), Vienna, 13-33, (1991)

Connerney, J.E.P., R. Baron, T. Satoh, and T. Owen, Images of excited H_3^+ at the foot of the Io flux tube in Jupiter's atmosphere, *Science*, **262**, 1035-1038, (1993)

Connerney, J.E.P., M.H. Acuña, N.F. Ness, and T. Satoh, New models of Jupiter's magnetic field contrained by the Io flux tube footprint, *J. Geophys. Res.*, **103**, 11929-11939, (1998)

Cowley, S.W.H., *et al.*, Ulysses observations of anti-sunward flow on Jovian polar cap field lines, *Planet. Space Sci*, **41**, 987, (1993)

Cowley, S.W.H., *et al.*, Plasma flow in the Jovian magnetosphere and related magnetic effects: Ulysses observations, *J. Geophys. Res.*, **101**, 15197, (1996)

Cravens, T.E., E. Howell, J.H. Waite, and G.R. Gladstone, Auroral oxygen precipitation at Jupiter, *J. Geophys. Res.*, **100**, 17153-17161, (1995)

CSHELL user's manual, Revision 2.0.1, T. Greene and A. Denault, (1994)

de Bergh, C., A. Martin, T. Owen, D, Gautier, J.-P. Maillard, B.L. Lutz and P. Drossart, Paper presented at *Workshop on Variable Phenomena in Jovian Planetary Systems*, Anapolis MD, July 13-16, (1992)

Dinelli, B.M., S. Miller, and J. Tennyson, Bands of H_3^+ up to $4\nu_2$: Rovibrational transitions from first principles calculations, *J. Mol. Spectrosc.*, **153**, 718-725, (1992)

Dinelli, B.M., S. Miller, N. Achilleos, H.A. Lam, M. Cahill, J. Tennyson, M.-F. Jagod, T. Oka, J.-C. Helico, and T.R. Geballe, UKIRT observations of the impact and consequences of Comet Shoemaker-Levy 9 on Jupiter, *Icarus*, **126**, 107-125, (1997)

Dougherty, M.K., D.J. Southwood, A. Balough, and E. J. Smith, Field-aligned currents in the Jovian magnetosphere during the Ulysses flyby, *Planet. Space. Sci.*, **41**, 291-300, (1993)

Drossart, P., J.-P. Maillard, J. Caldwell, S.J. Kim, J.K.G. Watson, W.A. Majewski, J. Tennyson, S. Miller, S.K. Atreya, J.T. Clarke, J.H. Waite, and R. Wagener, Detection of H_3^+ on Jupiter, *Nature*, **340**, 539-541, (1989)

Drossart, P., J.-P. Maillard, J. Caldwell, and J. Rosenqvist, Line-resolved spectroscopy of the Jovian H_3^+ auroral emissionat 3.5 micrometers, *Astrophys. J.*, **402**, L25-L28, (1993)

Dungey, J.W., *Phys. Rev. Lett*, **6**, 47, (1961)

Erikson, G.M., and R.A. Wolf, *Geophys. Res. Lett.*, **7**, 897, (1980)

Festou, M.C., S.K. Atreya, T.M. Donahue, B. R. Sandel, D. E. Shemansky, and A. L. Broadfoot, Composition and thermal profiles of the Jovian upper atmosphere

determined by the Voyager ultraviolet stellar occultation experiment, *J. Geophys. Res.*, **86**, 5715-5735, (1981)

Geballe, T.R., M.-F. Jagod and T. Oka, *Astrophys. J.*, **408**, L109-L112, (1993)

Geballe, T.R., T. Oka, Detection of H_3^+ in interstellar space, *Nature*, **384**, 334-335, (1996)

Gérard, J.-C., D. Grodent, R. Prangé, J.H. Waite, G.R. Gladstone, V. Dols, F. Paresce, A. Storrs, L. Ben Jaffel, and K.A. Franke, A remarkable auroral event on Jupiter observed in the ultraviolet with the Hubble Space Telescope, *Science*, **266**, 1675-1678, (1994a)

Gérard, J.-C., V. Dols, R. Prangé, and F. Paresce, The morphology of the north Jovian ultraviolet aurora observed with the Hubble Space Telescope, *Planet. Space. Sci.*, **42**, 905-917, (1994b)

Greene, T., *et al.*, *Proc. SPIE*, **1946**, 313, (1993)

Grodent, D., G.R.Gladstone, J.-C. Gérard, V. Dols, and J.H. Waite, Simulation of the morphology of the Jovian UV north aurora observed with the Hubble Space Telescope, *Icarus*, **128**, 306-321, (1997)

Gross, S.H. and S.I. Rasool, The upper atmosphere of Jupiter, *Icarus*, **3**, 311-322, (1964)

Harris, W., J.T. Clarke, M.A. McGrath, and G.E. Ballester, Analysis of Jovian auroral H Ly-α emission (1981-1991), *Icarus*, **124**, 350-365, (1996)

Hawkins, S.E., III, A.F. Cheng, and L.J. Lanzerotti, Bulk flows of hot plasma in the Jovian magnetosphere: a model of anisotropic fluxes of energetic ions, *J. Geophys. Res.*, **103**, 20031, (1998)

Herbst, E., and W. Klemperer, *Astrophys. J.*, **185**, 505, (1973)

Hill, T.W., Inertial limit on corotation, *J. Geophys. Res.*, **84**, 6554-6558, (1979)

Hill, T.W., and A.J. Dessler, Plasma motions in the planetary magnetospheres, *Science*, **252**, 410-415, (1991)

Hirschfelder, J.O., *J. Chem. Phys.*, **6**, 795, (1938), and references therein

Horanyi, M., T.E. Cravens, and J.H. Waite, The precipitation of energetic heavy ions into the upper atmopshere of Jupiter, *J. Geophys. Res.*, **93**, 7251-7271, (1988)

Hunten, D.M., Atmospheres and ionospheres, in *Jupiter (Studies of the interior, atmosphere, magnetosphere and satellites)*, ed. T. Gehrels, Tuscon: University Arizona Press, 23-31, (1976)

Hunten, D.M. and A.J. Dessler, Soft electrons as a possible heat source for Jupiter's thermosphere, *Planet. Space. Sci.* **25**, 817-821, (1977)

Ingersoll, A.P., A.R. Vasavada, B. Little, C.D. Anger, S.J. Bolton, C. Alexander, K.P. Klaasen, and the Galileo SSI Team, Imaging Jupiter's aurora at visible wavelengths, *Icarus*, **135**, 251-264, (1998)

Kane, M.B., *et al.*, Hot ions in Jupiter's magnetodisc: a model for Voyager 2 low-energy charged particle measurements, *J. Geophys. Res.*, **100**, 19473, (1995)

Kao, L., T. Oka, S. Miller, and J. Tennyson, A table of astronomically important rovibrational transitions for the H_3^+ molecular ion, *Astrophys. J. Suppl.*, **77**, 317-329, (1991)

Kim, Y.H., J. L. Fox and H.S. Porter, Densities and vibrational distribution of H_3^+ in the Jovian auroral ionosphere, *J. Geophys. Res.*, **97**, 6093-6101, (1991)

Kim, Y.H., J.L. Fox, and H.S. Porter, On H_3^+ density profiles in the Jovian auroral ionosphere, *J. Geophys. Res.*, **87**, 6093-6101, (1992)

Kim, Y.H., J.J. Caldwell, and J.L. Fox, High-resolution ultraviolet spectroscopy of Jupiter's aurora with Hubble Space Telescope, *Astrophys. J.*, **447**, 906-914, (1995)

Kim, S.K., J. Caldwell, A.R. Rivolo, R. Wagener, and G.S. Orton, Infrared polar brightening on Jupiter, 3, Spectrometry from the Voyager 1 IRIS experiment, *Icarus*, **64**, 233-248, (1985)

Kim, S.K., P. Drossart, J. Caldwell, and J.-P. Maillard, Temperature of the Jovian auroral zone inferred from 2-μm H_2 quadropole line emissions, *Icarus*, **84**, 54-61, (1990)

Lam, H.A., N. Achilleos, S. Miller, J. Tennyson, L.M. Trafton, T.R. Geballe, and G.E. Ballester, A baseline spectroscopic study of the infrared auroras of Jupiter, *Icarus*, **127**, 379-393, (1997)

Leu, M.T., M.A. Biondi, and R.Johnsen, Measurements of recombination of electrons with H_3^+ and H_5^+, *Phys. Rev. A.*, **8**, 413-419, (1973)

Livengood, T.A., T. Kostiuk, F. Espenak, and J.J. Goldstein, Temperature and abundances in the Jovian auroral stratosphere, 1, Ethane as a probe of the millibar region, *J. Geophys. Res.*, **98**, 18813-18822, (1993)

Maillard, J.P., E. Lellouch, J.H. Waite, B. Bézard, P. Drossart, J.Y. Mandin and V. Dana, Search for ionospheric winds in Jupiter from the H_3^+ emissions, *American Astronomical Society*, DPS meeting **31**, #73.07, (1999)

McConnell, J.C. and T. Majeed, H_3^+ in the Jovian Ionosphere, *J. Geophys. Res*, **92**, 8570-8578, (1987)

Miller, S., R.D. Joseph and J. Tennyson, Infrared emissions of H_3^+ in the atmosphere of Jupiter in the 2.1 and 4.0 micron region, *Astrophys J.*, **360**, L55-L58, (1990)

Miller, S., J. Tennyson, S. Lepp and A. Dalgarno, Identification of features due to H_3^+ in the infrared spectrum of supernova 1987A, *Nature*, **355**, 420-422, (1992)

Miller, S., N. Achilleos, G.E. Ballester, H.A. Lam, J. Tennyson, T.R. Geballe and L.M. Trafton, Mid-To-Low latitiude emission from Jupiter, *Icarus* **130**, 57-67, (1997a)

Miller, S., N. Achilleos, H.A. Lam, B.M. Dinelli, and R. Prangé, The impact of comet Shoemaker-Levy 9 on the Jovian ionosphere and aurorae, *Planet. Space. Sci.*, **45**, 1237-1250, (1997b)

Morgan, D.D., D.A. Gurnett, W.S. Kurth, and F. Bagenal, The source of Jovian auroral hiss observed by Voyager 1, *J. Geophys. Res.*, **99**, 21213-21224, (1994)

Neale, L., S. Miller, and J. Tennyson, Spectroscopic properties of the H_3^+ molecule: a new calculated line list, *Astrophys. J.*, **464**, 516-520, (1996)

Oka, T., and T.R. Geballe, Observations of the fundamental 4 micron band of H_3^+ in Jupiter, *Astrophys. J.*, **351**, L53-56, (1990)

Pilcher, C.B., and J.S. Morgan, *Astrophys. J.*, **238**, 375, (1985)

Prangé, R., New evidence for the role of photo-electrons in the H_2 dayglow of the giant planets, *Astron. Astrophys.* **161**, L1-L4, (1986)

Prangé, R., D. Rego, and J.-C. Gérard, Auroral Lyman α and H_2 bands from the giant planets, 2, Effect of the anisotropy of the precipitating particles on the interpretation of the 'color ratio', *J. Geophys. Res.*, **100**, 7513-7521, (1995)

Prangé, R., D. Rego, L. Pallier, L. Ben Jaffel, C. Emerich, J. Ajello, J. T. Clarke and G. E. Ballester, Detection of self-reversed Lyα lines from the Jovian aurorae with the Hubble Space Telescope, *Astrophys. J.*, **484**, L169-L173, (1997)

Prangé, R., D. Rego, L. Pallier, J.E.P. Connerney, P. Zarka, and J. Queinnec, Detailed study of FUV Jovian auroral features with the post-COSTAR HST faint object camera, *J. Geophys. Res.*, **103**, 20195-20215, (1998)

Rees, D., and T.J. Fuller-Rowell, Thermospheric responce and feedback to auroral inputs, in *Auroral Physics* , eds. C.-I. Meng, M.J. Rycroft, and L.A. Frank, 51-65, Cambridge Univ. Press, Cambridge, (1991)

Rego, D., N. Achilleos, T. Stallard, S. Miller, R. Prangé, M. Dougherty and R.D. Joseph, Supersonic winds in Jupiter's aurorae, *Nature*, **399**, 121-124, (1999)

Rego, D., S. Miller, N. Achilleos, R. Prangé, and R.D. Joseph, Latitudinal profiles of the Jovian IR emissions of H_3^+ at 4 microns with the NASA Infrared Telescope Facility, *Icarus*, **147**, 366-385, (2000)

Russell, C.T., K.K. Khurana, M.G. Kivelson, and D.E. Huddleston, Substorms at Jupiter: Galileo observations of transient reconnection in the near tail, *Adv. Space. Sci.*, **26**, 1499-1504, (2000)

Satoh, T., J.E.P. Connerney, and R.L. Baron, Emission source model of Jupiters H_3^+ aurorae: A generalized inverse analysis of images, *Icarus*, **122**, 1-23, (1996)

Satoh, T., and J.E.P. Connerney, Jupiter's H_3^+ emissions viewed in corrected jovimagnetic coordinates, *Icarus*, **141**, 236-252, (1999)

Sommeria, J., L. Ben Jaffel, R. Prangé, On the existance of supersonic jets in the upper atmosphere of Jupiter, *Icarus,* **119**, 2-24, (1995)

Sutcliffe, B.T., and J. Tennyson, The infrared spectrum of H_3^+ and its isotopomers, *J. Chem. Soc. Faraday. Trans. 2*, **82**, 1151-1162, (1986)

Suzuki, H., *Prog. Theor. Phys.*, **62**, 936, (1979)

Tennyson, J., and S. Miller, H_3^+: from first principles to Jupiter, *Contemporary Physics*, **35**, 105-116, (1994)

Thomson, J.J., Further experiments on positive rays, *Phil. Mag.*, **24**, 209, (1912)

Tokunaga *et al.*, *Proc. SPIE*, **1235**, 131, (1990)

Trafton, L.M., D.F. Lester, and K.L. Thompson, Unidentified emission lines in Jupiter's northern and southern 2μm aurorae, *Astrophys. J.*, **343**, L73-L76, (1989)

Trafton, L.M., T.R. Geballe, S. Miller, J. Tennyson, and G.E. Ballester, Detection of H_3^+ from Uranus, *Astrophys. J.*, **405**, 761-766, (1993)

Trafton, L.M., V. Dols, J.-C. Gérard, J.H. Waite, G.R. Gladstone, and G. Munhoven, HST spectra of the Jovian ultraviolet aurora: Search for heavy ion preciptiation, *Astrophys. J.*, **507**, 955-967, (1998)

Waite J.H., T.E. Cravens, J. Kozyra, A.F. Nagy, S.K. Atreya and R.H. Chen, Electron precipitation and related aeronomy on the Jovian thermosphere and ionosphere, *J. Geophys. Res.*, **88**, 6143-6163, (1983)

Waite, J.H., F. Bagenal, F. Seward, C. Na, G.R. Gladstone, T.E. Cravens, K.C. Hurley, J.T. Clarke, R. Elsen, and S.A. Stern, ROSAT observations of the Jupiter aurora, *J. Geophys. Res.*, **99**, 14799-14808, (1994)

Waite, J.H., G.R. Gladstone, W.S. Lewis, P. Drossart, T.E. Cravens, A.N. Maurellis, B.H. Mauk, and S. Miller, Equatorial X-ray emissions: implications for Jupiter's high exospheric temperatures, *Science*, **276**, 104-108, (1997)

Zarka, P., Auroral radio emissions at the outer planets: Observations and theories, *J. Geophys. Res.*, **103**, 20159-20194, (1998)